

FLEXURAL BEHAVIOUR OF GLULAM BEAMS AT AMBIENT AND ARCTIC
TEMPERATURES UNDER IMPACT LOADING

COMPORTEMENT EN FLEXION DES POUTRES EN BOIS LAMELLÉ-COLLÉ À
TEMPÉRATURE AMBIANTE ET ARCTIQUE SUJET AUX CHARGES D'IMPACT

A Thesis Submitted to the Division of Graduate Studies
of the Royal Military College of Canada
by

Nicole Valerie Wight, RMC
Captain

In Partial Fulfillment of the Requirements for the Degree of Master of Applied Science in
Civil Engineering

July 2022

©This thesis may be used within the Department of National Defence but copyright for
open publication remains the property of the author.

Acknowledgements

I would like to thank my supervisors, Dr. Christian Viau and Dr. Patrick Heffernan for their support and supervision over the past two years. Their knowledge and expertise have made the completion of this research possible.

I would like to especially thank Mr. Dexter Gaskin for all his assistance and hard work in the laboratory with helping to construct the testing frame, the instrumentation set-up and the conduct of the testing. His skills, knowledge, and experience ensured that the testing was successful and his practical ideas and suggestions of modifications to the system were instrumental to ensuring that the research was completed. I would also like to thank Mr. Steve VanVolkingburgh for all his input and additional advice throughout the construction and testing phase.

I would also like to thank Captain (Retired) Matthew Beirnes for his design and implementation of the construction of the drop hammer, as well as the preliminary Solidworks model.

The help of OCdt Hannah Robison and OCdt Alejandro Ramos Rodriguez was greatly appreciated during strain gauge installation, marking of damaged beams and during extreme cold testing.

I would like to extend a special thanks to my fiancé, Louis. Without your love, support and motivation throughout the past two years this would not have been possible. Lastly, I would like to thank my family for their support, guidance and interest in my research over the last two years.

Abstract

An increase in the exposure of structures to accidental and malicious blast explosions over the last three decades has led to a desire to increase our understanding of blast load effects on structures. High magnitude, short duration loading events, such as blast explosions and impacts, have the potential to generate catastrophic effects on infrastructure and to cause loss of life. Although design provisions for engineered wood products are included in Canada's current blast design standard, CSA S850, how these structural materials respond to blast and impact loads across a wide range of high strain rates has not been well documented. Additionally, threats to Canada's national security, specifically our need to defend Canada's North, have become increasingly urgent on the current global stage. With a requirement for an increasing presence in the North, the rise of new threats to National Security, and the need to build more environmentally sustainable buildings, the use of wood to construct blast and impact resistant structures that can be used in all areas of Canada is critical for construction in the future. It is for these reasons that an experimental program was carried out to investigate the flexural behaviour of glued-laminated timber (glulam) subjected to impact loading under ambient and extreme cold temperatures.

Quasi-static four point bending flexural tests were conducted on three 137 mm x 267 mm x 2500 mm normal temperature beams, four 137 mm x 178 mm x 1650 mm normal temperature beams, and three 137 mm x 178 mm x 1650 mm cold temperature beams to obtain average 1-minute flexural strength values. This resulted in an overall average strength increase factor (SIF) of 1.20.

Dynamic impact testing was conducted using the newly established drop weight impact testing facility at the Royal Military College of Canada, capable of imparting up to 23 kJ of energy onto small to full scale structural elements. Six 137 mm x 267 mm x 2500 mm normal temperature beams, four 137 mm x 178 mm x 1650 mm normal temperature beams, and four 137 mm x 178 mm x 1650 mm cold temperature beams were tested under dynamic loading in order to determine high strain rate effects and their behaviour under extreme loading and extreme temperature conditions.

For strain rates in the range of 0.67 to 1.05 s⁻¹, an average dynamic increase factor (DIF) on the modulus of rupture (MOR) and modulus of elasticity (MOE) of the large glulam beams was determined to be 1.13 and 1.20 respectively. For strain rates from 1.13 to 1.38 s⁻¹, the small normal temperature beams response resulted in a DIF on the MOR and MOE of 1.20 and 1.22 respectively. The cold temperature beams resulted in an increase on MOE of 1.18 under both static and dynamic conditions when compared to their normal temperature counterparts. The dynamic cold beams experienced a dynamic increase on the MOR over the normal temperature dynamic beams of 1.14. This resulted in a DIF on the MOR and MOE of 1.34 and 1.21 respectively for strain rates from 1.14 to 1.31 s⁻¹. The observed increase in strength for the dynamic cold temperature beams remains inconclusive due to the smaller number of samples.

Lastly, the beams were modeled using single degree of freedom (SDOF) analysis and conservation of energy was investigated. The study showed that SDOF analysis models the behaviour of glulam beams under impact very well, accurately estimating the maximum displacement.

Résumé

Une augmentation de l'exposition des structures aux explosions accidentelles et malveillantes au cours des trois dernières décennies a créé un intérêt d'augmenter notre compréhension des effets d'explosions sur les structures. Les chargements de grande amplitude et brève durée, tels que les explosions et les impacts, ont le potentiel de générer des effets catastrophiques sur l'infrastructure et de causer des pertes de vie. Bien que les produits en bois d'ingénierie soient inclus dans la norme canadienne sur la conception des structures soumises à des charges d'explosion, le CSA S850, la façon dont ces matériaux structuraux réagissent aux charges d'explosion et d'impact avec des taux de déformation élevés n'est pas couramment documentée en détail. De plus, les menaces à la sécurité nationale du Canada, en particulier notre besoin de défendre le Nord canadien, sont devenues de plus en plus urgentes. Avec l'exigence d'avoir une présence grandissante dans le Nord, l'ascension de nouvelles menaces à la sécurité nationale, et la nécessité de construire des bâtiments écologiquement, l'utilisation du bois pour construire des structures résistantes aux explosions et aux chocs qui peuvent être utilisées dans toutes les régions du Canada est essentielle pour le développement de l'industrie de construction. C'est pour ces raisons qu'un programme expérimental a été réalisé pour étudier le comportement en flexion du bois lamellé-collé soumis aux chargements d'impact sous des températures ambiantes et extrêmement froides.

Des expérimentations de flexion à quatre points quasi-statiques ont été effectuées sur trois poutres à température normale mesurant 137 mm x 267 mm x 2500 mm, quatre poutres à température normale mesurant 137 mm x 178 mm x 1650 mm et trois poutres à température froide mesurant 137 mm x 178 mm x 1650 mm pour obtenir les résistances de flexion normalisées à une période de chargement d'une minute. D'après les résultats de ces expérimentations, un facteur d'augmentation de force de 1,20 a été déterminé.

Des expérimentations dynamiques d'impact ont été conduites avec la nouvelle installation de recherche d'impact au Collège militaire royal du Canada, capable de transmettre jusqu'à 23 kJ d'énergie auprès des éléments structuraux. Six poutres à température normale mesurant 137 mm x 267 mm x 2500 mm, quatre poutres à température normale mesurant 137 mm x 178 mm x 1650 mm et quatre poutres à température froide mesurant 137 mm x 178 mm x 1650 mm ont été soumises à des chargements dynamiques afin de déterminer leur comportement aux taux de déformation élevé, aux chargements d'impact et de températures extrêmes.

Pour des taux de déformation de 0,67 à 1,05 s⁻¹, un facteur d'augmentation dynamique sur le module de rupture et le module d'élasticité des grandes poutres lamellé-collé était respectivement 1,13 et 1,20. Pour des taux de déformation de 1,13 à 1,38 s⁻¹, les petites poutres à température normale ont démontré un facteur d'augmentation dynamique sur le module de rupture et le module d'élasticité respectivement de 1,20 et 1,22. Les poutres à température froide ont subi une augmentation sur le module d'élasticité de 1,18 dans les tests statiques et dynamiques comparé à leurs tests équivalents à température normale. Les poutres à température froides dynamiques par rapport aux à celles chargées de façon dynamiques à température normale ont subi une augmentation sur le module de rupture de 1,14. Ces tests ont démontré un facteur d'augmentation dynamique sur le module de rupture et le module d'élasticité respectivement de 1,34 et 1,21 pour les taux de déformation de 1,14 à 1,31 s⁻¹. Les résultats reliés à l'augmentation de la résistance observée pour les poutres dynamiques à température froide sont moins conclusifs à cause du petit

nombre d'essais.

Enfin, les poutres ont été modélisées à l'aide d'une analyse à un seul degré de liberté pour les expérimentations dynamiques. Le principe de conservation d'énergie a aussi été étudié. L'étude a démontré que l'analyse à un seul degré de liberté modèle très bien le comportement des poutres en bois lamellé-collé sous des charges d'impact, estimant avec précision le déplacement maximal.

Table of Contents

Acknowledgements	ii
Abstract	iii
Résumé.....	iv
Table of Contents	vi
List of Figures	ix
List of Tables.....	xiii
List of Symbols	xv
List of Acronyms.....	xvii
Chapter 1: Introduction	1
1.1 Background	1
1.2 Aim.....	2
1.3 Objectives.....	2
1.4 Methodology and Scope.....	3
1.5 Contributions.....	4
1.6 Document Organization	4
Chapter 2: Literature Review	6
2.1 General	6
2.2 Wood as an Engineering Material	6
2.2.1 Properties of Wood.....	6
2.2.2 Engineered Wood Products	7
2.2.3 Behavior of Wood Under Extreme Cold.....	8
2.3 Impact Loading	11
2.3.1 Behavior of Wood Under Short Load Duration and High Strain Rates	11
2.3.2 Behavior of Material Under Impact Loading at Extreme Cold Temperatures	14
2.4 Blast Loading	14
2.4.1 Blast Wave Characteristics.....	14
2.4.2 Behavior of Timber under Blast Loading.....	15
2.4.3 CSA S850: Design and Assessment of Buildings Subjected to Blast Loads	18
2.5 Modelling Blast, Impact and Wood	19
2.5.1 Use of SDOF System to Represent Structural Elements.....	19
2.6 Summary	20
Chapter 3: Experimental Program.....	22
3.1 General	22

3.2	Description of Test specimens	25
3.3	Static Testing.....	29
3.4	Dynamic Testing	30
Chapter 4:	Experimental Results.....	36
4.1	General	36
4.2	Normal Temperature Testing – Large Dimensioned Beams.....	36
4.2.1	Static Testing Results	36
4.2.2	Practice Beam DNP1-267	39
4.2.3	Dynamic Testing Results	41
4.2.4	Failure Modes.....	47
4.3	Effects of Extreme Cold Temperature Testing – Small Dimensioned Beams	48
4.3.1	General	48
4.3.2	Cold Temperature Monitoring and Measurement	48
4.3.3	Static Testing.....	51
4.3.4	Multiple Impacts to DN1-178	55
4.3.5	Dynamic Testing	56
4.3.6	Failure Modes.....	63
4.4	Summary	67
Chapter 5:	Discussion	69
5.1	General	69
5.2	Normal Temperature Testing – Large Beams	70
5.3	Cold Temperature Testing – Small Beams.....	74
5.4	Overall Averages and High strain rate effects.....	86
5.5	Summary	86
Chapter 6:	Modeling and Results.....	88
6.1	General	88
6.2	SDOF Analysis.....	88
6.2.1	Validation of the SDOF Analysis Method to Represent Glulam	90
6.2.2	Appropriateness of the Current Design Codes and the Proposed Methodologies to Estimate Glulam Deflection and Resistance Under Impact Loads	98
6.3	Conservation of Energy.....	107
6.4	Summary	112
Chapter 7:	Conclusions and Recommendations.....	114
7.1	Summary	114
7.2	Conclusions	114

7.3	Supporting Conclusions	115
7.4	Recommendations for Future Research	115
	References	117
	Appendices	122
	Appendix A : Detailed Drawing of Impact Hammer	A-1
	Appendix B : Test Results of Glulam Specimens	B-1

List of Figures

Figure 2-1: Cross section of a tree trunk (Nziengui et al., 2020)	7
Figure 2-2: Wood stress-strain relationship originally proposed by Buchanan in 1990 as found in Lacroix (2017).....	7
Figure 2-3: Examples of finger joints originally from Breyer et al. (2007) but reproduced from Lacroix (2017).....	8
Figure 2-4: Specimen failure under four point bending: (a)Typical shear failure at 20°C (b)Typical tension failure at -40°C (Drake et al. 2015).....	11
Figure 2-5: Duration of various loads (Jansson 1992)	11
Figure 2-6: Madison Curve (Syron, 2010)	12
Figure 2-7: Typical Friedlander waveform (US Army Corps of Engineers, 2008)	15
Figure 2-8: Light-frame wood stud walls subjected to shock tube testing: (a) OSB sheathed wall; (b) Plywood sheathed wall (Viau and Doudak 2015)	16
Figure 2-9: CLT structures pre-blast (Weaver et al. 2018)	17
Figure 2-10: Representative dynamic failure loads of glulam beams (Lacroix and Doudak 2018a)	18
Figure 2-11: Structure idealised as a SDOF system.....	20
Figure 3-1: Preparation of the test sample for strain gauges. From left to right: sanding, sanded surface, compressed air, strain gauge and glue, soldering of tabs and leads.....	25
Figure 3-2: Strain, displacement, and temperature instrument location on the large beams.....	26
Figure 3-3: Neoprene and rigid insulation installed over thermocouple	27
Figure 3-4: Installed thermocouples in test beam	28
Figure 3-5: Delmhorst Navigator Pro Moisture Meter.....	28
Figure 3-6: Static test setup: (a) Large beam; (b) Small beam.....	30
Figure 3-7: Static test setup schematic for large beams	30
Figure 3-8: Impact hammer test apparatus oblique view with cardinal directions marked.....	31
Figure 3-9: Impact hammer test apparatus: (a) Side sketch; (b) Dimensioned view	32
Figure 3-10: Sketch of dynamic specimen reaction frame and loading beam	33
Figure 3-11: Instrumentation overview.....	35
Figure 4-1: SN2-267 Resistance and strain over time.....	38
Figure 4-2: SN2-267 Resistance and displacement over time	38
Figure 4-3: Static tests resistance versus displacement over time.....	39
Figure 4-4: Resistance versus displacement of 20 of the impacts to DNP1-267	40
Figure 4-5: Applied force over time DN3-267.....	44
Figure 4-6: Applied force, dynamic resistance, beam displacement and drop weight displacement over time for DN3-267	45

Figure 4-7: Dynamic resistance and tensile strain over time DN3-267	45
Figure 4-8: DN3-267 dynamic resistance versus midspan displacement with stiffness highlighted	46
Figure 4-9: Dynamic resistance versus midspan displacement for all dynamically tested beams	46
Figure 4-10: Failure of SN1-267, south side of beam and a close-in view	47
Figure 4-11: Failure of DN2-267, North side of beam, a close-in view and the bottom of the beam from left to right.	47
Figure 4-12: Footage from the high-speed phantom camera of DN2-267 at the beam’s maximum deflection.....	47
Figure 4-13: Temperature over time at different beam depths.....	49
Figure 4-14: SN3-178 Resistance and strain over time.....	53
Figure 4-15: SC3-178 Resistance and strain over time.....	53
Figure 4-16: SN3-178 Resistance and displacement over time	54
Figure 4-17: SC3-178 Resistance and Displacement Over Time.....	54
Figure 4-18: Static small normal and cold temperature tests resistance versus displacement over time.....	55
Figure 4-19: Resistance versus displacement of three of the impacts to DN1-178.....	56
Figure 4-20: Applied force over time DN3-178 on left and DC4-178 on right	59
Figure 4-21: Applied force, dynamic resistance, and beam and drop-weight displacement over time for DN3-178.....	59
Figure 4-22: Applied force, dynamic resistance, and beam and drop-weight displacement over time for DC4 178	60
Figure 4-23: Dynamic resistance and tensile strain over time DN3-178	61
Figure 4-24: Dynamic resistance and tensile strain over time DC4-178.....	61
Figure 4-25: DN3-178 dynamic resistance versus midspan displacement with stiffness highlighted	62
Figure 4-26: DC4-178 dynamic resistance versus midspan displacement with stiffness highlighted	62
Figure 4-27: Dynamic resistance versus midspan displacement for all dynamically tested small beams	63
Figure 4-28: Failure of a static normal temperature specimen, SN1-178, within the testing apparatus	64
Figure 4-29: Failure of a static cold temperature specimen, SC1-178, within the testing apparatus	64
Figure 4-30: Failure of a dynamic normal temperature specimen, DN1-178 in the testing pit.....	64
Figure 4-31: Failure of a dynamic cold temperature specimen, DC1-178 in the testing pit	64
Figure 4-32: Footage from the high-speed phantom camera of DN1-178 at the beam’s maximum deflection.....	65

Figure 4-33: Footage from the high-speed phantom camera of DC2-178 at the beam’s maximum deflection.....	65
Figure 4-34: Shear failures in static normal temperature test specimen SN2-178.....	66
Figure 4-35: Combined shear and flexural failure in static normal temperature test specimen SN4-178	66
Figure 4-36: Shear and flexural failure in a dynamic cold temperature test specimen SN4-178..	66
Figure 5-1: Resistance versus midspan displacement for all dynamic and static tests	71
Figure 5-2: DIF on MOR for all dynamic large beams.....	73
Figure 5-3: DIF on MOE for all dynamic large beams	73
Figure 5-4: Representative failures between static and dynamic beams.....	74
Figure 5-5: MOR values for all small beam tests.....	76
Figure 5-6: MOE values for all small beam tests.....	76
Figure 5-7: Resistance versus midspan displacement for a small beam dynamic and static test at cold and ambient temperatures.....	81
Figure 5-8: DIF on the MOR when compared to their static temperature counterparts for all small dynamic beams.....	81
Figure 5-9: DIF on the MOE when compared to their static temperature counterparts for all small dynamic beams.....	82
Figure 5-10: Representative failures between static normal temperature beams and static cold temperature beams	83
Figure 5-11: Representative failures between dynamic normal temperature beams and dynamic cold temperature beams.....	84
Figure 5-12: Shear and combined shear and flexural failures in static and dynamic beams.....	85
Figure 5-13: Relative increase in strength compared to strain rates	86
Figure 6-1: Structure idealised as a SDOF system.....	89
Figure 6-2: Forcing function used for SDOF system for DN1-267	91
Figure 6-3: Resistance function for DN5-267.....	92
Figure 6-4: Experimental and SDOF resistance-time and displacement-time histories for the elastic dynamic test on DN2-267	93
Figure 6-5: Experimental and SDOF resistance-time and displacement-time histories for the failure dynamic test on DN5-267	96
Figure 6-6: Resistance function for a normal temperature beam for Case 1 and Case 2	101
Figure 6-7: Experimental and SDOF resistance-time and displacement-time histories for the elastic dynamic test on DN3-267	102
Figure 6-8: Experimental and SDOF resistance-time and displacement-time histories for the elastic dynamic test on DN2-178	102
Figure 6-9: Experimental and SDOF resistance-time and displacement-time histories for the failure dynamic test of DN2-178.....	105

Figure 6-10: Conservation of energy balance for the failure drop of DN1-267.....	110
Figure 6-11: Conservation of energy balance for the failure dynamic test of DC3-178.....	112
Figure B-0-1: Dynamic Test Results for Specimen DN1-267	B-3
Figure B-0-2: Damage for Specimen DNP1-267	B-4
Figure B-0-3: Dynamic Test Results for Specimen DN1-267	B-6
Figure B-0-4: Damage for Specimen DN1-267	B-7
Figure B-0-5: Dynamic Test Results for Specimen DN2-267	B-9
Figure B-0-6: Damage for Specimen DN2-267	B-10
Figure B-0-7: Dynamic Test Results for Specimen DN3-267	B-12
Figure B-0-8: Damage for Specimen DN3-267	B-13
Figure B-0-9: Dynamic Test Results for Specimen DN4-267	B-15
Figure B-0-10: Damage for Specimen DN4-267	B-16
Figure B-0-11: Dynamic Test Results for Specimen DN5-267	B-18
Figure B-0-12: Damage for Specimen DN5-267	B-19
Figure B-0-13: Dynamic Test Results for Specimen DN1-178	B-21
Figure B-0-14: Damage for Specimen DN1-178	B-22
Figure B-0-15: Dynamic Test Results for Specimen DN2-178	B-24
Figure B-0-16: Damage for Specimen DN2-178	B-25
Figure B-0-17: Dynamic Test Results for Specimen DN3-178	B-27
Figure B-0-18: Damage for Specimen DN3-178	B-28
Figure B-0-19: Dynamic Test Results for Specimen DN4-178	B-30
Figure B-0-20: Damage for Specimen DN4-178	B-31
Figure B-0-21: Dynamic Test Results for Specimen DC1-178	B-33
Figure B-0-22: Damage for Specimen DC1-178	B-34
Figure B-0-23: Dynamic Test Results for Specimen DC2-178	B-36
Figure B-0-24: Damage for Specimen DC2-178	B-37
Figure B-0-25: Dynamic Test Results for Specimen DC3-178	B-39
Figure B-0-26: Damage for Specimen DC3-178	B-40
Figure B-0-27: Dynamic Test Results for Specimen DC4-178	B-42
Figure B-0-28: Damage for Specimen DC4-178	B-43

List of Tables

Table 2-1: Effects of temperature and moisture content on clear wood mechanical properties compared to 20°C. Partially reproduced from Gerhards (1982).....	9
Table 3-1: Experimental Program	23
Table 3-2: Summary of testing protocol	34
Table 4-1: Static test results large beams	37
Table 4-2: Summary of 20 elastic dynamic tests on DNP1-267	41
Table 4-3: Dynamic test results of large dimensioned beams.....	43
Table 4-4: Midpoint and failure temperatures for dynamic and static tests at various depths inferred from sample beam	50
Table 4-5: Static test results small normal temperature beams	52
Table 4-6: Static test results small cold temperature beams	52
Table 4-7: Summary of three elastic dynamic tests on DN1-178	56
Table 4-8: Dynamic test results small normal temperature beams.....	58
Table 4-9: Dynamic test results small cold temperature beams	58
Table 5-1: Summary of static and dynamic averages key properties for large beams	71
Table 5-2: DIF summary for all large beams on the MOR and MOE.....	72
Table 5-3: Results of statistical analysis on the large beam MOR and MOE	72
Table 5-4: Results of statistical analysis of the small beams	77
Table 5-5: DIF summary for all normal temperature small beams on the MOR and MOE.....	78
Table 5-6: DIF summary for all small beams on the MOR and MOE.....	79
Table 5-7: Effect of cold on mean MOR and MOE.....	79
Table 5-8: Modification factors for determining dynamic strength.....	86
Table 6-1: Elastic dynamic tests compared to SDOF models large normal temperature beams...	94
Table 6-2: Elastic dynamic tests compared to SDOF models small normal temperature beams..	94
Table 6-3: Failure dynamic tests compared to SDOF models for large normal temperature beams	96
Table 6-4: Failure dynamic tests compared to SDOF models for small normal temperature beams	97
Table 6-5: Failure dynamic tests compared to SDOF models for small cold temperature beams	97
Table 6-6: Modification factors for determining dynamic strength	100
Table 6-7: Elastic dynamic tests compared to SDOF models large normal temperature beams.	103
Table 6-8: Elastic dynamic tests compared to SDOF models small normal temperature beams	103
Table 6-9: Failure dynamic tests compared to SDOF models for large normal temperature beams	105

Table 6-10: Failure dynamic tests compared to SDOF models for small normal temperature beams	106
Table 6-11: Failure dynamic tests compared to SDOF models for small cold temperature beams	106
Table 6-12: Energy comparison for large beam elastic drops.....	108
Table 6-13: Energy comparison for large beam destructive drops	109
Table 6-14: Energy comparison for small normal temperature beam elastic dynamic tests	110
Table 6-15: Energy comparison for small normal temperature beam destructive dynamic tests	111
Table 6-16: Energy comparison for small cold temperature beam destructive dynamic tests	111

List of Symbols

f_b	Specified strength in bending
f_c	Maximum compressive stress
i_r	Specific reflected impulse
i_r^-	Negative specific reflected impulse
k	Stiffness
k_e	Equivalent spring stiffness
\bar{m}	Distributed mass
m_c	Half of the mass of the load transfer beam
t_o	Positive phase duration
t_o^-	Negative phase duration
y	Displacement
\dot{y}	Velocity
\ddot{y}	Acceleration
y_{Rmax}	Displacement at the time of peak resistance
x_{eq}	Distance from support to point of application of equivalent inertia force
ET_{beam}	Beam's total absorbed energy
F_e	Equivalent force
$F(t)$	Applied force
I	Moment of inertia
K_D	Load duration factor
KE_{beam}	Beam's kinetic energy
K_H	System factor
K_L	Load factor or lateral stability factor
K_{LM}	Load mass factor
K_m	Mass factor
K_{Sb}	Service condition factor
K_x	Curvature factor
K_{Zbg}	Size factor
L	Clear span
M_{Beam}	Mass of the beam
M_{LTB}	Mass of the load transfer bar and rollers
M_t	Total mass of the structure
M_e	Equivalent mass
P_{max}	Maximum applied load
P_r	Maximum reflected pressure
P_r^-	Negative reflected pressure
R	Standoff
R_{max}	Peak resistance
$R(t)$	Dynamic resistance
R_u	Ultimate resistance
$R(y)$	Resistance function in terms of displacement
S	Section modulus
S_D	Dynamic design strength
SL	Stress level factor
S_s	Specified material strength

T	Natural period
T_r	Time to failure in minutes
UE_{beam}	Beam's strain energy
$V(t)$	Dynamic reaction
W	Charge weight
W_{hammer}	Work done by the hammer
y_w	Displacement of the weighted box
Z	Scaled distance
Δt	Change in time
$\dot{\epsilon}$	Strain rate
ϵ_{f-c}	Compressive strain at the time of peak resistance
ϵ_{f-t}	Tensile strain at the time of peak resistance
ϕ	Factor of safety
o	First time step
man	Manufacturer provided value
n	N^{th} time step
$n-1$	Time step before the n^{th} time step
d	Dynamic testing
s	Static testing

List of Acronyms

BS	Bending Strength
CF	Cold Factor
CFS	Canadian Forces Station
CLT	Cross Laminated Timber
COV	Coefficient of Variation
DIF	Dynamic Increase Factor
EWP	Engineered Wood Product
FSP	Fibre Saturation Point
Glulam	Glue Laminated Timber
LOP	Level of Protection
LSL	Laminated Strand Lumber
LVDT	Linear Variable Differential Transformer
LVL	Laminated Veneer Lumber
LEED	Leadership in Energy and Environmental Design
MDF	Medium Density Fiberboard
MF	Melamine-Formaldehyde
MOE	Modulus of Elasticity
MOR	Modulus of Rupture
MUF	Melamine-Urea-Formaldehyde
OSB	Oriented Strand Board
PSL	Parallel Strand Lumber
PRF	Phenol-Resorcinol-Formaldehyde
SHPB	Split-Hopkinson Pressure Bar
SDOF	Single Degree of Freedom
SIF	Strength Increase Factor
TNT	Trinitrotoluene
UHPFRC	Ultra High Performance Fibre Reinforced Concrete

Chapter 1: Introduction

1.1 Background

An increase in the exposure of structures to accidental and malicious blast explosions over the last three decades has led to a desire to increase the knowledge of blast load effects on structures. High magnitude, short duration loading events, such as blast explosions and impacts, have the potential to generate catastrophic effects on infrastructure and to cause loss of life. Further, the use of wood as a material for building taller and more prominent structures has increased. However, despite wood being mentioned in blast design standards (ASCE 2011; CSA 2012; US Army Corps of Engineers 2018), these provisions, relative to reinforced concrete and steel, are lacking in quantity and are based on limited early research, mostly consisting of qualitative works on light-frame wood shelters (Marchand 2002).

As our desire to create sustainable infrastructure increases, so does the motivation to use more wood in the design of buildings. A study completed in 1996 looked at four categories of a building's lifecycle by examining a hypothetical three-storey generic office building constructed of wood, steel and concrete structural systems. They found that the initial embodied energy of a steel building and concrete building were 1.82 and 1.39 times greater than wood, respectively (Cole and Kernan 1996). Since the time of this study, the use of wood as a building material and the use of engineered wood products has grown, as well has our ability to use wood for uses that were not approved in 1996, making wood products an even more viable and environmentally sound option. Wood is being increasingly chosen as a building material for many reasons. Wood reduces greenhouse gases from construction by not using energy intensive materials, reduces greenhouse gases through the sequestering of carbon in the wood, promotes better thermal performance through tighter building envelopes, allows for faster construction times and helps support sustainable forest management policies (Ministry of Natural Resources and Forestry 2021; Ministry of Natural Resources and Forestry and Ministry of Municipal Affairs 2017). In order to have a construction material of high quality and low variability, the industry of engineered wood products (EWPs) has grown to include cross laminated timber (CLT), parallel strand lumber (PSL), laminated veneer lumber (LVL), laminated strand lumber (LSL) and glued laminated timber (glulam) (Ministry of Natural Resources and Forestry 2021). In particular, glulam and CLT have been used increasingly in new mid to high rise construction including the roof of the Richmond's Olympic Oval skating arena in Canada, an 18-storey student residence in Canada, headquarters of the Swiss media corporation Tamedia in Zurich, and the Seville's Metropol Parasol in Spain (Ministry of Natural Resources and Forestry and Ministry of Municipal Affairs 2017) .

Threats to Canada's national security, specifically our need to defend Canada's North, have become increasingly urgent on the current global stage. Canada's most recent defence policy, Strong, Secure, Engaged, indicates that Canada's national defence assets will increase their presence in the Arctic in the long term (Canadian Department of National Defence 2017). In addition, Canada's Arctic and Northern Policy Framework lists one of its main goals as ensuring that the "Canadian Arctic and North and its people are safe, secure and well-defended" (Government of Canada 2019a). The requirement to defend Canada's North and increase presence in this region has become incredibly prevalent with the current global security environment. Countries with arctic interests have been increasing their military presence in the North, making

Canadian Arctic sovereignty a priority (Stefanovich 2022). Canadian Forces Station (CFS) Alert, located 817 km from the geographic North Pole, represents not only the most northerly permanently inhabited place in Canada, but also in the world. This station experiences extreme temperatures faced by few inhabited places in the world. During the summer months there are approximately 28 frost-free days, and the average daily temperature is 10°C. During the winter months the average daily temperature is -40°C, with the record low being recorded at -50°C, (Government of Canada 2019b). As such, materials that can withstand these temperatures are critical to expanding infrastructure in Northern Regions of Canada, as well as the importance of understanding how extreme cold affects a material's properties. Already, large infrastructure constructed with engineered wood products are being developed for use in colder regions of Canada. The Macaisagi Bridge, with a 180 ton capacity, in northern Quebec, was built in 2011 out of CLT and glulam, spanning 68 m and experiencing temperatures as low as -45°C (Wang et al. 2016).

With a requirement for an increasing presence in the North, the rise of new threats to National Security, and the need to build more environmentally sustainable buildings, the use of wood to construct blast and impact resistant structures that can be used in all areas of Canada is critical for construction in the future.

With the rise in threats to our infrastructure, blast design provisions have been introduced in several countries around the world, notably CSA S850 in Canada. CSA S850 covers the design and assessment of buildings subject to blast loads in Canada and provides the means of determining dynamic strengths through strength increase factors (SIF), bringing the reported strength of the material down to an average value, and dynamic increase factors, DIF, which reflect the apparent strength increase experienced by materials when exposed to high strain rates (CSA 2012). Although these factors have been developed in detail for steel and concrete, there has been relatively little research conducted into wood's ability to withstand flexural loads over a large variety of strain rates and to the author's knowledge no testing has been done relating to wood's impact or blast flexural resistance under arctic temperatures.

1.2 Aim

The aim of this research project was to investigate the flexural behaviour of glued-laminated timber (glulam) beams subjected to impact loading, specifically examining high strain-rate effects, and their behaviour under normal temperature and extreme cold conditions.

1.3 Objectives

In order to achieve the above aim, two series of glulam beams were investigated with the following objectives.

Series 1:

- Validate the newly established drop hammer facility and experimental set-up against existing experimental results.
- Investigate the ability of a large-scale impact hammer to generate high strain rates,

throughout the response of flexural wood elements.

- Investigate the flexural response and failure loads of glulam beams subjected to static and dynamic impact loading at ambient temperatures.
- Provide recommended DIF values for glulam beams subjected to the strain rates achieved under dynamic impact testing.
- Conduct single-degree-of-freedom (SDOF) modelling to provide estimation methods for the behaviours of glulam beams subjected to impact loading.

Series 2:

- Investigate the effects of extreme cold temperatures on the flexural behaviour of glulam beams under static and dynamic loading.
- Provide recommended DIF values for glulam beams subjected to the strain rates achieved under dynamic impact testing.
- Provide recommendations on the effects of extreme cold temperature on the response of glulam to static and dynamic loading.
- Conduct single-degree-of-freedom (SDOF) modelling to provide estimation methods for the behaviours of glulam beams subjected to impact loading.

1.4 Methodology and Scope

In order to achieve the above objectives, the following methodology was used:

- Perform a detailed literature review of timber properties under dynamic and blast loading, timber design parameters, behaviour of timber under cold temperatures, blast wave characteristics and SDOF modelling.
- Conduct static and dynamic testing of ambient temperature beams in order to establish their resistance curves and flexural failure modes, as well as a recommended SIF and DIF.
- Conduct static and dynamic testing of extreme cold temperature beams in order to establish their resistance curves and flexural failure modes, as well as a recommended SIF and DIF.
- Develop SDOF modelling and compare its predictions to experimental results.

The scope of this project is limited to glulam beams which in conjunction with cross laminated timber panels generally form the load bearing elements for a wood construction project. Two sizes of glulam were tested and were limited by the size of the testing pit and the size of the freezer for the cold temperature beam specimens. The beams were all simply supported with lateral supports at their ends to represent typical wood connections.

Dynamic testing was done to simulate the effects of far-field blast explosions using an impact load. While blast loading is applied to a structure as a pressure over time, impact loading will generally be concentrated at a point on the beam. In this experimental testing a loading bar was used in order to create an area of constant moment, zero shear force in the central third of the beam, and to spread the applied load. This was used in order to approximate a far field blast load using an impact load. Using the impact hammer and a loading bar can provide a good comparison and approximation of blast loading with a more predictable loading pattern, duration and magnitude.

Testing was limited to two temperatures, ambient and extreme cold temperatures. Throughout the document the beams will continue to be referred to as cold temperature beams. This terminology is used to refer to beams that have an average internal temperature at failure of -43.5°C during static testing and -47.1°C under dynamic testing. The temperature for the beams at failure was chosen to be comparable to the coldest average temperatures experienced in the Arctic regions of Canada.

1.5 Contributions

Through this research the dynamic response of wood under distributed impact loading at ambient and cold temperatures were determined, contributing to the body of research that will inform recommended design factors in the next Canadian Blast Design Standard.

1.6 Document Organization

This document has been written and prepared in accordance with the traditional format and organization laid out in the Thesis Preparation Guidelines for the Royal Military College of Canada (Royal Military College of Canada 2015).

Chapter 1 outlines the requirement for the research project, its aim, and scope.

Chapter 2 contains the literature review focussing on the properties of wood, impact loading, blast loading, behaviour of glulam under blast loading, and SDOF of wood.

Chapter 3 highlights the experimental program detailing the static and dynamic testing procedures and set up as well as a thorough description of the beam specimens and instrumentation.

Chapter 4 presents the experimental results obtained on the beam specimens for static and dynamic testing.

Chapter 5 presents a discussion of the static and dynamic test results. This includes a determination of the dynamic increase factor (DIF) and comparison to the SDOF model.

Chapter 6 discusses the SDOF analysis conducted. This chapter investigates the model description, and the limitations of the modelling.

Chapter 7 highlights the most significant findings of the research project and highlights areas for future study.

Appendix A includes detailed drawings of the impact hammer, support and loading system and instrumentation placement.

Appendix B contains the experimental dynamic results of all tests conducted on glulam specimens. Typical data presented in this appendix includes a brief synopsis of each test, as well as relevant test results and photographs taken after testing.

Chapter 2: Literature Review

2.1 General

Both accidental and intentional blasts have occurred more regularly in the last three decades, creating catastrophic effects on infrastructure and loss of life. Incidents such as terrorist bombings of the Murrah Federal Building in Oklahoma City, United States (1995), and Mumbai attacks, Mumbai, India (2008), and accidental explosions such as Lac-Mégantic rail disaster, Canada (2014) and the Port of Beirut explosion, Lebanon (2020) have all increased the desire to create and retrofit buildings to be resistant to blast effects (Moon 2009; Ullah et al. 2017; Viau and Doudak 2015). In addition to this, the use of wood as a material for building taller and more prominent structures has increased. However, despite wood being mentioned in blast design standards (ASCE 2011; CSA 2012; US Army Corps of Engineers 2018), these provisions, relative to reinforced concrete and steel, are lacking in quantity and are based on limited early research, mostly consisting of qualitative works on light-frame wood shelters (Marchand 2002). Materials that inherently have more blast resistant capability such as concrete and steel have generally been the focus of blast design standards (ASCE 2011; CSA 2012; Joint Departments of the Army Air Force and Navy and the Defense Special Weapons Agency 2002; US Army Corps of Engineers 2008). The below literature review focuses on wood as an engineering material, including its properties at high strain rates and under extreme cold conditions, the properties of blast waves and impact loading, as well as the use of SDOF systems to represent structural elements response to these loading patterns.

2.2 Wood as an Engineering Material

The following section will further investigate the properties of wood, the recent developments in engineered wood products, the behaviour of wood under extreme cold and the behaviour of wood under high strain rates.

2.2.1 Properties of Wood

Wood's mechanical properties differ along its three directions (longitudinal, radial, and tangential) making it an orthotropic material. Since wood comes from a living organism the way in which that organism grows affects properties such as the wood's density, irregularities such as knots and strength. The various sections of a tree trunk can be seen in Figure 2-1. Specifically of note, as will be discussed in wood's response to extreme cold, are the areas of latewood and earlywood present within a sample. Each annual ring of a tree will be composed of these two components. 40-80% of the growth ring will be comprised of earlywood, which is grown early on in the season where there is more moisture in the environment creating larger cells. As the growth of the tree slows down later in the growth season, there is less moisture readily available and growth slows, producing smaller, denser and stronger cells (Domec 2002).

Wood is also known to have properties that are very dependent on the rate and duration of the applied load. Adding to the complexity of wood testing, is that clear wood, or wood that has no visible defects, will perform differently than common wooden members typically used in construction, which contain natural defects (Lacroix and Doudak 2018b). This means that some experimental results using clear wood may not always be representative of real-life behavior.

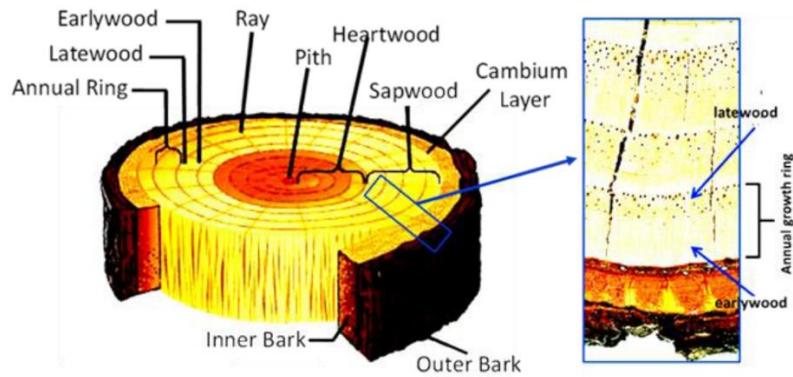


Figure 2-1: Cross section of a tree trunk (Nziengui et al., 2020)

Wood is being increasingly chosen as a building material for many reasons. Wood sequesters carbon when it is cut down, aiding to reduce greenhouse gases. It also reduces greenhouse gases from construction by not using energy intensive materials, it promotes better thermal performance through tighter building envelopes, allows for faster construction times and helps support sustainable forest management policies (Ministry of Natural Resources and Forestry 2021; Ministry of Natural Resources and Forestry and Ministry of Municipal Affairs 2017).

The stress strain relationship for a wooden member can be seen in Figure 2-2 . This curve, originally proposed by Buchanan in 1990 (reproduced in Lacroix 2017), shows that the tensile stress-strain relationship follows linear elastic behaviour, until brittle fracture. The compressive behaviour is represented by a bi-linear curve with yielding occurring at the maximum compressive stress, f_c , followed by a linearly falling branch that is a ratio of the wood's initial modulus of elasticity.

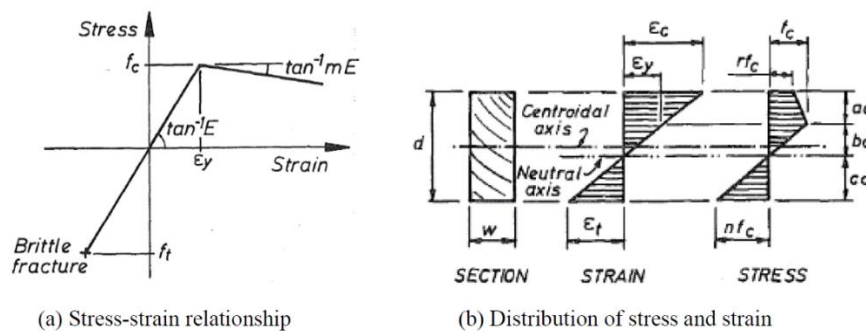


Figure 2-2: Wood stress-strain relationship originally proposed by Buchanan in 1990 as found in Lacroix (2017)

2.2.2 Engineered Wood Products

In order to obtain a construction material of higher quality, with less inherent variability, the industry of engineered wood products has grown including cross laminated timber (CLT), parallel

strand lumber (PSL), laminated veneer lumber (LVL), laminated strand lumber (LSL) and glue laminated timber (glulam) (Ministry of Natural Resources and Forestry 2021). Glulam and CLT especially have been used increasingly in new mid to high-rise construction including the roof of the Richmond’s Olympic Oval skating arena in Canada, an 18-storey student residence in Canada, headquarters of the Swiss media corporation Tamedia in Zurich, and the Seville’s Metropol Parasol in Spain (Lacroix and Doudak 2018a; Ministry of Natural Resources and Forestry and Ministry of Municipal Affairs 2017). Engineered wood products improve the reliability of wood properties by reducing the effects of defects and shrinkage compared with non-engineered products (Ministry of Natural Resources and Forestry and Ministry of Municipal Affairs 2017).

Glulam is an engineered wood product that uses layers of lumber glued together with a strong adhesive, with all grains of wood connected in the same direction. This product will very often include finger joints which are used to create longer single pieces of wood than would normally be created by using mass timber, as can be seen in Figure 2-3. The adhesive is designed so that its capacity is always equal or greater than that of the wood. Glulam can be used to achieve very large spans and can also be formed into curved shapes, making it a very useful material for supporting structural members. Glulam is commonly used in post and beam, heavy timber structures and wood bridges as headers, beams, girders, purlins, columns, and heavy trusses (Canadian Wood Council 2021).

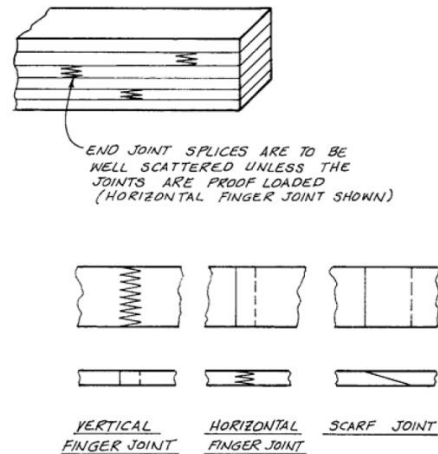


Figure 2-3: Examples of finger joints originally from Breyer et al. (2007) but reproduced from Lacroix (2017)

2.2.3 Behavior of Wood Under Extreme Cold

As mentioned in Section 1.1, Canada’s arctic region represents an area increasingly important to Canada’s sovereignty and national security. With increasing international interest and our requirement to operate in the arctic, materials that are able to be employed in the extreme environments of Northern Canada is of great importance.

Although studies surrounding the behaviour of wood under extreme heat has been studied on many occasions in order to evaluate its fire resistance, the studies evaluating the effects of extreme cold on wood’s properties are more limited.

Gerhards (1982) summarized data from various reports outlining the effects of moisture content and temperature on the mechanical properties of clear wood. It was surmised that almost all mechanical properties of wood increase as both moisture content (below the fibre saturation point (FSP)) and temperature decrease. Table 2-1 shows the effects of temperature and moisture content on clear wood properties compared to 20°C. As can be seen in the table the higher the moisture content the more the strength and stiffness increase at lower temperatures indicating that the formation of ice crystals may have a large impact on the strength of wood at low temperatures. However, regardless of the moisture content there is a large increase in bending strength and a lesser increase in stiffness at low temperatures. The study also suggested that certain properties of wood such as the proportion of late wood to early wood in a specimen will affect its mechanical response to temperature and moisture content (Gerhards 1982).

Table 2-1: Effects of temperature and moisture content on clear wood mechanical properties compared to 20°C. Partially reproduced from Gerhards (1982)

Property	Moisture content %	Relative change in mechanical property from 20°C	
		-50°C %	50°C %
Modulus of elasticity parallel to the grain	0	+11	-6
	12	+17	-7
	> FSP	+50	n/a
Bending strength	≤ 4	+18	-10
	11-15	+35	-20
	18-20	+60	-25
	≥ FSP	+110	-25

Schmidt and Pomeroy (1990) investigated the bending of a conifer branch at subfreezing temperatures and found that the modulus of elasticity (MOE) increased in decreasing temperatures increasing the branches rigidity. They postulated that this was due to ice crystals forming in the frozen wood (Schmidt and Pomeroy 1990).

Green and Evans (2008) looked at the immediate effects of temperature on the MOE of green and dry lumber, investigating the effects on 2x4 pieces of lumber at 4% and 12% moisture content, as well as green lumber between -26°C to +66°C. For all moisture contents they found that as the temperature decreased the MOE increased. They found that the dryer wood (4% moisture content) was less sensitive to changes in temperature than those of higher moisture content (Green and Evans 2008). Jiang et al. (2014) investigated the compressive strength and MOE parallel to the grain of oak at ultra-low and high temperatures, investigating results in the range from -196°C to 220°C. The clear wood specimens investigated were 20 mm x 20 mm x 30 mm. This study involved the largest range and most extreme temperatures of any of the other studies. They found that the failure pattern of the specimens varied depending on the temperature, with four patterns and temperature ranges being identified. They also found that the lower the temperature the stronger and stiffer the specimens were with increases of 283% for the compressive strength and 146% for the MOE parallel to the grain when the temperature decreased from 23°C to -196°C (Jiang et al. 2014).

Szmutku et al. (2013) reported a strength reduction in spruce wood that had previously been

frozen. The moisture content of their logs was much greater than that typically used in construction, with the logs having between 150% and 159% moisture content. The testing occurred at room temperature. Their results indicated that the formation of ice crystals within the cell structure of the wood could damage cells and cause decreases in mechanical properties once the wood was unfrozen, especially when the freezing rate was slow ($-1^{\circ}\text{C}/\text{h}$). They also found that cyclic temperatures affected the MOE, MOR and compressive strength (Szmurku et al. 2013). Contrary to this Zhao et al. (2015) investigated the effects of low temperature cyclic treatments on the MOE of birch wood using temperatures ranging from -196°C to 20°C . However, they found that after four cycles at low temperature that the MOE of wood was not decreased at all, indicating that wood was relatively resistant to the temperature changes (Zhao et al. 2015).

Aryilmis et al. (2010) investigated the effects of temperatures ranging from -30°C to $+30^{\circ}\text{C}$ on the bending strength (BS) and MOE of plywood, medium density fiberboard (MDF), and oriented strand board (OSB). They found that the BS and MOE of each wood-based panel increased with decreasing temperatures. They found that the most dramatic increase in BS and MOE occurred between -10°C to $+10^{\circ}\text{C}$. They suggested that this increase in strength was due to the formation of ice crystals on the wood cell walls, with samples having an initial moisture content between 8-9% depending on the type of wood panel (Aryilmis et al. 2010). Bekhta and Marutzky (2007) investigated the effects of temperatures ranging from -40°C to $+40^{\circ}\text{C}$ on the BS and MOE of particle board. They also found that lower temperatures meant an increase in BS and MOE. They estimated that this was due to the cellulose and lignin in wood increasing their strength due to the molecules approaching one another and forging stronger bonds (Bekhta and Marutzky 2007).

Drake et al. (2015) looked at the effects of temperature and moisture content on the shear behaviour of glulam beams. They investigated two moisture contents, 12% and 28%, and three different temperatures, -40°C , 0°C and 20°C . Although they were investigating the shear failure of the beams, they found that at -40°C that the failure mechanism changed from a shear failure to a flexural failure which can be seen in Figure 2-4. They found that the lower the temperature the higher the strength and stiffness observed. They also found that the higher moisture content beams experienced greater gains of strength and stiffness. However, these observations were complicated by the fact that the failure mechanism of the beams changed at -40°C . They suggested that this stiffening and strength increase may be due to the combined effects of the formation of ice crystals, as was postulated in previous studies, the stiffening of cellulose fibrils and the stiffening of the adhesives used (Drake et al. 2015). Wang et al. (2016) investigated the effects of low temperature on the block shear strength of Norway spruce glulam joints, looking at the performance of three different adhesives in temperatures ranging from 20°C to -60°C . Over the entire range they found that the block shear strength did not show any statistically significant change, but importantly also indicated that the three adhesives investigated, phenol-resorcinol-formaldehyde (PRF), melamine-formaldehyde (MF) and melamine-urea-formaldehyde (MUF) were unaffected by low temperatures (Wang et al. 2016). Lastly, Yang et al. (2021) investigated the effects of freeze-thaw cycles on the properties of glulam exposed to an outdoor environment by looking at the thickness swelling rate, static bending strength, elastic modulus, shear strength and the peeling rate of the adhesion layer. The specimens were subjected to twenty-one aging cycles, with each cycle lasting sixteen hours, half of the specimens at -20°C and the other half at 20°C , and testing occurring every seven cycles. They found the dimensional stability of the wood to be unaffected but observed a gradual decrease in the bending strength and MOE. They found that for low density wood (air dried density of $0.40\text{ kg}/\text{m}^3$) that the bending strength of the wood was the most affected by freeze thaw cycles, but that for high density wood (air dried density of $0.66\text{ kg}/\text{m}^3$) that the shear strength of

the adhesive layer was more affected. For the high density wood, a decrease of 37.8% for the bending strength and 24.6% for the MOE was observed and for the low density wood a decrease of 41.7% for the bending strength and 36.7% for the MOE was observed (Yang et al. 2021).



Figure 2-4: Specimen failure under four point bending: (a) Typical shear failure at 20°C (b) Typical tension failure at -40°C (Drake et al. 2015)

In summary, wood has been shown to have an increase in both strength and stiffness at reduced temperatures. This may be due to several reasons including the formation of ice crystals or the stiffening of cellulose fibrils, and in the case of glulam the stiffening of the adhesives used. Glulam has been shown to increase in strength at lower temperatures, although the studies were designed to investigate shear failure rather than flexural, making direct comparisons difficult. Additionally, no studies could be found investigating both cold and high strain rate effects on glulam beams. Moisture content has also been shown to greatly affect the strength and stiffness of wood at low temperatures and cyclic temperatures have been shown to have a negative affect on strength and stiffness.

2.3 Impact Loading

The rate by which a load is applied, known as the rate of loading, can significantly affect the material properties of a structural member. This is especially important when considering impact and blast resistance as the duration of loading is generally much shorter than normal design loads (i.e. dead, live, snow). Figure 2-5 highlights the duration range for a variety of loads.

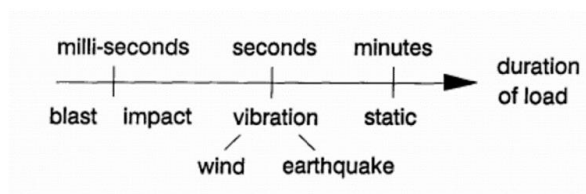


Figure 2-5: Duration of various loads (Jansson 1992)

2.3.1 Behavior of Wood Under Short Load Duration and High Strain Rates

Generally in wood design, the duration of the load affect is derived from the Madison Curve shown in Figure 2-6 (Syron 2010). As can be seen from the curve, the shorter the duration of load the more load the wood will be able to support. This is due to creep effects in wood. However, at

a load duration of two seconds the load duration factor plateaus. When the load duration is less than two seconds, proposed curve and the effects of creep do not increase. It is in these cases that the effects of high strain rates must also be considered, which causes additional increases in material capacity.

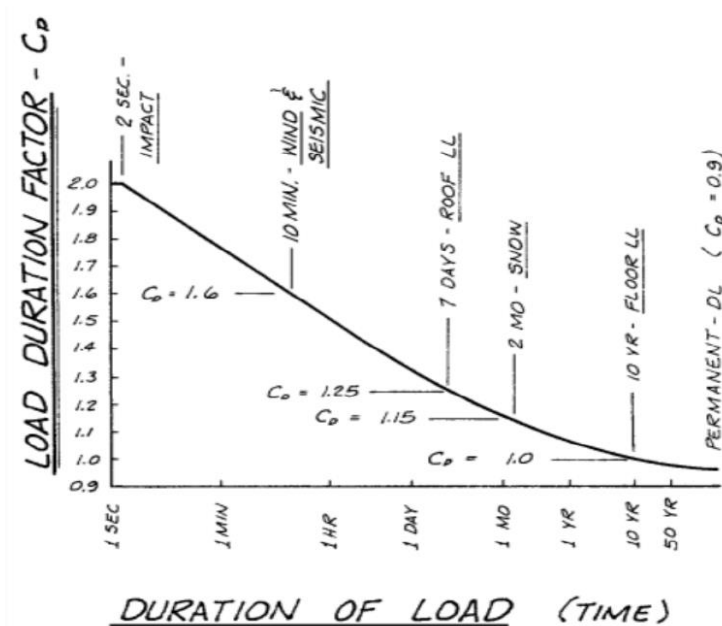


Figure 2-6: Madison Curve (Syron, 2010)

Karacabeyli and Barrett (1993), developed a trend relationship between stress level and the time to failure by looking at data from multiple different studies considering time to failure between one second and 500 hours. In this way failure loads can be normalized to a 100% strength value which corresponds to a testing time of 1 minute using Equation [2.1] (Karacabeyli and Barrett 1993).

$$SL = 100.0 - 3.5 \log_{10} T_r \quad [2.1]$$

Where SL is the stress level factor for the beam and T_r is the time to failure in minutes.

Nadeau et al. studied the fracture mechanisms of wood and determined that the delayed fracture of wood at high loading rates is due to subcritical crack growth (Nadeau et al. 1982). In 1916 Elmendorf had conducted impact bending tests on very small beams using the Hatt-Turner drop testing machine. These tests indicated a 1.78 times increase in strength when the static to impact load was considered at a load duration of 0.015 s (Gilbertson and Bulleit 2013).

Cousins (1974) looked at the effects of strain rate and moisture content on the failure of wood at the microscopic level under tensile forces. Although the dimensions of the samples are small and not representative of actual wood members in structures, it does give an indication of how failure may be occurring at the cellular level. Specifically, the authors investigated the rates of failure that were considered as transwall (i.e., failure through the cell walls) and intrawall

failures (ie failure between cell walls). The results indicated that the higher moisture content affected the strength of the hemicellulose and lignin, which compose the outer wall of the cells, with their strength greatly increasing at high strain rates. This indicated that the strength of wood at high strain rates can be correlated to the moisture content and some of these strengths increases occur at the cellular level (Cousins 1974).

Mindess and Madsen (1986) looked at the fracture of wood under impact loading (345 kg from a 610 mm height) by looking at three specimen types. The first type was clear wood, the second type had a 35 mm notch sawn into the bottom of the beam directly under the point of impact, and the third specimen type had a large knot located on the bottom face approximately 50 mm from the point of loading. The authors examined the failure mechanisms of the wood by looking at high-speed camera footage. The failure mechanism for all beams was similar with crushing occurring at the point of impact followed by a single crack from the bottom of the beam to the point of impact, followed by tensile failure. The failure occurred through the notch and through the knot in the second and third sample indicating the importance of defects in the failure mechanism of the wood. Most importantly, the dynamic failure mode differed to that observed under static loading (Mindess and Madsen 1986).

Jansson (1992) noted while investigating the impact bending strength of wooden beams that the impact energy is converted to both strain energy and kinetic energy. The amount and type of energies converted during testing will tend to differ significantly between test setups, depending on the instrumentation of the specimen, the height and weight of the dropped weight, and the way in which the forces are transferred to the specimen. As part of the experimental program, a load cell was used at the point of impact, to allow for the decoupling of the applied load and the inertial forces of the beam using modal analysis. A strength decrease of 15% was exhibited in the weaker specimens when looking at short term loading (10 ms) once the dynamic effects were separated from the static strength of the specimen (Jansson 1992).

Bragov and Lomunov (1997) conducted 20 mm diameter split Hopkinson pressure bar tests and plane wave impact experiments of various wood species in order to examine the impact resistance and ability to dampen impact loads when used as a packing material for sensitive materials. At an average strain rate of $1.5 \times 10^3 \text{ s}^{-1}$ a 150% increase in compressive strength parallel to the grain was observed, relative to static strength. A linear stress-strain relationship was observed under the compressive loading of the wood (Bragov and Lomunov 1997).

Neumann et al. (2011) looked at the impact compressive strength of spruce wood using a servo-hydraulic impact test facility in order to investigate its behaviour under large deformations, for consideration of its use as transport packaging material for radioactive materials. Neumann found that at an impact speed of 3 m/s, which correlated to a strain rate of 30 s^{-1} , a 30% increase in compressive strength was observed (Neumann et al. 2011).

Gilbertson and Bulleit (2013) conducted 64 tests using the standard split-Hopkinson pressure bar (SHPB) test in order to evaluate the behaviour of wood at high strain rate ($70 - 340 \text{ s}^{-1}$), short duration loads ($70 - 150 \mu\text{s}$). The split-Hopkinson pressure bar was initially used to study the effects of high strain rate on the behaviour of metals and this testing was also used to validate its use for assessing the properties of wood. They found increases in the strength of wood for high strain rate compression and their data concluded that the Madison curve could be used for design, with their results indicating that slightly higher load duration factors could be accommodated

(Gilbertson and Bulleit 2013).

2.3.2 Behavior of Material Under Impact Loading at Extreme Cold Temperatures

Beirnes et al. (2019) looked at the impact resistance of thin ultra high performance fibre reinforced concrete (UHPFRC) panels. Modular panels were tested under extreme cold temperatures meant to simulate arctic temperatures, with testing being conducted at an average temperature of -55°C. At cold temperatures, the panels experienced, on average, a strength increase of 10% under quasi-static loading. At smaller drop heights of 350 mm and 500 mm the cold temperature beams exhibited a large increase in the residual strength compared to their ambient temperature counterparts after impact. Results at higher drop heights were inconclusive (Beirnes et al. 2019).

2.4 Blast Loading

2.4.1 Blast Wave Characteristics

Explosions can be classified in multiple ways. They can be defined based on their type (physical, chemical, electrical, and nuclear), the state of the explosive (solid, liquid, or gas), the class of explosive (high and low order explosives), and shape of the blast wave (spherical and hemispherical) (Cormie et al. 2020; Ngo et al. 2007; Ullah et al. 2017). The two parameters that most affect the pressure and impulse felt by the building due to a blast wave are the charge weight, W , and the standoff (distance from the detonation site), R (Cormie et al. 2020). Since explosives can be made and composed of various types of materials, TNT is used as a reference explosive (Ullah et al. 2017). In this way, the power and energy due to various explosions generated from various explosive materials can be compared to one another (Ullah et al. 2017). These two parameters are used in the Hopkinson-Cranz blast scaling law, see Equation [2.2], to define a scaled distance, Z , that can then be used to determine the blast wave characteristics (Ngo et al. 2007).

$$Z = \frac{R}{W^{1/3}} \quad [2.2]$$

The blast wave that follows detonation is caused by “the expansion of the hot gases at extremely high pressure [causing] a shock wave that moves outward at high velocity” (Ullah et al. 2017). The pressure-time history of this wave is approximated by the Friedlander waveform equation, seen in Figure 2-7 (US Army Corps of Engineers 2008). The red line shows the pressure that will be felt by a wall perpendicular to the blast wave over time as a result of reflection. The pressure will first reach a maximum reflected pressure, P_r (Cormie et al. 2020). This decreases to ambient pressure over the positive phase duration, t_o , and the area under the curve is referred to as the specific reflected impulse, i_r . The pressure then drops below ambient, to the negative reflected pressure, P_r^- . The pressure occurs over the negative phase duration, t_o^- , and the area under the curve is referred to as the negative specific reflected impulse, i_r^- . The side walls and roof will also be exposed to a similar time history except that they will be exposed to side-on or incident pressures defined by P_s , i_s , P_s^- , and i_s^- . The phase durations will remain the same. The reflected pressure will always be higher than the incident pressure as the air molecules have time to build-up on the surface facing the blast before being reflected. The blast wave is often simplified to a triangular distribution whose pressure and impulse remains the same, but whose phase duration time is

modified so that the area under the curve remains the same (Cormie et al. 2020). This allows for a structure's response to be determined more easily, such as through close-form numerical solutions.

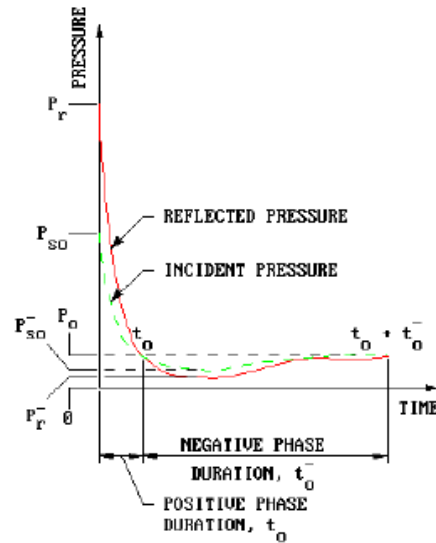


Figure 2-7: Typical Friedlander waveform (US Army Corps of Engineers, 2008)

2.4.2 Behavior of Timber under Blast Loading

Laminated strand lumber was evaluated by Syron (2010) to better understand the behaviour of high-performance wood composite under blast loading that could be used in the configuration of wooden wall panels. The effect of strain rate on the modulus of elasticity and component strength were investigated. It was observed, under dynamic tensile loading, that the strain rate did not affect the modulus of elasticity nor the strength. However, under compression loading, increases in strength and MOE were observed for strain rates between 1×10^{-5} and $1 \times 10^{-1} \text{ s}^{-1}$ (Syron 2010).

Jacques et al. (2014) investigated spruce-pine-fir lumber specimens under shock tube-simulated blast loading which was used in order to generate a pressure-impulse combination that would create the highest strain rate possible and exceed the dynamic MOR of the specimen. Under strain rates between $6 \times 10^{-6} \text{ s}^{-1}$ and 0.4 s^{-1} and considering inertial effects, it was observed that the MOR increased as a function of higher strain rates, while no such statistically significant increase could be determined for the MOE and strain at rupture. Brittle flexural failures resulting from rupture of the tension fibre was the most common dynamic failure mode. An average dynamic increase factor (DIF) for the MOR of 1.41 was determined at an average strain rate of $2.1 \times 10^{-1} \text{ s}^{-1}$ (Jacques et al. 2014).

Viau and Doudak (2015) investigated the behaviour and retrofit options for light-frame wood stud walls subjected to blast loads (Viau and Doudak 2015). Various sheathing configurations were investigating, including 11mm oriented strand boards (OSB) and 18.5mm plywood, as well as some configurations reinforced with Welded Wire Mesh (WWM). The objective was to discover how typical light frame wood walls behave when subjected to severe blast loads, and potential reinforcement methodologies. It was observed during the tests that when the sheathing was able to transfer the load to the studs that failure of the studs was a flexure failure,

however the failure mode was brash. The elements that were sheathed with only OSB showed a premature failure of the sheathing before reaching the full capacity of the studs, as can be seen in Figure 2-8 (a). In addition, this sheathing failure created large amount of high-velocity flying debris. The walls sheathed with plywood performed much better than those with OSB. In the wall specimens sheathed with plywood, the failure of the studs occurred first followed by a mid-height failure of the sheathing in flexure, as can be seen in Figure 2-8 (b). However, this failure mode still had debris caused by studs. Looking at the failure mode for the studs used with the plywood sheet, it was found that the nail connections between the sheathing and stud withdrew, due to their weak capacity to resist the force in an out of plane direction. As such screws were used in the set of wall panels that were tested that had both OSB and plywood sheathing, one over-top the other. This test reduced the amount of debris greatly and allowed the full structural response in the studs to be developed. Lastly, the walls that were equipped with WWM allowed the sheathing to properly distribute the load and minimised the amount of debris (Viau and Doudak 2015).

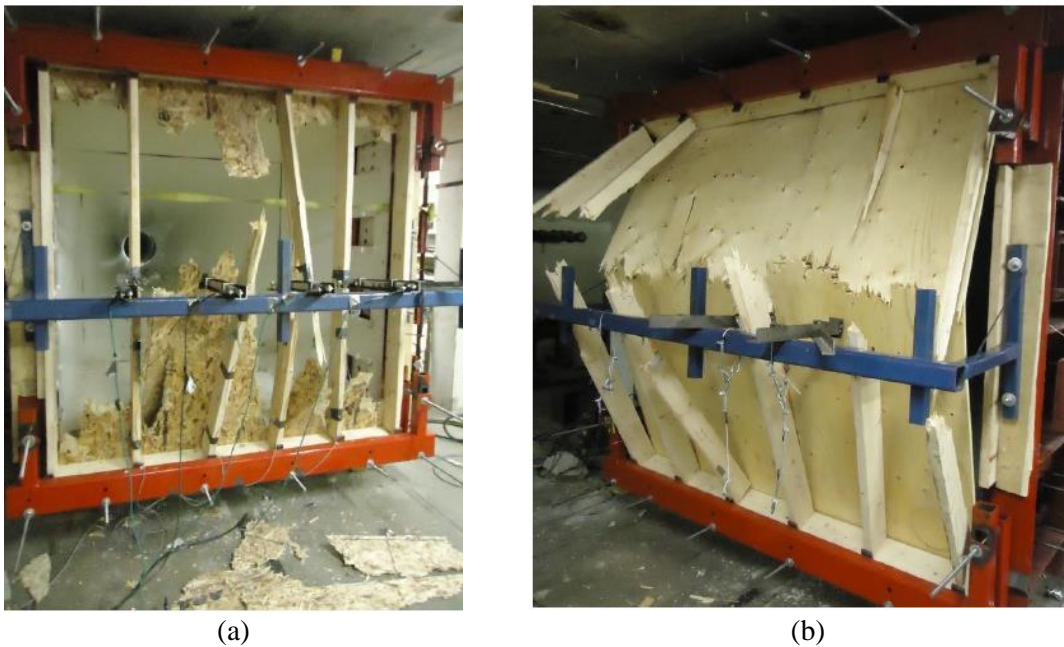


Figure 2-8: Light-frame wood stud walls subjected to shock tube testing: (a) OSB sheathed wall; (b) Plywood sheathed wall (Viau and Doudak 2015)

In 2016, a series of live blast experiments were conducted on three, two-storey, single-bay CLT structures (Weaver et al. 2018). The tests, although using only two stories, simulated the gravity loading of a five-storey building at the first-floor front panel of the structure by using precast concrete blocks. The buildings were exposed, first, to a blast that was designed to ensure the response remained elastic and, second, a set of tests to bring the structures into their plastic range. Before conducting dynamic testing, CLT panels were loaded to failure monotonically by using an actuator applying a constant axial load and a load tree applying a gradually increasing out of plane load. The panels generally failed at a knot, finger joint, or sloped grain. For the explosive testing, the structures tested are seen in Figure 2-9. All structures were placed so that they were 22.9 m away from the charge. For the first test 30.4 kg of TNT was used in order to displace the structure within its elastic limit and 90.3 kg of TNT was used to displace the structure to

approximately 1.5 times its elastic limit. The charges were detonated 0.46 m above the ground. There was no observed damage after the elastic tests and damage was almost exclusively concentrated to the outside walls of the structure during the inelastic tests. The test data was compared to the values predicted by Kingery and Bulmash curves. There was good agreement between the peak pressures observed, but there were differences in the experimental impulse. This is likely due to the Kingery and Bulmash curves not considering clearing effects. Another important observation was that the panels rebound response often exceeded the inbound response, highlighting the need to focus further testing on the negative phase of the blast pressure and not solely focus on the positive phase (Weaver et al. 2018).



Figure 2-9: CLT structures pre-blast (Weaver et al. 2018)

Poulin et al. (2018) conducted shock tube testing on CLT panels of two different thicknesses, three-ply (105 mm thick) and five-ply (175 mm thick). In terms of dynamic failure modes of the panels, differences were observed between the main failure mode in the monotonic testing compared to the dynamic. Static testing resulted in flexural failures. During dynamic testing some of the CLT panels failed in rolling shear, whereas others failed in flexure. Based on the ratio of the static to dynamic resistances, a DIF of 1.28 for the resistance was determined for the panels with a coefficient of variation of 0.06, whereas the stiffness did not appear to be affected by the increased strain rates. Since the panels were all the same size, and with only two separate thicknesses, it is not evident as to why the failure mechanisms fluctuated between a solely flexural failure and a rolling shear failure followed by flexural failure (Poulin et al. 2018).

Although EWPs are currently included in some blast design standards, glulam's response to blast loading is not well documented (Lacroix and Doudak 2018a). Shock tube tests were performed at the University of Ottawa in response to this gap in literature, testing 70 beams and columns under blast loading with three different cross sections (Lacroix 2017). The beams were found to experience a brash flexural failure dynamically, compared to the simple or splintering static flexural failures (Lacroix and Doudak 2018a). During the static tests, the beams failed either at a knot or a finger joint. During the dynamic tests, the beams that had a finger joint in the outer tension laminate within the two load application points had the failure initiate from this location.

Beams with staggered finger joints were found to have failure modes more similar to static loading. Beams with multiple laminates across their widths, often had greater crack propagation and splintering compared to those with a single laminate across their width (Lacroix 2017). This can be seen in Figure 2-10. Figure 2-10 (a)-(c) represent brush failures. Figure 2-10 (d) and (e) show crack propagation and splintering that was observed in beams with multiple laminates across the member width. Beams with staggered finger joints, Figure 2-10 (e), resembled the static failure mode. There was a significant difference observed in the value for the DIF, depending on the failure mode of the beam. As such, the study recommended a DIF of 1.14 for strain rates between 0.14 and 0.51 s^{-1} , but only for cases where continuous finger-joints (single laminate width) or closely aligned finger-joints (multiple laminates width) are not located in the high moment region. Otherwise, the recommended DIF was unity. It was recommended that the structure's resistance curve be represented as linear elastic as the beams did not have a ductile response after going past their peak resistance (Lacroix and Doudak 2018a). Similar observations were made by Viau and Doudak (2021a) resulting in a DIF of 1.10 for strain rates between 0.37 to 0.51 s^{-1} for glulam beams. They also looked at the effects of multiple pressure-impulse combinations and found that as long as the elastic limit of the member is not passed, the wood member remains undamaged (Viau and Doudak 2021a). Throughout all the above studies, simply supported boundary conditions were used.

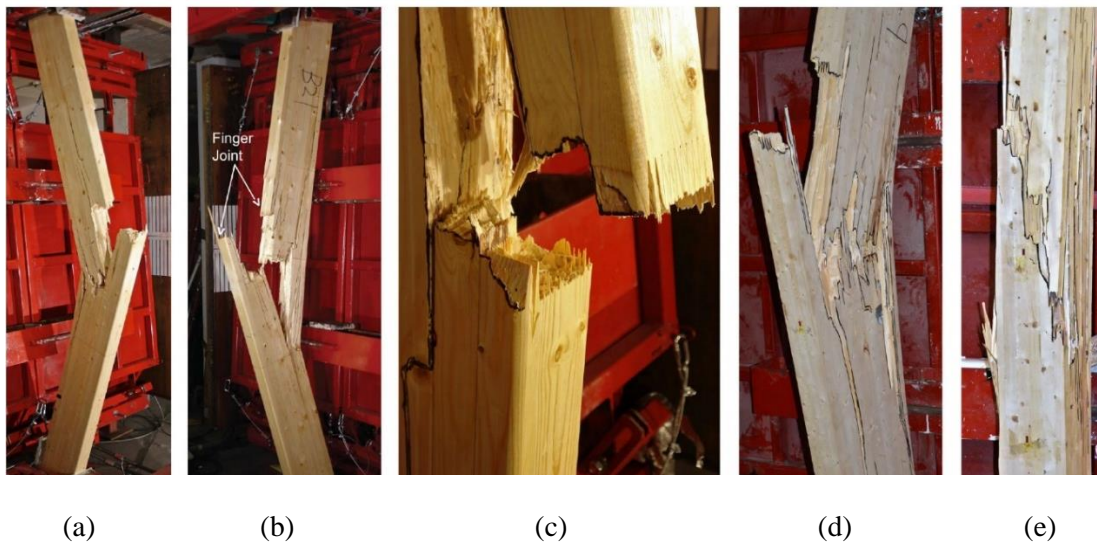


Figure 2-10: Representative dynamic failure loads of glulam beams (Lacroix and Doudak 2018a)

2.4.3 CSA S850: Design and Assessment of Buildings Subjected to Blast Loads

The Canadian blast standard, CSA S850 (2012), aims to minimise the damage and casualties caused by blasts, with the recognition that these will never be completely eliminated. The standard aims to accomplish its main objective through four main design and performance objectives: limiting progressive structural collapse, limiting damage to structural components, mitigating damage to the building envelope, and minimizing flying and falling debris. However, due to the unpredictable nature, severity, and location of blasts, there is great uncertainty in the prediction of these loads (CSA 2012).

Each building is assigned a level of protection (LOP) and each structural element is assigned a component damage level depending on the element's importance in the structure and the chosen LOP. These damage levels are then converted to a response limit, which are described as either a maximum allowable deflection or rotation for a member, which is then outlined for various types of materials (CSA 2012). For example, a building that requires a low LOP is one where progressive collapse is mitigated, but the building will not be able to remain function after an attack. For a primary structural component in a building that requires a low LOP, a moderate damage level is tolerated, which will in turn affect the level of deflection and rotation accepted in the design of that member depending on the element type, material and properties.

When considering a material's properties there are two main factors that the standard applies to consider the material's in-situ strength and the effects of high strain rate. The SIF brings the specified static material strength from the 5th percentile values to the mean values. The DIF is a factor that reflects the apparent strength increase experienced by materials when exposed to high strain rates. Both factors are applied to the specific material static strength in order to calculate a dynamic design strength. Recommended strength increase factors for various materials can be found in Table 7.1 of CSA S850. The values recommended for glulam are an SIF of 1.2 and a DIF of 1.4 for far field blasts (Z greater than or equal to $1.2 \text{ m/kg}^{1/3}$). There are no recommended values for glulam in near field. The standard recommends using SDOF analysis when the dynamic response and failure of the system can be accurately represented by such a system (CSA 2012).

2.5 Modelling Blast, Impact and Wood

2.5.1 Use of SDOF System to Represent Structural Elements

The structural response to blast and impact loading is often based on approximating the structural system as SDOF system. SDOF analysis is the recommended and default analysis method per CSA S850, due to its relative simplicity and ease of use compared to other methods. However, it can only be used when a single deformation mode controls the dynamic structural response.

This method has been used successfully for many different material types and throughout the many studies investigated was successfully used to model experimental results of wood systems that have simply supported boundary conditions including wood studs, coated wood panels, light-frame wood stud walls, glulam beams and CLT panels (Jacques et al. 2014; Lacroix and Doudak 2018a; Lavarney and Pollino 2015; Parlin et al. 2014; Poulin et al. 2018; Viau and Doudak 2021b). However, when realistic end connections are considered as part of the system instead of idealised simply supported boundary conditions, SDOF responses were found to not always well-represent the system (McGrath and Doudak 2021; Viau and Doudak 2019, 2021a). SDOF modelling has also been used to predict the behaviour of extreme cold UHPFRC specimens subject to impact loading (Beirnes et al. 2019).

The approach outlined by Biggs (1964) has been used to transform actual structural elements into equivalent SDOF systems. This approach takes the real structural system and converts it into a lumped mass and spring system through the use of a mass factor and takes the load applied to structure that is modified through the use of a load factor. These can be conveniently lumped together into a load mass factor that can then be used to determine the period of the structure. The equivalent system is chosen so that the deflection of the SDOF system is the same as that for a

significant point on the structure (for example the midspan of a beam). The behaviour of the material is defined using a resistance function, where the resistance of an element is “*the internal force tending to restore the element to its unloaded static position*” (Biggs 1964). The resistance in the analysis will be defined based on the loading conditions of the structure. Figure 2-11 shows a structure idealised as a SDOF system.

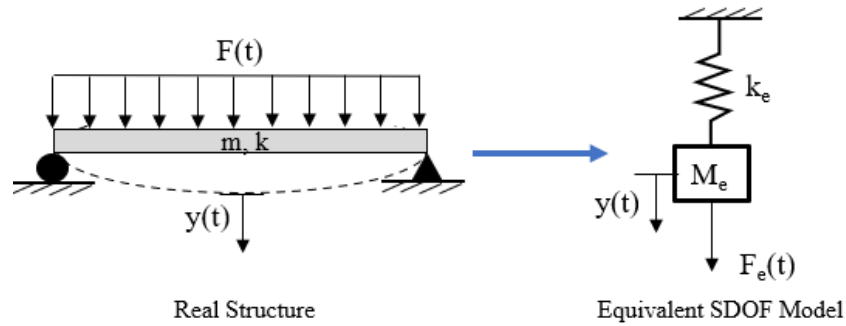


Figure 2-11: Structure idealised as a SDOF system

For the purpose of SDOF analysis blast loads are idealised as a triangular distribution with an instantaneous rise time to the incident or reflected pressure and a decrease to a time, t_d , such that the area under the curve represents the impulse of the actual blast (CSA 2012). The negative phase is often disregarded (CSA 2012). Damping is often ignored as it does not affect the peak displacement in a structural response, which is deflection of interest when dealing with blast loading (Biggs 1964). The displacement to be designed for is as outlined in the required response limit for the structural element outlined in CSA S850 and above in Section 2.4.3 The SDOF system is then solved using the equation of motion and by equating the kinetic energy, potential energy and work done by the system. The equation of motion in terms of the real system is defined in Equation [2.3].

$$K_m M_t \ddot{y} + K_L k y = K_L F(t) \quad [2.3]$$

Where K_m is the mass factor, M_t is the total mass of the structure (including tributary masses), \ddot{y} is the acceleration, K_L is the load factor, k is the stiffness of the system, y is the displacement and $F(t)$ is the force (Biggs 1964).

2.6 Summary

Wood is a complex material whose properties differ along its tangential, radial, and longitudinal directions. When considering wood’s behaviour when subject to cold temperatures it has been shown to have an increase in both strength and stiffness at reduced temperatures. This may be due to several reasons including the formation of ice crystals or the stiffening of cellulose fibrils, and in the case of glulam the stiffening of the adhesives used. Moisture content has an effect on its behaviour at cold temperatures. Under strain rates of 0.14 to 0.51 s^{-1} representative large scale wood products have experienced increases in strength and occasionally increases in stiffness. Most notable in these studies is that for glulam where continuous finger-joints (single laminate

width) or closely aligned finger-joints (multiple laminates width) are not located in the high moment region, a DIF of 1.14 on the resistance is recommended (Lacroix and Doudak 2018a). The impact behaviour of glulam has not been well documented across a broader range of strain rates and loading regimes. The above studies also highlight the importance of defects in wood in initiating failure. To the author's knowledge there have been no studies conducted considering the effects of the impact resistance of glulam beams under extreme cold temperatures.

Chapter 3: Experimental Program

3.1 General

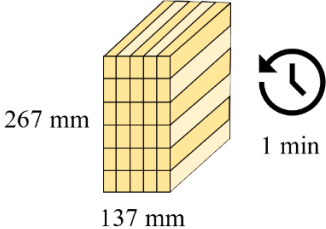
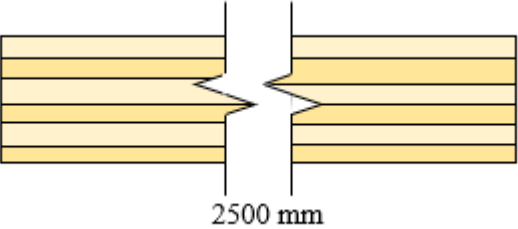
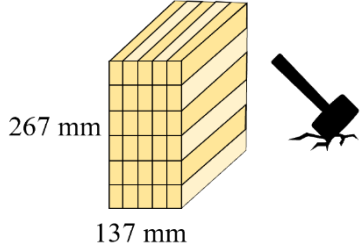
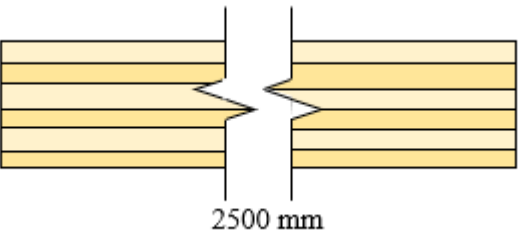
An experimental program was conducted using quasi-static and dynamic drop-hammer impact loading. Specimens were tested both under ambient and extreme cold temperatures to examine their viability for use in the arctic. These were separated into two series. The results of the experimental program are meant to act as input for the validation of SDOF modelling, which is the subject of Chapter 6.

In order to expand the range of strain rates for which the dynamic load relationship with glulam's behaviour is known, glulam specimens of similar dimension, and identical glulam beam construction, grade, and wood species as those used in recent full-scale shock tube testing taking place at the University of Ottawa Shock Tube Test Facility (Lacroix and Doudak 2018a; Viau and Doudak 2021a). As such the same manufacturer, similar specimen size, and same specimen length were kept constant for this study. These specimens were 137 mm x 267 mm x 2500 mm, with a clear span of 2265 mm. These beams consisted of Series 1, hereafter referred to as the "large beams", and were used in order to verify the test set-up against existing experimental results. They were also used in order to determine the DIF for glulam over a wider range of strain rates. The term "large beams" is used, as they were larger in depth and length than the beams used to investigate the effects of cold, in order to provide the reader with an intuitive indication of the group of beams being discussed.

Series 2, hereafter referred to as the "small beams", consisted of a second specimen size that was used to test the effects of extreme cold on the beams due to the constraints of the freezer size. The size of these specimens was chosen to maintain a similar depth to length ratio. These beams were 137 mm x 178 mm x 1650 mm, with a clear span of 1479 mm. The term "small beams" is used, as they were smaller in depth and length than the beams in Series 1, in order to provide the reader with an intuitive indication of the group of beams being discussed.

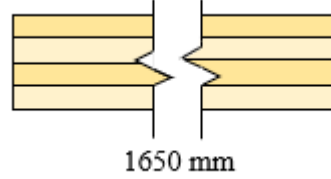
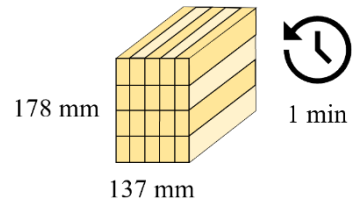
Across Series 1 and 2, a total of ten specimens were tested statically and fourteen specimens were tested dynamically. The experimental study program can be seen in Table 3-1. The nomenclature of the experimental test specimen consists of a series of alphanumerical characters. The first letter of each specimen number indicates whether the beam was tested quasi-statically (S) or dynamically (D). The second letter indicates the temperature the specimens were tested at, ambient temperature or normal temperature (N) and cold temperature (C). As an exception to this nomenclature, one specimen (DNP1-267) has an extra letter in its name. P for practice as this specimen was used in order to finalise the experimental set-up, the instrumentation and the drop height and weight. The number following the letters indicates the specimen number of that group. Finally, the number after the dash indicates the specimen depth in mm (-267 or -178).

Table 3-1: Experimental Program

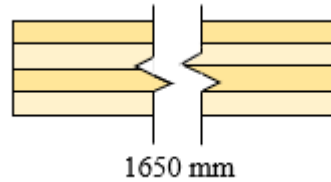
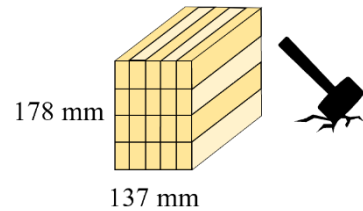
Specimens	Objective
Series 1 - Large Beams	
<p>SN1-267 SN2-267 SN3-267</p>  <p>267 mm 137 mm 1 min</p>  <p>2500 mm</p>	<p>Validate newly established drop hammer facility and confirm experimental set-up</p> <p>Expand range of strain rates glulam has been tested under</p>
<p>DNP1-267 DN1-267 DN2-267 DN3-267 DN4-267 DN5-267</p>  <p>267 mm 137 mm</p>  <p>2500 mm</p>	

Series 2 - Small Beams

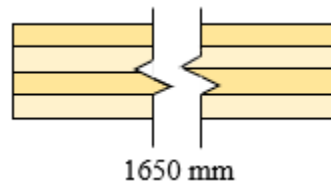
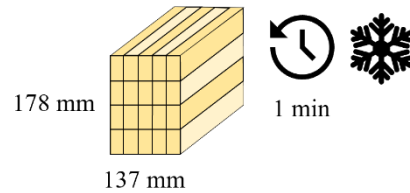
SN1-178
SN2-178
SN3-178
SN4-178



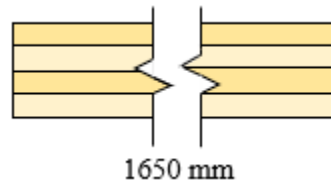
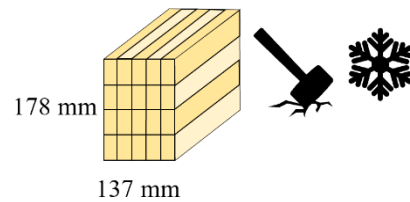
DN1-178
DN2-178
DN3-178
DN4-178



SC1-178
SC2-178
SC3-178



DC1-178
DC2-178
DC3-178
DC4-178



Investigate the effects of extreme cold temperature on the static and dynamic behaviour of glulam under impact loading

Expand range of strain rates glulam has been tested under

Quasi-static four point bending flexural tests were conducted on all specimen types to obtain average 1-min strength values. These values differ from specified design values and allowed the SIF for each batch to be obtained. The specimens were simply supported, and the small specimens were tested at both ambient and extreme cold temperatures. The experimental set-up will be further discussed in Section 3.3. Dynamic impact testing was accomplished using the RMC drop-hammer impact test facility. The specimens were simply supported, and the small specimens were tested at both ambient and extreme cold temperatures. In comparison with the dynamic results this allowed the DIF values for each specimen to be calculated. The dynamic test set-up is further discussed in Section 3.4.

3.2 Description of Test specimens

NordicLam+ 24F-ES grade glulam beams were tested under quasi-static and dynamic loading in order to document high strain-rate effects and their behaviour under extreme loading conditions. Specimens with multilaminated widths were chosen in order to minimize the effects of finger joints, as observed in previous research (Lacroix and Doudak 2018). For the remainder of the description and discussion in further chapters, “large beams” will be used to describe the 137 mm x 267 mm x 2500 mm beams and “small beams” will be used to describe the 137 mm x 178 mm x 1650 mm beams.

All beams were placed in a moisture and temperature-controlled room for a minimum of two months. The room was monitored on an hourly basis for both moisture and temperature resulting in an average ambient relative humidity of 58.4% and an average temperature of 20.1°C. All beams were prepared for testing through the recording of finger joint locations, any large defects, photographing, measuring of lengths and dimensions, as well as the installation of four strain gauges.

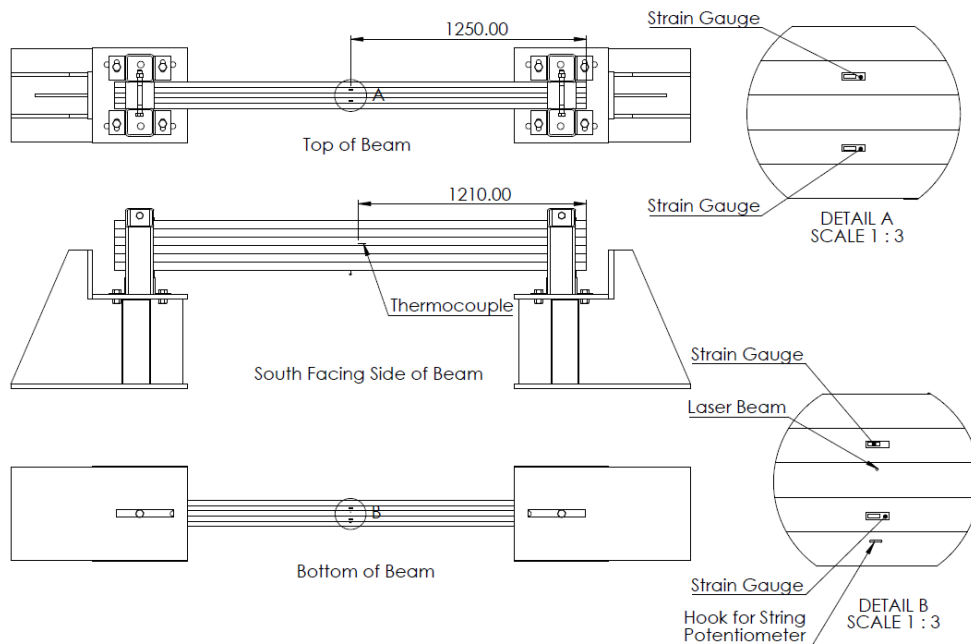
Prior to the installation of the strain gauges, the wood surface was prepared using medium grade sandpaper, and cleaned using compressed air. The strain gauges were then adhered to the surface using Tokyo Measuring Instruments Lab CN general purpose glue. This process can be seen in Figure 3-1. The glue’s operating temperature was from -196 to +120 °C. All strain gauges were of 120 Ω resistance.



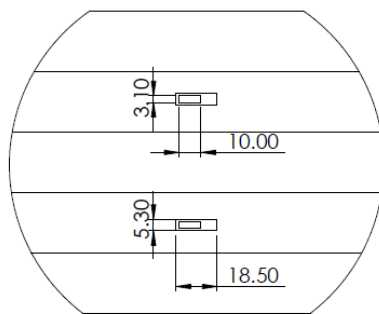
Figure 3-1: Preparation of the test sample for strain gauges. From left to right: sanding, sanded surface, compressed air, strain gauge and glue, soldering of tabs and leads

Two strain gauges were placed on the tension side of the beam on the beam’s centreline,

40 mm from each outer edge of the beam. Two strain gauges were also placed on the compression side. All strain gauges attached to the normal temperature beams were low elastic strain gauges from Tokyo measurements lab, designed specifically for materials with a low elastic modulus, such as wood. All gauges had a 10 mm gauge length. All strain gauges used on the cold temperature beams, needed to be able to withstand temperatures of up to -70°C and as such general-purpose gauges from Micro Measurements were used with a 12.7 mm gauge length. A steel zinc plated screw hook 38 mm long and 2.8 mm outer diameter was screwed into all dynamic beams to a depth of 15 mm located on the tension side of the beam 20 mm from the edge. This provided a connection point for the string potentiometer. The instrumentation placement can be seen in Figure 3-2.

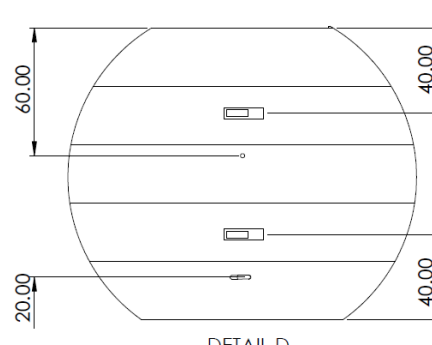


(a) Strain, displacement, and temperature instrumentation location on the large beams.



DETAIL C
SCALE 1 : 2

(b) Dimensions of normal temperature strain gauges



DETAIL D
SCALE 1 : 2

(b) Placement of strain gauges, laser and string potentiometer on the bottom of the beam

Figure 3-2: Strain, displacement, and temperature instrument location on the large beams

Additionally, all beams were equipped with a thermocouple adhered to their side approximately 8 cm from the centreline as can be seen in Figure 3-2. Type T thermocouples were used, and the same CN general purpose glue was used as an adhesive. All cold temperature dynamic beams also had a 76.2 mm x 76.2 mm neoprene foam square 3.2 mm thick adhered overtop of them. This was done to ensure that the thermocouples would measure the beam temperature and would not be affected by the air temperature. During testing an additional a piece of rigid DuroFoam insulation 76.2 mm x 76.2 mm square and 25.4 mm thick was placed overtop of the neoprene. This installation can be seen in Figure 3-3.

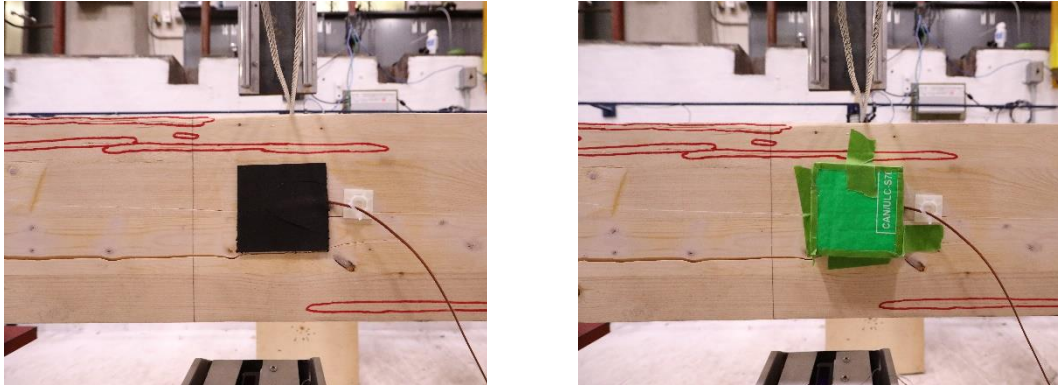


Figure 3-3: Neoprene and rigid insulation installed over thermocouple

All cold specimens were placed into a cold temperature freezer at -70°C for a minimum of seven days prior to testing. A test beam was placed in the freezer with thermocouples installed at depths of 63mm, 42 mm, 21 mm and on the surface with neoprene and foam insulation coverings as described above. The thermocouples were located at a minimum 63.5mm from an outer edge. These allowed the internal freezing temperature of the beams to be monitored to determine how long it took the beams to freeze and allowed correlation of internal testing temperatures to those obtained in all other beams. These thermocouples were not installed in all beams in order to ensure that holes were not drilled into the beams causing an unintentional defect that could initiate failure. Any free space around the thermocouple wire was filled with polyvinyl acetate. Using this monitoring methodology, it was determined that the internal temperature of the wood normalized to -69.1°C at all depths after approximately 15 hours in the freezer. The installed thermocouples can be seen in Figure 3-4.

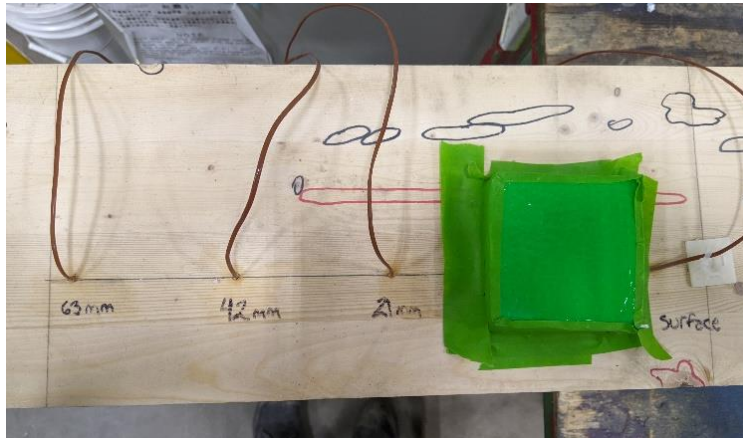


Figure 3-4: Installed thermocouples in test beam

Prior to testing all, specimens were weighed, and their moisture content measured. A Tramex Moisture Encounter Plus pinless moisture meter was initially used to measure the surface moisture content of the beams, resulting in moisture contents between 11-14%. However, since a pinned moisture meter provides a better measurement of the interior moisture, the beam's moisture content was additionally measured using a Delmhorst Navigator Pro Moisture Meter (shown in Figure 3-5) calibrated to the wood type. All cold specimens had their moisture content taken before being placed in the freezer. The moisture meter's pins were inserted to a depth of 24 mm. The average moisture content of the large beams, small normal temperature beams, and small cold temperature beams was 8.53% (COV 0.05), 9.05% (COV 0.05), and 8.56% (COV 0.03) respectively at the time of testing. The average weights of the large beams, small normal temperature beams, and small cold temperature beams was 47.6 kg (COV 0.01), 21.2 kg (COV 0.02), and 21.1 kg (COV 0.02) respectively at time of testing.



Figure 3-5: Delmhorst Navigator Pro Moisture Meter

3.3 Static Testing

Quasi-static four point bending flexural tests were conducted on three large normal temperature beams, four small normal temperature beams, and three small cold temperature beams to obtain average 1-minute flexural strength values. This allowed the SIF for this sample of wood beams to be determined, and to have accurate strengths and stiffnesses values with which to compare the dynamic results. This also allowed for the effects of cold temperature on the static behaviour of beams to be determined. The test methodology was adapted from ASTM D198 (ASTM International 2021), with modifications made to keep the dynamic tests comparable. This included slight modification to the load bearing blocks which were flat instead of curved, and the use of a linear variable differential transformer (LVDT) as a load measurement device instead of a wire or yoke deflectometer.

The force was applied using a hydraulic MTS system and was recorded through a load cell located within the hydraulic head. The displacement was recorded using a LVDT connected at the beam's midspan. The specimens' strain deformations were measured using two strain gauges positioned on the tension side of the beam and two on the compression side of the beam at midspan. The beam's temperature at testing was recorded using a type T thermocouple.

For the large beams, the first sample was loaded at a displacement-controlled rate of 1 mm/min resulting in a time failure of 24.7 mins and the remaining two beams were loaded at a rate of 2 mm/min resulting in a time to failure of 12.06 mins and 11.35 mins. The small beams were all tested at a rate of 1 mm/min. This resulted in an average time to failure of 15.2 mins for the small normal temperature beams and 13.4 mins for the cold temperature beams. The average time from removing the cold temperature beams from the freezer to the approximate midpoint of testing was 18.5 mins.

The beams were simply supported and used the same rollers and load transfer bar that was used for the dynamic tests. The roller plates at the load-application points and ends measured 150 mm in length to avoid crushing of the wood during testing. A clear-span of 2,265 mm was used throughout testing for the large beams and 1,479 mm for the small beams, with the load being applied at the beam third points. The static set-up with the large beams can be seen in Figure 3-6 (a) and the static set-up with the small beams can be seen in Figure 3-6 (b). A schematic of the test setup can be seen in Figure 3-7.

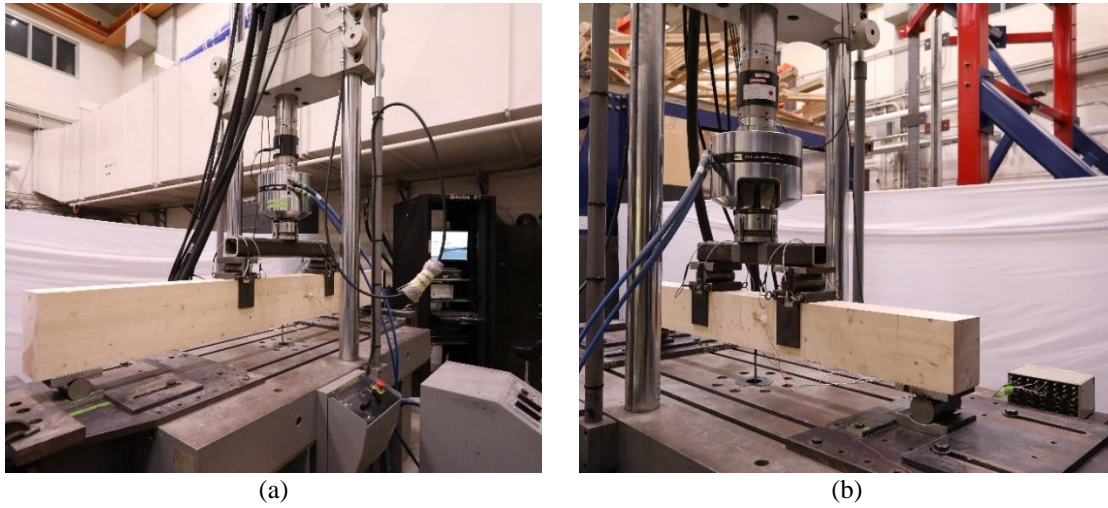


Figure 3-6: Static test setup: (a) Large beam; (b) Small beam

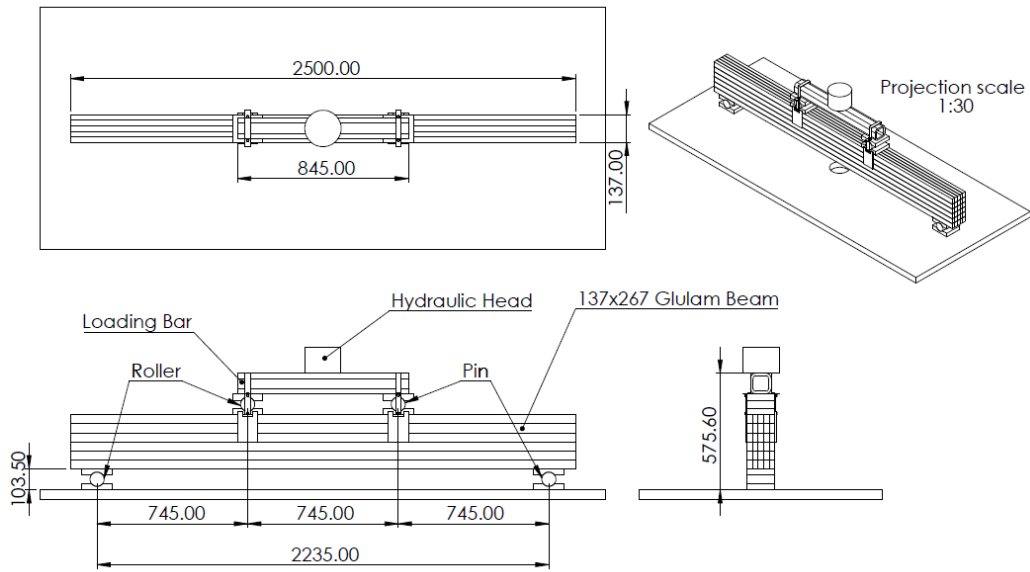


Figure 3-7: Static test setup schematic for large beams

3.4 Dynamic Testing

Dynamic impact testing was conducted using the newly established drop weight impact testing facility at the Royal Military College of Canada, capable of imparting up to 23 kJ of energy onto small to full scale structural elements. The six-meter-tall impact hammer consists of two sets of supported rails along which a drop weight box travels using six pillow block ball bearings to guide the box. The box weighs 99.1 kg and can be increased in weight by adding a lid (42.6 kg) and up to eleven plates weighing approximately 25.6 kg each, up to a maximum drop weight of 423.3 kg. The impact hammer testing apparatus can be seen in Figure 3-8 and Figure 3-9. More

detailed engineer drawings can be seen in Appendix A. The hammer is equipped with a data acquisition system capable of recording data at a rate of 500,000 samples per second. The box is equipped with a linear encoder to record the drop height and determine the box's velocity upon impact. An electromagnet was employed to lift the drop weight to the desired drop height and was disengaged to release the box.

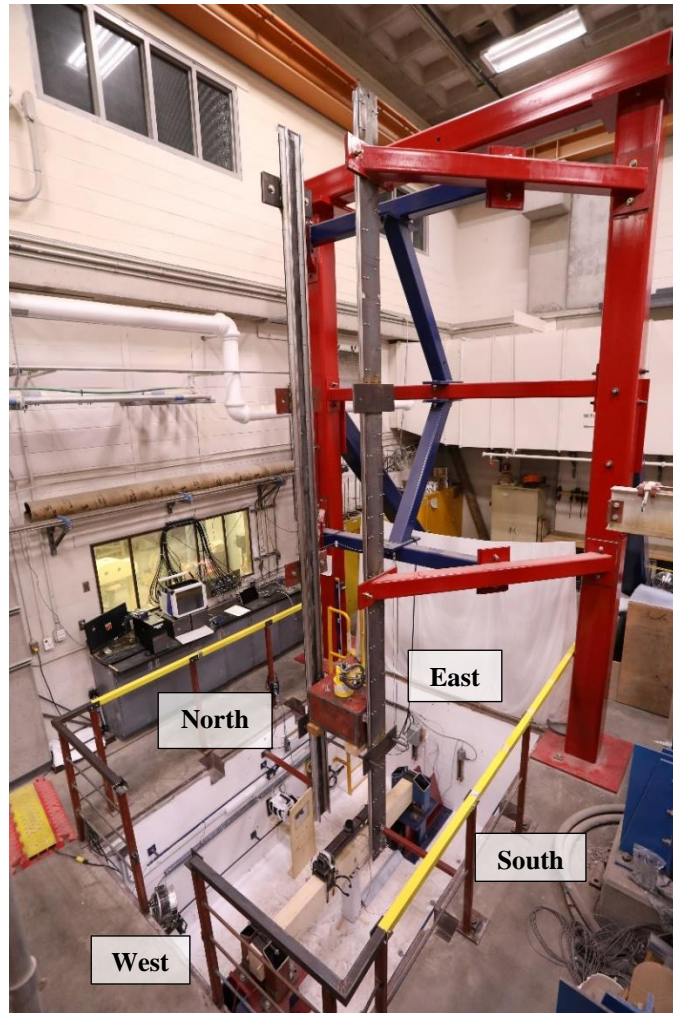
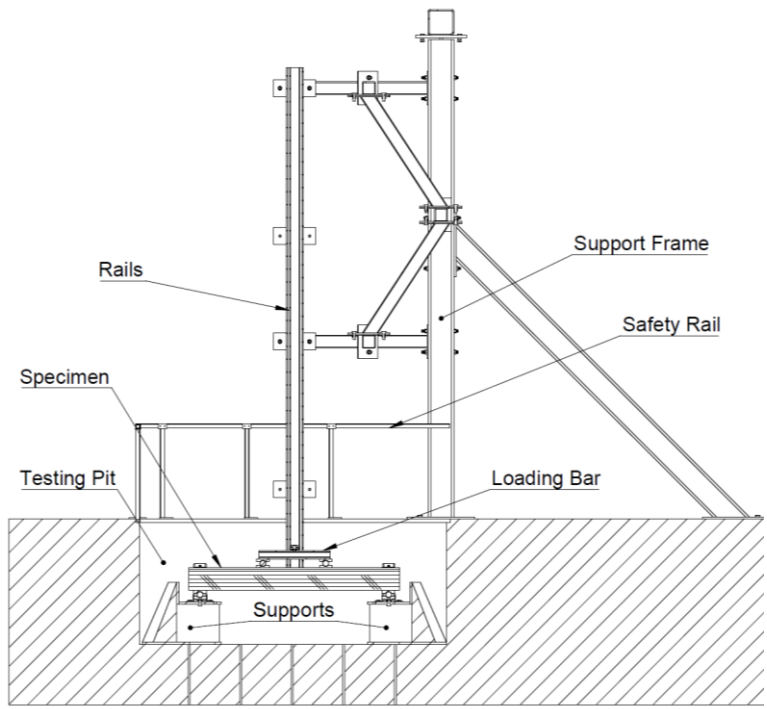
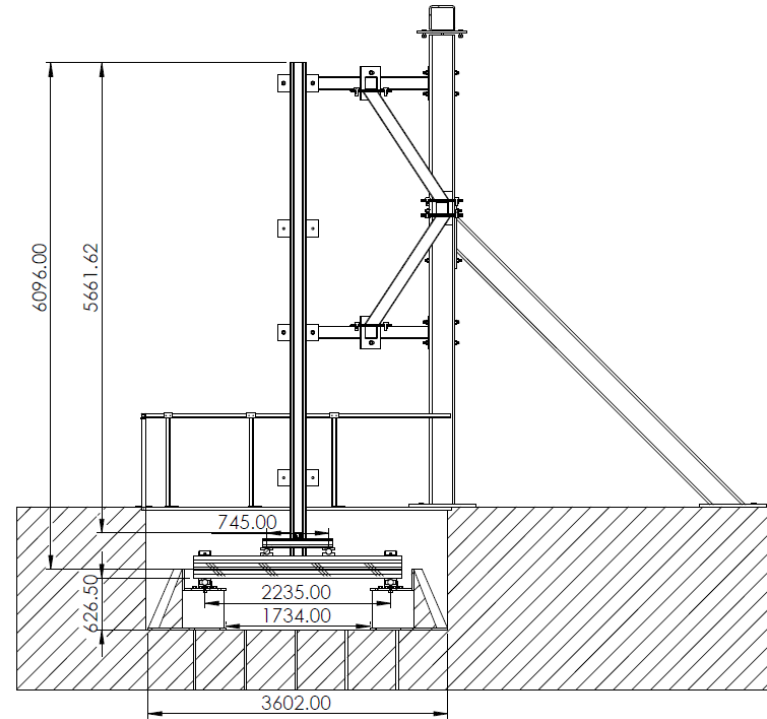


Figure 3-8: Impact hammer test apparatus oblique view with cardinal directions marked



(a)



(b)

Figure 3-9: Impact hammer test apparatus: (a) Side sketch; (b) Dimensioned view

Loading and boundary conditions identical to those described for the static test setup were used for the dynamic testing. Due to the nature of the loading and the likelihood of beam instability during response, lateral supports were provided at the beam ends. Additionally, brace plates were placed on top of the beam at each end in order to prevent upward motion of the beam after initial impact. End supports were designed to allow for piezoelectric force sensors to be placed at each support, seamlessly integrated with the roller and pin. The load application points, consisting of a steel pin and roller, were designed such that they allowed movement, but with enough restraint to keep all components together during and after impact. Welded saddles and elasticized rubber cord prevented any tipping in the system and ensured that movement was restrained to the vertical plane. A steel load transfer beam allowed for the impact load to be transferred to the beam at two points to allow for a region of constant moment and no shear force. An additional force transducer was placed on the load transfer beam to monitor the applied load. A laser and string potentiometer were used to determine the beam's displacement-time history at the beam's midspan. Three high speed cameras were used, capturing images at 10,000 fps, 1,000 fps and 500 fps, to record the beam's behaviour, potential failure location, and to check for the beam's displacement in the case of discrepancies between the laser and string potentiometer. Two strain gauges on the tension side of the beam and two on the compression side of the beam at midspan were used to monitor the specimen's strain-time histories. The beam's surface temperature was monitored using a thermocouple. A detailed drawing of the dynamic test set-up with a large beam in place can be seen in Figure 3-10. Figure 3-11 shows the instrumentation placement on the beam and orients one to the directions of the test pit.

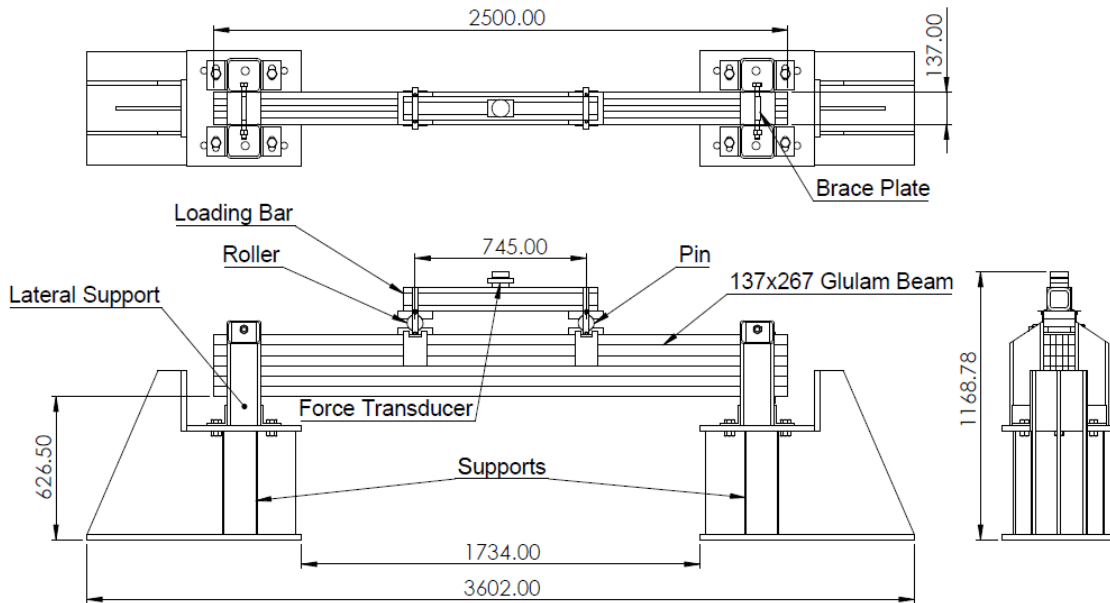


Figure 3-10: Sketch of dynamic specimen reaction frame and loading beam

Specimen DNP1-267 was used as the initial practice beam in order to solidify the test set-up and determine the failure dynamic test height and weight of the weighted box. The specimen was subjected to a total of 31 dynamic tests prior to flexural failure. The first 10 dynamic tests were used to finalise and calibrate the experimental test set-up. The remaining 21 dynamic tests were

used to incrementally bring the beam to failure. Although other studies have looked at the effects of multiple pressure-impulse combinations and found that as long as the elastic limit of the member is not passed, the wood member remains undamaged (Viau and Doudak 2021a), the effects of the multiple impacts were also evaluated in this study and are further discussed in section 4.2.2 below. DN1-178 was also subjected to multiple dynamic tests in order to determine the correct drop height for the small beams. This drop height and weight was converged upon much faster, with the beam being subjected to a total of five impacts. DC1-178 was subjected to two dynamic tests in order to find the failure height for the cold specimens.

Following this each other normal temperature dynamic specimen was subject to three dynamic tests. The first dynamic test consisted of a 99.1 kg mass dropped from a height of 400 mm in order to ensure that all instrumentation was reading properly. For the normal temperature large beams, a second dynamic test was done with a 99.1 kg mass dropped from a height of 2000 mm. This dynamic test was used in order to verify the SDOF system proposed in section 6.2.16.1 and to investigate the transfer of energy in the system. Lastly a 244.7 kg mass dropped from a height of 2000 mm was used to induce flexural failure in the beam. The normal temperature small beams were also subjected to three dynamic tests for the same reasons, however this involved 99.1 kg dropped from 400mm, 99.1 kg dropped from 1800 mm and finally 141.7 kg dropped from 1800 mm. The cold temperature dynamic beams were only subjected to one dynamic test in order to preserve their internal cold temperature, 141.7 kg dropped from 2000 mm. The weights and heights used for each test is summarised in Table 3-2.

Table 3-2: Summary of testing protocol

Specimen	Number of Tests	Weight kg	Height mm
DNP1 -267	31(see summary in section 4.2.2)	99.1 - 244.7	200 - 2000
DN1-267			
DN2-267		99.1	400
DN3-267	3	99.1	2000
DN4-267		244.7	2000
DN5-267			
		99.1	400
		99.1	1800
DN1-178	5	99.1	2000
		141.7	1600
		141.7	1800
DN2-178		99.1	400
DN3-178	3	99.1	1800
DN4-178		141.7	1800
			1800
DC1-178	2	141.7	2000
DC2-178			
DC3-178	1	141.7	2000
DC4-178			

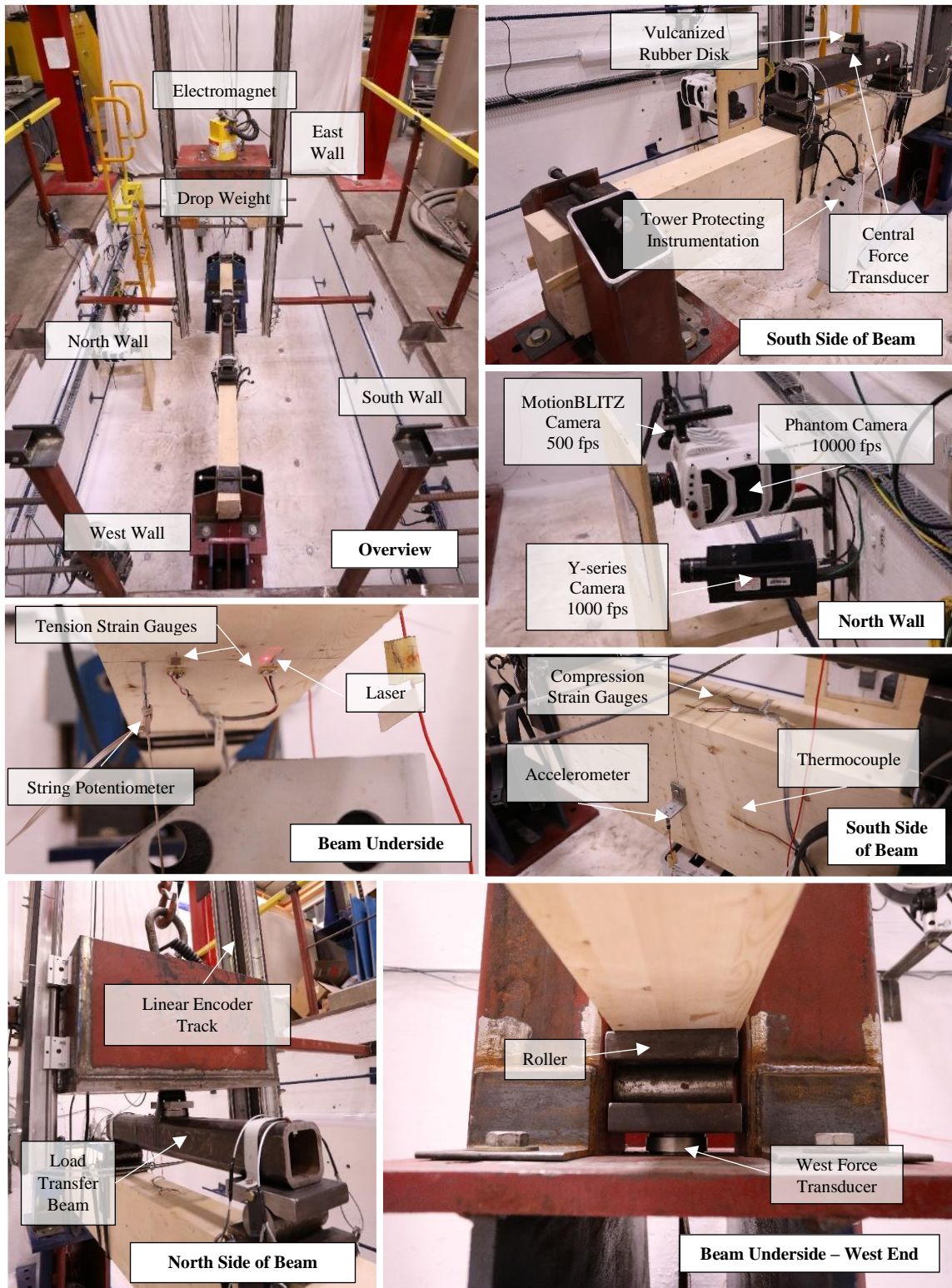


Figure 3-11: Instrumentation overview

Chapter 4: Experimental Results

4.1 General

This section will present the experimental results from both the static and dynamic testing. The chapter is separated into two major sections. Firstly, the testing of the larger dimensioned beams (137 mm x 267 mm x 2500 mm) is presented. Secondly, the testing of the smaller dimensioned beams (137 mm x 178 mm x 1650 mm) is presented, including the effects of extreme cold temperatures.

4.2 Normal Temperature Testing – Large Dimensioned Beams

4.2.1 Static Testing Results

As mentioned in section 3.3, the static large dimension beam tests were conducted using two separate loading rates. The first being slower than the other as the time to failure for the specimens was not known. As mentioned in Chapter 2, the duration of loading has a large impact on the ability of wood to withstand a load. As such, the failure loads for each wood beam were normalized to a 100% strength value which corresponds to a testing time of 1 minute using Equation [4.1] (Karacabeyli and Barrett 1993).

$$SL=100.0-3.5\text{Log}_{10}T_r \quad [4.1]$$

Where SL is the stress level factor in the beam and T_r is the time to failure in minutes.

Failure of the specimens was determined to be the point at which the beams experienced a sudden drop in load and could no longer support additional load. The flexural stiffness was taken as the slope of the resistance displacement curve from 40% to 90% of the beam's ultimate capacity. These percentages were kept constant for determining the beams' dynamic stiffness. The SIF has been taken as the ratio of the beam's measured MOR to that provided by the manufacturer multiplied by a load duration factor of 1.25 bringing the beam from a standard load duration to a short load duration. This factor is taken from Foschi et al. (1989), who discuss the methodology employed in the calibration procedure and the reliability levels adopted for CSA-O86. The beam size was also taken into account by applying a size factor, K_{zbg} , taken from CSA O86 to the manufacturer provided MOR so that the values obtained experimentally could be directly compared. For the large beams a K_{zbg} of 1.24 was used. Although with the currently code the lateral stability of the beam would govern with a lateral stability factor of 1.00 the size effects must be considered when directly comparing the values of the SIF as opposed to following a design calculation. The MOR and MOE of the beams were calculated based on the flexural response of the beams, considering the beam's response under four-point bending and using Equation [4.2] and [4.3].

$$MOE = \frac{23 \times k \times L^3}{1296 \times I} \quad [4.2]$$

$$MOR = \frac{R_{max} \times L}{6 \times S} \quad [4.3]$$

Where k is the stiffness taken from 40% to 90% of the beam's resistance displacement curve, L is the clear span, I is the moment of inertia of the beam, R_{max} is the peak resistance of the beam taken as the maximum load applied to the beam, and S is the section modulus.

The results from the static tests can be seen in Table 4-1, including the obtained maximum applied load (P_{max}), time-to-failure, normalized static peak resistance ($R_{s,max}$), the displacement at the time of peak resistance (y_{Rmax}), stiffness (k), strain rate ($\dot{\epsilon}$), MOR, SIF, and MOE.

Table 4-1: Static test results large beams

	P_{max} kN	Time to Failure mins	$R_{s,max}$ kN	$y_{s,Rmax}$ mm	k kN/m	$\dot{\epsilon}$ ($\times 10^{-6}$) s^{-1}	MOR MPa	SIF	MOE MPa
SN1-267	240.4	24.7	252.7	22.3	10,663	2.19	59.3	1.24	10,231
SN2-267	249.3	12.1	259.1	22.2	11,369	4.98	61.2	1.28	11,032
SN3-267	237.2	11.4	246.3	21.1	11,347	4.21	58.0	1.22	11,013
Average	242.3	16.0	252.7	21.9	11,126	3.79	59.5	1.25	10,757
Std Dev	5.1	6.1	5.2	0.5	327	1.18	1.3	0.03	373
COV	0.02	0.38	0.02	0.02	0.03	0.31	0.02	0.02	0.03

The average peak resistance for the normalized static tests was 252.7 kN with a coefficient of variation (COV) of 0.02, correlating to an average SIF of 1.25. The average stiffness was 11,126 kN/m with a COV of 0.03. The average MOR for the beams was 59.5 MPa and the average MOE was 10,759 MPa.

Figure 4-1 and Figure 4-2 show a typical specimen's behavior over time (SN2-267's). Figure 4-1 show the beam's strain and load over time. The strain in all four strain gauges linearly increases with the load over time, with small drops occurring whenever a superficial crack appears in the beams face. For the purpose of the graph, the compression strain gauges have been plotted in the positive direction. Figure 4-2 shows the beam's displacement and measured resistance over time. As with the strain, the beam's displacement linearly varies with the beam's resistance until failure. Figure 4-3 shows the beam resistance versus displacement for all static tests. As can be visually seen the ultimate resistances, displacements, and slope of the line for all beams remains very similar.

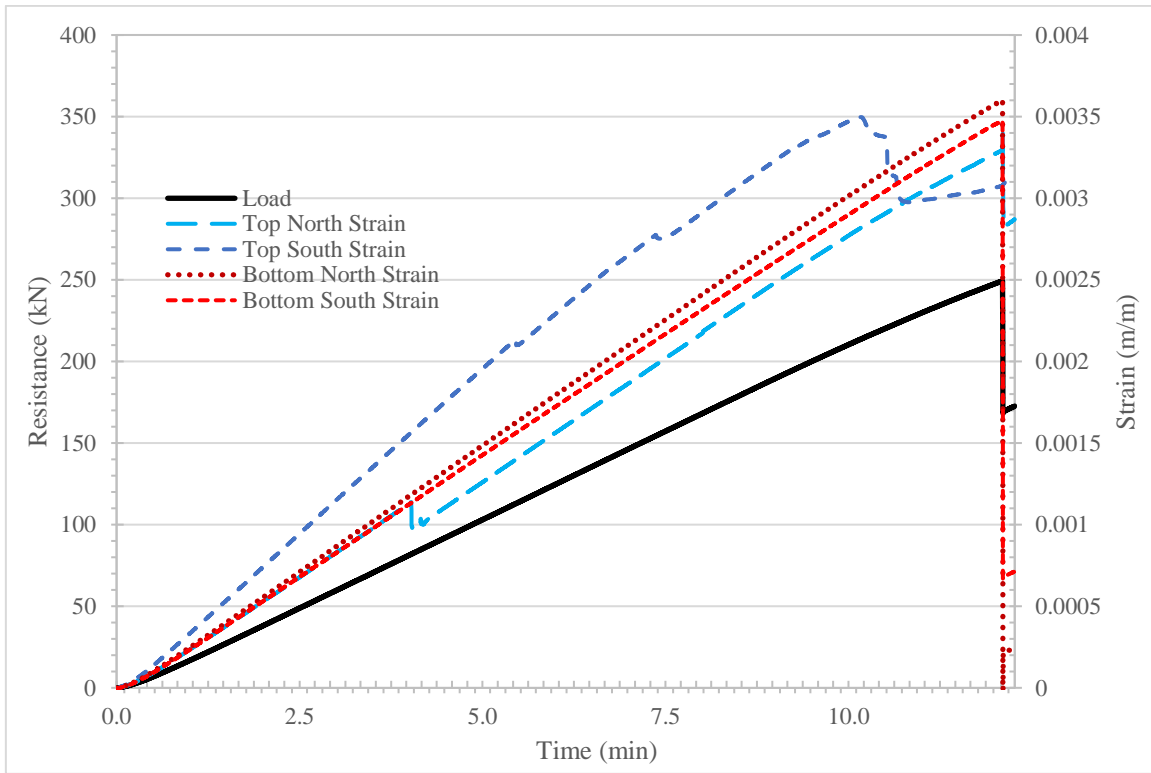


Figure 4-1: SN2-267 Resistance and strain over time

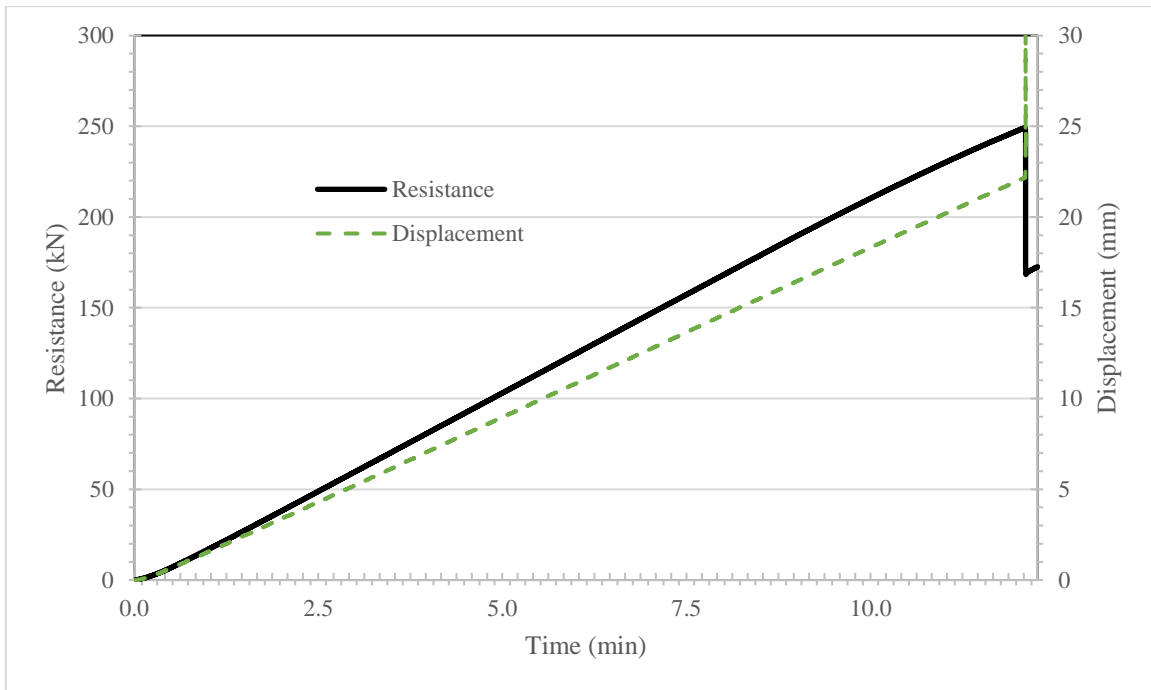


Figure 4-2: SN2-267 Resistance and displacement over time

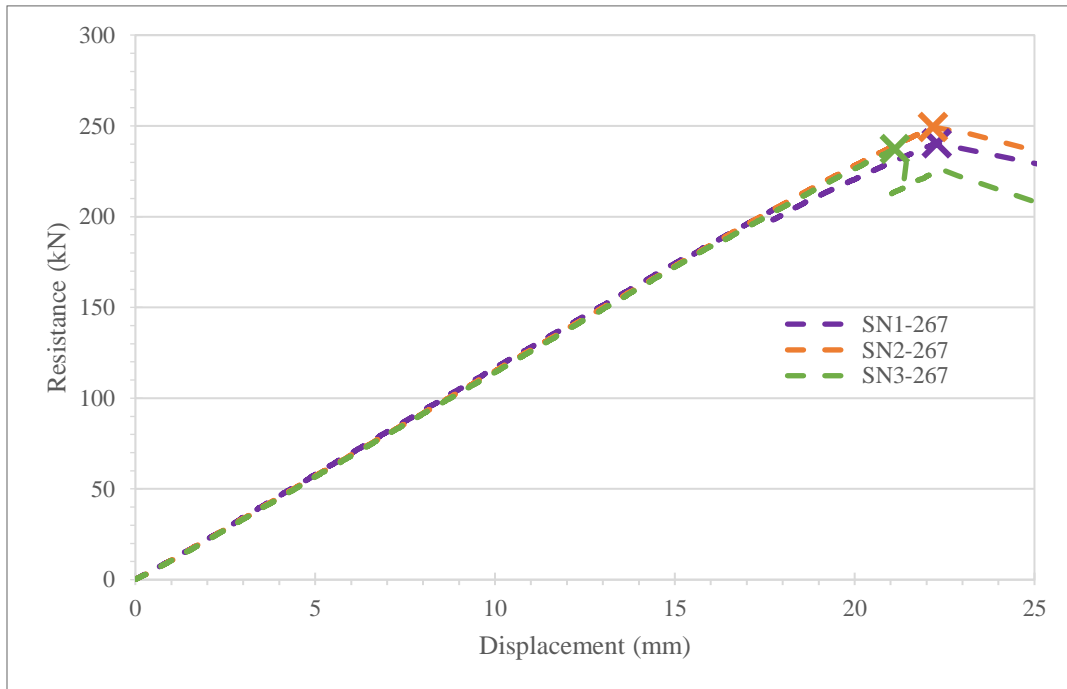


Figure 4-3: Static tests resistance versus displacement over time

4.2.2 Practice Beam DNP1-267

As mentioned in Chapter 3, DNP1-267 was impacted 28 more times than the other large beams in order to finalize the test set-up and determine a proper drop height and weight. It was intended that this beam would not be included in the experimental results if these multiple hits affected the beam's overall resistance or changed the beam's behaviour. These multiple hits did not alter the beam's response and also provide proof of the linear elastic nature of a beam exposed to multiple impacts before reaching its peak resistance. Below, in Figure 4-4, the resistance versus displacement of each of 20 impacts that were delivered to the beam can be seen. The graph highlights that the beam's stiffness did not change dramatically between hits, indicating the lack of damage in the beam. Small superficial cracks began to develop during dynamic test 28, although the overall stiffness and behaviour of the beam remained unaffected. Dynamic test 28 represented 87.8% of the beam's total resistance. Table 4-2 shows the drop weight, height, maximum dynamic resistance, displacement at the time of peak resistance, stiffness (taken from 40-90% of the beam's resistance versus displacement relationship). The average stiffness obtained through the tests was 12,584 kN/m with a standard deviation of 420 kN/m and a coefficient of variation of 0.03. This shows that there is a very small amount of variation in the beam's stiffness and no overall degradation from multiple impacts. In addition, looking at the percent difference of the stiffness between the average stiffness obtained from all hits, all drops were within 5.7% of the average. This indicates that the beam stiffness is not affected by the multiple hits and that the variation is due to the erratic nature of some aspects of impact testing, such as vibrations.

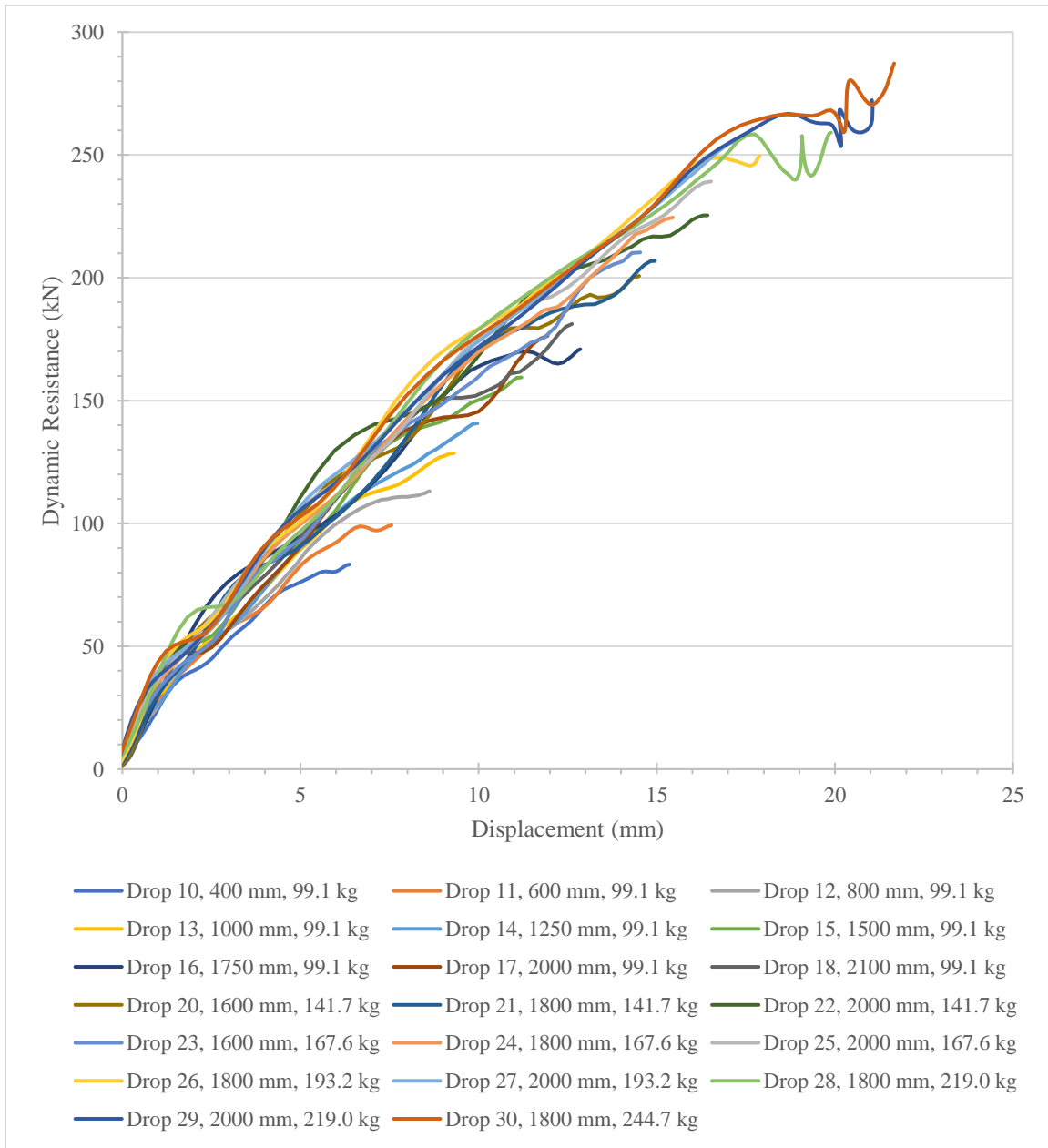


Figure 4-4: Resistance versus displacement of 20 of the impacts to DNP1-267

Table 4-2: Summary of 20 elastic dynamic tests on DNP1-267

Dynamic Test Number	Weight kg	Height mm	Dynamic Resistance kN	Displacement at Max Resistance mm	Stiffness kN/m
10	99.1	400	83.3	6.4	12,598
11	99.1	600	99.3	7.6	12,513
12	99.1	800	113.1	8.6	13,280
13	99.1	1,000	128.6	9.3	11,895
14	99.1	1,250	140.8	10.0	12,801
15	99.1	1,500	159.4	11.2	12,815
16	99.1	1,750	170.9	12.9	12,626
17	99.1	2,000	176.3	11.9	12,638
18	99.1	2,100	181.2	12.6	11,615
20	141.7	1,599	200.7	14.5	12,107
21	141.7	1,800	206.8	15.0	12,566
22	141.7	2,000	225.4	16.4	13,304
23	167.6	1,600	210.3	14.5	12,390
24	167.6	1,800	224.5	16.7	12,423
25	167.6	2,000	239.2	16.5	12,344
26	193.2	1,801	249.6	17.9	13,309
27	193.2	2,000	256.0	17.2	12,356
28	219.0	1,800	259.1	19.9	12,842
29	219.0	2,000	272.3	21.0	12,649
30	244.7	1,800	287.2	21.7	12,617
				Average	12,584
				Std Dev	420
				COV	0.03

4.2.3 Dynamic Testing Results

Dynamic failure of the beam specimens was determined to occur at the peak resistance, consistently followed by a sudden drop in resistance. Statically, the resistance can be obtained by calculating the summation of the reactions. However, the same cannot be done with regard to the measured dynamic reactions, as the measured dynamic reactions are dependant on both boundary conditions, resistance of the specimen, and the applied load (Biggs 1964). Particularly, the weight of the load transfer beam, rollers, and pins had to be considered when calculating the dynamic resistance of the beam. Equations for the determination of the dynamic resistance have been previously derived for glulam specimens subjected to simulated blast loading, during which a load-transfer device was used (Lacroix 2017). The dynamic resistance of a simply supported beam under four-point bending can be determined using Equations [4.4] and [4.5].

$$R(t) = \frac{6}{L} \times \left[V(t) \times x_{eq} + 0.5 \times \left(\frac{L}{3} - x_{eq} \right) \times F(t) \right] \quad [4.4]$$

$$x_{eq} = \frac{0.102\bar{m} \times L^2 + 0.290m_c \times L}{0.319\bar{m} \times L + 0.870m_c} \quad [4.5]$$

Where $R(t)$ is the beam's dynamic resistance, $V(t)$ is the dynamic reaction, $F(t)$ is the applied force, L is the beam's clear span, x_{eq} is the distance from the support to the point of application of the equivalent inertia force, \bar{m} is the distributed mass of the beam and m_c is half of the mass of the load transfer beam lumped at the load application point.

The stiffness was taken as the slope of the resistance displacement curve from 40% to 90% of the beam's ultimate capacity as with the static tests. Similarly, the MOE and MOR for the beams were calculated using Equations [4.2] and [4.3]. The beam's displacement was calculated as the average between the laser and the string potentiometer. Since the laser and string potentiometer are both located on different parts along the beam's width, a more accurate view of the entire beam's global displacement response could be gained. In any cases where the difference in displacements between the laser and the string potentiometer differed by more than 1.2 mm (approximately 6.2% of the beam mid-span deflection at peak resistance), the displacements were then corroborated with those obtained by the high-speed cameras in order to determine which measurement device was more accurate. The displacement was then taken from only the laser, which was more accurate when considering the behavior of DNP1-267 and DN4-267.

The results from the dynamic tests are summarized in Table 4-3, including the dynamic peak resistance ($R_{d,max}$), the displacement at the time of peak resistance ($y_{d,Rmax}$), stiffness (k), average compressive and tensile strain at the time of peak resistance (ϵ_{f-c} and ϵ_{f-t}), strain rate ($\dot{\epsilon}$), MOR, MOE, time-to-failure, and duration of load. All specimens resulted in a flexural failure.

For strain rates between 0.67 to 1.05 s⁻¹, the average dynamic peak resistance was 285.6 kN with a coefficient of variation (COV) of 0.05. The average stiffness was 13,368 kN/m with a COV of 0.06. The average MOR for the beams was 67.3 MPa and the average MOE was 12,924 MPa.

Table 4-3: Dynamic test results of large dimensioned beams

	$R_{d,max}$	$y_{d,Rmax}$	k	ε_{f-c} ($\times 10^{-3}$)	ε_{f-t} ($\times 10^{-3}$)	$\dot{\varepsilon}$	MOR	MOE	Time to Failure	Duration of Load
	kN	mm	kN/m	m/m	m/m	s^{-1}	MPa	MPa	ms	ms
DNP1-267	295.0	22.3 ¹	12,069	-3.18	3.40	1.05	70.2	11,821	10.7	13.3
DN1-267	271.2	16.5	13,738	-2.91	2.93	0.88	63.4	13,158	6.6	11.0
DN2-267	287.5	21.2	12,614	-3.47	2.67	0.67	67.9	12,264	7.7	12.6
DN3-267	301.0	20.4	13,300	-3.74	3.54	0.73	70.3	12,714	7.6	12.1
DN4-267	263.2	18.4 ¹	13,963	-3.61	4.05	1.01	62.2	13,549	6.5	12.1
DN5-267	295.5	18.6	14,522	-3.58	3.49	0.86	69.6	14,039	7.2	12.2
Average	285.6	19.6	13,368	-3.42	3.35	0.87	67.3	12,924	7.7	12.2
Std Dev	13.8	1.9	825	0.29	0.44	0.14	3.3	751	1.4	0.7
COV	0.05	0.10	0.06	-0.08	0.13	0.16	0.05	0.06	0.18	0.06

¹ These displacements were taken solely from the laser displacement whereas all other maximum displacements were taken as an average of the laser and string potentiometer.

Figure 4-5 shows the applied force over time for DN3-267 recorded by the central force transducer. As can be seen, the impact force was often applied as a two peaked force-time history. As the impact weight initially impacted the specimen, the initial impact force caused the specimen, load transfer bar, and central force transducer (all three moving in unison) to accelerate away from the weight, causing a decrease in the recorded force. The weight then shortly caught up to the beam, applying the remaining force until failure was achieved.

This series of events was confirmed by viewing the overlays of the beam's displacement and that of the linear encoder on the weight box. As shown in Figure 4-6 the black line represents the applied force as measured by the central force transducer. In brown, the dynamic resistance-time history of the beam is seen. The yellow line indicates the beam's mid-span displacement, taken as the average of the linear potentiometer and laser. All displacements were recorded so that the positive direction indicates the downward deflection of the beam. The teal line represents the path of the linear encoder. The linear encoder was zeroed at the rest position of the beam, where all negative values indicate it's travel down the supporting rails to the beam and positive values indicate it's travel after impact. What is of note is that the linear encoder initially experiences greater displacement than the beam before the two items resume contact. This is likely caused by two phenomena. The first is that the central force transducer was protected by a vulcanized rubber disk so that metal would not impact directly onto metal. This disk visibly deformed and was replaced after every dynamic test. The permanent deformation in the rubber and compression of it during testing is the result of some of the linear encoder's extra displacement at each time step. The second cause for this difference is that the weight is on top of the beam. The displacement measurements are taken on the bottom of the beam. Since the measurements are in milliseconds it is logical that the measurements in the bottom of the beam would trail the top. The second peak in the applied force is seen to coincide with the maximum displacement of the linear encoder. The average displacement in the beam is seen to have a peak shortly after the peak resistance of the beam is reached. This is followed by a slight decrease in mid-span displacement as the beam breaks and occurs at the same time as the weight (indicated by the linear encoder) rebounds traveling back up the rails. The beam then continues to deflect as the failure propagates through the depth of the member.

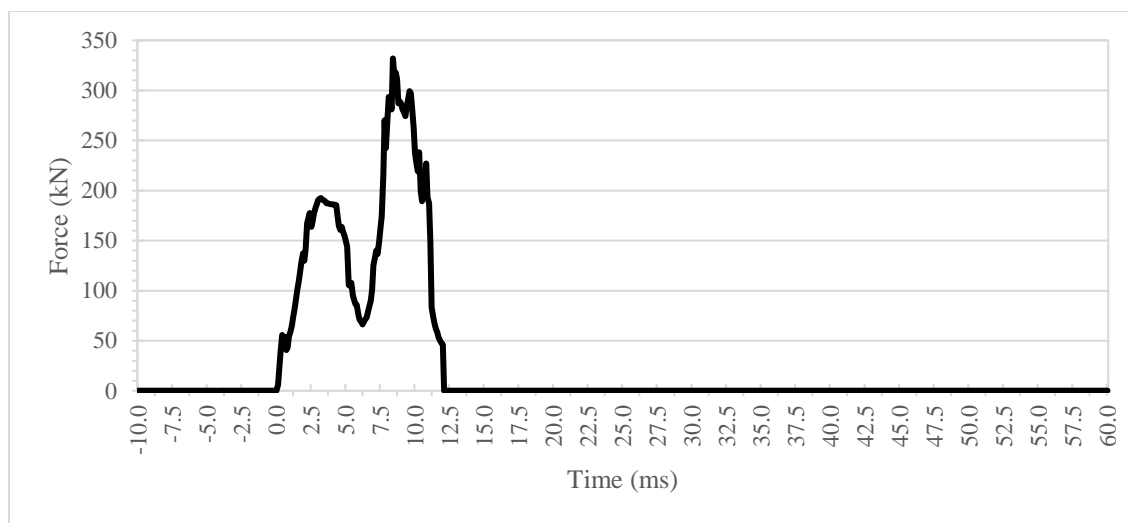


Figure 4-5: Applied force over time DN3-267

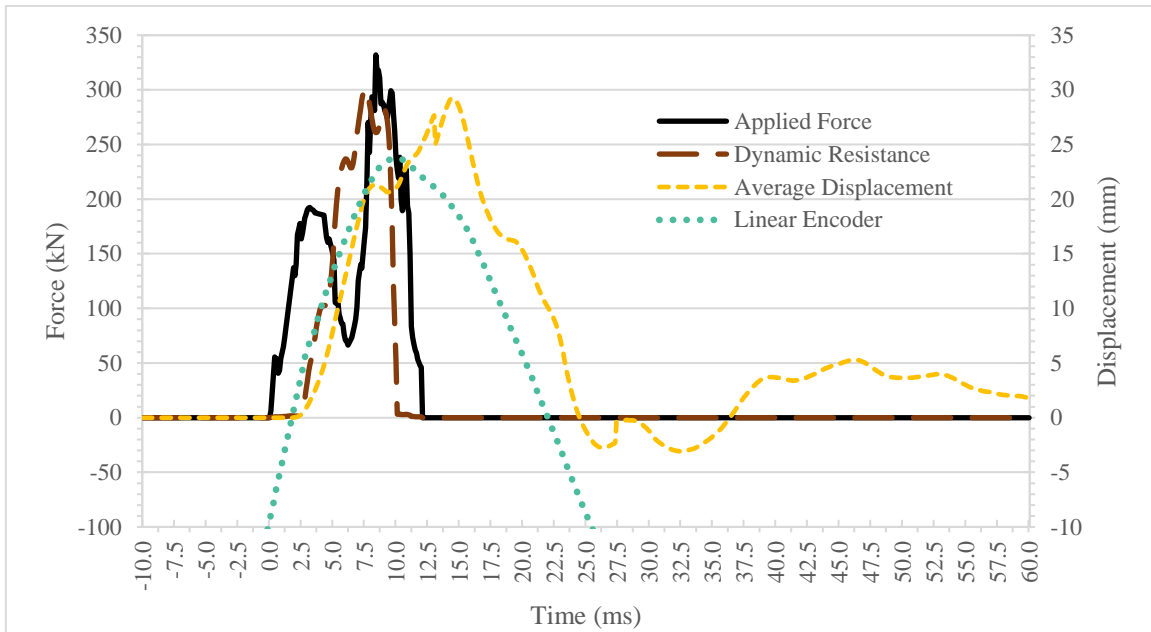


Figure 4-6: Applied force, dynamic resistance, beam displacement and drop weight displacement over time for DN3-267

Figure 4-7 shows the dynamic resistance and tensile strain over time. As can be seen, both strain gauges reach their peak shortly after the peak resistance before the cracks in the beam become so great that they either cause debonding or breaking of the strain gauge or exceeds the bounds of the measurements it can measure. Multiple strain gauges were employed in case of failure in one before the peak resistance was obtained. In these cases, only the values from the undamaged strain gauge were used. Figure 4-8 shows the dynamic resistance versus displacement for beam DN3-267. The slope used for the beam's stiffness is shown in yellow.

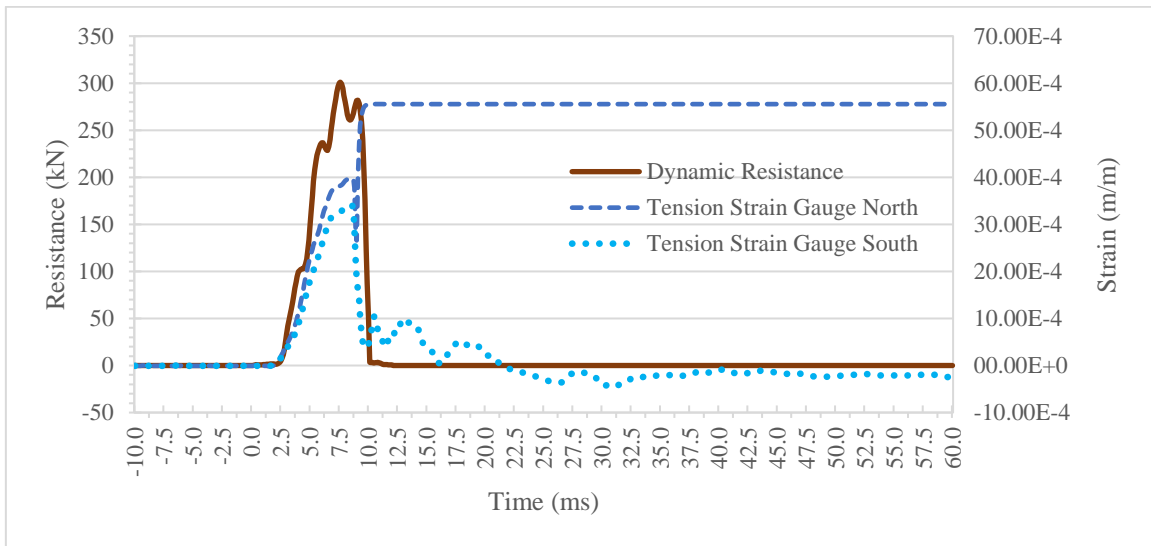


Figure 4-7: Dynamic resistance and tensile strain over time DN3-267

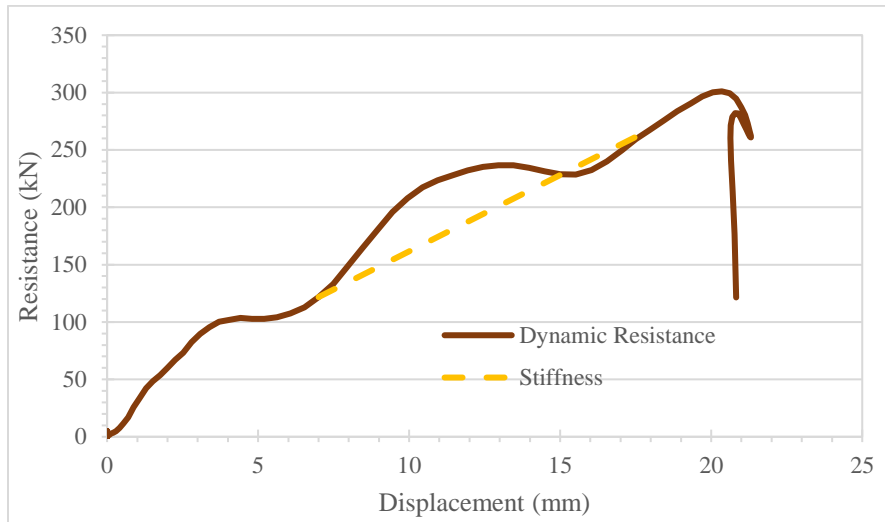


Figure 4-8: DN3-267 dynamic resistance versus midspan displacement with stiffness highlighted

The resistance curves for all dynamically tested large beams can be seen in Figure 4-9. The ‘X’ on each curve represents the dynamic peak resistance of the respective specimen. This graph indicates the presence of similarities in response between the specimens. Compared to the static resistance-curves, more variability is apparent in the graphs of these curves, which is to be expected under impact loading. All beams behaved in a linear elastic manner until a brittle failure occurs, with little-to-no post-peak resistance.

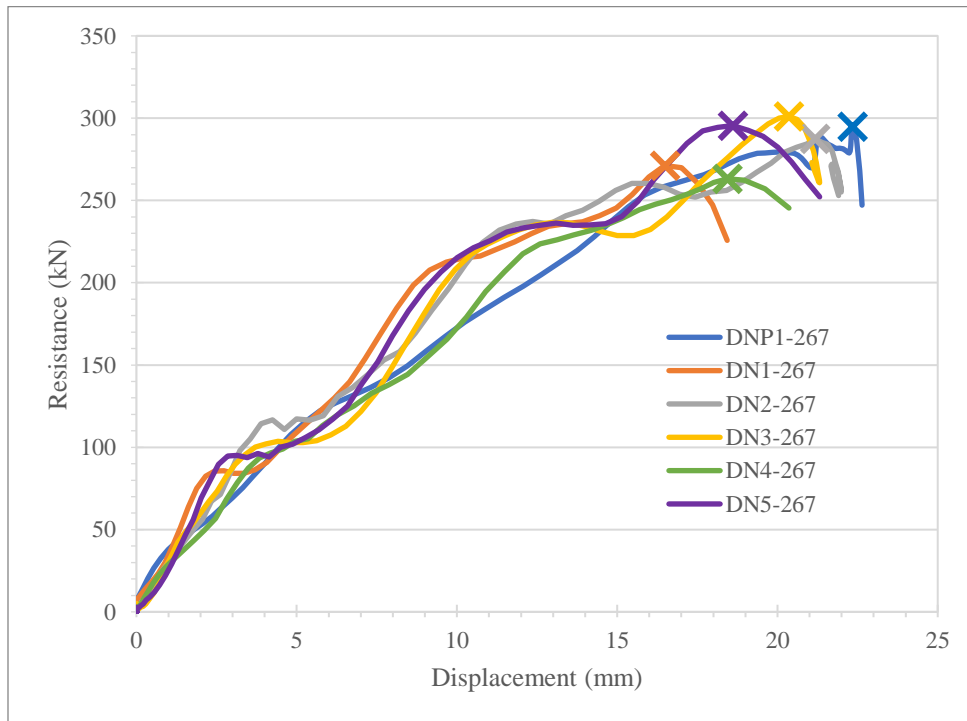


Figure 4-9: Dynamic resistance versus midspan displacement for all dynamically tested beams

4.2.4 Failure Modes

Both the static and dynamically tested large beams had a brittle flexural failure that initiated at a knot or natural defect. The static failure of SN1-267 can be seen in Figure 4-10 and the dynamic failure of DN2-267 can be seen in Figure 4-11. Figure 4-12 shows footage from the phantom high-speed camera at the beam's maximum deflection after failure. Within these images the beam's failure pattern is better observed in the dynamic beams. The failure initiation and pattern will be discussed in more detail in Chapter 5.

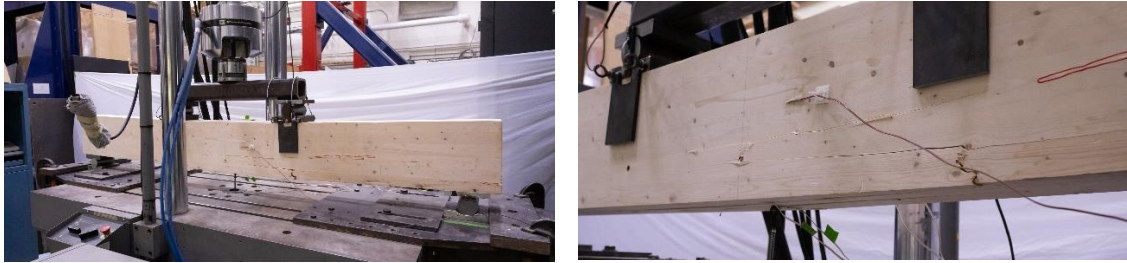


Figure 4-10: Failure of SN1-267, south side of beam and a close-in view

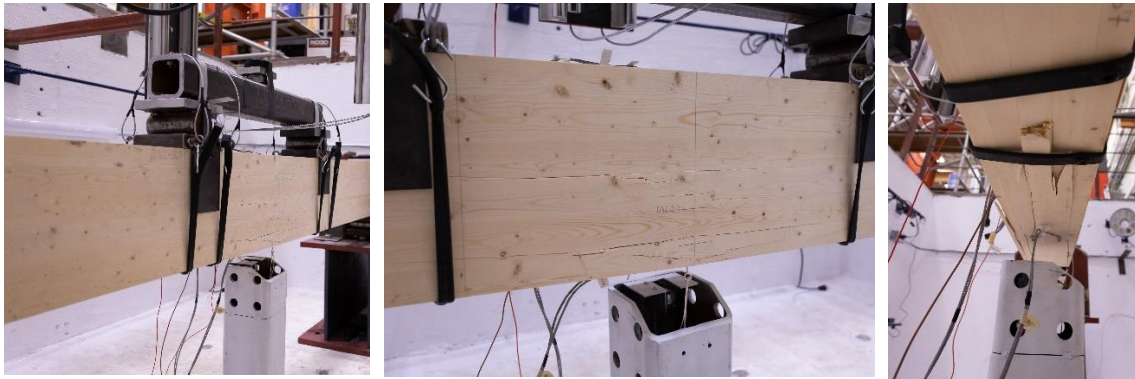


Figure 4-11: Failure of DN2-267, North side of beam, a close-in view and the bottom of the beam from left to right.

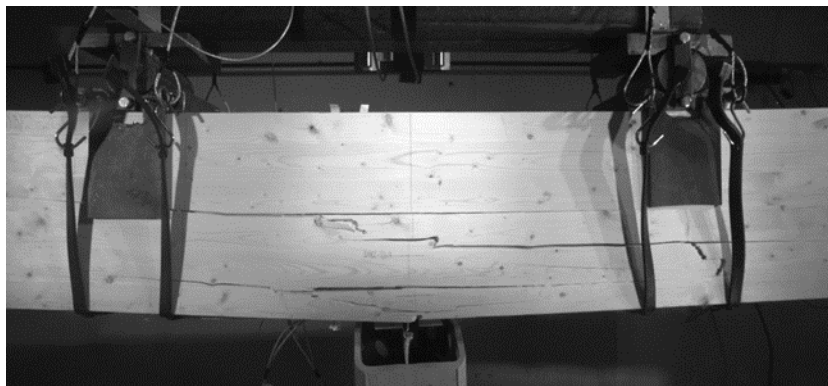


Figure 4-12: Footage from the high-speed phantom camera of DN2-267 at the beam's maximum deflection

4.3 Effects of Extreme Cold Temperature Testing – Small Dimensioned Beams

4.3.1 General

As mentioned above, smaller dimensioned beams were chosen to test the effects of extreme cold temperature on glulam due to the size constraints of the freezer. This also caused additional unforeseen consequences in the testing regime and will allow for recommendations for future testing. Although this will be discussed in detail below and in Chapter 5 it is important to note that although the testing of extreme cold beams has yielded important observations, the results are not conclusive and highlight the requirement for further testing. Importantly the presence of defects in the central third of the beam was critical to initiating a bending failure in the beam. When considering a normal span length for a building, defects will always be present. However, since the span length of the beams tested was short, due to size constraints of the freezer, defects were not always present in the span length tested. In the ensuing sections it should be kept in mind the failure mode of the beam, whether in flexure (desired) or shear, as this was found to have an effect on the results. The results based on bending alone will be considered in Chapter 5 when the DIF factors are determined; however, all results will be presented in the sections below. Identical failure criteria and criteria for determining the beam's stiffness as that of the larger beams were used for the small beams.

4.3.2 Cold Temperature Monitoring and Measurement

In order to provide an accurate estimate of the internal temperatures of all beams that were placed in the freezer, one test beam (SC3-178) was prepared in the manner outlined in Section 3.2 after it had been tested statically. Upon conditioning, SC3-178 was removed from the freezer and the temperature was then monitored over time. The output of this test allowed for the temperature-time curves to be used to relate the internal temperatures to those of the various tests conducted outside of the freezer. Figure 4-13 shows the temperature over time for four thermocouples installed at depths of 63 mm, 42 mm, 21 mm, and a surface thermocouple, which was protected from the ambient air temperature with insulation. These lines are indicated in Figure 4-13. The surface temperature was likely colder than that at a depth of 21 mm due to the insulation covering it. This would mean that the wood around the thermocouple would not warm up as quickly as the overall surface and first few millimetres of the beam. The rate of warming of the beam was the fastest at a depth of 21mm at a rate of $1.03^{\circ}\text{C}/\text{min}$, followed by the insulated surface temperature at $0.77^{\circ}\text{C}/\text{min}$ and the 42 mm depth at $0.72^{\circ}\text{C}/\text{min}$. The slowest rate was observed at 63 mm close to the centre of the beam at $0.36^{\circ}\text{C}/\text{min}$.

The recording could not be started immediately after removal from the freezer, hence the temperature over time is recorded from 1 min 50 sec to 28 min and 50 sec after removal from the freezer. The green vertical lines on the image represent the testing time of the dynamic tests which occurred at 18 min 30 sec (DC2-178, DC4-178) and 18 min 40 sec (DC1-178, DC3-178) after removal from the freezer. The average of these times corresponds to the approximate mid-point of the static test duration. The yellow vertical lines represent the various static test failure times which occurred at 26 min 42 sec (SC1-178), 25 min 48 sec (SC2-178) and 23 min 24 sec (SC2-178) after removal from the freezer. The approximated testing temperatures at the various depths and test failure times are summarised in Table 4-4. The surface thermocouple temperatures recorded during

the tests are also compared to the values obtained by the test beam. As can be seen, there is good agreement between the surface temperature of the beam with multiple thermocouples installed and the values obtained during each of the tests. There is a greater discrepancy in some of the tests where the thicker piece of foam insulation did not adhere well to the surface of the beam. As a result, the average estimated temperature for all static beams was -46.8°C at the test midpoint, -43.5°C at failure, and was -47.1°C for all dynamic beams at failure.

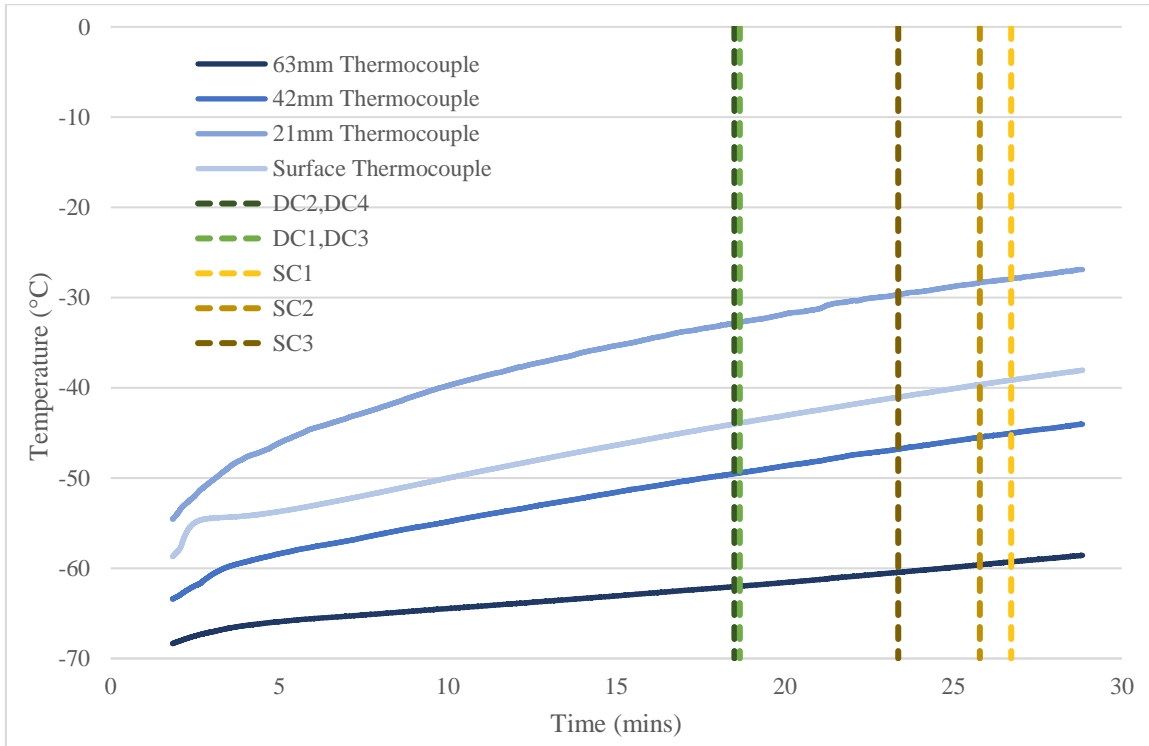


Figure 4-13: Temperature over time at different beam depths

Table 4-4: Midpoint and failure temperatures for dynamic and static tests at various depths inferred from sample beam

Beam with Multiple Thermocouples							From Insulated Surface of Tested Specimen	
Specimen	Time After Removal from Freezer min	Average Temp °C	63mm Thermocouple °C	42mm Thermocouple °C	21mm Thermocouple °C	Surface Thermocouple °C	Surface Thermocouple °C	Difference °C
Midpoint of Static Tests								
SC1-178	20.2	-46.2	-61.5	-48.5	-31.7	-42.9	-39.5 ¹	-3.4
SC2-178	18.7	-47.0	-62.0	-49.4	-32.7	-43.9	-46.0	2.1
SC3-178	18.1	-47.3	-62.2	-49.8	-33.1	-44.3	No Data	n/a
Failure of Static Tests								
SC1-178	26.7	-42.9	-59.3	-45.0	-27.9	-39.1	-35.5 ¹	-3.6
SC2-178	25.8	-43.3	-59.6	-45.5	-28.3	-39.6	-42.4	2.8
SC3-178	23.4	-44.5	-60.5	-46.8	-29.7	-41.0	No Data	n/a
Failure of Dynamic Tests								
DC1-178	18.7	-47.0	-62.0	-49.4	-32.7	-43.9	-42.2	-1.7
DC2-178	18.5	-47.1	-62.1	-49.5	-32.8	-44.0	-42.4	-1.6
DC3-178	18.7	-47.0	-62.0	-49.4	-32.7	-43.9	-32.1 ²	-11.8
DC4-178	18.5	-47.1	-62.1	-49.5	-32.8	-44.0	-33.5 ²	-10.5

¹This test only had the thicker piece of insulation foam installed on it and was not well sealed off from the air temperatures.

²For both these tests the thicker piece of insulation foam did not adhere well to the surface of the beam, letting in exterior air and causing an increase in the temperature felt by the thermocouple.

4.3.3 Static Testing

As mentioned in Section 4.2.1, Equation [4.1] was used in order to normalize the beam resistances to be that of a 1 min 100% strength value in order to provide a proper reference point for determining the DIFs. Similar to the larger dimensioned specimens, failure was deemed to coincide with the point at which the beams experienced a sudden drop in load and could no longer support additional load. The stiffness was taken as the slope of the resistance displacement curve from 40% to 90% of the beam's ultimate capacity. These percentages were kept constant for determining the beams' dynamic stiffness. The SIF has been taken as the ratio of the beam's measured MOR to that provided by the manufacturer multiplied by a factor of 1.25 bringing the beam from a standard duration load to a short duration load and multiplied by a size factor, K_{Zbg} , of 1.35. It is important to note that CSA O86 limits the value of K_{Zbg} , to 1.3. However, this is not because size effects plateau at this point, but because that is the limit of size beams have been tested for. As such, the actual calculated value was kept instead of reducing the value to 1.3. The MOR and MOE of the beams were calculated using Equations [4.2] and [4.3].

Summaries of the experimental test results from the static normal and cold temperature tests can be seen in Table 4-5 and Table 4-6, respectively, including the obtained maximum load (P_{max}), time-to-failure, normalized static peak resistance ($R_{s,max}$), the displacement at the time of peak resistance (Δ_{Rmax}), stiffness (k), strain rate ($\dot{\epsilon}$), MOR, SIF, MOE, surface temperature, and failure mode. Out of the four static normal temperature beams, two failed in flexure, one failed in shear and a second in combined flexure and shear. The average peak resistance for all normalized static normal temperature tests was 185.6 kN with a COV of 0.12. The average peak resistance for the normalized static normal temperature beams that failed only in bending was 166.3 kN with a COV of 0.02, correlating to an average SIF of 1.13. This value is lower than the value obtained under the static testing of the large beams; however, still quite similar. The average stiffness for all normalized static normal temperature tests was 11,900 kN/m with a COV of 0.02. As would be expected, when only the bending failures are considered, the stiffness does not change dramatically, with the average stiffness being 11,667 kN/m with a COV of 0.01. The average MOR for all normal temperature beams was 64.5 MPa and the average MOE was 10,905 MPa. When considering only the beams that failed in bending the MOR was 58.4 MPa and the MOE was 10,809 MPa. The average surface temperature of the normal temperature beams was 19.7°C.

Out of the three static cold temperature beams, two failed in flexure while one failed in combined flexure and shear. The average peak resistance for all normalized static cold temperature tests was 175.9 kN with a COV of 0.09. The average peak resistance for the normalized static cold temperature beams that failed only in bending was 168.9 kN with a COV of 0.08, correlating to an average SIF of 1.14. This is lower than observed with the large beams but is very similar to the value of 1.13 obtained with the small beams. The average stiffness for all normalized static cold temperature tests was 13,835 kN/m with a COV of 0.01. As would be expected, when only the bending failures are considered, the stiffness does not change dramatically, with the average stiffness being 13,852 kN/m with a COV of 0.01. The average MOR for all cold temperature beams was 61.6 MPa and the average MOE was 12,774 MPa. When considering only the beams that failed in bending the MOR was 59.1 MPa and the MOE was 12,779 MPa. The average temperature (taken from three depths and the surface thermocouple) of the cold temperature beams at failure was -43.5°C and the average surface temperature at failure was -39.9°C. More detailed indications of internal temperature of various depths for the various beams at midpoint of testing and at failure can be seen in Table 4-4 above.

Table 4-5: Static test results small normal temperature beams

	P_{max}	Time to Failure	$R_{s,max}$	$y_{s,Rmax}$	k	$\dot{\epsilon}$ ($\times 10^{-6}$)	MOR	SIF	MOE	Insulated Surface Temperature at Failure	Failure Mode
	kN	mins	kN	mm	kN/m	s^{-1}	MPa		MPa	$^{\circ}C$	
SN1-178	157.0	13.3	163.4	14.1	11,493	5.48	57.5	1.11	10,668	20.9	Flexure
SN2-178	182.5	13.6	190.0	15.3	12,245	4.74	66.2	1.28	11,228	20.8	Shear
SN3-178	162.4	14.6	169.3	14.0	11,841	4.98	59.3	1.15	10,950	20.5	Flexure
SN4-178	209.7	19.3	219.6	17.9	12,024	5.08	75.0	1.45	10,773	16.7	Combined flexure and shear
Average	177.9	15.2	185.6	15.3	11,901	5.07	64.5	1.25	10,905	19.7	
Std Dev	20.7	2.4	22.0	1.6	275	2.64	6.9	0.13	212	1.7	
COV	0.12	0.16	0.12	0.10	0.02	0.05	0.11	0.11	0.02	0.09	

Table 4-6: Static test results small cold temperature beams

	P_{max}	Time to Failure	$R_{s,max}$	$y_{s,Rmax}$	k	$\dot{\epsilon}$ ($\times 10^{-6}$)	MOR	SIF	MOE	Insulated Surface Temperature at Failure	Failure Mode
	kN	mins	kN	mm	kN/m	s^{-1}	MPa		MPa	$^{\circ}C$	
SC1-178	175.5	13.0	182.9	13.0	13,760	6.44	64.1	1.24	12,725	-39.1	Flexure
SC2-178	182.1	13.4	189.8	13.4	13,800	4.95	66.5	1.28	12,762	-39.6	Combined flexure and shear
SC3-178	149.1	10.9	155.0	10.9	13,945	4.99	54.2	1.05	12,834	-41.0	Flexure
Average	168.9	12.4	175.9	12.4	13,835	5.46	61.6	1.19	12,774	-39.9	
Std Dev	14.2	1.1	15.1	1.1	79	0.70	5.3	0.10	45	0.8	
COV	0.08	0.09	0.09	0.09	0.01	0.13	0.09	0.09	0.00	0.02	

As can be observed in Table 4-5 and Table 4-6, the overall strength of the beams does not seem to be affected by extreme cold temperatures, while the stiffness of the beam seems to be affected, with those that are colder being much stiffer than the normal temperature beams. These observations will be discussed in greater detail in Chapter 5.

Figure 4-14 and Figure 4-16 shows SN3-178’s behavior over time and Figure 4-15 and Figure 4-17 show SC3-178’s behaviour over time. Figure 4-14 and Figure 4-15 shows both beam’s strain and resistance over time. The strain in all four strain gauges linearly increases with the load over time with small drops occurring whenever a surface crack appears in the beams face. For the purpose of the graph the compression strain gauges have been plotted in the positive direction. Figure 4-16 and Figure 4-17 shows the beam’s displacement and measured resistance over time. As with the strain, the beam’s displacement linearly varies with the beam’s resistance until failure.

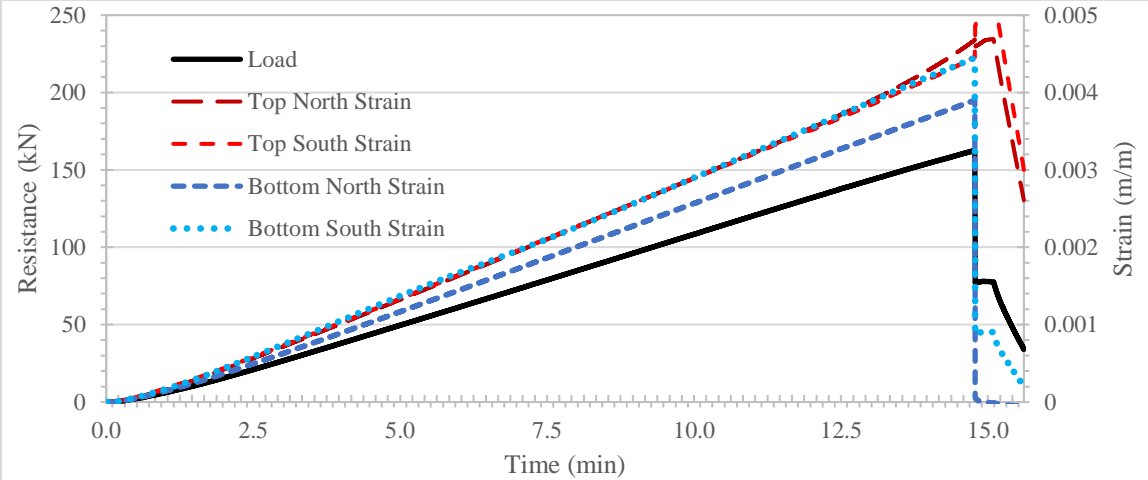


Figure 4-14: SN3-178 Resistance and strain over time

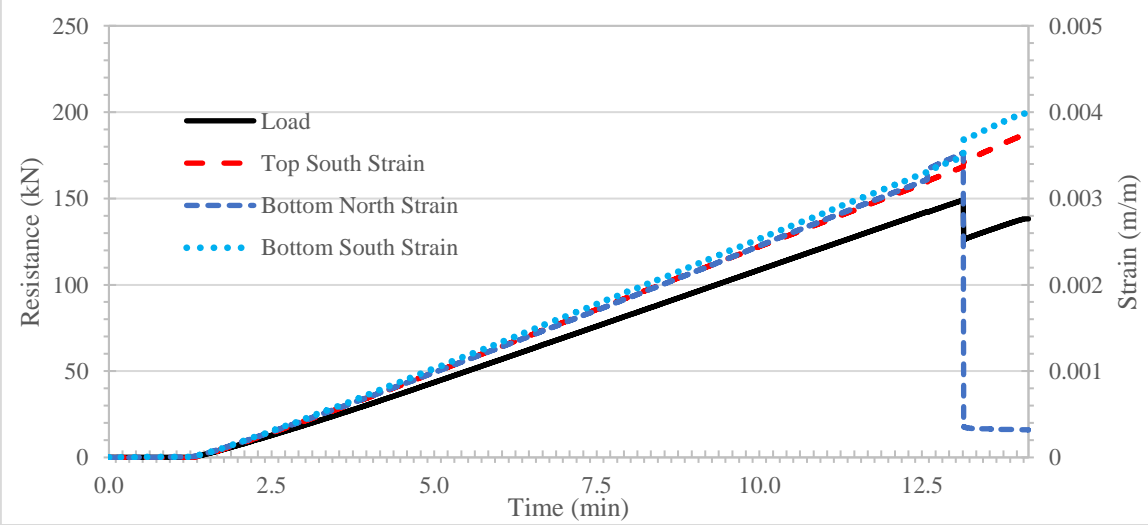


Figure 4-15: SC3-178 Resistance and strain over time

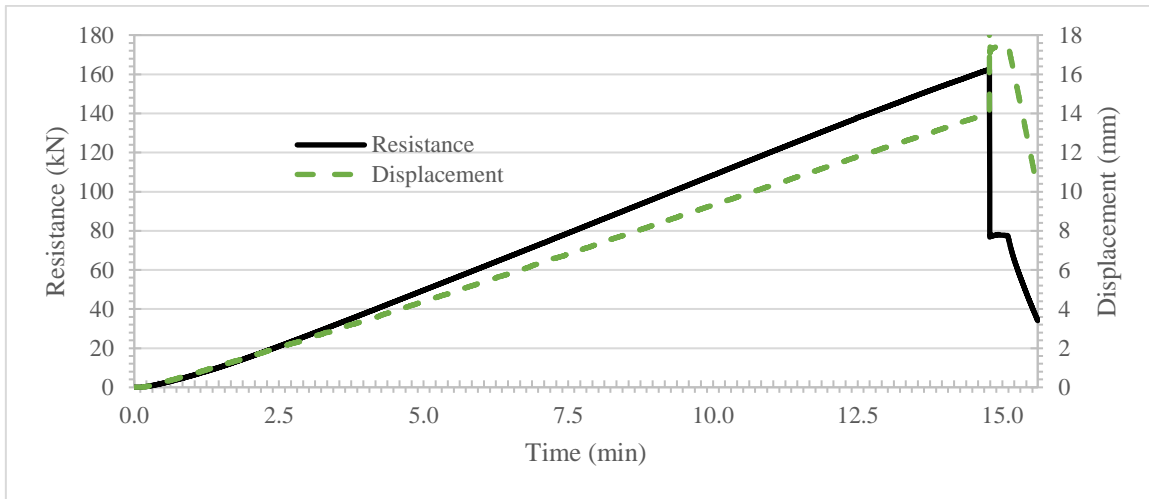


Figure 4-16: SN3-178 Resistance and displacement over time

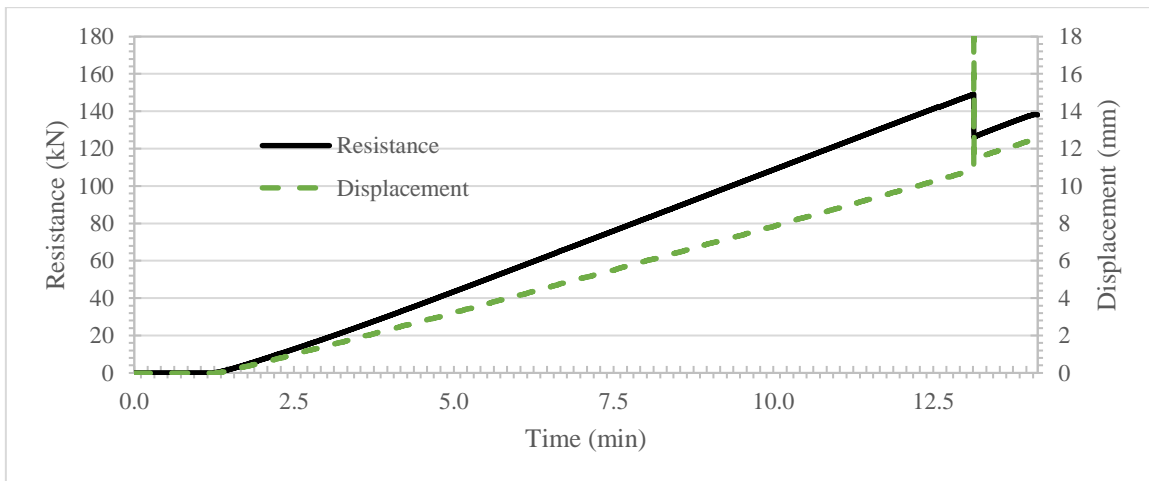


Figure 4-17: SC3-178 Resistance and Displacement Over Time

Figure 4-18 shows the beam resistance versus displacement for all static normal temperature and cold temperature tests, with the normal temperature tests indicated in warm colours and the cold temperature tests indicated in blues. The solid lines in the image are the beams that failed in flexure. The dotted line in the graph are the beams that failed either in shear or combined flexure and shear. As can be visually seen the ultimate resistances, displacements, and slope of the line for the normal temperature beams, when compared to one another, remain very similar. The two beams that failed in shear or combined flexure and shear do have a much higher resistance than the two that failed only in flexure. The ultimate resistances, displacements, and slope of the line for the cold temperature beams, when compared to one another, also remain very similar. Once again, the resistance of the beam that failed in combined flexure and shear is higher than those that failed in only flexure. The slope of resistance to displacement line from 40% to 90% of the beam's ultimate capacity was taken as the beam's stiffness. When comparing the cold beams to the normal temperature beams, one can see that the cold beams' stiffnesses are greater than that of the normal temperature beams, but that the beams' resistances remains similar.

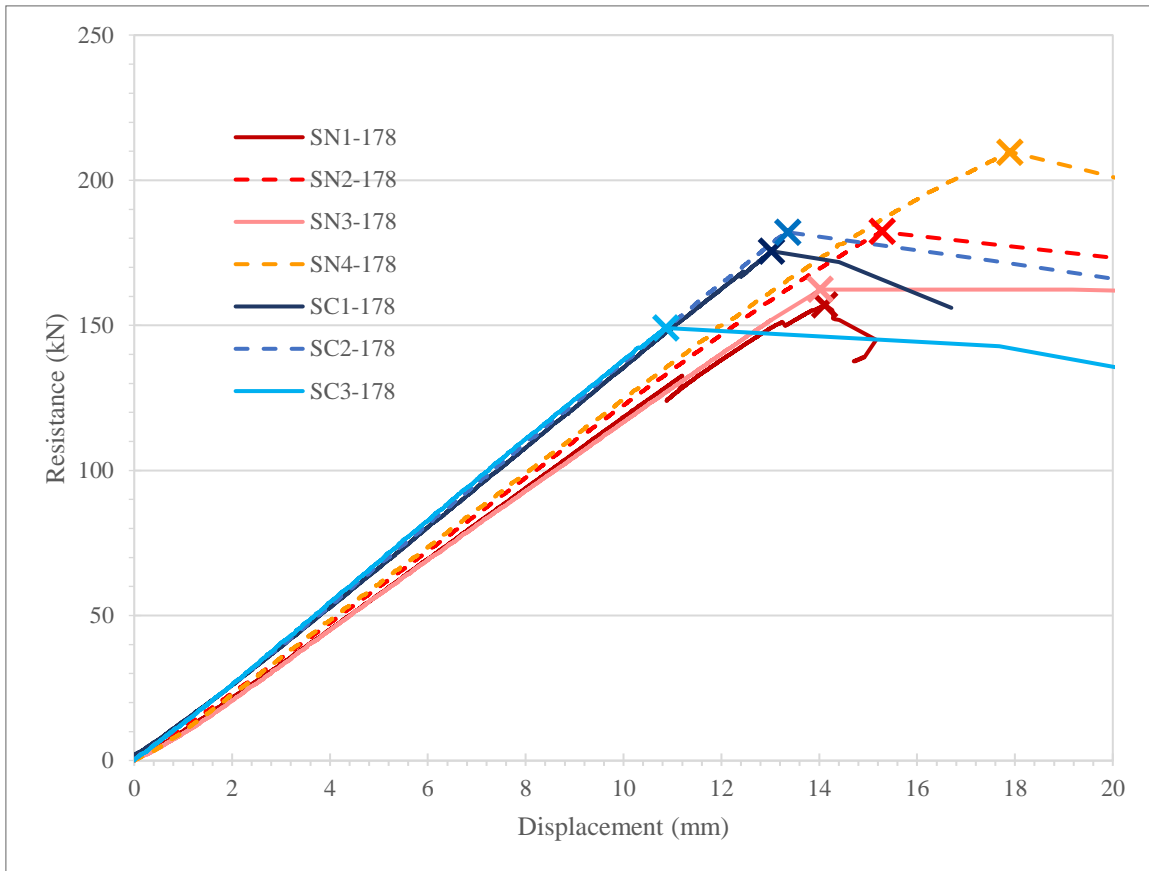


Figure 4-18: Static small normal and cold temperature tests resistance versus displacement over time

4.3.4 Multiple Impacts to DN1-178

As mentioned in Chapter 3, DN1-178 was impacted twice more than the other small normal temperature beams in order to finalize the test set-up and determine a proper drop height and weight. These multiple hits did not alter the beam's response and also provides proof of the linear elastic nature of a beam exposed to multiple impacts before reaching its peak resistance. Below in Figure 4-19 you can see the resistance versus displacement of three of the impacts that were delivered to the beam. The first impact is not included, as this test is from a short height only to determine if the instrumentation is reading correctly. As can be seen from the image, the beam's stiffness did not change dramatically between hits.

Table 4-7 shows the drop weight, height, maximum dynamic resistance, displacement at the time of peak resistance, stiffness (taken from 40-90% of the beam's resistance versus displacement relationship). The average stiffness obtained through the tests was 13,498 kN/m with a standard deviation of 1,139 kN/m and a coefficient of variation of 0.08. In addition, looking at the percent difference of the stiffness between the average stiffness obtained from all hits, all dynamic tests were within 10.8% of the average. This indicates that the beam stiffness is not affected by the multiple hits and that the variation is due to the erratic nature of some aspects of impact testing, such as vibrations caused by the natural frequencies of various components.

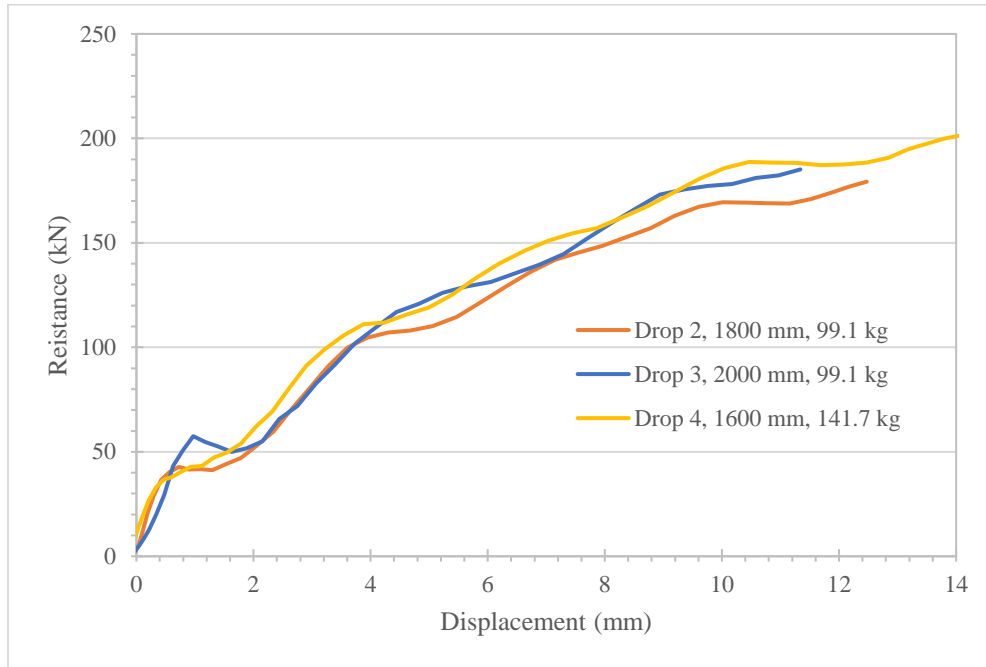


Figure 4-19: Resistance versus displacement of three of the impacts to DN1-178

Table 4-7: Summary of three elastic dynamic tests on DN1-178

Dynamic test	Weight kg	Height mm	Dynamic Resistance kN	Displacement at Max Resistance mm	Stiffness kN/m
2	99.1	1,800	179.3	12.1	13,466
3	99.1	2,000	185.1	11.8	14,908
4	141.7	1,600	201.3	13.7	12,119
Average					13,498
Std Dev					1,139
COV					0.08

4.3.5 Dynamic Testing

Dynamic failure of the beam specimens was determined to occur at the peak resistance, consistently followed by a sudden drop in resistance. All dynamic cold specimens were tested approximately 18.5 mins after leaving the freezer. This time was chosen to align with the approximate midpoint of the static cold temperature tests. The dynamic resistance was determined as outlined in Section 4.2.3 using Equations [4.4] and [4.5]. The stiffness was taken as the slope of the resistance displacement curve from 40% to 90% of the beam's ultimate capacity as with the static tests. As such, this range was deemed to have the most accurate representation of the beams stiffness and strain rate. Similarly the MOE and MOR for the beams was also calculated using

Equations [4.2] and [4.3]. Similar to the larger dimensioned specimens, the beam's displacement measurements were taken as the average between the laser and the string potentiometer. Since the laser and string potentiometer are both located on different parts of the beam's width, a more accurate view of the entire beam's global displacement response could be gained. In any cases where the difference in displacements between the laser and the string potentiometer differed by more than 1.07 mm (approximately 8.5% of the total beams deflection) the displacements were then compared with those obtained by the high-speed cameras in order to determine which measurement device was more accurate. The displacement was then taken from only the laser, which was more accurate when considering the behavior of DN4-178 and DC1-178.

The results from the dynamic tests can be seen in Table 4-8 and Table 4-9, including the dynamic peak resistance ($R_{d,max}$), the displacement at the time of peak resistance (y_{Rmax}), stiffness (k), average compressive and tensile strain at the time of peak resistance (ϵ_{f-c} and ϵ_{f-t}), strain rate ($\dot{\epsilon}$), MOR, MOE, time-to-failure, duration of load and failure mode.

All of the normal temperature dynamic specimens failed in flexure. For strain rates between 1.13 to 1.38 s^{-1} , the average dynamic peak resistance for the normal temperature beams was 204.4 kN with a coefficient of variation (COV) of 0.04. The average stiffness for the normal temperature beams was 14,695 kN/m with a COV of 0.08. The average MOR for the beams was 69.9 MPa and the average MOE was 13,160 MPa.

One of the dynamic cold temperature beams failed in shear, DC1-178. For strain rates between 1.14 to 1.31 s^{-1} , the average dynamic failure resistance for the cold temperature beams was 230.3 kN with a coefficient of variation (COV) of 0.02. The average stiffness for the cold temperature beams was 17,053 kN/m with a COV of 0.03. The average MOR for the beams was 79.5 MPa and the average MOE was 15,474 MPa. If only the flexural failures are considered, the average dynamic failure resistance for the cold temperature beams was 231.5 kN with a coefficient of variation (COV) of 0.02. The average stiffness for the cold temperature beams was 17,236 kN/m with a COV of 0.02. The average MOR for the beams was 79.4 MPa and the average MOE was 15,526 MPa. As can be seen from these values, the beam that failed in shear, had very similar failure value to the other beams and as such the results do not differ greatly when this beam's data is omitted.

From comparing the above values for cold and normal temperature specimens, an apparent increase in strength can be observed under dynamic loading. Similar to the static test results, the beams' stiffnesses are also greater, as was the same with the static testing. This will be discussed in greater detail in Chapter 5.

Table 4-8: Dynamic test results small normal temperature beams

	$R_{d,max}$	$y_{d,Rmax}$	k	ϵ_{f-c} ($\times 10^{-3}$)	ϵ_{f-t} ($\times 10^{-3}$)	$\dot{\epsilon}$	MOR	MOE	Time to Failure	Duration of Load	Failure Mode
	kN	mm	kN/m	m/m	m/m	s ⁻¹	MPa	MPa	ms	ms	
DN1-178	210.7	14.9	12,892	-4.62	4.35	1.36	73.4	11,822	6.4	9.5	Flexure
DN2-178	207.7	13.4	16,141	-3.12	3.70	1.13	70.8	14,393	6.0	10.0	Flexure
DN3-178	190.3	12.1	14,341	-3.57	3.41	1.38	64.8	12,788	5.7	9.6	Flexure
DN4-178	208.9	11.5 ¹	15,407	-3.08	3.87	1.33	70.7	13,639	5.4	9.4	Flexure
Average	204.4	13.0	14,695	-3.60	3.83	1.30	69.9	13,160	5.9	9.6	
Std Dev	8.2	1.3	1,222	0.62	0.34	0.10	3.1	959	0.4	0.2	
COV	0.04	0.10	0.08	-0.17	0.09	0.08	0.04	0.07	0.06	0.02	

¹ These displacements were taken solely from the laser displacement whereas all other maximum displacements were taken as an average of the laser and string potentiometer.

Table 4-9: Dynamic test results small cold temperature beams

	$R_{d,max}$	$y_{d,Rmax}$	k	ϵ_{f-c} ($\times 10^{-3}$)	ϵ_{f-t} ($\times 10^{-3}$)	$\dot{\epsilon}$	MOR	MOE	Time to Failure	Duration of Load	Failure Mode
	kN	mm	kN/m	m/m	m/m	s ⁻¹	MPa	MPa	ms	ms	
DC1-178	226.8	12.7 ¹	16,504	No Data	3.94	1.25	79.8	15,319	5.4	8.9	Shear
DC2-178	226.0	11.7	17,640	-3.22	No Data	1.28	79.2	16,313	5.5	9.1	Flexure
DC3-178	229.2	13.0	16,702	-3.76	3.52	1.14	78.1	14,893	5.9	10.0	Flexure
DC4-178	239.4	11.7	17,364	-2.84	4.02	1.31	81.0	15,372	5.5	10.3	Flexure
Average	230.3	12.3	17,053	-3.27	3.83	1.25	79.5	15,474	5.6	9.6	
Std Dev	5.4	0.6	465	0.38	0.22	0.06	1.0	519	0.2	0.6	
COV	0.02	0.05	0.03	-0.11	0.06	0.05	0.01	0.03	0.03	0.06	

¹ These displacements were taken solely from the laser displacement whereas all other maximum displacements were taken as an average of the laser and string potentiometer.

Figure 4-20 shows the applied force over time for DN3-178 on the left and DC4-178 on the right, recorded by the central force transducer. As can be seen in the image, the force was applied as a two peaked force, similar to the larger dimensioned specimens. As the impact weight initially impacts the beam, the initial impact force causes the beam, load transfer bar and central force transducer to accelerate away from the weight, causing a decrease in the recorded force. The weight then catches up to the beam, applying the remaining force until failure. This path is confirmed by viewing the overlays of the beam's displacement and that of the linear encoder on the box, investigated in Figure 4-21 for DN3-178 and Figure 4-22 for DC4-178. The applied load on the cold temperature beams was higher than that of the normal temperature beams as the weight was dropped from a higher height.

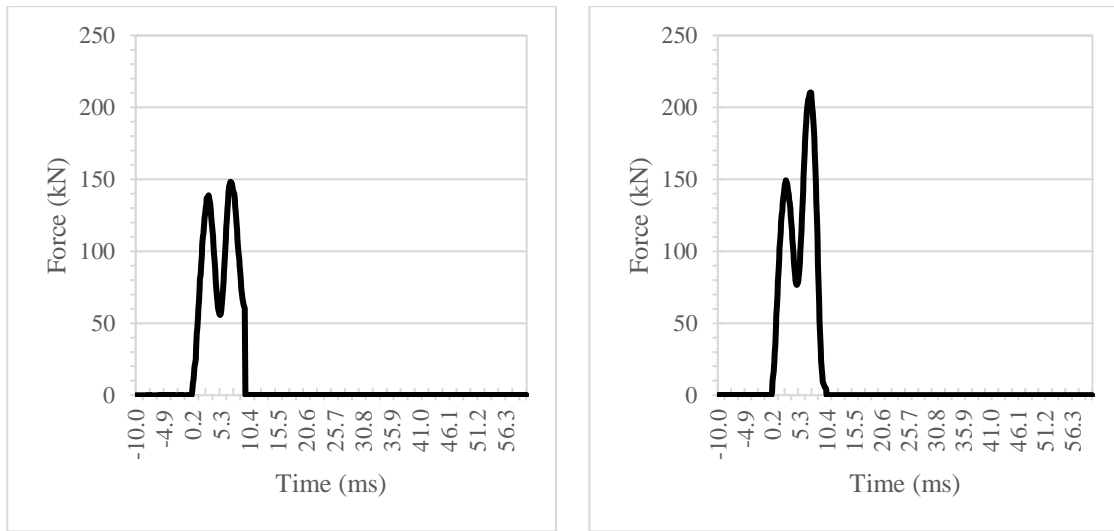


Figure 4-20: Applied force over time DN3-178 on left and DC4-178 on right

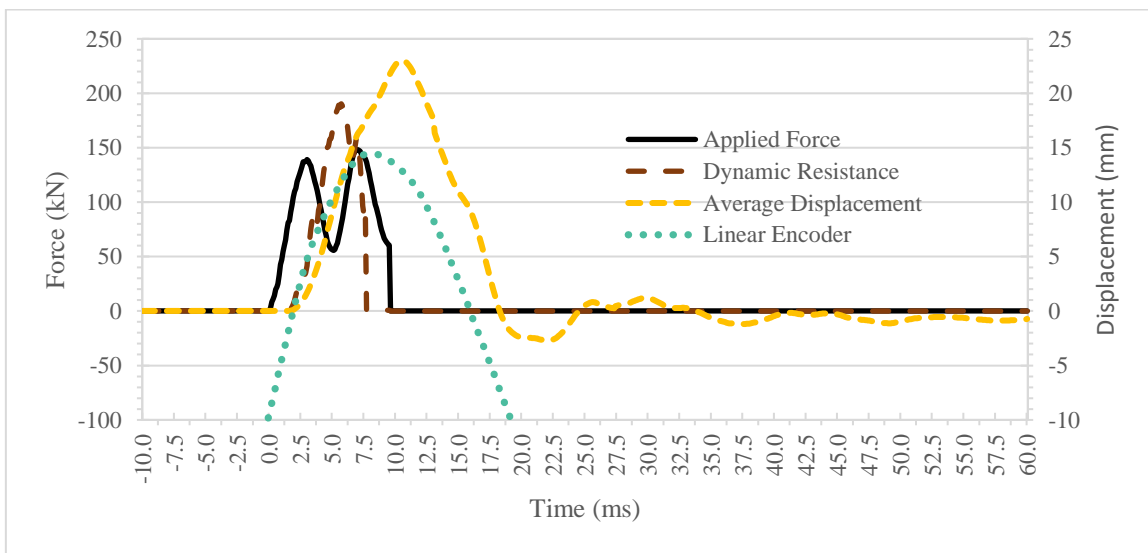


Figure 4-21: Applied force, dynamic resistance, and beam and drop-weight displacement over time for DN3-178

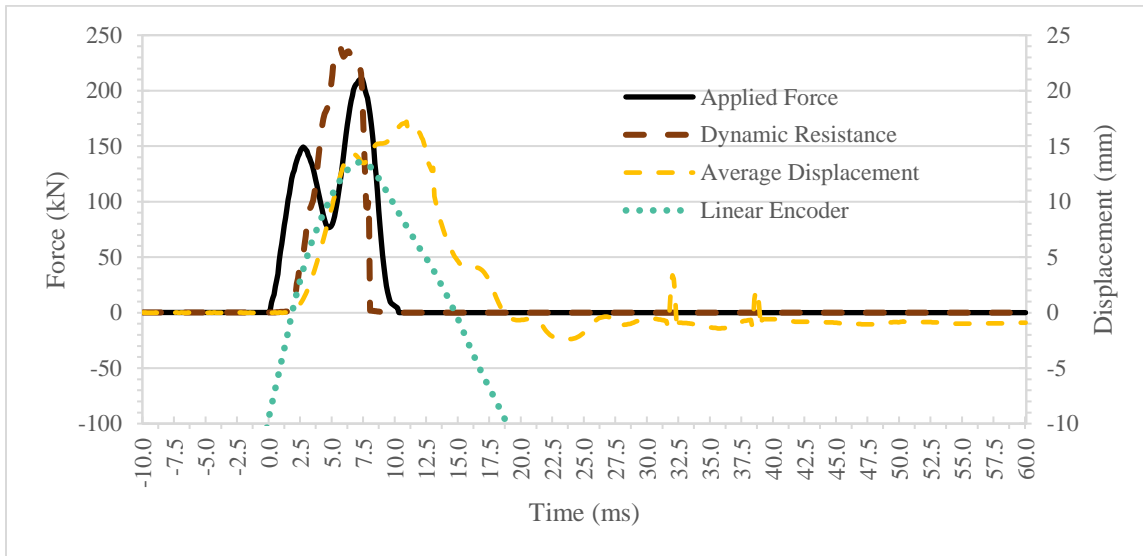


Figure 4-22: Applied force, dynamic resistance, and beam and drop-weight displacement over time for DC4 178

The average displacement in the beam is seen to have a peak shortly after the peak resistance of the beam is reached. This is followed by a slight decrease as the beam breaks and occurs at the same time as the weight (indicated by the linear encoder) rebounds traveling back up the rails. The beam then continues to deform as the failure spreads, however, the deformation after impact is not important to the study at hand due to the brittle fracture of the wood, its linear elastic behavior and lack of post-peak resistance.

Figure 4-23 and Figure 4-24 show the dynamic resistance and tensile strain over time. As can be seen in the image the strain increases with increasing resistance. Both gauges reach their peak shortly after the peak resistance before the cracks in the beam become so great that they either cause de-bonding or breaking of the strain gauge, or exceed the bounds what can be measured. As can be seen from the images, multiple strain gauges were employed in case of failure in one before the peak resistance was obtained. In these cases, only the values from the undamaged strain gauge were used.

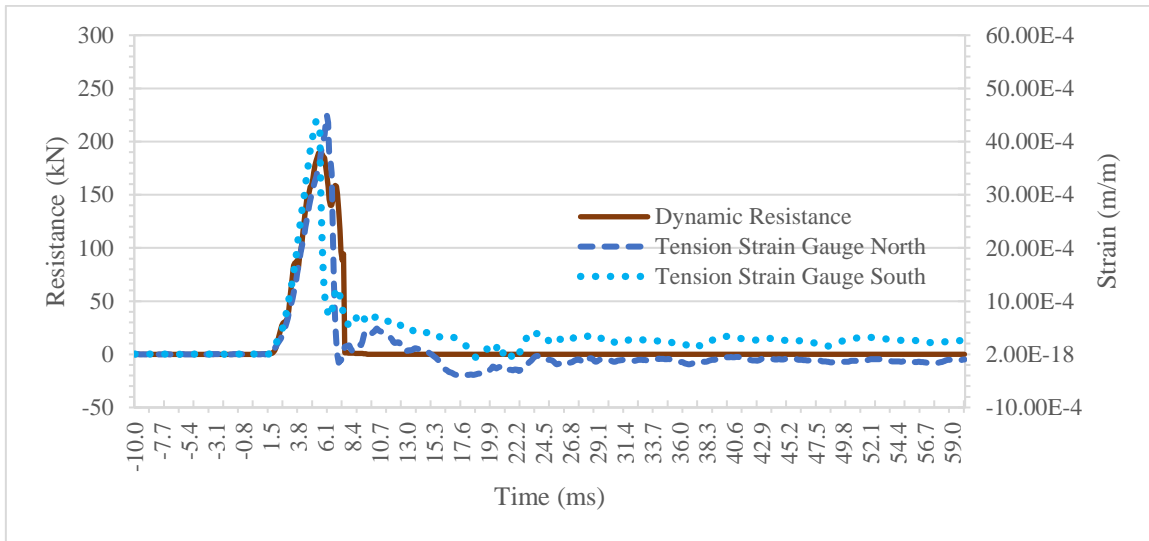


Figure 4-23: Dynamic resistance and tensile strain over time DN3-178

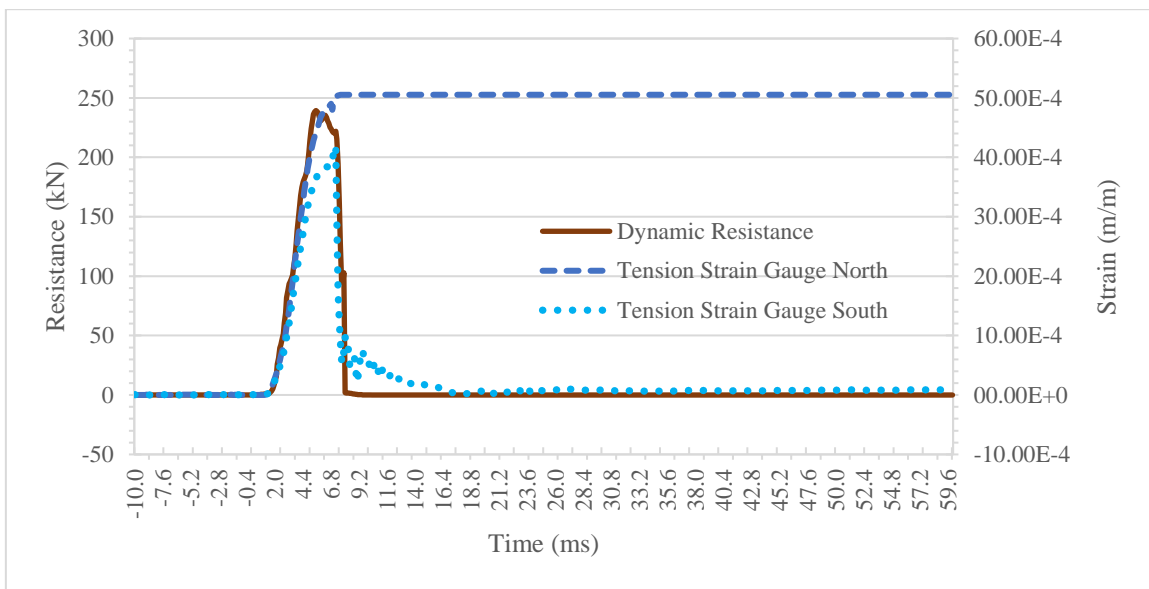


Figure 4-24: Dynamic resistance and tensile strain over time DC4-178

Figure 4-25 and Figure 4-26 show the dynamic resistance versus displacement for beam DN3-178 and DC4-178. The slope used for the beam's stiffness is shown by the yellow dashed line. The graphs indicate why 40-90% of the beams overall capacity was chosen for the stiffness. There appears to be an initial stiffness that changes slope once the system settles and becomes less accurate near the maximum. The increased stiffness and dynamic resistance of the cold beam is also apparent in this image.

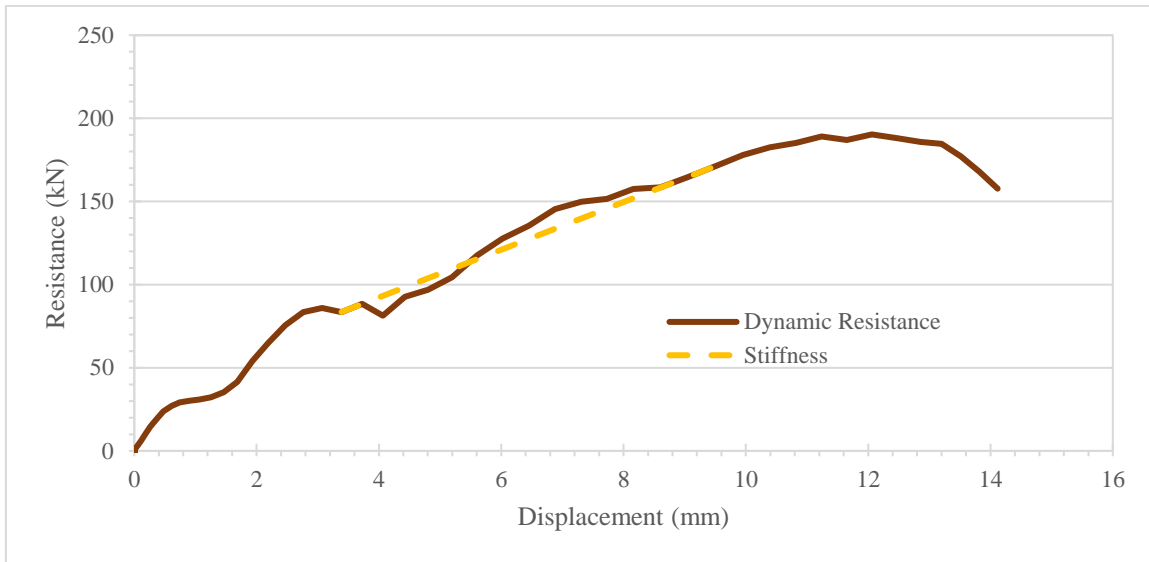


Figure 4-25: DN3-178 dynamic resistance versus midspan displacement with stiffness highlighted

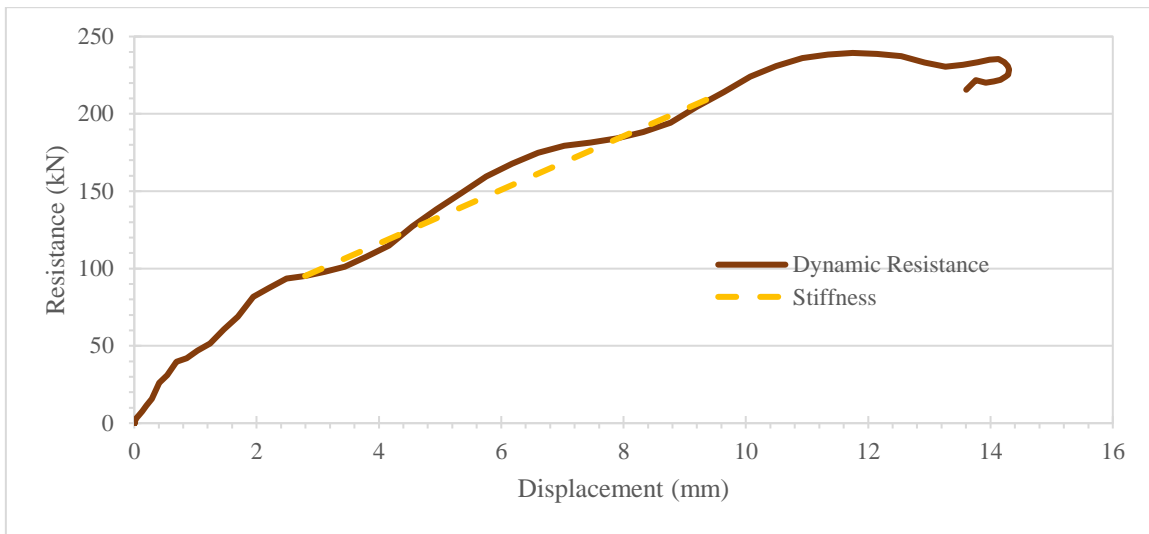


Figure 4-26: DC4-178 dynamic resistance versus midspan displacement with stiffness highlighted

The resistances versus displacements for all dynamically tested small beams can be seen in Figure 4-27. The ‘X’ on each line represents the maximum dynamic resistance of the beam, which was deemed to be failure. All normal temperature beams are shown in warm colours. All cold temperature beams are shown in blue. The one beam that failed in shear is shown by the dotted line. Common amongst all beams, the initial stiffness of the system settling can be seen, which is not representative of the rest of the curve. Following this one can see a secondary slope from approximately 40-90% of the beam’s dynamic behavior before failure. The waviness in the reaction versus displacement is a product of the dynamics of the system, the measurement of the system and the vibrations that occur within a dynamic system. More variability is apparent in the graphs of these curves compared to those seen in the static tests, which is to be expected under impact

loading. All beams behavior in a linear elastic manner until a brittle failure occurs, with no residual strength or post-peak resistance. The increased dynamic resistance of the cold temperature beams compared to the normal temperature beams is evident in this graph as is the increased stiffness. The values associated with this will be further evaluated in Chapter 5.

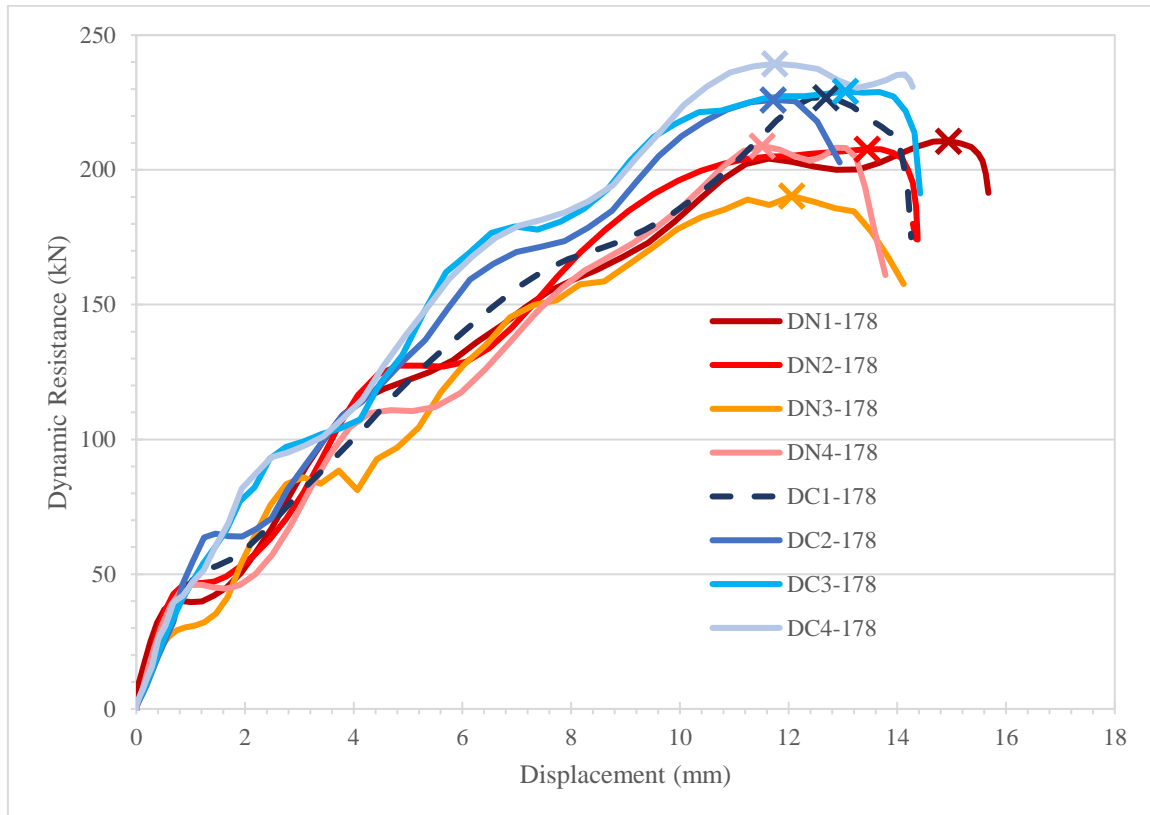


Figure 4-27: Dynamic resistance versus midspan displacement for all dynamically tested small beams

4.3.6 Failure Modes

All beams responded in a linear elastic manner and all beams that had a flexural failure exhibited a brittle tensile failure initiating at a knot or natural defect. However, some of the small beams failed in shear or combined flexural and shear, which is discussed in greater detail in Chapter 5. Figure 4-28 and Figure 4-29 show views of the failed static beams within the static experimental set-ups. The cracks are very visible within the static normal temperature beam, SN1-178. They are much less visible in the static cold temperature beam displayed, SC1-178. Figure 4-30 and Figure 4-31 show images of the failed dynamic beams within the testing pit. Differences in the crack propagation between the dynamic normal temperature beams and dynamic cold temperature beams was not as visible. Figure 4-32 and Figure 4-33 show footage from the phantom high-speed camera at the beam's maximum deflection after failure. Within these images the beam's failure pattern is better observed in the dynamic beams.

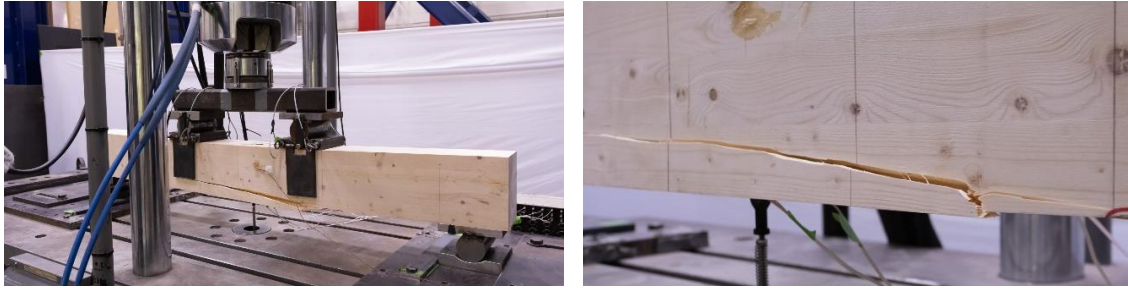


Figure 4-28: Failure of a static normal temperature specimen, SN1-178, within the testing apparatus



Figure 4-29: Failure of a static cold temperature specimen, SC1-178, within the testing apparatus



Figure 4-30: Failure of a dynamic normal temperature specimen, DN1-178 in the testing pit



Figure 4-31: Failure of a dynamic cold temperature specimen, DC1-178 in the testing pit

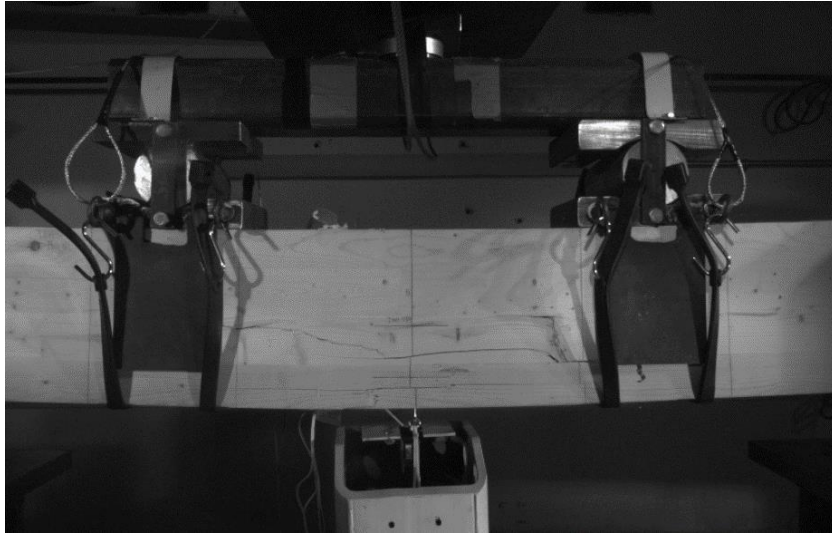


Figure 4-32: Footage from the high-speed phantom camera of DN1-178 at the beam's maximum deflection



Figure 4-33: Footage from the high-speed phantom camera of DC2-178 at the beam's maximum deflection

Figure 4-34 shows SN2-178, a static normal temperature beam that failed in shear. Figure 4-35 shows SN4-178, a static normal temperature beam that failed in combined flexure and shear. Figure 4-36 shows DC1-178, a dynamic cold temperature beam that failed in shear. These failures will be further discussed in Chapter 5 but will not be analysed in detail as the focus of the study was on the flexural failure of the beams. Its influence on the obtained failure values and effect on DIF values will be discussed.

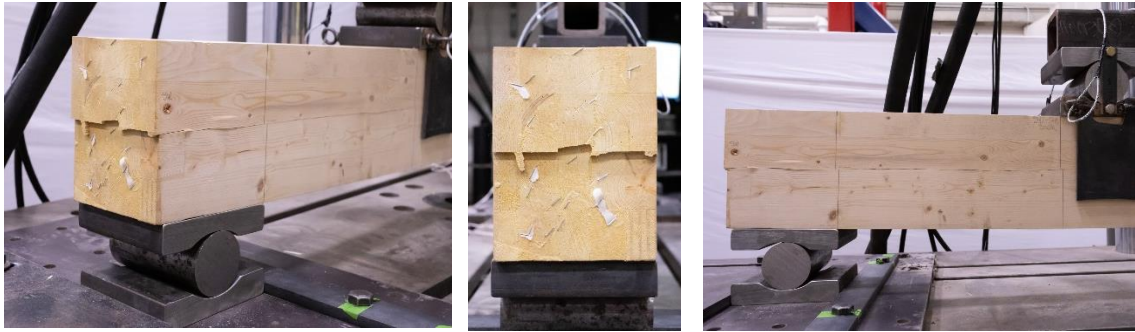


Figure 4-34: Shear failures in static normal temperature test specimen SN2-178



Figure 4-35: Combined shear and flexural failure in static normal temperature test specimen SN4-178



Figure 4-36: Shear and flexural failure in a dynamic cold temperature test specimen SN4-178

4.4 Summary

In summary, the static and dynamic behaviour of large and small glulam specimens under cold and normal temperature were investigated. The average displacement at failure, stiffness, MOR, MOE and strain rate were obtained through full-scale testing. Initial observations indicate an increase in the dynamic resistance and stiffness of glulam subjected to impact loading. They also indicate an increase in stiffness when beams are at extreme cold temperatures. There also appears to be a greater increase in strength of the cold specimens under dynamic loading when compared to the normal temperature counterparts. The quantification of this will be discussed in Chapter 5.

All larger dimensioned beams failed in flexure. The average peak resistance for the normalized static tests of the larger dimensioned beams was 252.7 kN with a coefficient of variation (COV) of 0.02, correlating to an average SIF of 1.25. The average stiffness was 11,126 kN/m with a COV of 0.03. The average MOR for the beams was 59.5 MPa and the average MOE was 10,759 MPa. For strain rates between 0.67 to 1.05 s⁻¹, the average dynamic peak resistance of the large dimensioned beams was 285.6 kN with a COV of 0.05. The average stiffness was 13,368 kN/m with a COV of 0.06. The average MOR for the beams was 67.3 MPa and the average MOE was 12,924 MPa.

Out of the four static smaller normal temperature beams, two failed in flexure, one failed in shear and a second in combined flexure and shear. The average peak resistance for the normalized static normal temperature beams that failed only in bending was 166.3 kN with a COV of 0.02, correlating to an average SIF of 1.13. The average stiffness was 11,667 kN/m with a COV of 0.01. The MOR was 58.4 MPa and the MOE was 10,809 MPa. The average surface temperature of the normal temperature beams at failure was 19.7°C. All of the smaller normal temperature dynamic specimens failed in flexure. For strain rates between 1.13 to 1.38 s⁻¹, the average dynamic peak resistance for the normal temperature beams was 204.4 kN with a COV of 0.04. The average stiffness for the normal temperature beams was 14,695 kN/m with a COV of 0.08. The average MOR for the beams was 69.9 MPa and the average MOE was 13,160 MPa. The average surface temperature of the normal temperature beams at failure was 19.2°C.

Out of the three static smaller cold temperature beams, two failed in flexure while one failed in combined flexure and shear. The average peak resistance for the normalized static cold temperature beams that failed only in flexure was 168.9 kN with a COV of 0.08, correlating to an average SIF of 1.14. The average stiffness was 13,852 kN/m with a COV of 0.01. The MOR was 59.1 MPa and the MOE was 12,779 MPa. The average temperature (taken from three depths and the surface thermocouple) of the static cold temperature beams at failure was -43.5°C and the average insulated surface temperature at failure was -39.9°C at failure. One of the dynamic cold temperature beams failed in shear, with the rest failing in flexure. For strain rates between 1.14 to 1.31 s⁻¹, the average dynamic failure resistance for the cold temperature beams for the beams that failed in flexure was 231.5 kN with a COV of 0.02. The average stiffness for the cold temperature beams was 17,236 kN/m with a COV of 0.02. The average MOR for the beams was 79.4 MPa and the average MOE was 15,526 MPa. The average temperature (taken from three depths and the surface thermocouple) of the cold temperature dynamic beams at failure was -47.1°C and the average insulated surface temperature at failure was -44.0°C at failure.

All beams had a linear elastic brittle failure. The failure patterns when comparing static

testing to dynamic testing did not differ greatly. Under static testing the cold temperature beams appeared to be subject to less splintering than the normal temperature beams, which may be caused by the frozen ice crystals keeping some of the wood's fibres together. These items will be further discussed in Chapter 5.

Chapter 5: Discussion

5.1 General

The following chapter will discuss the implications of the obtained results. Specifically, it will discuss the DIF factors obtained and discuss how this may impact future iterations of CSA S850, as well as other relevant improvements to design guidelines. It will discuss the statistical analysis done to support these results, which will lead to recommendations for future research in Chapter 7.

The use of identical spans, boundary conditions, and loading conditions allowed for a direct comparison between the static and dynamic test results for the purpose of quantifying high strain-rate effects on the glulam specimens. The DIF on the peak resistance was calculated using Equation [5.1].

$$DIF = \frac{MOR_d}{MOR_s} \quad [5.1]$$

Where DIF is the dynamic increase factor, MOR_d is the dynamic modulus of rupture and MOR_s is the static modulus of rupture.

In accordance with CSA S850, the dynamic design strength of the material can be determined in accordance with Equation [5.2].

$$S_D = SIF \times DIF \times S_S \quad [5.2]$$

Where S_D is the dynamic design strength, SIF is the strength increase factor, DIF is the dynamic increase factor and S_S is the specified material strength. CSA S850 currently provides recommended values for the SIF and DIF for wooden products. The recommended SIF for visually graded lumber is 1.9, machine graded lumber is 1.5 and glulam and engineered wood products is 1.2 (CSA 2012). The value of the DIF for visually graded lumber, machine graded lumber, glulam and engineered wood products is 1.4 in flexure (CSA 2012).

CSA O86, Engineering Design in Wood, makes use of a load duration factor, K_D , in order to account for short term loading (1.15), standard term loading (1.00) and long-term loading (0.65) due to wood's strong dependence on load duration, as discussed in Chapter 2 (CSA 2016). Currently, CSA S850 does not permit the use of a load duration factor in addition with a DIF (CSA 2012). However, this current study as well as other research indicates that its inclusion would better represent the overall behaviour of wood under blast and impact, accounting for material strength, wood's response to high strain rates, and wood response to the duration of load.

All static bending tests were normalized to a 1 min duration load. In order to make just comparisons, a duration of load modification factor, K_D , was applied to the manufacturer provided strength factors in order to bring their standard duration strength value to a 1 min value. A load duration factor of 1.25 was chosen as the loads are of very short duration, which is taken from Foschi et al. (1989), who discuss the methodology employed in the calibration procedure and the

reliability levels adopted for CSA-O86. The size factor, K_{Zbg} , was determined for each of the beams and the size effect on the beam removed before the SIF for the beams was calculated. The maximum value for K_{Zbg} in CSA-O86 is currently 1.3, however this is only due to the size of beams tested when the factors were determined. As such a value of 1.24 was used for the large beams and a value of 1.35 for the small beams. As discussed in Chapter 4, an overall average SIF of 1.20 was observed based on the experimental values obtained in this study.

In the below analysis, t-tests were used in order to determine if the obtained results were statistically significant. A two-tailed t-test with an alpha value of 0.05 was used to determine whether the differences between the group means could be reported as statistically significant (i.e. not due to material variability). This analysis was used in order to determine whether the observed difference in the means of the MOR and MOE were due to dynamic or cold effects, or whether the differences occurred by chance. In the below analysis, if the t-value is greater than the critical t-value and the probability value is less than 5% the results are deemed to be statistically different and are deemed to have not occurred by chance.

The following sections will look at the calculation of the DIF factors from the obtained data, and the statistical conclusions from its analysis.

5.2 Normal Temperature Testing – Large Beams

A comparison between the key parameters obtained through the testing of the large beams under static and dynamic testing can be seen in Table 5-1. Looking at these results it can be observed that the beams tested dynamically have a higher resistance, and consequently MOR, as well as a higher stiffness, and consequently higher MOE. This can also be seen visually in Figure 5-1, which shows the resistance curves for all static and dynamic large beam tests. Notably the obtained static stiffnesses are noticeably lower than the manufacturer provided value of 12,400 MPa. This could be due to boundary conditions applied in the static set-up or may be due to variability in the tested wood. As there were only three static tests conducted more detailed explanations can not be provided at this time.

Common amongst all dynamic specimens, the initial stiffness of the system settling can be seen within the first 5 mm, which is not representative of the overall resistance curve. One can then see a secondary stiffness from approximately 40-90% of the beam's dynamic behavior before failure. It is important to note two items related to these observations. The initial observed slope could be due to two factors. Firstly, it may be due to the applied boundary conditions on the member and a settling in the system. The lateral restraints as well as the plate to prevent uplift in the system may be causing slightly more constraint than was intended in their design. As it may create extra friction as the applied load increases and the beam begins to react more quickly it overcomes this initial partial restraint and the secondary slope represents the beam's response. Secondly, the initial stiffness could be due to perpendicular to grain crushing in the overall member before the flexural behaviour of the beam takes over. Although there was no crushing observed near the supports or loading points, except for DNP1-267 which had very minimal crushing after 31 hits, there may have been an initial compression in the wood fibres across the beam length in response to the impact load. As such, it was surmised that 40% and 90% of the total resistance better represented the beam's stiffness and beam strain rates.

The noise in the dynamic resistance curve is a product of the dynamics of the test setup,

affected by the properties of the measurement devices in the system and the vibrations that occur naturally within the test setup. In the graph, all dynamic tests are shown by solid lines and all static tests are shown in pastel dotted lines. The failure of each specimen is marked by an x.

Table 5-1: Summary of static and dynamic averages key properties for large beams

Parameter	Static	Dynamic
R_{max}	242.3	285.6
k (kN/m)	11,125	13,368
MOR	59.5	67.3
MOE	10,757	12,924

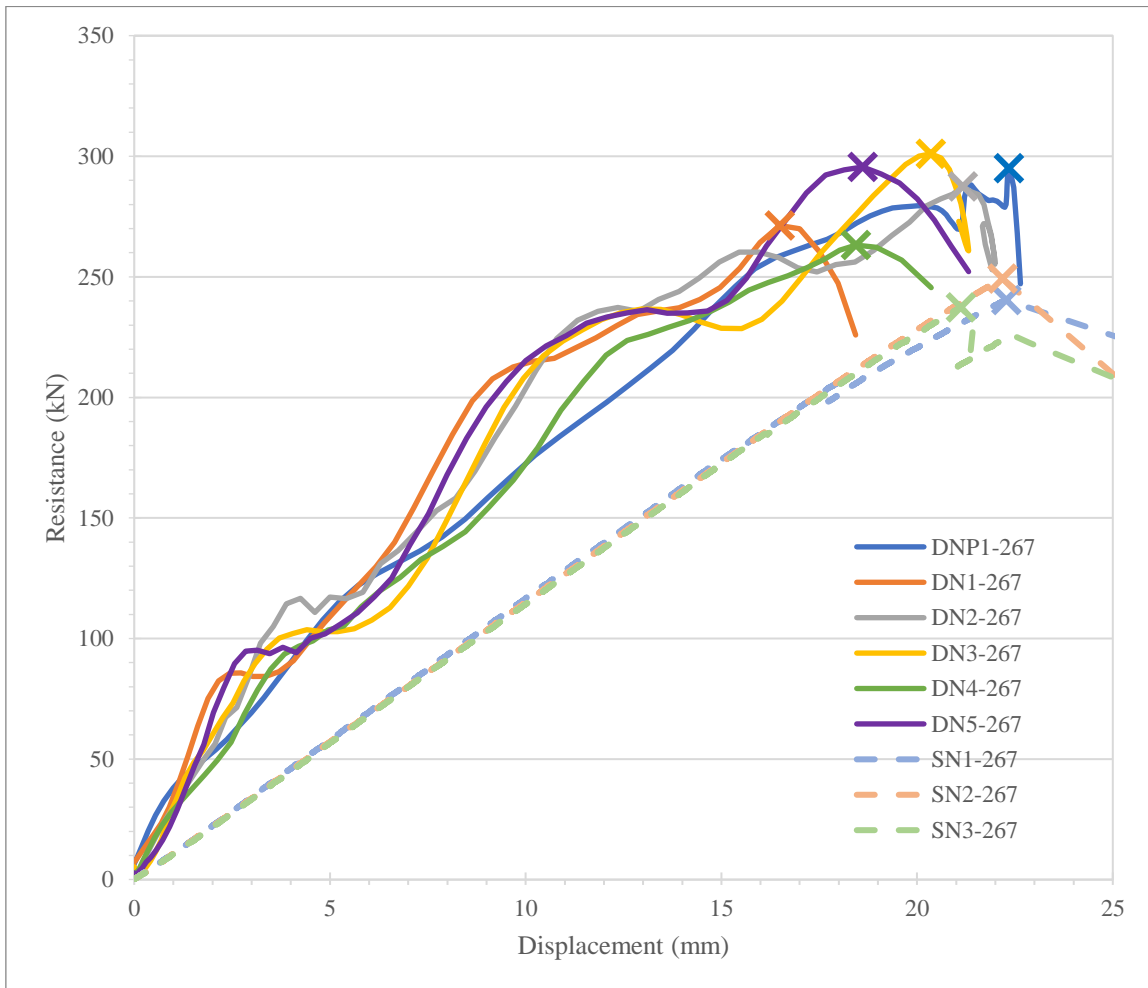


Figure 5-1: Resistance versus midspan displacement for all dynamic and static tests

For strain rates in the range of 0.67 to 1.05 s^{-1} , an average DIF of 1.13 on the MOR of the large glulam beams was determined, with a COV of 0.05. These observations were supported by statistical analyses by using a t-test, with a confidence interval of 95%. This value is very similar to the DIF of 1.14 for strain rates between 0.14 and 0.51 s^{-1} for glulam beams of multi laminate

widths subject to shock tube loading calculated by Lacroix and Doudak (2018a).

The beams were also seen to experience an increase in MOE by a factor of 1.20. These observations were supported by statistical analyses by using a t-test, with a confidence interval of 95%. While an increase on stiffness was not observed in recent studies on glulam beams (Lacroix and Doudak 2018b; Viau and Doudak 2021a) nor on CLT (Poulin et al. 2018; Viau and Doudak 2019), increases on the stiffness caused by high strain rates has been observed in stud walls (Lacroix and Doudak 2014). It is uncertain whether this increase was caused by strain rates or potentially by other factors, such as the dynamic experimental test setup. While great care was taken to prevent any type of fixities which could potentially increase the bending stiffness of the specimen (see Figure 3-11), further insights are needed to ensure this was not the case.

The results for the obtained DIF values for all large beams for both MOR and MOE can be seen in Table 5-2. Table 5-3 shows the results of the statistical analysis. The large t_{stat} value and the very low probability indicates that these results are statistically different and there is an incredibly low chance that this difference occurred by chance. As such, it can be stated that there is an increase in both beam strength and stiffness due to the high strain rates in glulam.

Table 5-2: DIF summary for all large beams on the MOR and MOE

Specimen	DIF - MOR	DIF -MOE
DNP1-267	1.18	1.10
DN1-267	1.07	1.22
DN2-267	1.14	1.14
DN3-267	1.18	1.18
DN4-267	1.05	1.26
DN5-267	1.17	1.31
Average	1.13	1.20
Std Dev	0.1	0.1
COV	0.05	0.06

Table 5-3: Results of statistical analysis on the large beam MOR and MOE

Comparison	Statistical test number	t_{stat}	t_{crit} two-tail	Probability $t_{stat} \leq t_{crit}$	Meaning of T-Test Results
Static to Dynamic MOR	L1	4.46	2.36	0.003	Statistically Different
Static to Dynamic MOE	L2	5.06	2.36	0.001	Statistically Different

Figure 5-2 shows the DIF on the MOR obtained for all large beams varying from 1.05 at the low end to 1.18 at its highest, with the mean value shown by the black dotted line. Figure 5-3 shows the DIF on the MOE obtained for all large beams varying from 1.10 at the low end to 1.31 at its highest, with the mean value shown by the black dotted line.

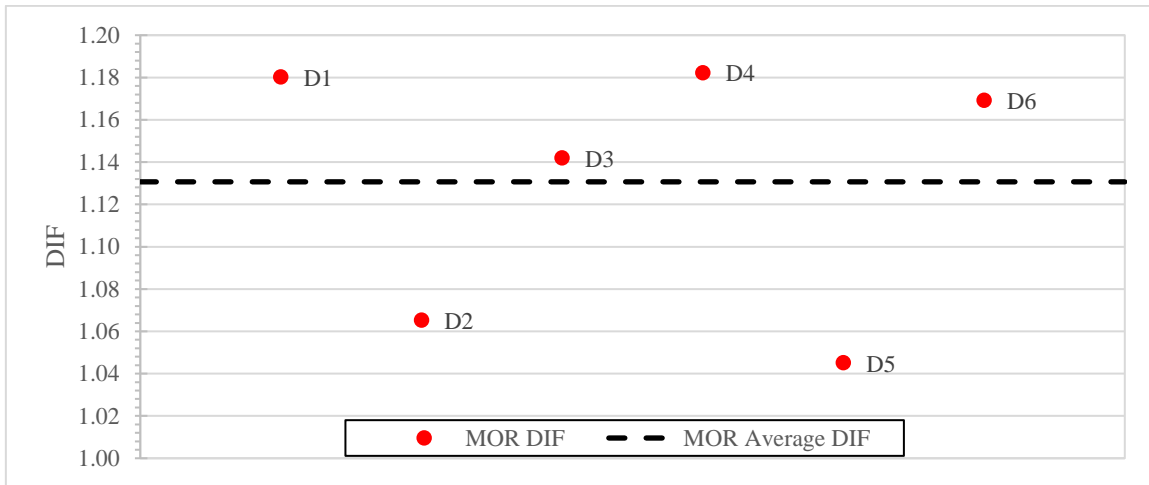


Figure 5-2: DIF on MOR for all dynamic large beams

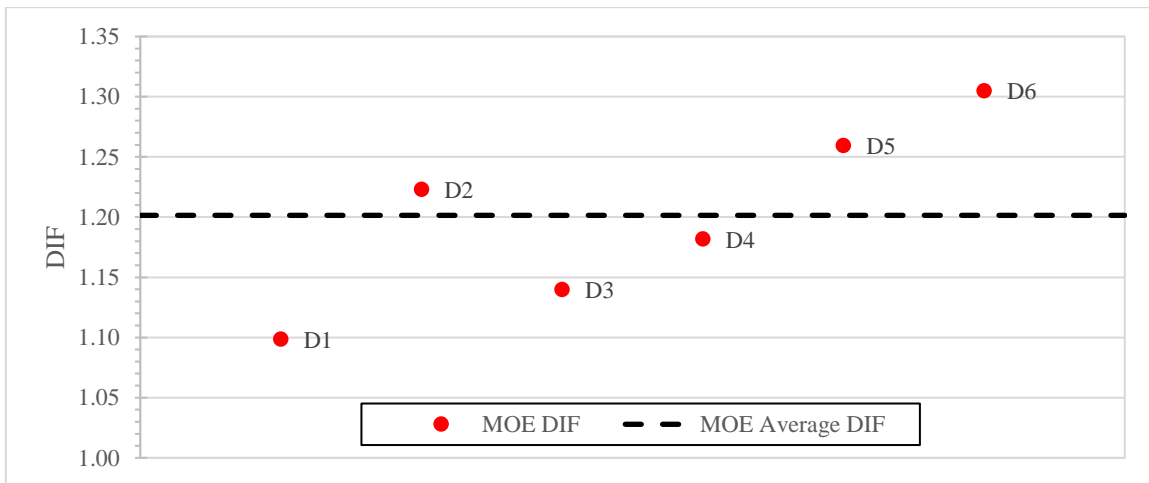


Figure 5-3: DIF on MOE for all dynamic large beams

Similar to the multi-laminate specimens tested by Lacroix and Doudak (2018b), the failure mode was a splintering tension failure with cracks propagating along the glulam layers and appearing to be staggered along the width of the beam. These staggered failure paths connected defects or finger joints in the bottom of the beam as opposed to the failure path being the shortest distance across the width. The failure modes observed between the static and dynamic specimens were similar, whereby all specimens responded to the loading in a linear elastic manner and exhibited a brittle tensile failure initiating at a knot or natural defect. The cracking examined in the dynamic beams sometimes appeared to propagate deeper through the specimen width than the static beams. As can be seen from Figure 5-4, in both static and dynamic cases the cracking propagates from the bottom tension side. The origin for the crack occurs at a knot either on the tensile bottom of the beam or else on either the north or south side of the beam in the lower tensile area. The cracks then propagate from this region. Although some of the cracking did pass through and follow the path of the finger joints in the wood, from the observations, no failures were initiated at a finger joint.

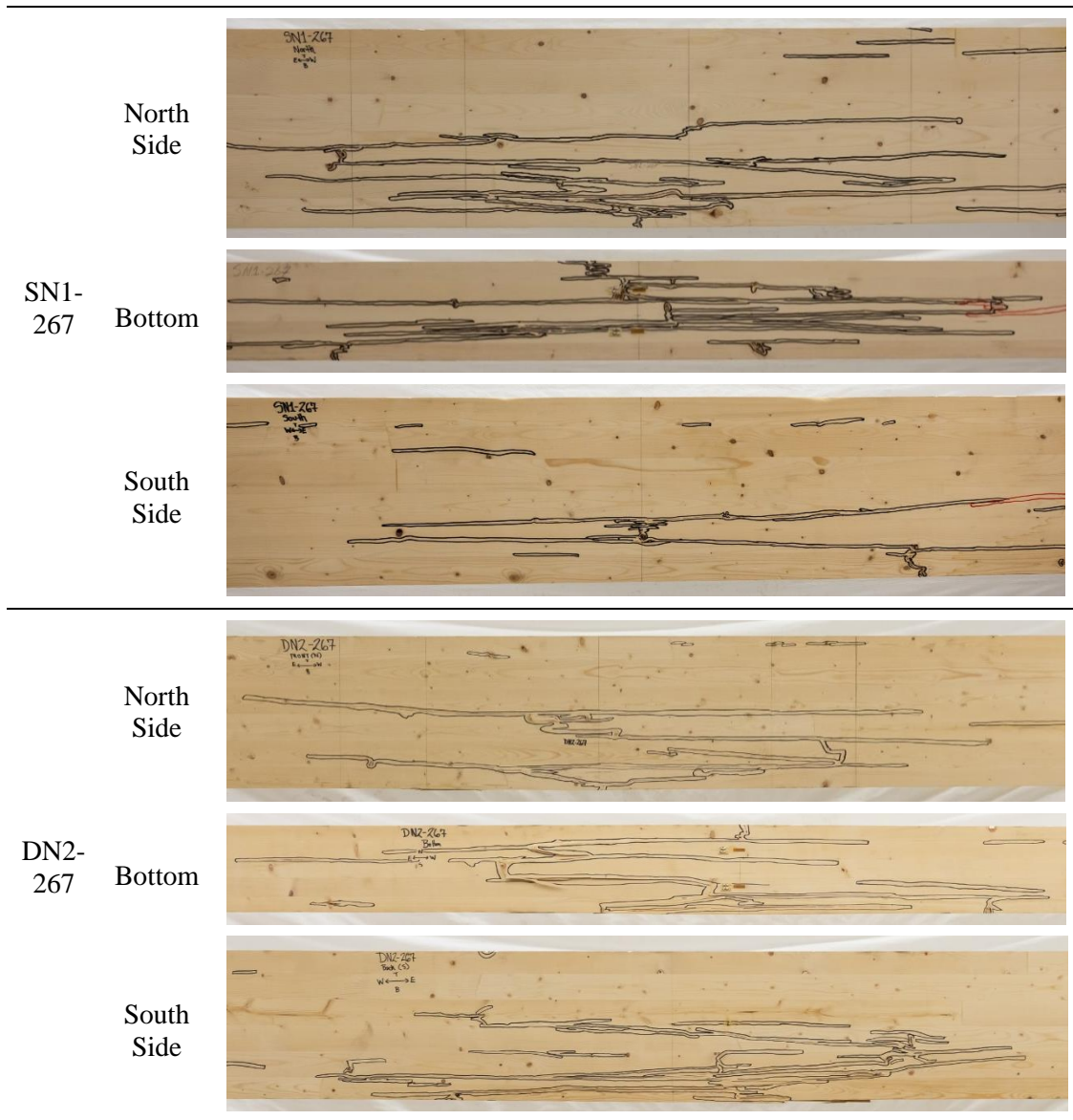


Figure 5-4: Representative failures between static and dynamic beams

5.3 Cold Temperature Testing – Small Beams

As mentioned in Chapter 4 some of the small beams failed in flexure while others failed in shear. Before testing the beams were checked for governing failure mode. Based on the calculations the shear capacity of the beams was 1.5 times the flexural capacity of the beams. As such, it is surprising that shear failures occurred. There are two potential causes for this.

Importantly, the presence of defects in the central third of the beam was critical to initiating a bending failure in the beam. When considering a normal span length for a building, defects will always be present. However, since the span length of the beam tested were short, due to size

constraints of the freezer, defects were not always present in the span length tested. Several of the small beams failed in what was described as shear failure or combined flexure and shear failure. The presence of natural defects proved to be critical to obtaining representative flexural failure in the beams. Although defects would be present in beams of a more realistic structural length, the presence of defects in small test beams would need to be chosen as to be representative of large beams. Secondly, there is a potential that splits may have formed in the beam due to the conditioning environment within the moisture controlled room or in the freezer, for any of the cold temperature beams, as the moisture contents achieved in the beam were relatively low.

For all the analysis presented below in this section, one can only compare outcomes pertaining to identical failure modes. It is for this reason that all tests which resulted in either a shear or combined shear and flexural failure were removed from the results when determining appropriate DIF values for MOR and MOE under the influence of cold temperature and dynamic effects.

In Figure 5-5 and Figure 5-6, all normal temperature static tests are shown in orange, and all normal temperature dynamic tests are shown in red. All cold temperature static tests are shown in light blue, and all cold temperature dynamic tests are shown in dark blue. A dot indicates a flexural failure, while an x represents a combined flexural and shear or shear failure. The averages, which do not include the combined flexure and shear and shear failures, are indicated by dotted lines. The MOR values can be seen in Figure 5-5, and the values for MOE can be seen in Figure 5-6 for all small beams.

Figure 5-5 shows the higher values that are obtained for the beam resistance when the failure is in shear or combined flexure and shear, resulting in artificially high values for failure. One can see visually from the graphs that the cold does not seem to affect the strength of glulam during static testing. However, the average MOR of the cold beams during dynamic testing is much higher than the normal temperature dynamic beams, indicating the cold does influence the behaviour of glulam during short duration loading, during which high strain rates are generated within the members.

When regarding Figure 5-6, as would be expected, the failure method does not change the beam's stiffness and as a result the addition or removal of the shear and combination failures results in very similar MOE values. This graph indicates there is an increased stiffness for the cold beams under both static and dynamic conditions. In addition, there is an increase in stiffness of the normal temperature dynamic specimens to the normal temperature static specimens and the cold temperature dynamic specimens to the cold temperature static specimens, as was observed with the large beams.

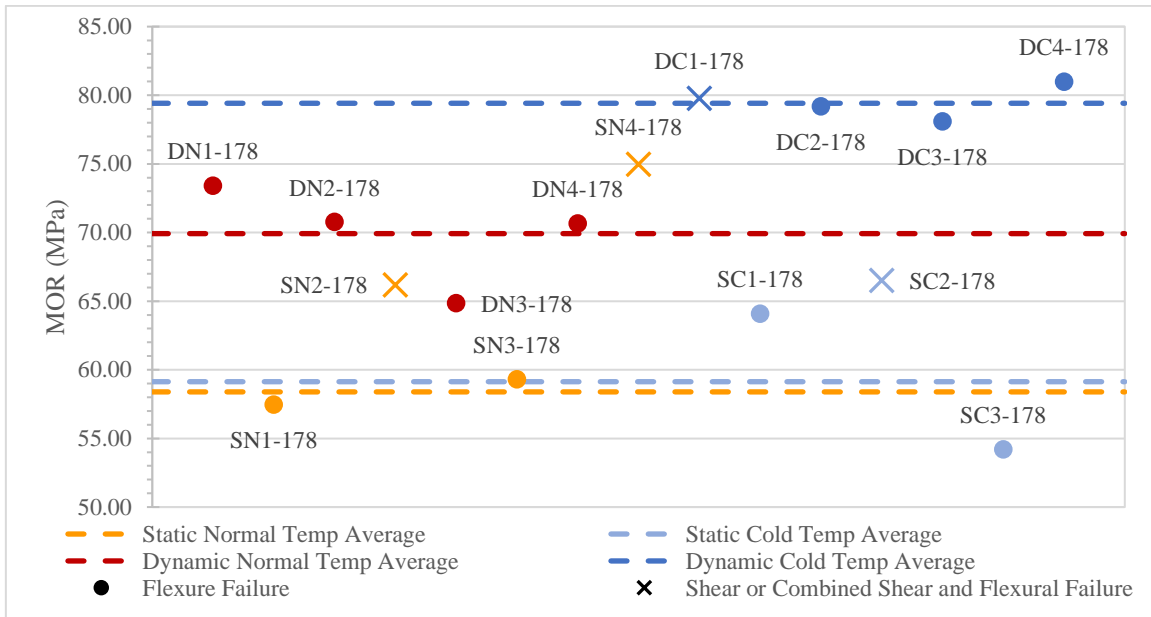


Figure 5-5: MOR values for all small beam tests

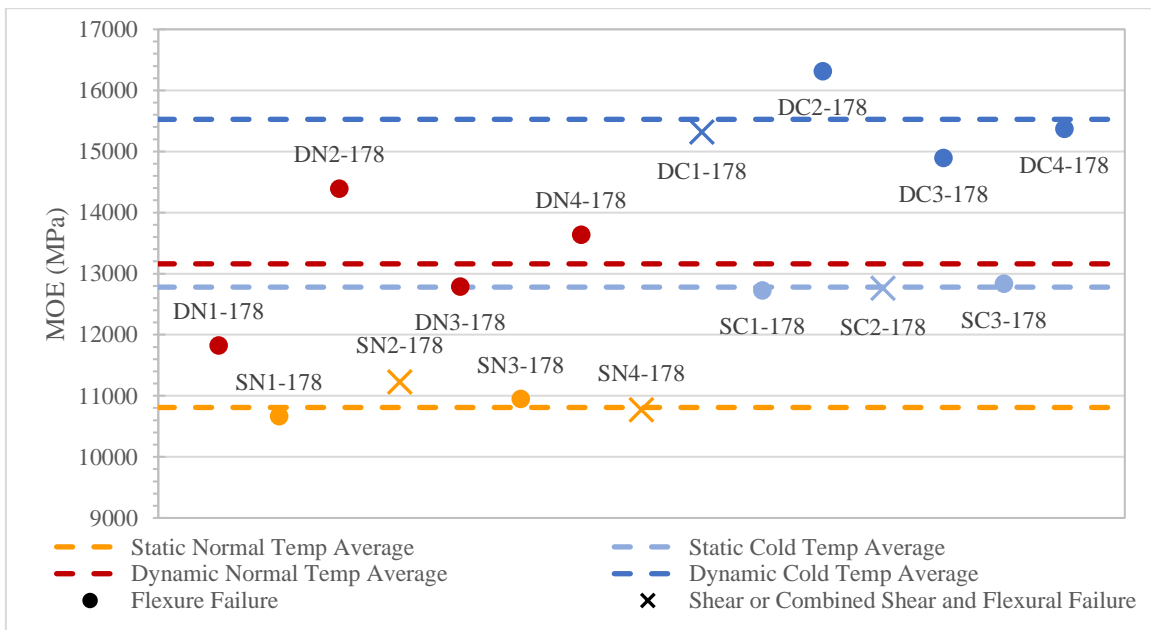


Figure 5-6: MOE values for all small beam tests

The analysis of the cold beams was more complex as there were several groups with which to compare to determine if the results of the cold had an effect of the beams strength or stiffness during both static testing and dynamic testing. The different groups revealed places where the cold did have an effect and areas where it did not appear to. It is for this reason that the results of the statistical analysis are presented first in Table 5-4. The results from these tests do not include any of the shear or combined failure values.

Table 5-4: Results of statistical analysis of the small beams

Comparison	Statistical test number	t_{stat}	t_{crit} two-tail	Probability $t_{stat} \leq t_{crit}$	Meaning of T-Test Results
Static normal temperature to cold temperature MOR	S1	0.15	12.71	0.907	Not Statistically Different
Static normal temperature to cold temperature MOE	S2	13.03	12.71	0.049	Statistically Different
Dynamic normal temperature to cold temperature MOR	S3	4.76	2.78	0.009	Statistically Different
Dynamic normal temperature to cold temperature MOE	S4	3.41	2.57	0.019	Statistically Different
Normal temperature static to dynamic MOR	S5	5.68	2.78	0.005	Statistically Different
Normal temperature static to dynamic MOE	S6	4.11	3.18	0.026	Statistically Different
Cold temperature static to dynamic MOR	S7	4.05	12.71	0.154	Not statistically Different
Cold temperature static to dynamic MOE	S8	6.53	4.30	0.023	Statistically Different
All temperature static to cold temperature dynamic MOR	S9	9.27	2.78	0.001	Statistically Different

Looking at these results outlined in Table 5-4, several key observations can be made. Firstly, statistical test S1 shows that there is no apparent difference between the sample MOR means when comparing the static normal temperature beams to the static cold temperature beams. The low t_{stat} value indicates that the means are very close to each other, as was seen above. As such, under static loading the cold temperature does not decrease or increase to MOR of the glulam beams. Test S2 reveals that the cold beams are stiffer than the normal temperature beams under static loading. Tests S3 and S4 compare the dynamic normal temperature and cold temperature tests to one another. The tests indicate that at high strain rates, there is a statistically significant difference in both their MOE and MOR compared to one another. Tests S5 and S6 compare the normal temperature static and dynamic test means for MOR and MOE. As with the large beams there is a statistical difference between both the MOR and MOE under the influence of high strain rates. Tests S7 and S8 compare the cold temperature static beams to the cold temperature dynamic beams. Test S7 indicates that there is no statistical difference between the cold temperature static tests and cold temperature dynamic tests, despite there being a large difference in their overall means. The high t_{crit} value indicates that this is due to variances and low number of samples reducing the degrees of freedom for the test and making the bar higher for saying that they are statistically different. In short there are not enough samples in order to make a definitive conclusion. In addition, the probability that these samples had the same mean was 0.154, which although greater than the alpha value of 0.05, is still relatively small. As such test S9 was conducted. This statistical analysis combined the normal and cold temperature static test into one group with which to

compare the MOR from the dynamic cold tests in order to increase the sample size. This was done as there was a small difference between the MOR for the statically tested beams and no statistical difference, and a large probability that these means could be considered to be the same ($p=0.907$). When this test was conducted it indicated that there was in fact a difference in the MOR observed between all statistic tests and the cold temperature dynamic tests. Although not conclusive, this suggests that if further testing was conducted a more conclusive trend would be determined. Lastly, test S8 indicates that there is a statistically significant difference between the MOE of the cold temperature static beams and that of the cold temperature dynamic beams. These trends will be further reinforced in the evaluation of the DIF factors and cold temperature factors.

Table 5-5 shows a summary of the DIF values for the small normal temperature beams on the MOR and MOE. For the purposes of calculating the DIF values the normal temperature beams were compared to the normal temperature beams and the cold temperature beams were compared to the cold temperature beams. For strain rates from 1.13 to 1.38 s^{-1} , the small normal temperature beams had a DIF on the MOR of 1.20 with a COV of 0.04. This is higher than the 1.13 that was observed with the large beams. However, the strain rates in these tests were greater than the range for 0.67 to 1.05 s^{-1} in the large beams. Additionally, some of the increase could be due to the fewer defects located in the smaller span length. With dynamic effects, since cracks do not have time to propagate in the same way as with static testing, the defect location and number may be even more critical in dynamic testing. The beams were seen to experience an increase in MOE by a factor of 1.22, which is very similar to the value of 1.20 from the large beam dynamic testing. These observations were both supported by statistical analyses by using a t-test, with a confidence interval of 95%.

Table 5-5: DIF summary for all normal temperature small beams on the MOR and MOE

Specimen	DIF - MOR	DIF -MOE
DN1-178	1.26	1.09
DN2-178	1.21	1.33
DN3-178	1.11	1.18
DN4-178	1.21	1.26
Average	1.20	1.22
Std Dev	0.1	0.1
COV	0.04	0.07

Table 5-6 shows a summary of the DIF values for the small cold temperature beams on the MOR and MOE. For strain rates from 1.14 to 1.31 s^{-1} , the small cold temperature beams had an average DIF on the MOR of 1.34 with a COV of 0.02. This observation was not supported by a confidence interval of 95%. As mentioned above this is due to the number of samples that failed in shear or combined shear and flexure, resulting in too few specimens to make a statistically significant conclusion. The observation is supported by a confidence interval of 84%. This indicates that although not conclusive, there is likely an increase in dynamic strength due to the cold effects. The beams were seen to experience an increase in MOE by a factor of 1.21, which is very similar to the value of 1.22 for the small normal temperature beams and 1.20 from the large beam dynamic testing. This observation was supported by statistical analyses by using a t-test, with a confidence interval of 95%. What is important to note, is that this value of 1.22 is made by comparing the static stiffness of the cold beams to the dynamic stiffness of the cold beams. It was noted earlier that the static cold beams were stiffer than the normal temperature static beams. As

such, there are cold effects that must be considered on top of dynamic effects.

Table 5-6: DIF summary for all small beams on the MOR and MOE

Specimen	DIF - MOR	DIF -MOE
DC2-178	1.34	1.28
DC3-178	1.32	1.17
DC4-178	1.37	1.20
Average	1.34	1.21
Std Dev	0.02	0.05
COV	0.02	0.04

Based on the data above, the cold appears to affect the beam’s dynamic strength differently from the static strength and affects glulam’s stiffness both statically and dynamically. It is for this reason that the values of MOE and MOR for the static and cold tests were also compared to one another. This is shown in Table 5-7. What is also important to note when looking at these overall values is that the static stiffness of the normal temperature beams is noticeably lower than the manufacturer provided value of 12,400 MPa. As with the large beams this could be due to boundary conditions applied in the static set-up or may be due to variability in the tested wood. As there were only two static normal temperature tests conducted that resulted in a flexural failure, more detailed explanations can not be provided at this time.

Table 5-7 shows that under static testing the cold has no effect on the beam’s MOR. However, the beams are 18% stiffer than the normal temperature beams. When the dynamic tests are compared, the cold beams are 14% stronger compared to their normal temperature counterparts and once again 18% stiffer. In Chapter 6 these will be referred to as the “Cold Factor” or CF. These values indicate that there should be considerations made for the cold temperature performance of wood if wood is expected to remain at cold temperatures for the duration of it’s use. The cold appears to influence the wood’s strength positively under dynamic effects. As such, designing for summer temperatures will not have adverse effects on the winter performance of the wood. All these observations are supported by statistical analysis as discussed above.

Table 5-7: Effect of cold on mean MOR and MOE

Comparison	Avg Normal Temperature Value (MPa)	Avg Cold Temperature Value (MPa)	“Cold factor”
Static normal temperature to cold temperature MOR	58.4	59.1	1.01
Static normal temperature to cold temperature MOE	10,809	12,779	1.18
Dynamic normal temperature to cold temperature MOR	69.9	79.4	1.14
Dynamic normal temperature to cold temperature MOE	13,160	15,526	1.18

Looking at the results from literature investigated in Chapter 2 it was expected that there would be an increase in strength observed under static testing. Gerhards (1982) found an 18%

increase in bending strength at 4% moisture content on clear wood at -50°C compared to 20°C . However, what is very important to note about these results is that this testing was on clear wood. As has been discussed previously, defects are very important for the flexural failure of wood and as such the effects of cold temperature on the overall matrix in the wood may be outperformed by the presence of defects. Drake et al. (2015) found increases in strength of glulam beams at -40°C , however this study was focussed on the shear failures of glulam. However, they found that freezing the beams shifted the failure mode to flexure at temperatures of -40°C . As such, although previous testing would indicate potential strength increases of glulam under cold temperatures, there are no directly comparable studies relating to the bending strength of glulam. The reasons that strength increases were not seen statically could be due to several factors. It was postulated that the increase in strength under dynamic conditions is likely due to the way cracks propagate under static testing versus dynamic testing. Under dynamic testing, the crack propagation happens slowly relative to the load duration. The ice crystals and water content in the wood fibres may affect the initial growth of microcracks, thus, potentially allowing the beam to reach a higher resistance before failure. Under static conditions, the frozen nature of the beams does not have as large an influence as the load is applied at a rate that does not affect crack propagation and does not seemingly allow time for any crystals formed within the wood fibres to affect propagation of cracks, thus not allowing the beam to reach a higher ultimate load. Since previous testing has been done on clear wood it may be that the location of knots and natural defects in the wood has an overreaching effect on the positive effects of extreme cold on the beams. Looking at previous research the beam moisture content also has been seen to have a large effect on the behaviour of the beams at extreme cold temperatures, likely due to the behaviour of frozen water molecules. Since the tested beams had a relatively low moisture content, beams tested at greater moisture contents may find strength increases under static loading. Lastly, there is very limited data on the behaviour of glulam under the effects of cold, with most studies being on clear wood or lumber, and as such the strength of glulam may not be as affected by the effects of cold due to grain size, early versus latewood percentages and the multilaminate layup of the wood. Increases in stiffness and consequently MOE were consistently observed across the studies discussed in Chapter 2 and were also observed when looking at the results obtained in this study. The increases in stiffness are likely due to the water content found within the cellular walls of the wood fibres.

Representative resistance curves for static and dynamic tests are shown in Figure 5-7, where the discussed trends above can be visualized. In the graph, the warm colored lines indicate the tests conducted under ambient temperatures. The blues lines indicate the tests done under extreme cold conditions. The graph shows that when comparing the static normal to static cold temperature tests, there is an increase in stiffness observed but no effect on the beam's resistance. When dynamic tests are compared to static tests there is an observed increase in strength and stiffness. Lastly, when the normal temperature dynamic and cold temperature dynamic beams are compared to one another, the cold beams are stiffer and reach higher peak resistance.

Common amongst all dynamic specimens, the initial stiffness of the system settling can be seen within the first 1 mm, which is not representative of the overall resistance curve. One can then see a secondary stiffness from approximately 40-90% of the beam's dynamic behavior before failure. As discussed in detail in Section 5.2 with the large beams, the initial slope could be due to imperfections in the boundary conditions or perpendicular to grain crushing in the member. As such, it was surmised that 40% and 90% of the total resistance better represented the beam's stiffness and beam strain rates. The noise in the resistance curve is a product of the dynamics of the dynamic test setup, affected by the properties of the measurement devices in the system and

the vibrations that occur naturally within the dynamic test setup.

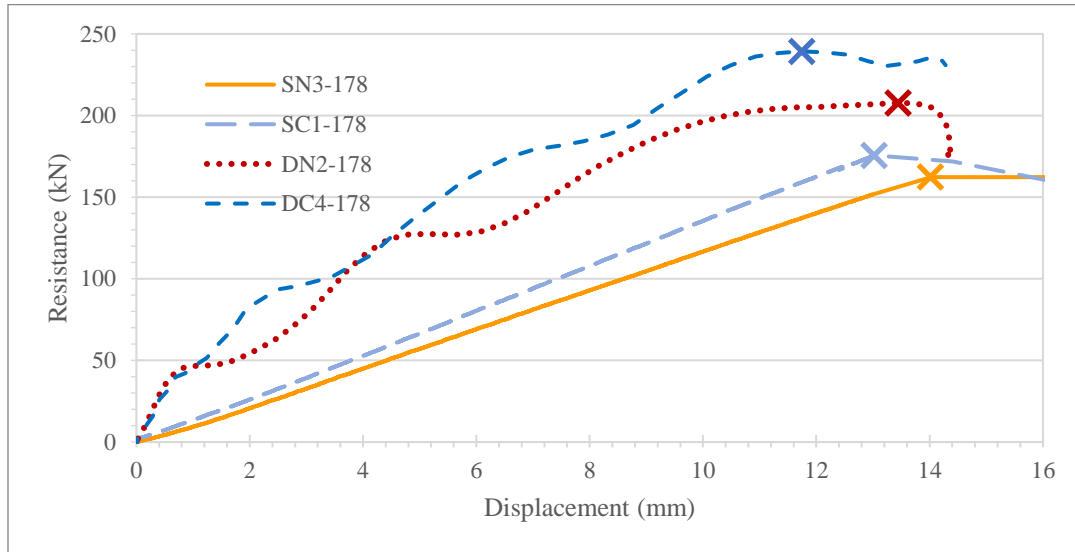


Figure 5-7: Resistance versus midspan displacement for a small beam dynamic and static test at cold and ambient temperatures

Figure 5-8 and Figure 5-9 show the DIF on MOR and MOE for the small beams, with the normal temperature DIF values shown in red and the cold temperature DIF values being shown in blue. Figure 5-8 shows the DIF on the MOR obtained for all small normal and cold temperature beams. The normal temperature beams DIF on MOR ranges from 1.11 to 1.26 with an average, shown by the dotted red line of 1.20. The cold temperature beams DIF on MOR ranges from 1.32 to 1.37 with an average, shown by the dotted blue line of 1.34. Figure 5-9 shows the DIF on the MOE obtained for all small normal and cold temperature beams when compared to their static temperature counterparts. The normal temperature beams' DIF on MOE ranges from 1.09 to 1.33 with an average, shown by the dotted red line of 1.22. The cold temperature beams DIF on MOE ranges from 1.17 to 1.28 with an average, shown by the dotted blue line of 1.21.

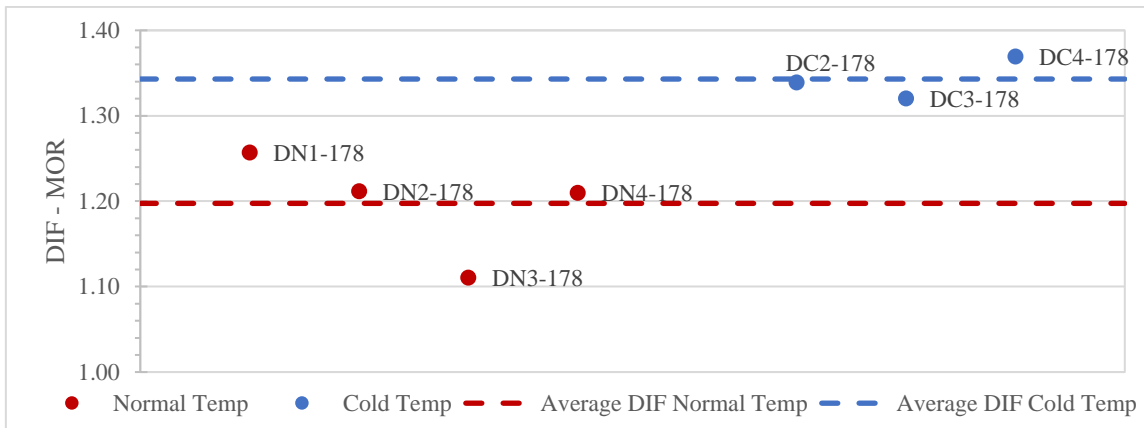


Figure 5-8: DIF on the MOR when compared to their static temperature counterparts for all small dynamic beams

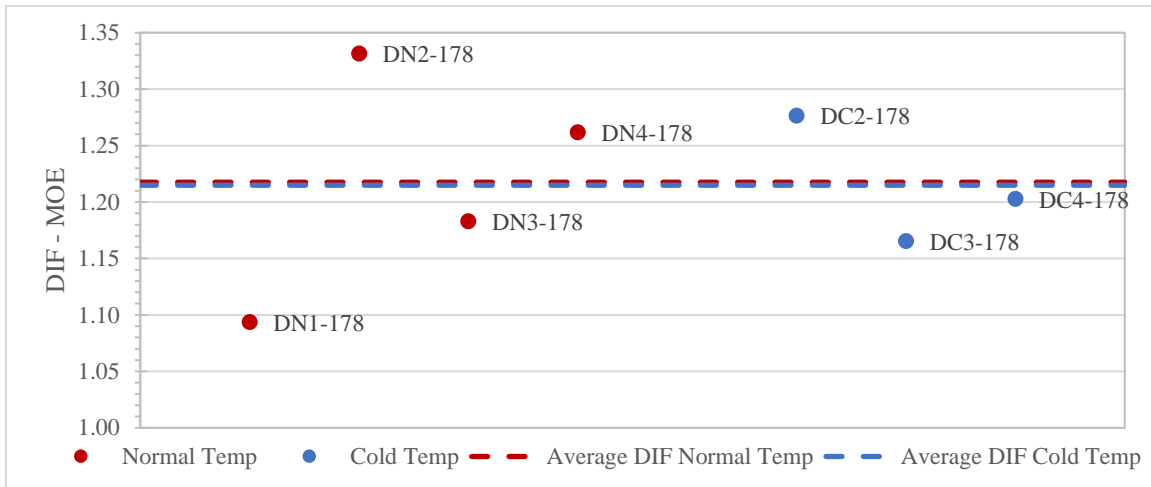


Figure 5-9: DIF on the MOE when compared to their static temperature counterparts for all small dynamic beams

The failure modes observed between the static and dynamic beams and the normal temperature and cold temperature beams were very similar when the beams failed in flexure. The cracking examined in the dynamic beams sometimes appeared to penetrate deeper than the static beams and resulted in more splintering. As can be seen from Figure 5-10 and Figure 5-11, in both static and dynamic cases the cracking propagates from the bottom tension side. The origin for the crack occurred at a knot either on the tensile bottom of the beam or else on either the North or South side of the beam in the lower tensile area. The cracks then propagated from this region. Although some of the cracking did pass through and follow the path of the finger joints in the wood, from the observations, no failures initiated at a finger joint. The failure pattern of the cold temperature beams did not seem to splinter or travel as far as the normal temperature beams under static testing. The cracks are very visible within the static normal temperature beam, SN1-178. They are much less visible in the cold temperature beam displayed, SC1-178. This is especially apparent in the failure images in Chapter 4, Figure 4-28 and Figure 4-29. This was observed between the other tests as well. It is possible that the presence of ice crystals within the cold specimens held the wood fibres together and the cracks did not propagate as far within the material. Differences in the crack propagation between the dynamic normal temperature beams and dynamic cold temperature beams was not as visible.

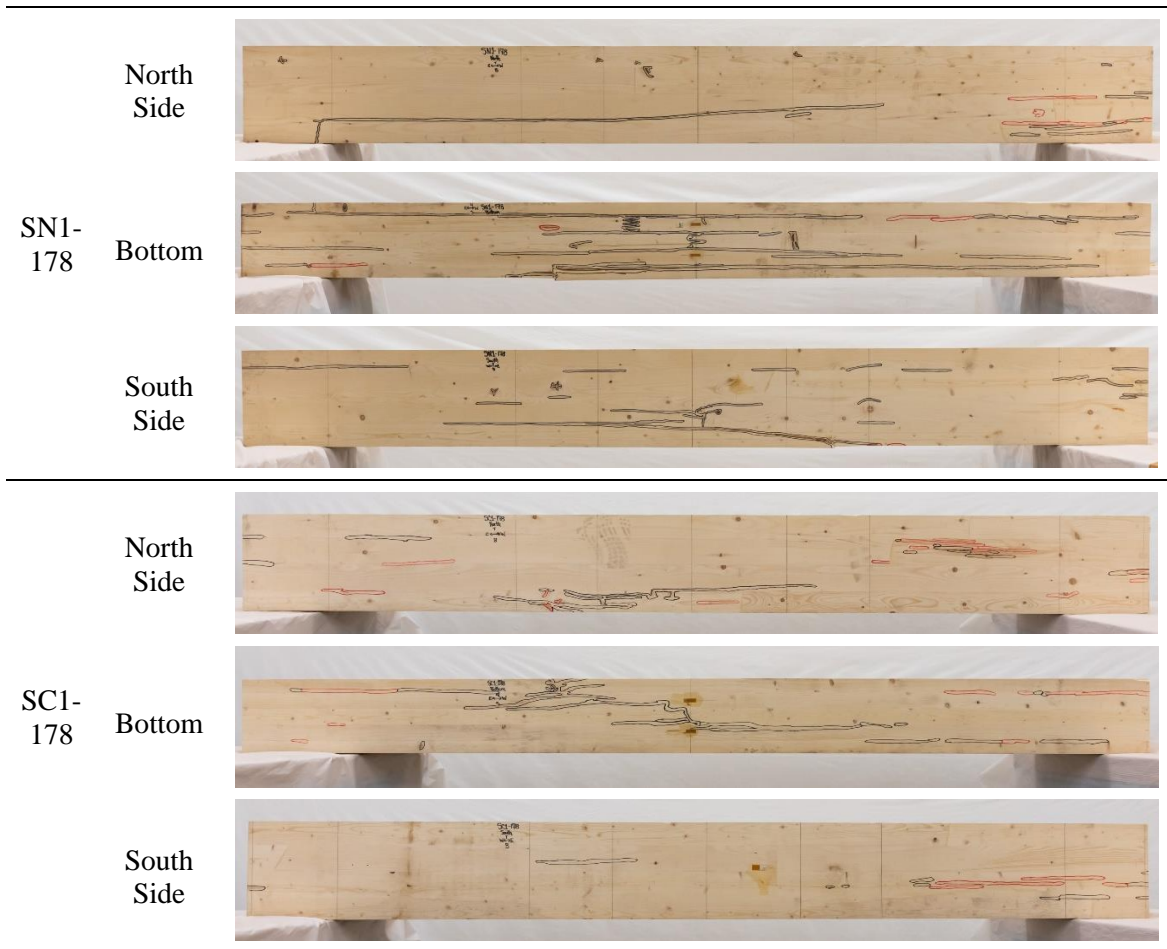


Figure 5-10: Representative failures between static normal temperature beams and static cold temperature beams

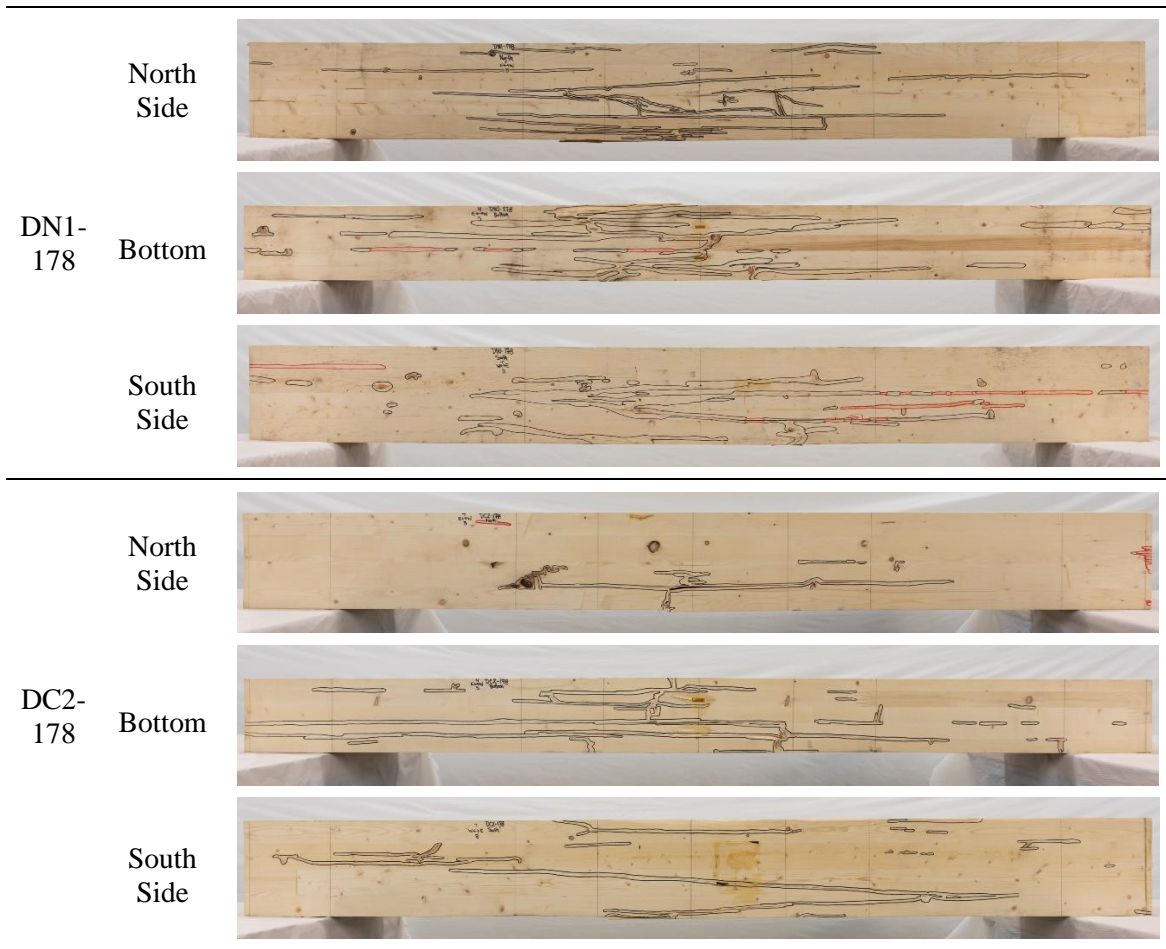


Figure 5-11: Representative failures between dynamic normal temperature beams and dynamic cold temperature beams

Figure 5-12 shows three different beams. The first, SN2-178, shows a static normal temperature beam that failed in shear. The second, SN4-178, shows a static normal temperature beam that failed in combined flexure and shear. The third, DC1-178, shows a dynamic cold temperature beam that failed in shear. These can also be seen in Chapter 4 in Figure 4-34, Figure 4-35, and Figure 4-36 which show the same beams in their experimental set-ups after failure. This type of failure was not desired and is likely a product of the lack of defects in the shorter beam length. In the future, it is recommended that greater care be taken in selecting the tension side of the beam to have a representative number and size of defects, as would be present in a real buildings span, in order for the beam's behaviour to be more representative of full span lengths.

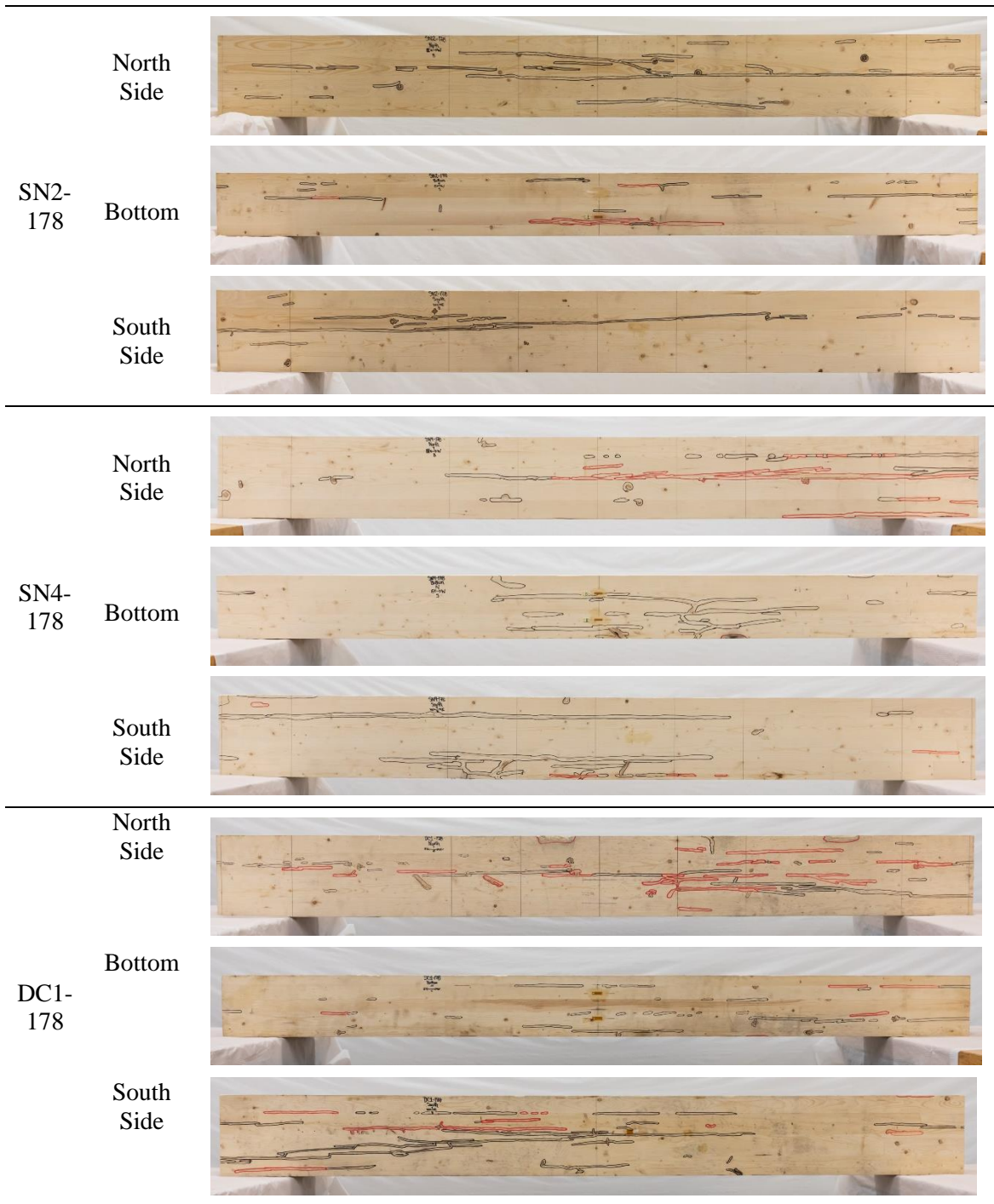


Figure 5-12: Shear and combined shear and flexural failures in static and dynamic beams

5.4 Overall Averages and High strain rate effects

Previous research on light-frame wood stud walls under blast loading conducted by Lacroix and Doudak (2014) compared their data obtained under static and dynamic testing along with those from five additional studies and found a logarithmic relationship between the strain rate and relative strength increase factor. As such, the DIF on the MOR and strain rates obtained from the large and small normal temperature beams under static and dynamic testing were plotted on a logarithmic scale. As can be seen in Figure 5-13 there does appear to be a logarithmic correlation with the data. This data should be correlated with additional data across a greater range of strain rates to see if an equation for a relationship could be proposed.

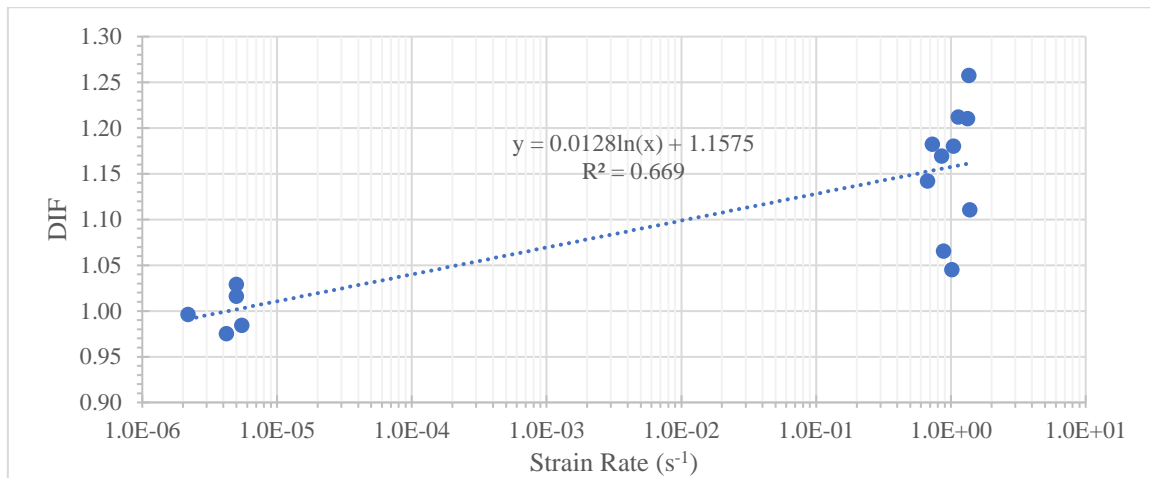


Figure 5-13: Relative increase in strength compared to strain rates

Although this relationship does potentially exist, the data needs to be correlated with a much greater range of tested specimens before a proposal could be made relating DIF to strain rate. As such, the overall averages obtained from both series of testing have been calculated as proposals for recommended DIF values for glulam. These results are presented in Table 5-8.

Table 5-8: Modification factors for determining dynamic strength

Valid for strain rates between 0.67 to 1.38 s ⁻¹ for glulam beams of multilaminate width, cold factor valid for beams with an average internal temperature of -47 °C	DIF _{MOR}	1.16
	DIF _{MOE}	1.21
	SIF	1.20
	CF _{d,MOR}	1.14
	CF _{MOE}	1.18

5.5 Summary

Looking at the results obtained from the testing of the small beams and large beams, the DIF values recommended in CSA S850 should be reassessed, based on the growing number of studies that address the subject and support differing values.

The use of a SIF of 1.2, as currently given in the CSA S850 (2012), is supported by the data obtained in this study when the beam size was adjusted for. For strain rates in the range of 0.67 to 1.38 s⁻¹, an average DIF on the MOR and MOE was determined to be 1.16 and 1.21 respectively. This is currently lower than the DIF on the MOR of 1.4 recommended in CSA S850. There are currently no recommendations for augmenting the beams MOE. The cold temperature beams resulted in an increase on MOE of 1.18 under both static and dynamic conditions when compared to their normal temperature counterparts. The dynamic cold beams experienced a dynamic increase of over the normal temperature dynamic beams of 1.14. This highlights the importance of considering glulam's behaviour under various environmental conditions.

For all tested beams the failure was a splintering tension failure with cracks propagating along the glulam layers and appearing to be staggered along the width of the beam. These staggered failure paths connected defects or finger joints in the bottom of the beam as opposed to the failure path being the shortest distance across the width. The failure modes observed between the static and dynamic specimens were similar, whereby all specimens responded to the loading in a linear elastic manner and exhibited a brittle tensile failure initiating at a knot or natural defect. The cracking examined in the dynamic beams sometimes appeared to propagate deeper in the specimen width than the static beams.

Chapter 6: Modeling and Results

6.1 General

The following chapter presents the SDOF modeling methodology and results of simply supported glulam beams subjected to impact loading, as well as the application of conservation of energy within the system and the key results. For all modelling comparisons, considering the SDOF and conservation of energy methods, the laser measurements were used for comparison due to its high accuracy and high degree of reliability when compared to other means of measuring mid-span displacements (e.g. string potentiometer). When the high-speed video cameras were consulted, it could be seen that the string potentiometer, especially during the elastic tests occasionally had slack in the string and recorded delayed displacements leading up to the maximum displacement. This was especially important when considering conservation of energy as the waviness and peaks caused by the string potentiometer, when integrated, exacerbated this effect. As such, all displacements referred to in the below chapter are those obtained from the laser.

Considering the SDOF analyses below, three sets of analyses were performed, and the predictions were compared with the experimental values. The first analysis consisted of validating the SDOF analysis methodology for glulam beams under impact loading by using experimental resistance and stiffnesses as inputs. Once validated, two SDOF analyses were conducted. Firstly, the values for the maximum resistance and stiffness of the beams were calculated as per the current Canadian blast code and manufacturer provided values. Secondly, the values and method recommended by the earlier Chapters of this document were utilized in order to verify the applicability of the factors and methods proposed in this thesis.

6.2 SDOF Analysis

Blast and impact loading are often based on approximating the structural system as a SDOF system, as described in Chapter 2. SDOF modeling is often used due to its simplicity, ease of implementation, and accuracy. Since there is a large amount of uncertainty in blast and impact loading, it is often more acceptable and preferable to use a simple representation of the structural elements rather than more rigorous detailed analysis due to the uncertainties already present within the loading. The use of SDOF modelling has been validated for many different wood systems that have simply supported boundary conditions including wood studs, coated wood panels, light-frame wood stud walls, glulam beams and CLT panels (Jacques et al. 2014; Lacroix and Doudak 2018a; Lavarney and Pollino 2015; Parlin et al. 2014; Poulin et al. 2018; Viau and Doudak 2021b).

A typical SDOF system will include the forcing function representing the applied load, a mass representing the structural element, and a spring idealizing the internal restoring force that resists the applied load (i.e. the resistance). The equivalent system is chosen so that the deflection of the SDOF system is identical as that for a point of interest (i.e. midspan) on the actual structure (Biggs 1964). While all structures will contain some amount of damping, it is often ignored during SDOF analysis if the load duration is short and when the peak inbound dynamic response is of interest. Transformation factors are used in order to transform a real system into a SDOF system with an equivalent mass, M_e , equivalent spring stiffness, k_e , and equivalent force, F_e . The transformation factors are defined as the ratio of the equivalent structural property over the actual

property. The resistance factor will be the same as the load factor since the resistance represents a system that resists the applied load (Biggs 1964). Often the load and mass factors are combined resulting in the following equation of motion:

$$K_{LM} M_t \ddot{y} + ky = F(t) \quad [6.1]$$

Where K_{LM} is the load mass factor, M_t is the total mass of the structure (including tributary masses), \ddot{y} is the acceleration, k is the stiffness of the system, y is the displacement and $F(t)$ is the applied force. This is visually represented in Figure 6-1.

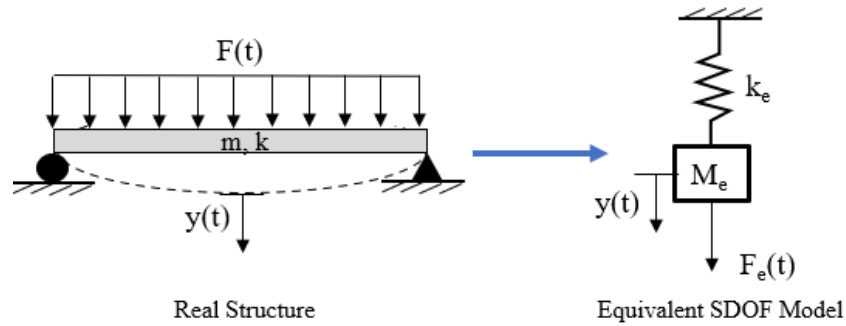


Figure 6-1: Structure idealised as a SDOF system

In the case of the system being modelled, there was both a distributed load (that of the glulam beams being investigated) and that of a concentrated load at the beam third locations (the load transfer bar assembly). As such, the load mass factor for a distributed mass was applied to the beam and a different load mass factor was applied to the load transfer bar. Transformation factors for beams are widely available for common loading scenarios. As such a concentrated mass factor of 0.87 and a uniform mass factor of 0.60 were used to represent the system as obtained from Biggs (1964). This resulted in the relationship described in Equation [6.2] to determine the system's equivalent mass within the equation of motion.

$$(K_{LM,concentrated} M_{LTB} + K_{LM,distributed} M_{Beam}) \ddot{y} + ky = F(t) \quad [6.2]$$

Where $K_{LM,concentrated}$ is the load mass factor for the concentrated mass, M_{LTB} is the mass of the load transfer bar and rollers, $K_{LM,distributed}$ is the distributed load mass factor, M_{Beam} is the mass of the beam, \ddot{y} is the acceleration, k is the stiffness of the system, y is the displacement and $F(t)$ is the applied force.

The solution for the SDOF model used was based on the Predictor Method described by Hetherington and Smith (1994) which is a numerical method that assumes constant acceleration in a time step. Equation [6.3] was used for the system, which uses the resistance as obtained from the beam's stiffness and ultimate resistance.

$$K_{LM} M_t \ddot{y} + R(y) = F(t) \quad [6.3]$$

Where K_{LM} is the load mass factor, M_t is the total mass of the structure, \ddot{y} is the acceleration, $R(y)$ is the system's resistance function and $F(t)$ is the applied force. At the first time step the velocity and displacement of the beam are assumed to be zero and as such the acceleration can be determined by Equation [6.4].

$$\ddot{y}_o = \frac{F(0) - R(y_o)}{K_{LM} M_t} \quad [6.4]$$

Where \ddot{y}_o is the acceleration in the first time step, $F(0)$ is the applied force in the first time step, $R(y_o)$ is the resistance at zero displacement, K_{LM} is the load mass factor, and M_t is the total mass of the structure. The velocity for the beginning of the next time step can subsequently be determined by the following:

$$\dot{y}_n = \dot{y}_{n-1} + \ddot{y}_{n-1} \Delta t \quad [6.5]$$

Where \dot{y} is the velocity, \ddot{y} is the acceleration and Δt is the chosen time step. The displacement for the beginning of the next time step can then be determined by:

$$y_n = y_{n-1} + \dot{y}_{n-1} \Delta t + \ddot{y}_{n-1} \Delta t^2 \quad [6.6]$$

Where y is the displacement, \dot{y} is the velocity, \ddot{y} is the acceleration and Δt is the chosen time step. Lastly, the displacement can be used to calculate the updated resistance by Equation [6.7] which can then be used along with the applied force in the time step to determine the new acceleration:

$$R(y) = ky \quad [6.7]$$

Where $R(y)$ is the system's resistance function, k is the stiffness and y is the displacement. It has been proven that the results using this method are accurate if the time interval chosen is no larger than one-tenth the natural period of the system (Biggs 1964). A time interval of 0.0001 sec was chosen as it was a convenient interval, did not consume too much computational power and was much less than one-tenth the natural period of the system, where the natural period was given by:

$$T = 2\pi \sqrt{\frac{K_{LM} M_t}{k}} \quad [6.8]$$

Where T is the natural period, K_{LM} is the load mass factor, M_t is the total mass of the structure, and k is the stiffness.

6.2.1 Validation of the SDOF Analysis Method to Represent Glulam

To determine the ability of a SDOF system to determine glulam beams ultimate deflection and resistance under impact, both the elastic dynamic test results, and the failure dynamic test results for each of the specimens were used to compare with the SDOF predictions. First the failure resistance for each beam and the stiffness obtained experimentally were used in order to determine

the ability of the SDOF system to represent glulam's behaviour, before manufacturer provided values and code values were used. In all cases the applied force to the system was not idealised. Instead, the applied force obtained from the central force transducer during each dynamic test was used as the forcing function in the system. An example of the forcing function used for DN1-267 can be seen in Figure 6-2.

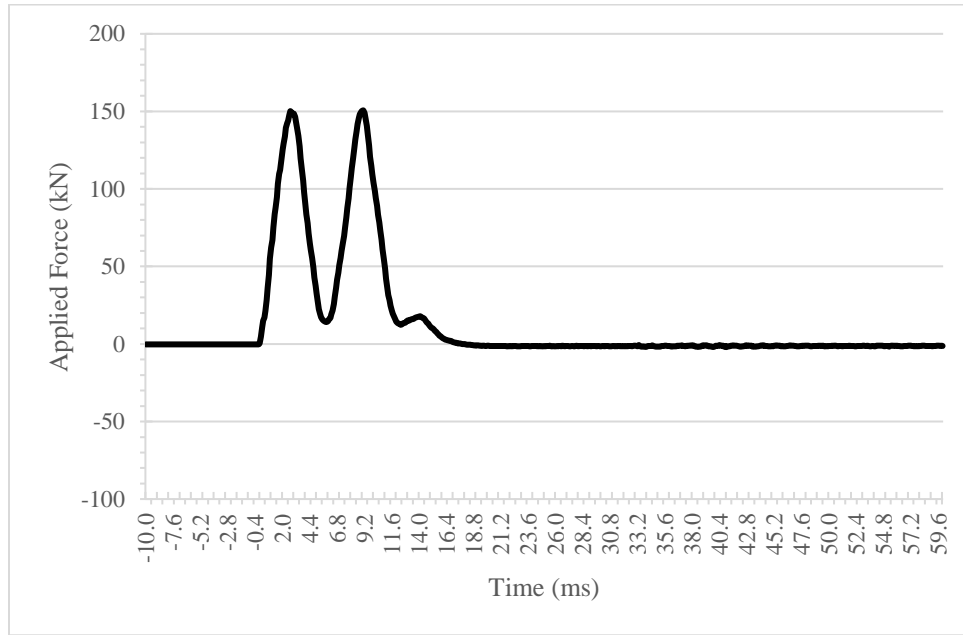


Figure 6-2: Forcing function used for SDOF system for DN1-267

This meant that for every beam a different loading function and resistance function which were used in order to look at the accuracy of the SDOF system. Using the resistance function and forcing function for each beam, the displacements could then be predicted using a SDOF system and the Hetherington and Smith method discussed above. An example resistance function for one of the large beams can be seen in Figure 6-3.

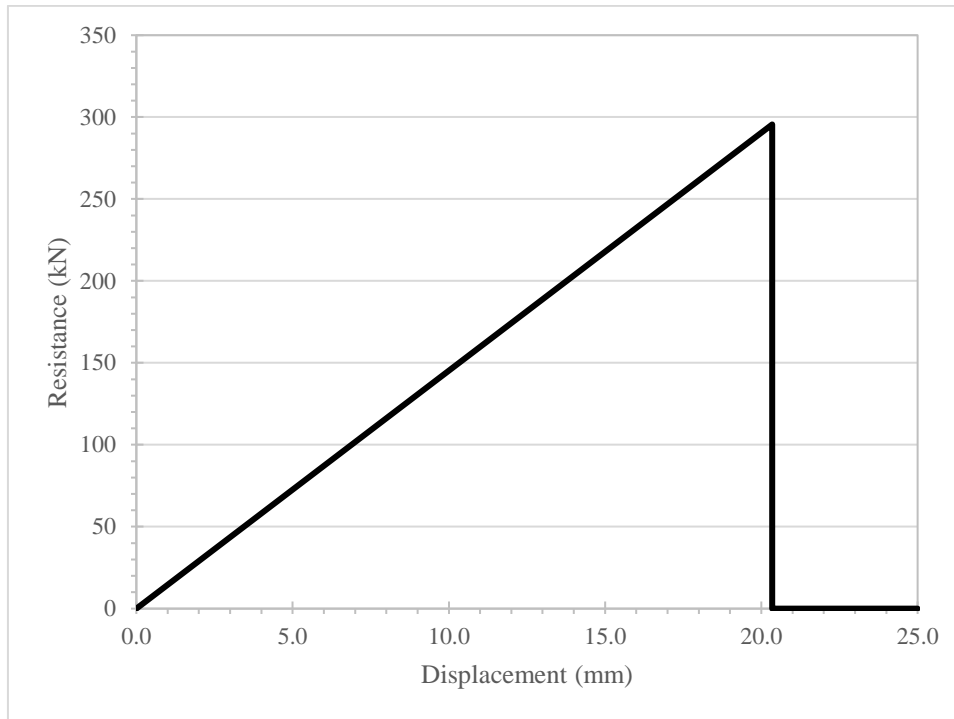


Figure 6-3: Resistance function for DN5-267

There were different comparisons looked at for the elastic and failure tests. For each elastic test the maximum displacement obtained from each SDOF system was compared to the maximum displacement measured. There was a phase shift that occurred between the maximum measured displacement and the displacement obtained from the SDOF system. This is qualified by a ratio of when the maximum displacement occurred in the SDOF system compared to when it occurred in the experimental results. The peak resistance, displacement at that resistance and the associated time shift for this value was also investigated.

Figure 6-4 shows the resistance and displacement over time for the real and SDOF systems for DN2-267 for an elastic dynamic test. The SDOF system can only be used to represent the system up until it begins to rebound as the load transfer beam rollers separate from the beam on the rebound, which makes the SDOF no longer a valid representation of the system. In dark and light yellow are the measured resistances and displacements respectively. In dark and light purple are the SDOF resistances and displacements respectively. As can be seen from the image the SDOF well represents the maximum displacement of the beam as well as the beam's resistance, with a small time shift in the SDOF system compared to the experimental results. The results from the elastic tests and comparison with the SDOF system for both the large and small normal temperature beams can be seen in Table 6-1 and Table 6-2 and respectively.

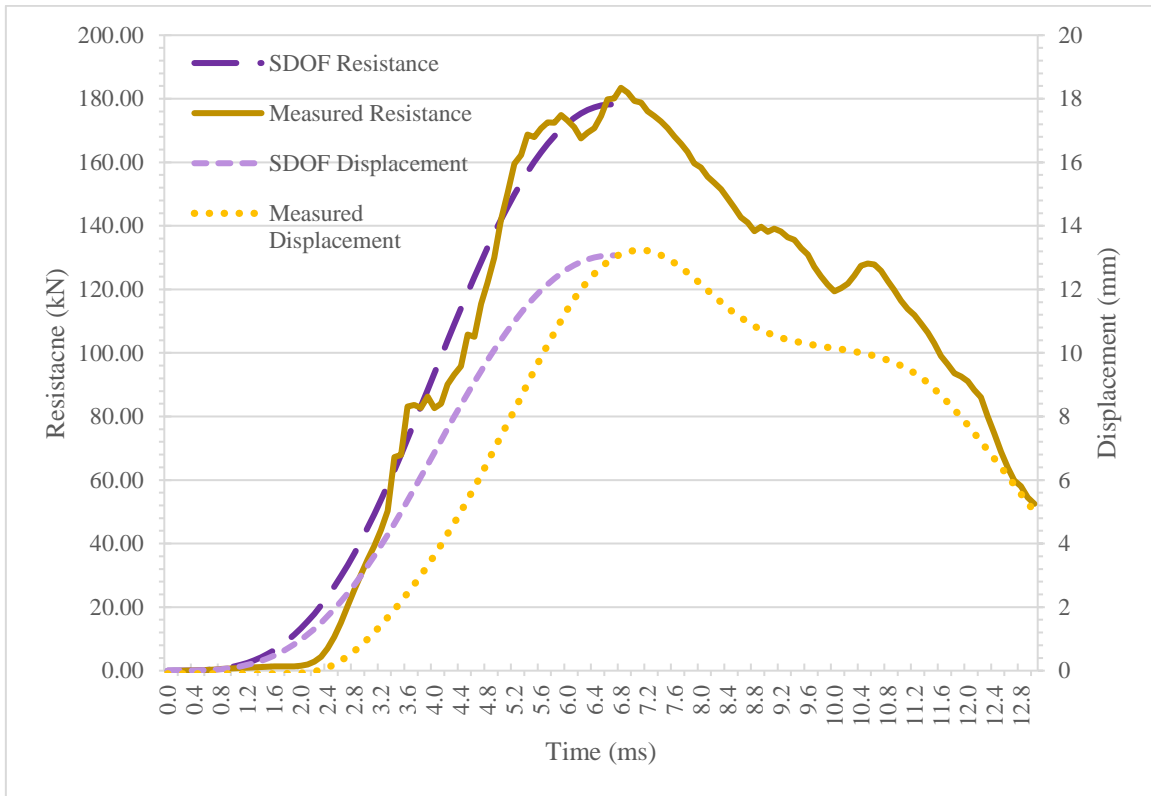


Figure 6-4: Experimental and SDOF resistance-time and displacement-time histories for the elastic dynamic test on DN2-267

Table 6-1: Elastic dynamic tests compared to SDOF models large normal temperature beams

Specimen	y_{max}	y_{SDOF}	y_{SDOF}/y_{max}	Time to y_{max} Ratio (SDOF/Exp)	$R_{d,max}$	$R_{SDOF,d,max}$	$R_{SDOF,d,max}/R_{d,max}$	$y_{d,Rmax}$	$y_{SDOF,d,Rmax}$	$y_{SDOF,d,max}/y_{d,max}$	Time to $R_{d,max}$ Ratio (SDOF/Exp)
	mm	mm			kN	kN	mm	mm	mm		
DNP1-267	12.9	11.2	0.87	0.98	176.3	135.5	0.77	11.9	11.2	0.94	1.06
DN1-267	13.3	12.8	0.96	0.88	182.0	175.7	0.97	13.0	12.8	0.99	0.94
DN2-267	13.0	13.1	1.00	0.89	183.4	178.2	0.97	12.6	13.1	1.04	0.99
DN3-267	13.5	13.4	0.99	0.91	185.0	177.6	0.96	13.5	13.4	0.99	0.88
DN4-267	13.5	12.9	0.95	0.88	189.0	179.8	0.95	13.3	12.9	0.97	0.93
DN5-267	13.3	12.6	0.94	0.87	183.8	182.4	0.99	13.2	12.6	0.95	0.90
Average			0.95				0.93			0.98	
Std Dev			0.04				0.08			0.03	
COV			0.04				0.08			0.03	

Table 6-2: Elastic dynamic tests compared to SDOF models small normal temperature beams

Specimen	y_{max}	y_{SDOF}	y_{SDOF}/y_{max}	Time to y_{max} Ratio (SDOF/Exp)	$R_{d,max}$	$R_{SDOF,d,max}$	$R_{SDOF,d,max}/R_{d,max}$	$y_{d,Rmax}$	$y_{SDOF,d,Rmax}$	$y_{SDOF,d,max}/y_{d,max}$	Time to $R_{d,max}$ Ratio (SDOF/Exp)
	mm	mm			kN	kN	mm	mm	mm		
DN1-178	12.7	11.8	0.93	0.88	179.3	152.4	0.85	12.1	11.8	0.97	0.98
DN2-178	11.5	10.8	0.94	0.84	170.2	174.4	1.02	10.9	10.8	0.99	0.95
DN3-178	12.0	12.3	1.03	0.86	179.0	176.9	0.99	11.9	12.3	1.04	0.93
DN4-178	11.2	11.2	1.00	0.84	172.6	172.7	1.00	10.4	11.2	1.07	1.00
Average			0.98				0.97			1.02	
Std Dev			0.04				0.07			0.04	
COV			0.04				0.07			0.04	

As shown in Table 6-1 and Table 6-2, good agreement between the SDOF system used and the experimental values were obtained, confirming the use of SDOF analysis as a dynamic analysis method for glulam beams under impact.

For the large normal temperature specimen elastic dynamic tests, the maximum displacement calculated in the SDOF system was on average 0.95 of the displacements recorded during testing. For all tests the SDOF system resulted in a displacement that was less than the experimental value, with the exception of DN2-267. The largest difference was with DNP1-267 at 0.87 of the displacement found in the experimental. At the beginning of the experimental test program, eight pillow block bearings were utilized to transport and guide the weighted box along the rails. It was found in the process of the 31 dynamic tests on DNP1-267 that eight bearings provided too much friction in the system and would impede the downward motion of the drop weight. To alleviate this, two of the bearings were removed, which allowed the box to travel downwards more freely, but this occurred after the elastic drop on DNP1-267 and may have affected the specimen's response leading to more discrepancy in this test. Looking at the other large specimens SDOF displacements are between 0.94 and 1.00 of the maximum displacements found during experimental testing. In all cases, the SDOF system predicted the maximum displacement occurring sooner than it did in reality, with an average ratio between the time the maximum displacement occurred under the SDOF system and experimentally being 0.90. The SDOF peak resistances were 0.77 to 0.99 of the experimental peak resistances with an average of 0.93. Looking at the displacement that occurred at those peak resistances the SDOF values were 0.94 to 1.04 of the values obtained experimentally with an average of 0.98. Once again, the peak resistances in the SDOF system almost always occurred before the peak resistance observed experimentally resulting in an average ratio between the two times of 0.95. This shows very good agreement between the SDOF system and the experimental results. The small discrepancies present in the results could be due to the slight differences in stiffness observed between the static and dynamic results.

For the small normal temperature specimen elastic dynamic tests, the maximum displacement calculated in the SDOF system was on average 0.98 of the experimental displacements. The SDOF maximum displacements were 0.93 to 1.03 of the values obtained experimentally. In all cases the SDOF system predicted the maximum displacement occurring sooner than it did in reality, resulting in an average ratio between the times of 0.86. The SDOF peak resistances were 0.85 to 1.02 of the experimental peak resistances with an average of 0.97. Looking at the displacement that occurred at those peak resistances the SDOF values were 0.97 to 1.07 of the values obtained experimentally with an average of 1.02. Once again, the peak resistances in the SDOF system always occurred before the peak resistance observed experimentally, resulting in an average ratio between the times of 0.97. Once again, this shows very good agreement between the SDOF system and the experimental results, validating the use of a SDOF system to represent glulam beams under impact.

For each destructive test, the displacement at peak resistance obtained from each SDOF system was compared to the displacement measured at failure (peak resistance). There was a phase shift that occurred between the peak displacement in the SDOF system and the peak that was measured, that was also quantified. Figure 6-5 shows the resistance and displacement over time for the real and SDOF systems for DN5-267 for a failure dynamic test. In dark and light yellow are the measured resistances and displacements respectively. In dark purple and light purple are the SDOF resistances and displacements respectively. As can be seen from the image, the SDOF well

represents the behaviour of the beam at failure.

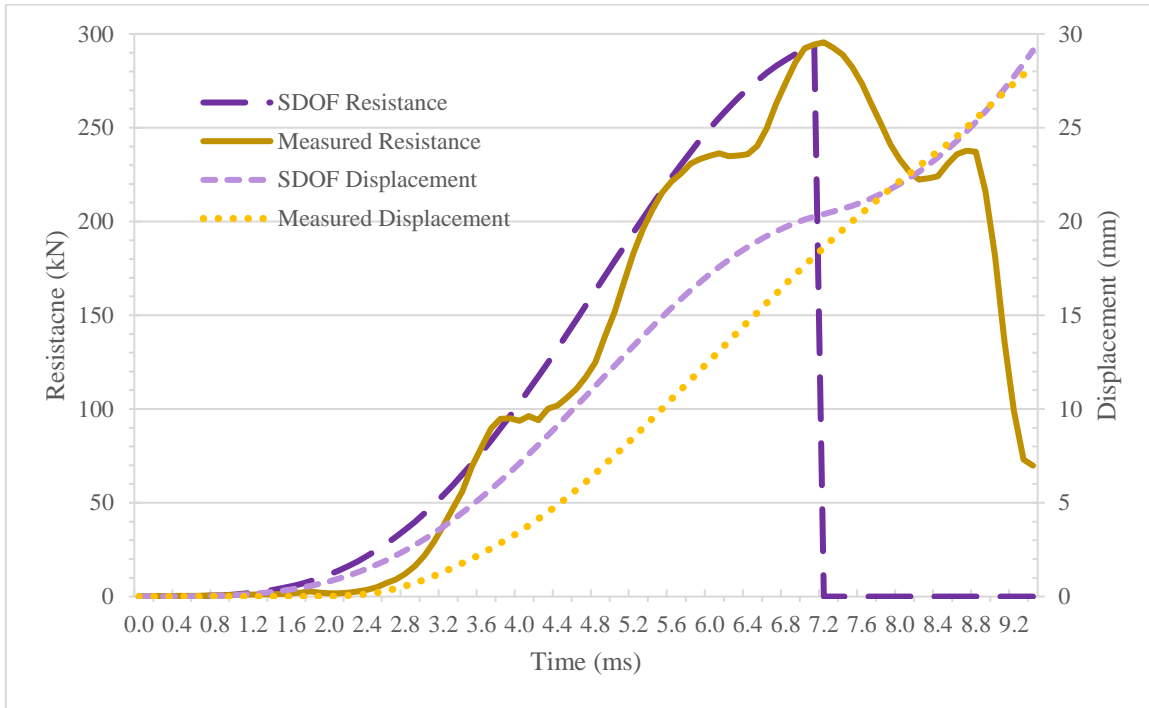


Figure 6-5: Experimental and SDOF resistance-time and displacement-time histories for the failure dynamic test on DN5-267

The results from the failure dynamic tests and comparison with the SDOF system for both the large and small normal temperature beams and small cold temperature beams can be seen in Table 6-3, Table 6-4, and Table 6-5 respectively.

Table 6-3: Failure dynamic tests compared to SDOF models for large normal temperature beams

Specimen	$y_{d,Rmax}$ mm	$y_{SDOF,d,Rmax}$ mm	$y_{SDOF,d,max}/y_{d,max}$	Time to $R_{d,max}$ (SDOF/Exp)	Ratio
DNP1-267	22.3	24.4	1.09	0.91	
DN1-267	16.5	19.7	1.19	1.00	
DN2-267	21.2	22.0	1.04	1.22	
DN3-267	20.4	22.6	1.11	1.36	
DN4-267	18.4	18.6	1.01	0.91	
DN5-267	18.6	20.3	1.09	0.99	
		Average	1.09		
		Std Dev	0.06		
		COV	0.05		

Table 6-4: Failure dynamic tests compared to SDOF models for small normal temperature beams

Specimen	$y_{d,Rmax}$	$y_{SDOF,d,Rmax}$	$y_{SDOF,d,max}/y_{d,max}$	Time to $R_{d,max}$ Ratio (SDOF/Exp)
	mm	mm		
DN1-178	14.9	16.3	1.09	0.91
DN2-178	13.4	12.9	0.96	0.87
DN3-178	12.1	13.1	1.08	0.93
DN4-178	11.5	13.5	1.17	1.00
		Average	1.08	
		Std Dev	0.08	
		COV	0.07	

Table 6-5: Failure dynamic tests compared to SDOF models for small cold temperature beams

Specimen	$y_{d,Rmax}$	$y_{SDOF,d,Rmax}$	$y_{SDOF,d,max}/y_{d,max}$	Time to $R_{d,max}$ Ratio (SDOF/Exp)
	mm	mm		
DC2-178	11.7	12.8	1.09	0.95
DC3-178	13.0	13.7	1.05	0.93
DC4-178	11.7	13.7	1.16	1.07
		Average	1.10	
		Std Dev	0.05	
		COV	0.04	

As shown in Table 6-3, Table 6-4, and Table 6-5, good agreement between the SDOF system used and the experimental values were obtained, confirming the use of SDOF analysis as a dynamic analysis method for glulam beams under impact at failure. For each of these tests the displacement at failure is compared.

For the large normal temperature specimen failure dynamic tests, the displacement at the peak resistance in the SDOF system was on average 1.09 of the experimental displacements. The SDOF displacements were 1.01 to 1.19 times the values obtained experimentally. The SDOF system peaked before the experimental results in some cases and afterwards in others, resulting in time to maximum resistance ratios of 0.91 to 1.36.

For the small normal temperature specimen failure dynamic tests, the displacement at the peak resistance in the SDOF system was on average 1.08 of the experimental displacements. The SDOF displacements were 0.96 to 1.17 times the values obtained experimentally. In almost all cases the SDOF system predicted failure occurring sooner than it did in reality, resulting in time to maximum resistance ratios of 0.87 to 1.00.

For the small cold temperature specimen failure dynamic tests, the displacement at the peak resistance in the SDOF system was on average 1.10 of the experimental displacements. The SDOF displacements were 1.05 to 1.16 times the values obtained experimentally. The SDOF system peaked before the experimental results in some cases and afterwards in others, resulting in time to maximum resistance ratios of 0.93 to 1.07.

In all cases for the failure drops the SDOF system on average predicted larger displacement than those that were obtained experimentally. This is to be expected as the SDOF system assumes ideal support conditions. Although every effort was made in the experiment to ensure the beams are simply supported, there is friction present within the experimental set-up which would slightly limit the displacements. This would be present within the rollers and pins as well as the brace plates and lateral supports, resisting the rotation in the beam. It is postulated that this was not apparent when looking at the elastic hits, because the displacements were much smaller and as such friction did not play as big a role in limiting the overall displacements.

Overall, this data indicates that a SDOF system of analysis is able to accurately predict the displacement of simply supported glulam elements under impact loading. As such, SDOF analysis can be used in the next section in order to predict beams displacements and resistances using manufacturer provided values and the current code recommended values as well as those that are recommended by this research.

6.2.2 Appropriateness of the Current Design Codes and the Proposed Methodologies to Estimate Glulam Deflection and Resistance Under Impact Loads

The following section looks at using SDOF analysis to predict the displacement and resistances in glulam beams under impact using CSA S850 with the specified strength coming from CSA O86 and manufacturer provided values. There are two cases that are investigated. First the beams are analysed using the values currently recommended in both codes. Secondly the factors recommended based on the research contained in this document will be presented. A discussion on the reasoning for each of the factors chosen will be discussed.

Currently, the dynamic design strength as laid out in CSA S850 is determined by the below equation:

$$S_D = SIF \times DIF \times S_S \quad [6.9]$$

Where S_D is the dynamic design strength, the SIF is the strength increase factor, the DIF is the dynamic increase factor and S_S is the specified static strength. The specified static strength of the beams under flexural loading can be determined by CSA O86. The strength of glulam under bending is determined by the lesser of Equation [6.10] and [6.11]:

$$S_{S1} = \phi \times f_b \times K_D \times K_H \times K_{Sb} \times K_T \times K_x \times K_{Zbg} \quad [6.10]$$

$$S_{S2} = \phi \times f_b \times K_D \times K_H \times K_{Sb} \times K_T \times K_x \times K_L \quad [6.11]$$

Where ϕ is the factor of safety, f_b is the specified strength in bending, K_D is the load duration factor, K_H is the system factor, K_{Sb} is the service condition factor, K_T is the treatment factor, K_x is the curvature factor, K_{Zbg} is the size factor and K_L is the lateral stability factor. For our investigation ϕ , K_H , K_{Sb} , K_T and K_x are all equal to 1.0. The factor of safety, ϕ , is set to 1.0 in order to allow direct comparison to the experimental results. The beam is evaluated as a single element meaning that the system factor, K_H , is 1.0. The service condition factor, K_{Sb} , is set to 1.0 as the beam is under dry service conditions. The treatment factor, K_T , is set to 1.0 as the beams were not treated with any strength reducing chemicals. The curvature factor, K_x , is set to 1.0 as the beams are straight.

The current iteration of CSA S850 states that a load duration factor greater than 1.0 cannot be used in conjunction with a DIF. However, the load duration factor is used to adjust the material strength to effects due to creep, where the DIF is due to the material strengths due to high strain rate effects. As such, it is the opinion of the author that both should be considered when investigating the effects of blast and impact loading. For SDOF Case 1, the value of 1.0 for K_D recommended by CSA S850 is used. For SDOF Case 2, a value of 1.25 is used for K_D , which is taken from Foschi et al. (1989), who discuss the methodology employed in the calibration procedure and the reliability levels adopted for CSA O86.

The size factor and the lateral stability factor are what would determine the specified strength of the beam. In the current version of CSA O86 the smaller of the two strengths would be chosen, depending on if the size of the beam or lateral stability would govern the behaviour of the beam. The value of K_L cannot be greater than 1.0. However, a value of 1.0 indicates that the beam is stable and has sufficient support in the lateral direction. As such, if K_L is equal to 1.0 it can be argued that the size of the beam or K_{Zbg} should instead govern. The maximum value for K_{Zbg} in CSA O86 is currently 1.3, however this is only due to the size of beams tested when the factors were determined. For Case 1, the lateral stability is said to govern the design and S_{S2} is used as the specified strength, as is currently recommended in CSA O86. In Case 2, it is proposed that the size of the beam govern and S_{S1} is used as the specified strength. The size factor, K_{Zbg} , was calculated using Equation [6.12].

$$K_{Zbg} = \left(\frac{130}{b}\right)^{\frac{1}{10}} \times \left(\frac{610}{d}\right)^{\frac{1}{10}} \times \left(\frac{9100}{L}\right)^{\frac{1}{10}} \quad [6.12]$$

Where b is the beam width, d is the beam depth, L is the clear span.

Lastly, in Case 1 the DIF on the MOR of 1.4 and SIF value of 1.2 provided in CSA S850 were used. In Case 2, a DIF on the MOR and MOE 1.16 and 1.21 respectively, were used. These values were as per the calculated averages in Chapter 5. A SIF of 1.2 was used and cold factors of 1.14 and 1.18 on the MOR and MOE were applied for comparing the SDOF analysis to the tests at cold temperature.

In order to determine the resistance function to be used for the SDOF system, the MOR provided by the manufacturer were used in conjunction with the factors discussed above. The average MOE from the static testing was used in order to compare the two models. This value was taken instead of the manufacturer provided value since as mentioned previously, the stiffness for this batch of beams was noticeably lower than the manufacturer provided value. As such, this represents a better comparison for the SDOF system. In order to determine the stiffness and ultimate resistance using the manufacturer provided MOE and MOR, Equation [4.2] and [4.3] were rearranged and combined with the required dynamic increase factors using the form seen in [6.13] and [6.14] for the normal temperature beams. For the cold temperature beams CFs were also applied and Equations [6.15] and [6.16] were used.

$$k_d = \frac{MOE_s \times DIF_{MOE} \times 1296 \times I}{23 \times L^3} \quad [6.13]$$

$$R_u = \frac{SIF \times DIF_{MOR} \times S_S \times 6 \times S}{L} \quad [6.14]$$

$$k_{d,cold} = \frac{MOE_s \times DIF_{MOE} \times 1296 \times I \times CF_{MOE}}{23 \times L^3} \quad [6.15]$$

$$R_{u,cold} = \frac{SIF \times DIF_{MOR} \times S_S \times 6 \times S \times CF_{MOR}}{L} \quad [6.16]$$

Where k_d is the dynamic stiffness, MOE_s is the MOE average from the static testing, DIF_{MOE} is the dynamic increase a factor on the MOE, I is the beam's moment of inertia, L is the clear span, R_u is the ultimate resistance, S_S is the specified static strength as calculated using Equation [6.10] or [6.11] and the manufacturer provided MOR, DIF_{MOR} is the dynamic increase factor on the MOR, SIF is the strength increase factor, S is the section modulus, $k_{d,cold}$ is the dynamic stiffness at cold temperature, $R_{u,cold}$ is the ultimate resistance at cold temperature, CF_{MOE} is the “cold factor” on the MOE calculated in Chapter 5 and CF_{MOR} is the “cold factor” on the MOR calculated in Chapter 5. The factors used for both cases are summarised in Table 6-6.

Table 6-6: Modification factors for determining dynamic strength

Factor	Case 1	Case 2
ϕ, K_H, K_{Sb}, K_T and K_x	1.0	1.0
K_D	1.0	1.25
K_L	1.0	K_{Zbg} governs
K_{Zbg}	K_L governs	1.24 (Large beams) 1.35 (Small beams)
DIF_{MOR}	1.4	1.16
DIF_{MOE}	n/a	1.21
SIF	1.2	1.20
$CF_{d,MOR}$	n/a	1.14
CF_{MOE}	n/a	1.18

An example of the resistance function used for a normal temperature beam for Case 1 and Case 2 can be seen in Figure 6-6 in blue and green respectively. Using the resistance function and forcing function (see Figure 6-2 for an example) for each beam, the displacements could then be predicted using a SDOF system and the Hetherington and Smith method discussed above. There were different comparisons looked at for the elastic and failure tests. For each elastic test the maximum displacement obtained from each SDOF system was compared to the maximum displacement measured. There was a phase shift that occurred between the maximum measured displacement and the displacement obtained from the SDOF system and that was also quantified. The peak resistance, displacement at that resistance and the associated time shift for this value was also investigated.

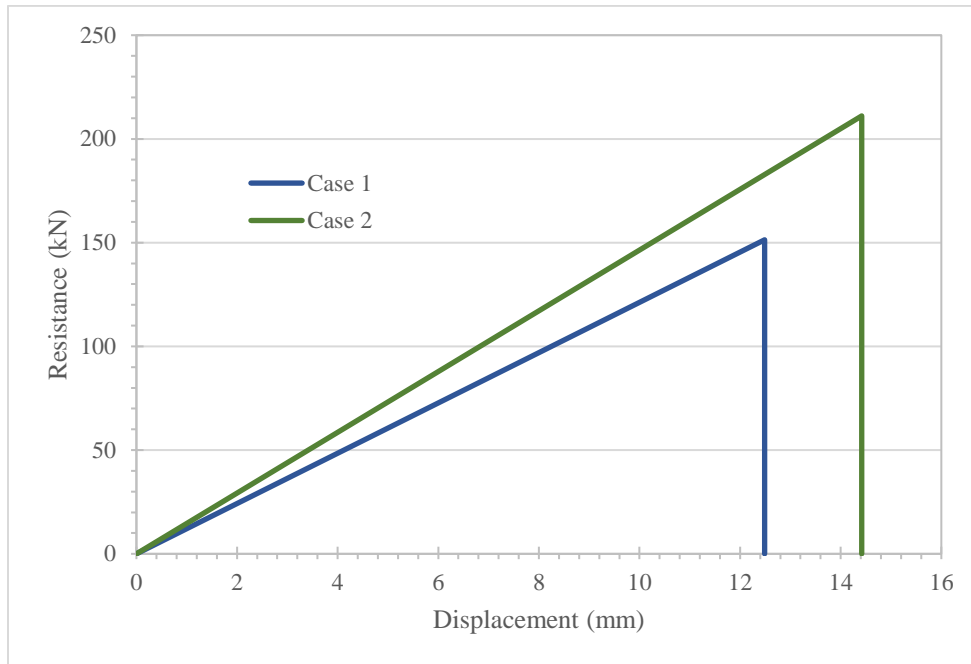


Figure 6-6: Resistance function for a normal temperature beam for Case 1 and Case 2

Figure 6-7 shows the resistance and displacement over time for the real and SDOF systems for DN3-267 for an elastic dynamic test. In this image all resistances are shown by the solid lines and the displacements by the small point dotted lines. The experimental values are shown in yellows, SDOF Case 1 in blues and SDOF Case 2 in greens. The SDOF system can only be used to represent the system up until it begins to rebound or until beam failure as the load transfer beam rollers separate from the beam on the rebound, which makes the SDOF no longer a valid representation of the system. Looking at this image one can see that Case 1, which represents the design values currently recommended in CSA S850, underestimates the resistance, and overestimates the displacement. Looking at Case 2, which represents the parameters that are recommended based on the experimental obtained factors, the resistance and displacement are closer to the experimental values, although slightly underestimated. Overall Case 2 has better agreement with the experimental values.

Figure 6-8 shows the resistance and displacement over time for the real and SDOF systems for DN2-178 for an elastic dynamic test. Looking at this image, one can see that Case 1, which represents the design values currently recommended in CSA S850, show that the beam fails under the elastic drop and consequently has higher displacements that measured. As was shown by the tests, the beams did not fail under the elastic drops. Case 2, which represents the parameters that are recommended based on the experimental obtained factors, shows very good agreement between the beam's resistance and displacement when comparing the SDOF system to the experimental results. The timing, as well as the magnitude, agrees well. Case 1 predicted that three out of the four small beams failed under their elastic loading.

The results from the elastic tests and comparison with the SDOF systems for both the large and small normal temperature beams for both Case 1 and Case 2 can be seen in Table 6-7 and Table 6-8 respectively.

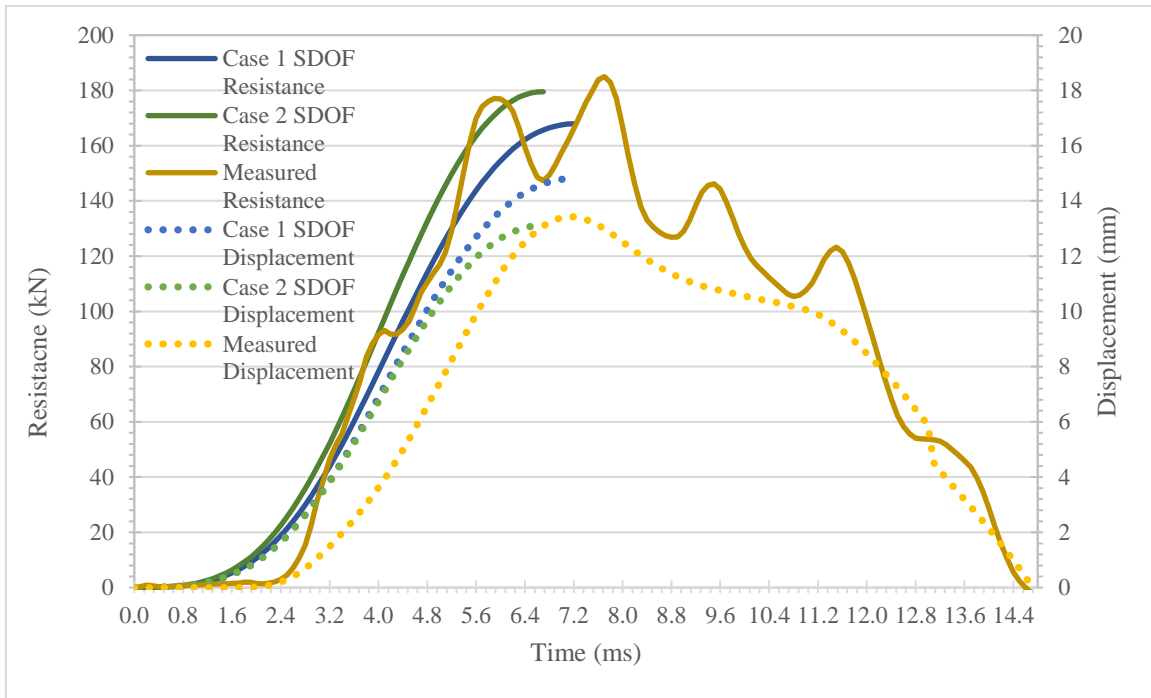


Figure 6-7: Experimental and SDOF resistance-time and displacement-time histories for the elastic dynamic test on DN3-267

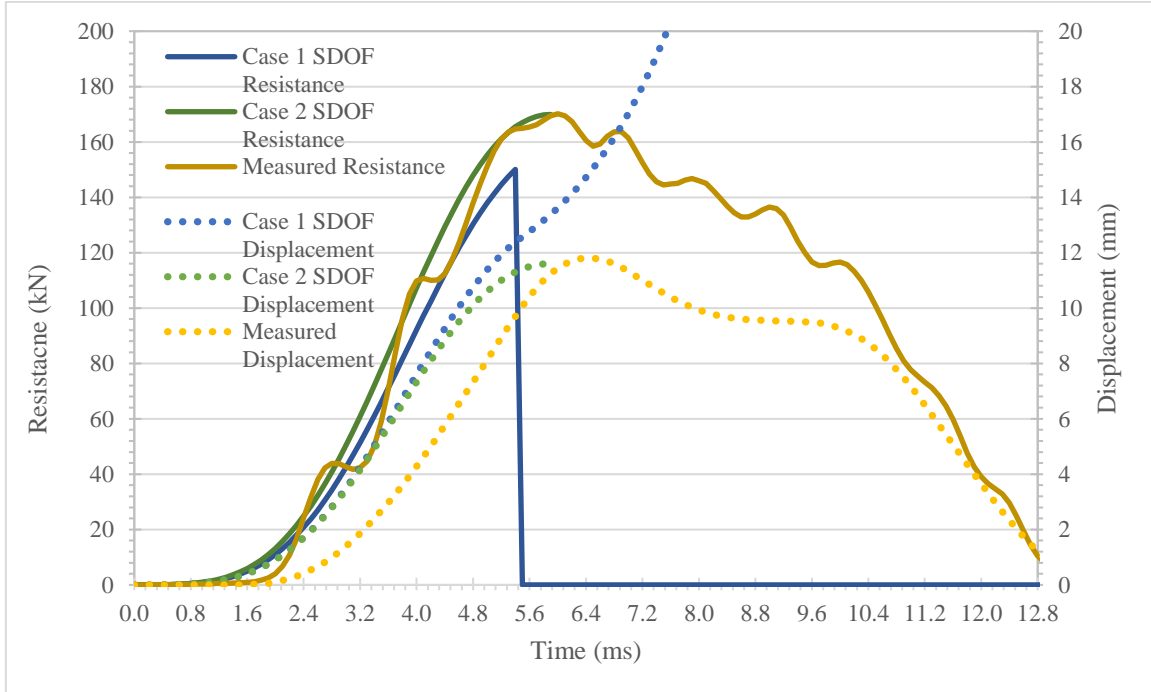


Figure 6-8: Experimental and SDOF resistance-time and displacement-time histories for the elastic dynamic test on DN2-178

Table 6-7: Elastic dynamic tests compared to SDOF models large normal temperature beams

Specimen	Case 1					Case 2				
	y_{SDOF}/y_{max}	Time to y_{max} Ratio SDOF/Exp	$R_{SDOF,d,max}/R_{d,max}$	$y_{SDOF,d,max}/y_{d,max}$	Time to $R_{d,max}$ Ratio SDOF/Exp	y_{SDOF}/y_{max}	Time to y_{max} Ratio SDOF/Exp	$R_{SDOF,d,max}/R_{d,max}$	$y_{SDOF,d,max}/y_{d,max}$	Time to $R_{d,max}$ Ratio SDOF/Exp
DNP1-267	0.91	0.99	0.75	0.98	1.08	0.80	0.94	0.80	0.87	1.03
DN1-267	1.09	0.96	0.90	1.12	1.03	0.96	0.88	0.96	0.99	0.94
DN2-267	1.13	0.96	0.91	1.17	1.06	1.00	0.89	0.97	1.04	0.99
DN3-267	1.10	0.96	0.91	1.10	0.94	0.97	0.89	0.97	0.97	0.87
DN4-267	1.09	0.95	0.88	1.10	1.00	0.97	0.88	0.94	0.98	0.93
DN5-267	1.11	0.96	0.91	1.11	1.00	0.98	0.88	0.97	0.98	0.92
Average	1.07	0.96	0.88	1.10	1.02	0.95	0.90	0.94	0.97	0.95
Std Dev	0.07	0.01	0.06	0.06	0.05	0.07	0.02	0.06	0.05	0.05
COV	0.07	0.01	0.06	0.05	0.05	0.07	0.03	0.06	0.05	0.05

Table 6-8: Elastic dynamic tests compared to SDOF models small normal temperature beams

Specimen	Case 1					Case 2				
	y_{SDOF}/y_{max}	Time to y_{max} Ratio SDOF/Exp	$R_{SDOF,d,max}/R_{d,max}$	$y_{SDOF,d,max}/y_{d,max}$	Time to $R_{d,max}$ Ratio SDOF/Exp	y_{SDOF}/y_{max}	Time to y_{max} Ratio SDOF/Exp	$R_{SDOF,d,max}/R_{d,max}$	$y_{SDOF,d,max}/y_{d,max}$	Time to $R_{d,max}$ Ratio SDOF/Exp
DN1-178	0.97	0.89	0.83	1.02	1.00	0.86	0.83	0.89	0.89	0.93
DN2-178	F ¹	F ¹	0.88	1.13	0.90	1.01	0.87	1.00	1.06	0.98
DN3-178	F ¹	F ¹	0.84	1.05	0.81	1.01	0.86	0.99	1.03	0.93
DN4-178	F ¹	F ¹	0.87	1.19	0.94	1.04	0.88	0.99	1.11	1.04
Average	-	-	0.86	1.10	0.91	0.98	0.86	0.97	1.02	0.97
Std Dev	-	-	0.02	0.07	0.07	0.07	0.02	0.05	0.08	0.04
COV	-	-	0.02	0.06	0.07	0.07	0.02	0.05	0.08	0.04

¹ Indicates that the model showed the beam failing under elastic conditions.

In Table 6-7 and Table 6-8 one can see the comparisons between Case 1, which uses the currently recommended parameters from CSA S850, and Case 2, which uses the recommended parameters based on the experimental results. One can see that both systems overall have good agreement with the experimental values when considering the large beams. The maximum displacement for the large beams calculated in the SDOF system for Case 1 was on average 1.07 of the displacements recorded during testing. Case 2 was 0.95 of the displacements recorded during testing. This means that Case 1 is more conservative than Case 2. However, this is still below the elastic limit. At the failure loads, Case 2 does have some conservatism, as will be seen below. The SDOF average peak resistances for Case 1 and Case 2 were 0.88 to 0.94 respectively of the experimental peak resistances. Looking at the displacements that occurred at those peak resistances, the SDOF displacements for Case 1 and Case 2 were an average of 1.10 and 0.97 respectively of the values obtained experimentally. The values for Case 2 are once again closer to the experimentally obtained values, but the resistance and displacement are slightly smaller than what was observed, making them unconservative.

When looking at the small beams, Case 1 predicted the failure of three out of the four beams under their elastic load, making it unrepresentative of these beams' response. The maximum displacement calculated in the SDOF system for Case 2 was on average 0.98 of the displacements recorded during testing, making it an excellent presentation of the behaviour of these beams. The SDOF peak resistances for Case 2 were on average 0.97 of the experimental peak resistances and the displacements that occurred at the peak resistance was 1.02 of the values obtained experimentally. For the small beams, Case 2 shows very good agreement between the beams' behaviour and the experimental results. Case 1 wrongly predicts failure on three of the four beams indicating that the values recommended in CSA S850 are too conservative.

For each destructive test the displacement at peak resistance obtained from each SDOF system was compared to the displacement measured at failure (peak resistance). There was a phase shift that occurred between the peak displacement in the SDOF system and the peak that was measured that was also quantified. Figure 6-9 shows the resistance and displacement over time for the real and SDOF systems for DN2-178 for a failure dynamic test. In this image all resistances are shown by the solid lines and the displacements by the small point dotted lines. The experimental values are shown in yellows, SDOF Case 1 in blues and SDOF Case 2 in greens. The black dotted lines represent the point of failure. In this way the displacement at peak resistance can be easily identified.

From the image, it is observed that Case 1 shows the beam failing much before the experimental peak resistance. The displacement predicted is also less than the value obtained experimentally. Case 2 has a much better overall fit, with the displacement at peak resistance being marginally overestimated which would result in a slightly conservative design. Overall, Case 2 has the better overall agreement with experimental values.

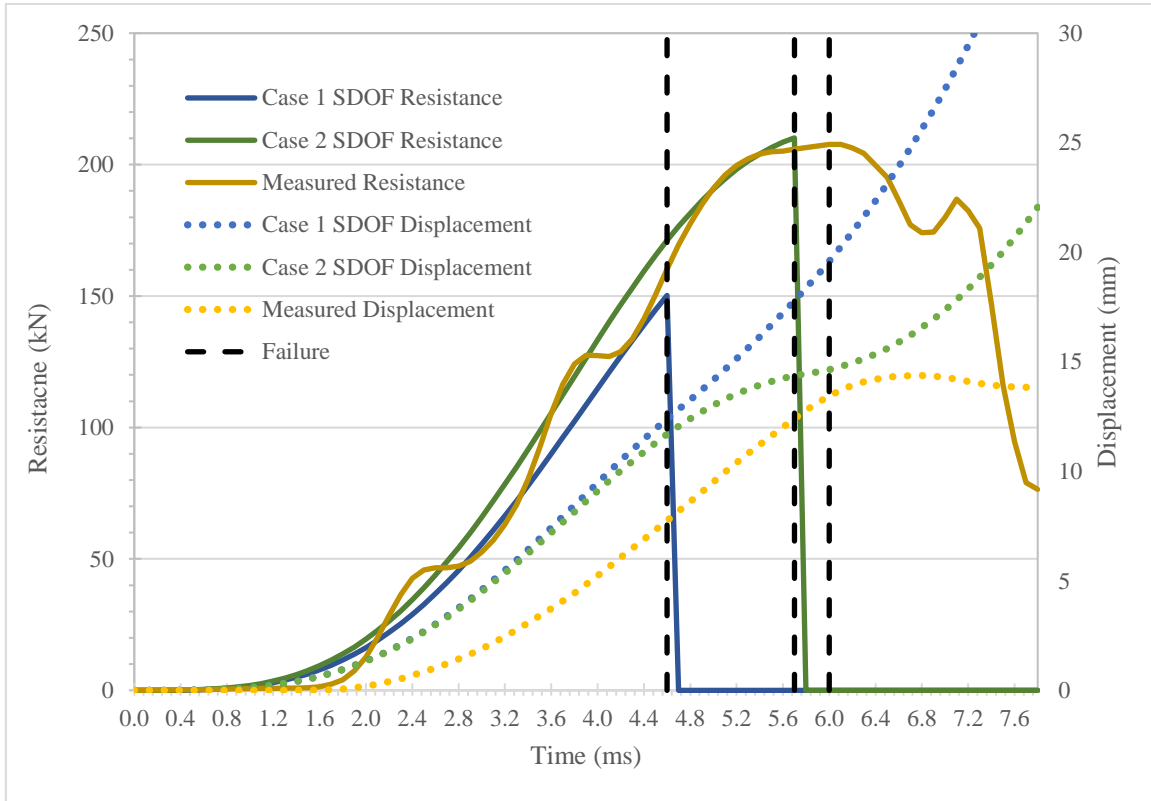


Figure 6-9: Experimental and SDOF resistance-time and displacement-time histories for the failure dynamic test of DN2-178

The results from the failure dynamic tests and comparison with the SDOF system for both the large and small normal temperature beams and small cold temperature beams can be seen in Table 6-9, Table 6-10, and Table 6-11 respectively.

Table 6-9: Failure dynamic tests compared to SDOF models for large normal temperature beams

Specimen	Case 1		Case 2	
	$y_{SDOF,d,max}/y_{d,max}$	Time to $R_{d,max}$ Ratio SDOF/Exp	$y_{SDOF,d,max}/y_{d,max}$	Time to $R_{d,max}$ Ratio SDOF/Exp
DNP1-267	0.87	0.56	0.93	0.66
DN1-267	1.18	0.92	1.26	1.11
DN2-267	0.92	0.82	0.96	1.03
DN3-267	0.95	0.80	1.02	0.95
DN4-267	1.06	0.89	1.13	1.06
DN5-267	1.05	0.86	1.12	0.97
Average	1.01	0.81	1.07	0.96
Std Dev	0.10	0.12	0.11	0.14
COV	0.10	0.15	0.11	0.15

Table 6-10: Failure dynamic tests compared to SDOF models for small normal temperature beams

Specimen	Case 1		Case 2	
	$y_{SDOF,d,max}/y_{d,max}$	Time to $R_{d,max}$ Ratio SDOF/Exp	$y_{SDOF,d,max}/y_{d,max}$	Time to $R_{d,max}$ Ratio SDOF/Exp
DN1-178	0.82	0.70	0.95	0.83
DN2-178	0.92	0.77	1.07	0.95
DN3-178	1.01	0.84	1.16	1.11
DN4-178	1.05	0.85	1.25	1.06
Average	0.95	0.79	1.11	0.98
Std Dev	0.09	0.06	0.11	0.11
COV	0.09	0.08	0.10	0.11

Table 6-11: Failure dynamic tests compared to SDOF models for small cold temperature beams

Specimen	Case 1		Case 2	
	$y_{SDOF,d,max}/y_{d,max}$	Time to $R_{d,max}$ Ratio SDOF/Exp	$y_{SDOF,d,max}/y_{d,max}$	Time to $R_{d,max}$ Ratio SDOF/Exp
DC2-178	1.02	0.80	1.14	1.05
DC3-178	0.93	0.75	1.03	0.98
DC4-178	1.03	0.80	1.17	1.07
Average	0.99	0.78	1.11	1.04
Std Dev	0.05	0.03	0.06	0.04
COV	0.05	0.03	0.05	0.04

When looking at the values in the table, both Case 1 and Case 2 have a good overall agreement with the experimental displacements. For the large normal temperature specimen failure dynamic tests, the displacement at the peak resistance in the SDOF system was on average 1.01 and 1.07 of the experimental displacements for Case 1 and Case 2 respectively. For the small normal temperature specimen failure dynamic tests, the displacement at the peak resistance in the SDOF system was on average 0.95 and 1.11 of the experimental displacements for Case 1 and Case 2 respectively. For the small cold temperature specimen failure dynamic tests, the displacement at the peak resistance in the SDOF system was on average 0.99 and 1.11 of the experimental displacements for Case 1 and Case 2 respectively. While both systems are quite accurate in terms of estimating the displacement, the failure in Case 1 always occurs much before the experimental one, with the failure resistance being inaccurately estimated, as seen in Figure 6-9. Additionally, at failure Case 1, has no redundancy resulting in it being unconservative for some beams, by underestimating the displacement. Case 2 does overestimate the displacement compared to experimental results. This means that Case 2 has more conservative in its estimation at failure.

Overall although Case 1 and Case 2 both agree well with the experimental results, when the time histories are plotted, the modification recommended to the factors used in Case 2 represent the behaviour of the beams under impact loading better. This is especially apparent with the normal temperature beams under elastic loading. It was also very apparent when considering the resistance time histories for the failure tests, where the Case 1 SDOF models fails much sooner than it should. Importantly, even if the proposed factors do not inherently make the SDOF analysis much more

accurate beyond the current method, the values proposed for CSA S850 apply more logically to the behaviour of the beam. For example, load duration effects are caused by a different phenomenon than high strain effects and therefore a load duration factor should be used in conjunction with a DIF.

6.3 Conservation of Energy

To confirm the validity of the dynamic experimental test setup and results, the principles of conservation of energy in the system were applied. This also enabled investigation into the energies that were being absorbed by the beam. The drop hammer converts potential energy from the hammer into the kinetic energy of the drop weight. This energy under impact is then transferred to both kinetic and strain energy within the beam, which when combined equals the energy absorbed by the beam. In theory, this energy should be equal to the work done by the impact hammer. However, some energy losses in the system are expected, such as through friction in the bearings of the weight, and vibrations in the rails. This correlates to the fact that the energy transmission is not solely downwards, as assumed in a perfect system, and that not all the drop weight's potential energy is converted into kinetic energy.

Previous studies have shown that the amount of work done by an impact hammer is often much lower than the systems theoretical potential energy, and using the kinetic energy lost by the hammer using impulse momentum relationships will not result in balanced system energies (Banthia et al. 1989; Beirnes et al. 2019). As such, the work done by the impact hammer was directly compared to the energy absorbed by the beam and the weight's conversion of potential to kinetic energy was not considered.

To determine the work done by the hammer, the area under its load displacement curve was calculated. The load was taken from the central force transducer and the displacement was taken from the linear encoder attached to the drop weight (See Figure 4-6). This calculation was done using Equation [6.17].

$$W_{hammer}(t_i) = W_{hammer}(t_{i-1}) + \frac{F(t_i) + F(t_{i-1})}{2} \times [y_w(t_i) - y_w(t_{i-1})] \quad [6.17]$$

Where W_{hammer} is the work done by the hammer, F is the load measured by the central force transducer, and y_w is the displacement of the weighted box as measured by the linear encoder.

To determine the beam's kinetic energy the midspan velocity of the beam was used which was derived from the beam's midspan displacement. The equivalent mass of the beam, as calculated in the SDOF system was used to determine the beam's kinetic energy. The kinetic energy was calculated as per Equation [6.18].

$$KE_{beam} = \frac{1}{2} M_t \dot{y}^2 \quad [6.18]$$

Where KE_{beam} is the beam's kinetic energy, M_t is the total factored mass, \dot{y} is the beam's midspan velocity.

The strain energy of the beam is the area under the dynamic resistance versus displacement curve. This was determined by the support force transducers, which were then added and converted to a dynamic resistance as per Equation [4.4]. The displacement was taken from the beam midspan and used in Equation [6.19].

$$UE_{beam}(t_i) = UE_{beam}(t_{i-1}) + \frac{R_d(t_i) + R_d(t_{i-1})}{2} \times [y_{beam}(t_i) - y_{beam}(t_{i-1})] \quad [6.19]$$

Where UE_{beam} is the beam's strain energy, R_d is the dynamic resistance, and y_{beam} is the beam's midspan displacement.

The total energy of the beam was then obtained by adding the kinetic and the strain energy as per Equation [6.20].

$$ET_{beam} = KE_{beam} + UE_{beam} \quad [6.20]$$

Where ET_{beam} is the beam's total absorbed energy, KE_{beam} is the beam's kinetic energy, and UE_{beam} is the beam's strain energy.

Using this methodology, the system energies were directly compared at the time of beam failure in the case of failed beams, coinciding with the peak resistance, and consistently followed by a sudden drop in resistance. When considering elastic specimens, the point of peak resistance was taken as the point of comparison, which was often synonymous with maximum mid-span displacement. The energy comparisons for the various elastic and destructive dynamic tests for the large beams can be seen in Table 6-12 and Table 6-13.

Table 6-12: Energy comparison for large beam elastic drops

Specimen	W_{hammer} J	ET_{beam} J	Percent Difference
DNP1-267	1,295	1,354	-4.5%
DN1-267	1,648	1,472	11.3%
DN2-267	1,675	1,458	13.9%
DN3-267	1,722	1,448	17.3%
DN4-267	1,671	1,526	9.1%
DN5-267	1,709	1,466	15.3%
Average	1,620	1,454	10.4%
Std Dev	148	51	7.2%
COV	0.09	0.04	0.69

Table 6-13: Energy comparison for large beam destructive drops

Specimen	W_{hammer}	ET_{beam}	Percent Difference
	J	J	
DNP1-267	4,358	4,017	8.1%
DN1-267	3,386	3,328	1.7%
DN2-267	3,691	3,582	3.0%
DN3-267	3,615	3,478	3.9%
DN4-267	3,582	3,511	2.0%
DN5-267	3,809	3,515	8.0%
Average	3,740	3,572	4.5%
Std Dev	304	213	2.7%
COV	0.08	0.06	0.60

Looking at the energy values from the large beam elastic drops, the average work accomplished by the hammer was 1,620 J. The average energy transferred to the beam was 1,454 J, resulting in an average percent difference of 10.4%. DNP1-267 is the only dynamic test that recorded more energy absorbed than work done by the hammer. This is likely due to inconsistencies and vibrations within the system that meant that all travel was not in the vertical direction. In addition to this, at the beginning of the experimental test program, eight pillow block bearings were utilized to transport and guide the weighted box along the rails. It was found in the process of the 31 dynamic tests on DNP1-267 that eight bearings provided too much friction in the system and would impede the downward motion of the drop weight. To alleviate this, two of the bearings were removed, which allowed the box to travel downwards more freely. This change occurred at dynamic test 19, after the elastic drop. It may be due to the excess friction in this elastic dynamic test compared to the others that a noticeable unbalance of energy was present since friction was not considered in these calculations.

When considering the energy balances for the destructive dynamic tests, the energies are even closer to being balanced. For all destructive tests, the work done by the hammer tends to be greater than the energy absorbed by the beam. For the large beam destructive dynamic tests, the average work accomplished by the hammer was 3,740 J. The average energy transferred to the beam was 3,572 J, resulting in an average percent difference of 4.5%. The largest energy difference was with DNP1-267 at 8.1% and the smallest difference was beam DN1-267 at 1.7%.

Figure 6-10 shows the various energies plotted up until the failure for DN1-267. After beam failure, the energies can no longer be directly compared due to the complex dispersion of energy upon failure and the rebound of the weighted box. In blue the total work done by the hammer can be seen. The total energy absorbed by the beam is shown in yellow. This is the sum of the kinetic energy shown in gray and the strain energy shown in orange. As would be expected, the work done by the hammer gradually increases after impact, increasing milliseconds faster than it is transferred into the beam. The beam's kinetic energy initially takes most of the energy in the beam, then as the beam reaches its maximum deflection begins to slow, and more of the impact energy is converted into strain energy.

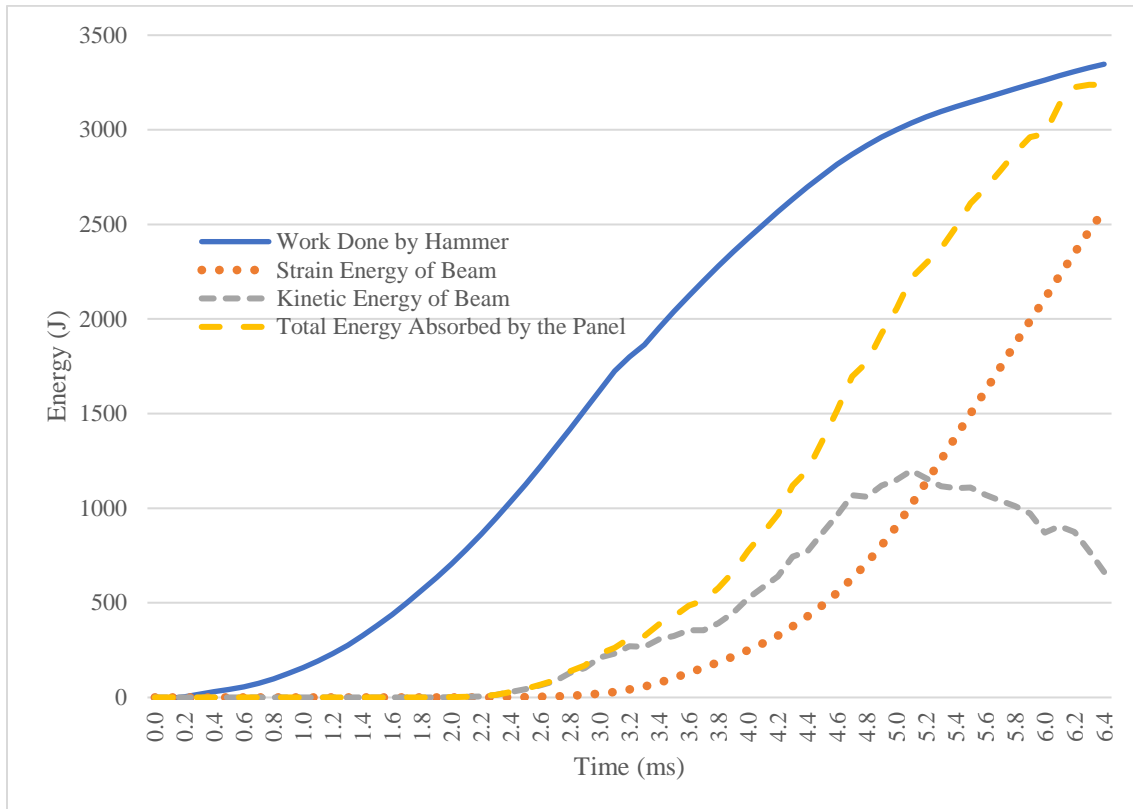


Figure 6-10: Conservation of energy balance for the failure drop of DN1-267

The energy comparisons for the various elastic and destructive dynamic tests for the normal temperature small beams and the destructive dynamic tests for the cold temperature small beams can be seen in Table 6-14 through Table 6-16.

Table 6-14: Energy comparison for small normal temperature beam elastic dynamic tests

Specimen	W_{hammer} J	ET_{beam} J	Percent Difference
DN1-178	1,252	1,390	-10.39%
DN2-178	1,238	1,184	4.43%
DN3-178	1,399	1,338	4.45%
DN4-178	1,194	1,160	2.82%
Average	1,271	1,268	0.33%
Std Dev	77	98	6.23%
COV	0.06	0.08	18.99

Table 6-15: Energy comparison for small normal temperature beam destructive dynamic tests

Specimen	W_{hammer}	ET_{beam}	Percent Difference
	J	J	
DN1-178	2,092	2,003	4.4%
DN2-178	1,888	1,768	6.6%
DN3-178	1,687	1,556	8.1%
DN4-178	1,737	1,629	6.5%
Average	1,851	1,739	6.4%
Std Dev	158	170	1.3%
COV	0.09	0.10	0.21

Table 6-16: Energy comparison for small cold temperature beam destructive dynamic tests

Specimen	W_{hammer}	ET_{beam}	Percent Difference
	J	J	
DC1-178	1,958	1,866	4.8%
DC2-178	1,906	1,826	4.3%
DC3-178	2,033	1,970	3.1%
DC4-178	1,943	1,856	4.5%
Average	1,960	1,879	4.2%
Std Dev	46	54	0.6%
COV	0.02	0.03	0.15

Looking at the energy values from the small normal temperature beam elastic dynamic tests, the average work accomplished by the hammer was 1,271 J. The average energy transferred to the beam was 1,268 J, resulting in an average percent difference of 0.33%. The elastic drop of DN1-178 is the only dynamic test among the small beams that recorded more energy absorbed than work done by the hammer. This small percent of greater energy absorbed is likely due to inconsistencies and vibrations within the system that meant that all travel was not in the vertical direction. Small lateral movements in the beam both side to side and back to front, as well as the compression of the vulcanised rubber disk, may affect the energy values.

Looking at the energy values from the small normal temperature beam destructive dynamic tests, the average work accomplished by the hammer was 1,851 J. The average energy transferred to the beam was 1,739 J, resulting in an average percent difference of 6.4%. The largest energy difference was with DN3-178 at 8.1% and the smallest energy difference was beam DN1-178 at 4.4%. Looking at the energy values from the small cold temperature beam destructive dynamic tests, the average work accomplished by the hammer was 1,960 J. This value is larger than the work done by the hammer in the small normal temperature tests since the weight was dropped from 2,000 mm instead of 1,800 mm as more force was required to fail the cold specimens. The average energy transferred to the beam was 1879 J, resulting in an average percent difference of 4.2%. The largest energy difference was with DC1-178 at 4.8% and the smallest energy difference was beam DC3-178 at 3.1%. The cold beams absorbed 7.8% more energy than the normal temperature small beams, indicating that they have a better resistance to impact loads than the normal temperature beams. Figure 6-11 shows the various energies plotted up until the failure of DC3-178, which is

very similar to the energy balances seen for DN1-267 in Figure 6-10.

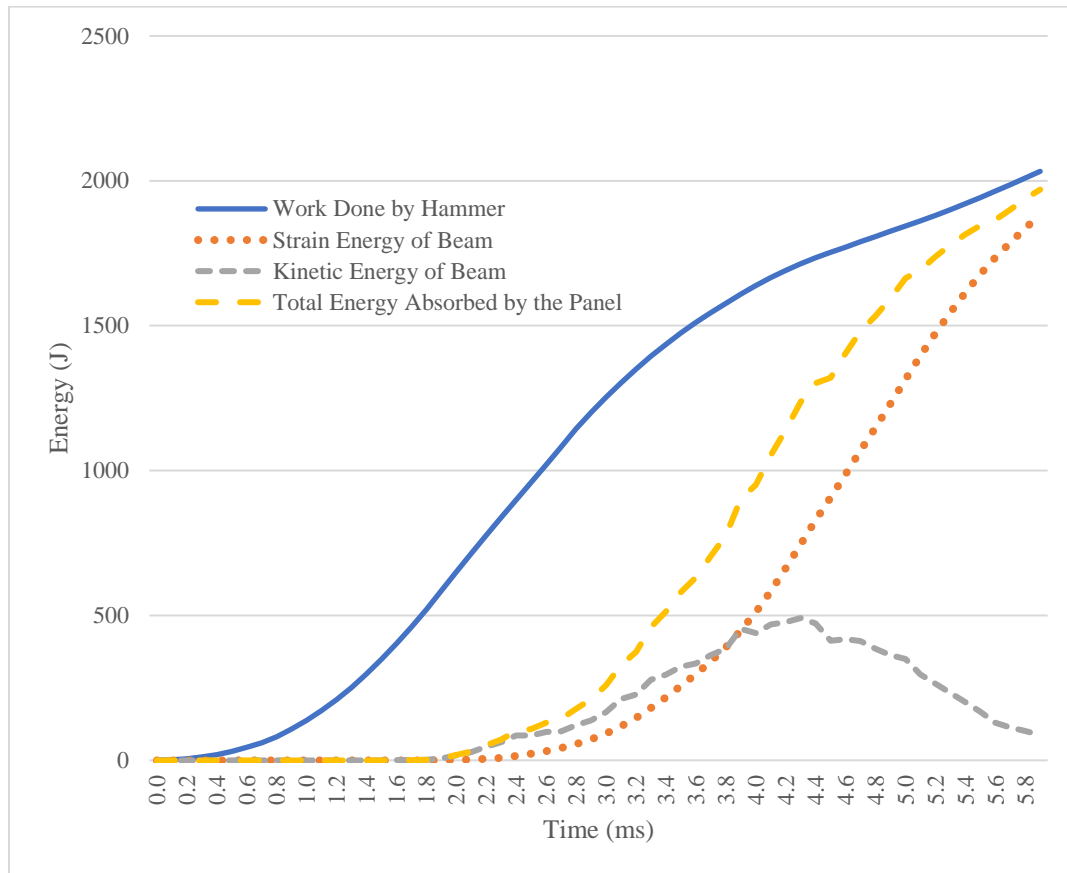


Figure 6-11: Conservation of energy balance for the failure dynamic test of DC3-178

Looking at the standard deviations for all failure tests, the results for energy from the hammer are very consistent test to test. This reinforces the repeatability advantage of impact testing versus blast testing.

6.4 Summary

In summary, SDOF analysis models the behaviour of glulam beams under impact very well, accurately estimating the maximum displacement, peak resistance, and displacement at peak resistance under elastic dynamic tests. The displacement at peak resistance was also accurately estimated for all failure tests, including the cold temperature specimens. The experimental values were first used to confirm the ability of a SDOF to represent glulam. The MOR provided by the manufacturer was used in conjunction with the factors discussed above. The average MOE from the static testing was used for the model. Overall Case 2, which represents the parameters that are recommended based on the experimental obtained factors, was in better agreement with the overall behaviour of the experimental system.

Conservation of energy for all elastic and destructive dynamic tests for the large and small beams were considered. The large beam elastic drops resulted in a percent difference of 10.4% between the work done by the hammer and the energy absorbed by the beams and for the large beam destructive drops this value was 4.5%. The small normal temperature beam elastic drops resulted in a percent difference of 0.33% between the work done by the hammer and the energy absorbed by the beams and for the small normal temperature beam destructive drops this value was 6.4%. The small cold temperature beam destructive drops resulted in a percent difference of 4.2% between the work done by the hammer and the energy absorbed by the beams. Only two of the drops resulted in energy calculations that indicated that more energy was absorbed by the beam than work done by the hammer. This discrepancy is likely due to other losses in the system caused by friction, the compression of vulcanized rubber disk, vibrations in the system and lateral movement. The cold beams absorbed 7.8% more energy than the normal temperature small beams, indicating that they have a better resistance to impact loads than the normal temperature beams.

Chapter 7: Conclusions and Recommendations

7.1 Summary

The aim of this research project was to investigate the behaviour of glulam beams subjected to impact loading, specifically examining high strain-rate effects, and their behaviour under normal temperature and extreme cold conditions.

An experimental test program was conducted at the Royal Military College of Canada using the newly establish drop hammer impact test facility. An experimental program was conducted using quasi-static and dynamic drop-hammer impact loading. A total of nine 137 mm x 267 mm x 2500 mm glulam beams and fifteen 137 mm x 178 mm x 1650 mm were tested under both ambient and extreme cold temperatures to examine their viability for use in the arctic.

Through this testing it was determined that the drop weight impact testing facility at the Royal Military College of Canada can be used in order to simulate impacts and investigate high strain rate effects on small- and full-scale structural elements. This testing facility can be used to investigate short duration load effects on materials, with average durations of load from 8.9 to 13.3 ms, correlating to strain rates between 0.67 to 1.38 s⁻¹.

One large beam was impacted 28 more times than the other large beams in order to finalize the test set-up and determine a proper drop height and weight. These multiple hits did not alter the beam's response and also provides proof of the linear elastic nature of a beam exposed to multiple impacts before reaching its peak resistance.

Cold temperature tests were conducted, with the beam internal temperatures correlated to a test beam with thermocouples at four separate depths. The average estimated temperature for all static small cold temperature beams was -46.8°C at the test midpoint and -43.5°C at failure. For the dynamic cold tests, the average failure temperature was -47.1°C.

Throughout testing the average failure loads, displacement at failure, stiffness, MOR, MOE and strain rate were all investigated for both large and small beams at ambient and extreme cold temperatures in order to determine the SIF, DIF and effects of extreme cold on the beams.

Lastly, SDOF modeling methodology was used to estimate the behaviour of simply supported glulam beams subjected to impact loading, and conservation of energy within the system was investigated.

7.2 Conclusions

Based on the findings of the current study, the following conclusion can be drawn:

- All tested beams had a linear elastic brittle load-displacement relationship, and all beams had failure initiate at a knot or natural defect. The failure patters when comparing static testing to dynamic testing did not differ greatly, although the cracks were slightly more prominent in the dynamic specimens.

- For strain rates in the range of 0.67 to 1.38 s⁻¹, an average DIF on the MOR and MOE for the glulam beams was determined to be 1.16 and 1.21 respectively. This highlights the need to reassess the DIF values recommended in CSA S850.
- The cold temperature beams absorbed 7.8% more energy than the normal temperature small beams under impact loading indicating that they have a better resistance to impact loads than the normal temperature beams. “Cold Factors” of 1.18 on the MOE both statically and dynamically and 1.14 on the MOR dynamically were determined for the tested temperature.
- An SDOF system of analysis is able to accurately predict the displacement of simply supported glulam elements under impact loading.

7.3 Supporting Conclusions

Based on the findings of the current study, the following supporting conclusion can be drawn:

- The testing resulted in an overall average SIF of 1.20, which aligns exactly with the value of 1.2 currently recommended in CSA S850.
- As long as impacts are kept below the peak resistance of the beam, multiple impacts do not degrade glulam’s stiffness.
- Under static testing the cold temperature beams appeared to be subject to less splintering than the normal temperature beams, which may be caused by the ice crystals keeping some of the wood’s fibres together. There was no influence under dynamic cold testing.
- The presence of defects is incredibly important for influencing failure in glulam. If members of reduced size are being tested, the presence of defects within the central third must be ensured, as these will be present in a full-scale specimen.
- The SDOF analyses indicated that the parameters that are recommended based on the experimental obtained factors, was in better agreement with the overall behaviour of the experimental system than the factors currently recommended in CSA S850.
- Conservation of energy was investigated to confirm the accuracy of the experimental results. All resultant energy calculations between the work done by the hammer and the energy absorbed by the beam were within 10.4% of each other at failure indicating no large energy losses in the system and confirming the accuracy of the instrumentation.

7.4 Recommendations for Future Research

Despite attempts within this research study to be conclusive in the response of glulam to impact loading under ambient and extreme cold conditions, there are areas for future research that should be conducted in order to expand on the data gathered herein and to expand the existing body

of knowledge on the subject of wood's behaviour under blast and impact loading.

Different beam cross sections, lengths, and laminate layup should be investigated as potential research variables. Previous research has indicated the important presence of finger-joint location in the failure mechanism of the beams, as such this represents an area for further research. This research has reinforced that the location of defects is important for determining where and how the beams will fail. This should be investigated in further detail, looking at what a critical defect size is, so that more scale elements can be tested.

The effect of realistic boundary conditions on the behaviour of glulam under impact and the use of connections as potential energy dissipaters should be investigated further. Different connection types and their respective resistance to blast loading should be examined.

Further cold temperature testing is required in order to confirm the preliminary results gained from cold sample testing. Multiple tests at a variety of temperatures should be investigated to see if a relationship can be drawn relating temperature to the strength gain observed, so that the effects of a wider variety of temperatures can be accounted for in design. In addition, cyclic temperature cycles should be investigated in the future under impact loading as previous studies have reported decreases in strength under cyclic temperature static testing.

Lastly, although SDOF analysis represents a good approximation of maximum displacement, more advanced modeling techniques such as FEA analysis should be considered as more advanced and detailed models for wood and EWPs, such as glulam, are developed.

References

- ASCE. 2011. Blast Protection of Buildings: ASCE/SEI 59-11 Blast Protection of Buildings.
- ASTM International. 2021. Standard Test Methods of Static Tests of Lumber in Structural Sizes: D198 – 21a. ASTM International, Pennsylvania, United States.
- Ayrilmis, N., Buyuksari, U., and As, N. 2010. Bending strength and modulus of elasticity of wood-based panels at cold and moderate temperatures. *Cold Regions Science and Technology*, **63**(1-2): 40-43.
- Banthia, N., Mindess, S., Bentur, A., and Pigeon, M. 1989. Impact testing of concrete using a drop-weight impact machine. *Experimental mechanics*, **29**(1): 63-69. doi:10.1007/BF02327783.
- Beirnes, M., Dagenais, M.-A., and Wight, G. 2019. Cold temperature effects on the impact resistance of thin, lightweight UHPFRC panels. *International Journal of Impact Engineering*, **127**: 110-121.
- Bekhta, P., and Marutzky, R. 2007. Bending strength and modulus of elasticity of particleboards at various temperatures. *Holz als Roh-und Werkstoff*, **65**(2): 163-165.
- Biggs, J. 1964. Introduction to structural dynamics. McGraw-Hill College.
- Bragov, A., and Lomunov, A. 1997. Dynamic properties of some wood species. *Le Journal de Physique IV*, **7**(C3): C3-487-C483-492.
- Breyer, D.E., Fridley, K.J., Cobeen, K.E., and Pollock Jr, D.G. 2007. Design of Wood Structures- ASD/LRFD. 6 ed. McGraw-Hill Education, USA.
- Canadian Department of National Defence. 2017. Strong, Secure, Engaged: Canada's Defence Policy
- Canadian Wood Council. 2021. Glulam. Available from <https://cwc.ca/how-to-build-with-wood/wood-products/mass-timber/glulam/> [accessed 16 June 2021 2021].
- Cole, R.J., and Kernan, P.C. 1996. Life-cycle energy use in office buildings. *Building and Environment*, **31**(4): 307-317. doi:10.1016/0360-1323(96)00017-0.
- Cormie, D., Mays, G., and Smith, P. 2020. Blast Effects on Buildings. Third Edition ed. ICE Publishing, London, England.
- Cousins, W. 1974. Effects of strain rate on the surface morphology of *Pinus radiata* broken by transverse tensile forces. *New Zealand J. Forest Sci*, **4**(1): 94-104.
- CSA. 2012. Design and assessment of buildings subjected to blast loads S850-12. CSA Group, Mississauga, ON.

- CSA. 2016. *Engineering Design in Wood: CSA O86-14*. CSA Group, Mississauga, ON.
- Domec, J.C. 2002. How do water transport and water storage differ in coniferous earlywood and latewood? *Journal of Experimental Botany*, **53**(379): 2369-2379. doi:10.1093/jxb/erf100.
- Drake, G., Berry, M., and Schroeder, D. 2015. Effect of cold temperatures on the shear behavior of glued laminated beams. *Cold Regions Science and Technology*, **112**: 45-50. doi:10.1016/j.coldregions.2015.01.002.
- Foschi, R.O., Folz, B., and Yao, F. 1989. *Reliability-based design of wood structures*. University of British Columbia Structural Research Series, Rep. No. 34, Vancouver, BC, Canada.
- Gerhards, C.C. 1982. Effect of moisture content and temperature on the mechanical properties of wood: an analysis of immediate effects. *Wood and Fiber Science*, **14**(1): 4-36.
- Gilbertson, C.G., and Bulleit, W.M. 2013. Load duration effects in wood at high strain rates. *Journal of materials in civil engineering*, **25**(11): 1647-1654.
- Government of Canada. 2019a. *Highlights of Canada's Arctic and Northern Policy Framework*. Available from <https://www.rcaanc-cirnac.gc.ca/eng/1567697304035/1567697319793> [accessed 07 June 2021 2021].
- Government of Canada. 2019b. *Canadian Forces Station Alert*. Available from <http://www.rcf-arc.forces.gc.ca/en/alert.page> [accessed 30 June 2021 2021].
- Green, D.W., and Evans, J.W. 2008. The immediate effect of temperature on the modulus of elasticity of green and dry lumber. *Wood and Fiber Science*, **40**(3): 374-383.
- Hetherington, J., and Smith, P. 1994. Structural response: incremental solution of equation of motion. *In Blast and Ballistic Loading of Structures*. Butterworth-Heinemann, London, UK.
- Jacques, E., Lloyd, A., Braimah, A., Saatcioglu, M., Doudak, G., and Abdelalim, O. 2014. Influence of high strain-rates on the dynamic flexural material properties of spruce–pine–fir wood studs. *Canadian journal of civil engineering*, **41**(1): 56-64.
- Jansson, B. 1992. *Impact loading of timber beams*. University of British Columbia.
- Jiang, J., Lu, J., Zhou, Y., Zhao, Y., and Zhao, L. 2014. Compression strength and modulus of elasticity parallel to the grain of oak wood at ultra-low and high temperatures. *BioResources*, **9**(2): 3571-3579.
- Joint Departments of the Army Air Force and Navy and the Defense Special Weapons Agency. 2002. *Design and Analysis of Hardened Structures to Conventional Weapons*. UFC 3-340-01 (TM-855-1), U.S.D.o. Defence, Washington, US.
- Karacabeyli, E., and Barrett, J. 1993. Rate of loading effects on strength of lumber. *Forest Products Journal*, **43**(5): 13.

- Lacroix, D., and Doudak, G. 2014. Investigation of Dynamic Increase Factors in Light-Frame Wood Stud Walls Subjected to Out-of-Plane Blast Loading. *Journal of Structural Engineering*, **141**: 04014159. doi:10.1061/(ASCE)ST.1943-541X.0001139.
- Lacroix, D., and Doudak, G. 2018a. Determining the dynamic increase factor for glued-laminated timber beams. *Journal of Structural Engineering*, **144**(9): 04018160.
- Lacroix, D., and Doudak, G. 2018b. Effects of high strain rates on the response of glulam beams and columns. *Journal of Structural Engineering*, **144**(5): 04018029.
- Lacroix, D.N. 2017. Investigating the behaviour of glulam beams and columns subjected to simulated blast loading. Université d'Ottawa/University of Ottawa.
- Lavarnway, D., and Pollino, M. 2015. Mitigation of air-blast pressure impulses on building envelopes through blast resistant ductile connectors. *Journal of Engineering and Architecture*, **3**(2): 9-24.
- Marchand, K.A. 2002. BAIT, BASS & RODS Testing Results. Applied Research Associates, Prepared for the USAF Force Protection Battlelab.
- McGrath, A., and Doudak, G. 2021. Investigating the response of bolted timber connections subjected to blast loads. *Engineering Structures*, **236**: 112112.
- Mindess, S., and Madsen, B. 1986. The fracture of wood under impact loading. *Materials and structures*, **19**(1): 49-53.
- Ministry of Natural Resources and Forestry. 2021. Building with wood. Available from <https://www.ontario.ca/page/building-with-wood> [accessed 08 June 2021 2021].
- Ministry of Natural Resources and Forestry and Ministry of Municipal Affairs. 2017. Ontario's Tall Wood Building Reference. Queen's Printer for Ontario.
- Moon, N. 2009. Prediction of blast loading and its impact on buildings. Department of Civil Engineering, National Institute of Technology Rourkela.
- Nadeau, J.S., Bennett, R., and Fuller, E.R. 1982. An explanation for the rate-of-loading and the duration-of-load effects in wood in terms of fracture mechanics. *Journal of Materials Science*, **17**(10): 2831-2840.
- Neumann, M., Herter, J., Droste, B.O., and Hartwig, S. 2011. Compressive behaviour of axially loaded spruce wood under large deformations at different strain rates. *European Journal of Wood and Wood Products*, **69**(3): 345-357.
- Ngo, T., Mendis, P., Gupta, A., and Ramsay, J. 2007. Blast loading and blast effects on structures—an overview. *Electronic Journal of Structural Engineering*, **7**(S1): 76-91.

- Parlin, N.J., Davids, W.G., Nagy, E., and Cummins, T. 2014. Dynamic response of lightweight wood-based flexible wall panels to blast and impulse loading. *Construction and Building Materials*, **50**: 237-245.
- Poulin, M., Viau, C., Lacroix, D.N., and Doudak, G. 2018. Experimental and analytical investigation of cross-laminated timber panels subjected to out-of-plane blast loads. *Journal of Structural Engineering*, **144**(2): 04017197.
- Royal Military College of Canada. 2015. Thesis Preparation Guidelines p. 20.
- Schmidt, R., and Pomeroy, J. 1990. Bending of a conifer branch at subfreezing temperatures: implications for snow interception. *Canadian Journal of Forest Research*, **20**(8): 1251-1253.
- Stefanovich, O. 2022. Canada looks to reinforce Arctic sovereignty through diplomacy, military, says minister. *In CBC News*
- Syron, W.D. 2010. Strain Rate-Dependent Behavior of Laminated Strand Lumber Department of Civil Engineering, University of Maine.
- Szmutku, M., Campean, M., and Porojan, M. 2013. Strength reduction of spruce wood through slow freezing. *European Journal of Wood and Wood Products*, **71**(2): 205-210.
- Ullah, A., Ahmad, F., Jang, H.-W., Kim, S.-W., and Hong, J.-W. 2017. Review of analytical and empirical estimations for incident blast pressure. *KSCE Journal of Civil Engineering*, **21**(6): 2211-2225.
- US Army Corps of Engineers. 2008. Structures to resist the effects of Accidental Explosions. United States Department of Defense UFC 3-340-02.
- US Army Corps of Engineers. 2018. PDC-TR 18-02: Analysis Guidance for Cross-Laminated Timber Construction Exposed to Airblast Loading. USACE Protective Design Center, Omaha, USA.
- Viau, C., and Doudak, G. Behaviour and retrofit options for light-frame wood stud walls subjected to blast loads. *In Proceedings of the 11th International Conference on Shock and Impact Loads on Structures*. Ottawa, CA, 14-15 May 2015 2015.
- Viau, C., and Doudak, G. Analytical modelling of heavy timber assemblies with realistic boundary conditions subjected to blast loading. *In Proc., CSCE 2019 Annual Conf.* Laval, QC, Canada: Canadian Society for Civil Engineering. 2019.
- Viau, C., and Doudak, G. 2021a. Behavior and Modeling of Glulam Beams with Bolted Connections Subjected to Shock Tube–Simulated Blast Loads. *Journal of Structural Engineering*, **147**(1): 04020305.
- Viau, C., and Doudak, G. 2021b. Dynamic analysis methods for modelling timber assemblies subjected to blast loading. *Engineering Structures*, **233**: 111945.

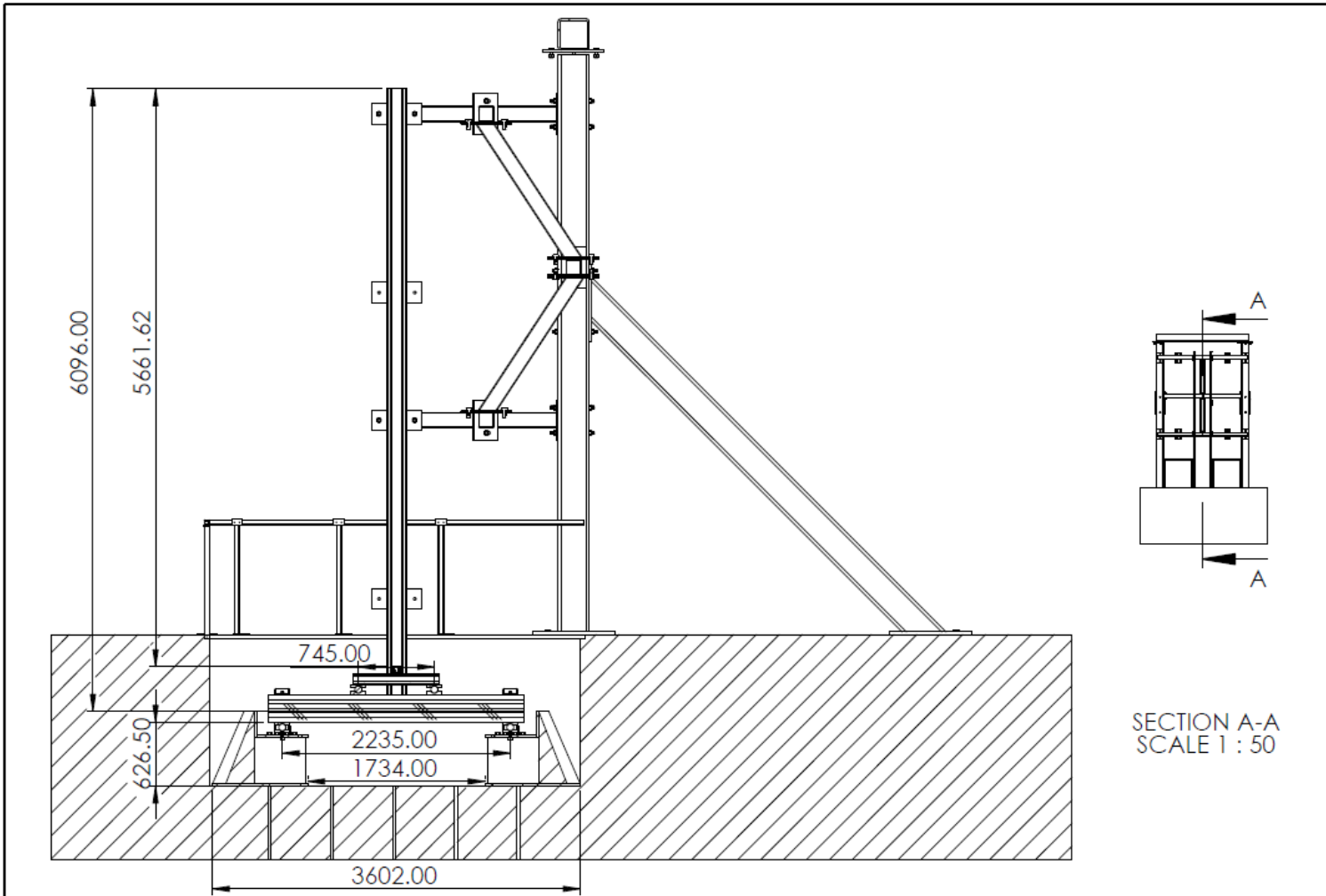
- Wang, X., Björnberg, J., Hagman, O., Ahmed, S.A., Wan, H., and Niemz, P. 2016. Effect of low temperatures on the block shear strength of norway spruce glulam joints. *BioResources*, **11**(4): 9638-9648.
- Weaver, M.K., Newberry, C.M., Podesto, L., and O’Laughlin, C. Blast testing of loaded cross-laminated timber structures. *In Structures Conference 2018: Blast, Impact Loading, and Response; and Research and Education*. 2018. American Society of Civil Engineers Reston, VA. pp. 400-411.
- Yang, R., Li, H., Dauletbek, A., Ashraf, M., Lorenzo, R., Sun, Y., and Wu, Y. 2021. Effects of Freeze-Thaw Cycles on Physical and Mechanical Properties of Glulam Exposed to Outdoor Environment. *Journal of Renewable Materials*, **9**(7): 1293.
- Zhao, L., Lu, J., Zhou, Y., and Jiang, J. 2015. Effect of low temperature cyclic treatments on modulus of elasticity of birch wood. *BioResources*, **10**(2): 2318-2327.



Appendices

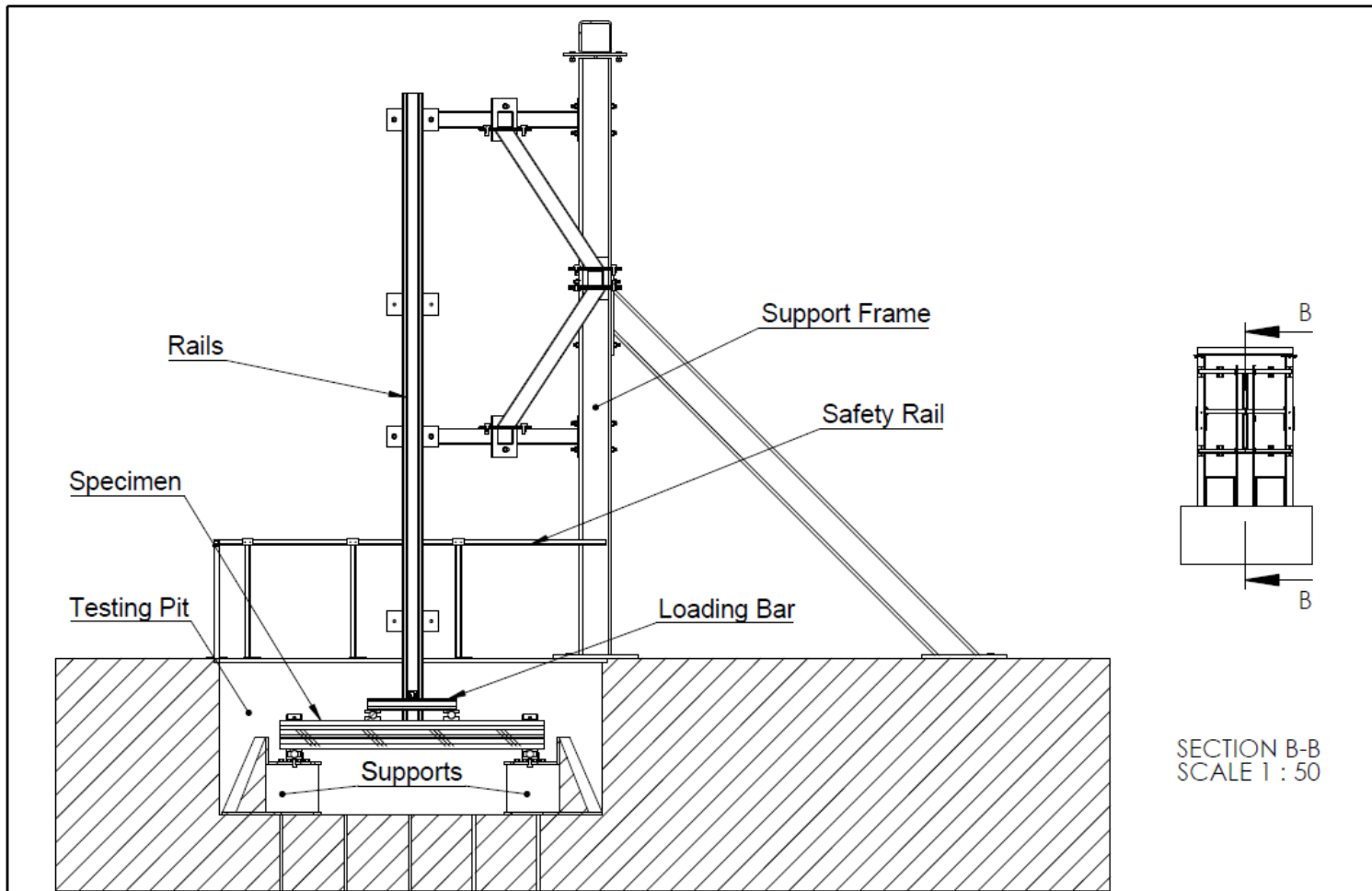
Appendix A: Detailed Drawing of Impact Hammer

This appendix contains drawings of the impact hammer and the associated supports and loading system that were used.


Drop-Hammer Overall View




MATERIAL MATIÈRE	WEIGHT MASSE	 RMCC ENGINEERING FACULTY CMRC FACULTÉ D'INGÉNIÉRIE	 SCALE ÉCHELLE 1:20 0	Drop Hammer Experimental Set-up		NUMBER NUMÉRO 2022	DWG. # / DESIGN# 001		
CREATED DATE DATE DE CRÉATION				NAME NOM	Capt. N. Wight			SHEET PAGE 1 OF 2	
REVISED MODIFIÉ				FILE NAME NOM FICHIER					
DRAWN DRESSÉ									



MATERIAL MATIÈRE	WEIGHT POIDS
CREATED DATE DATE DE CRÉATION	
SAVED SAUVÉGARDE	
FOLDER DOSSIER	

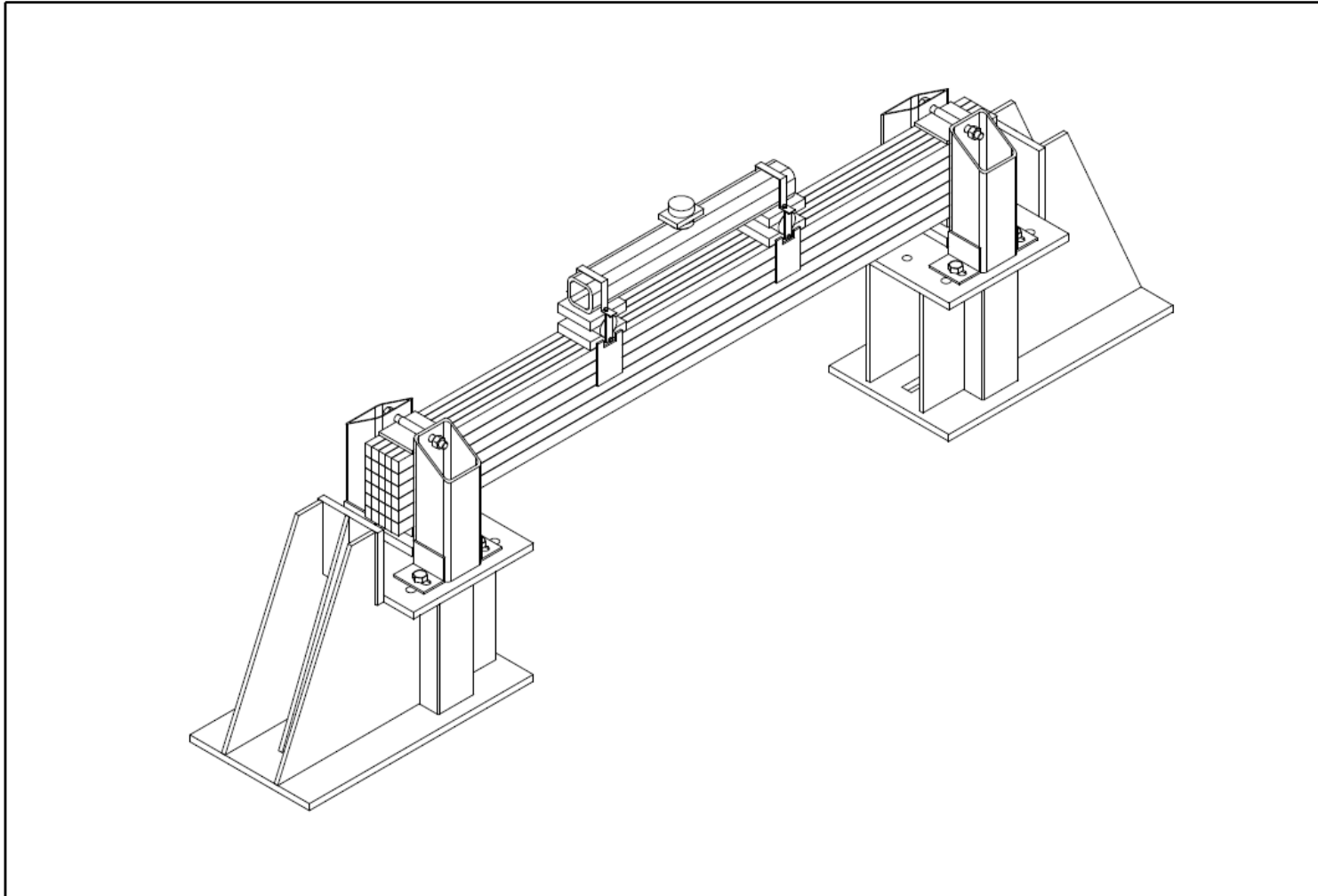

**RMCC
ENGINEERING
FACULTY**
 CMRC
**FACULTÉ
D'INGÉNIERIE**




 SCALE
 ÉCHELLE 1:20
 0

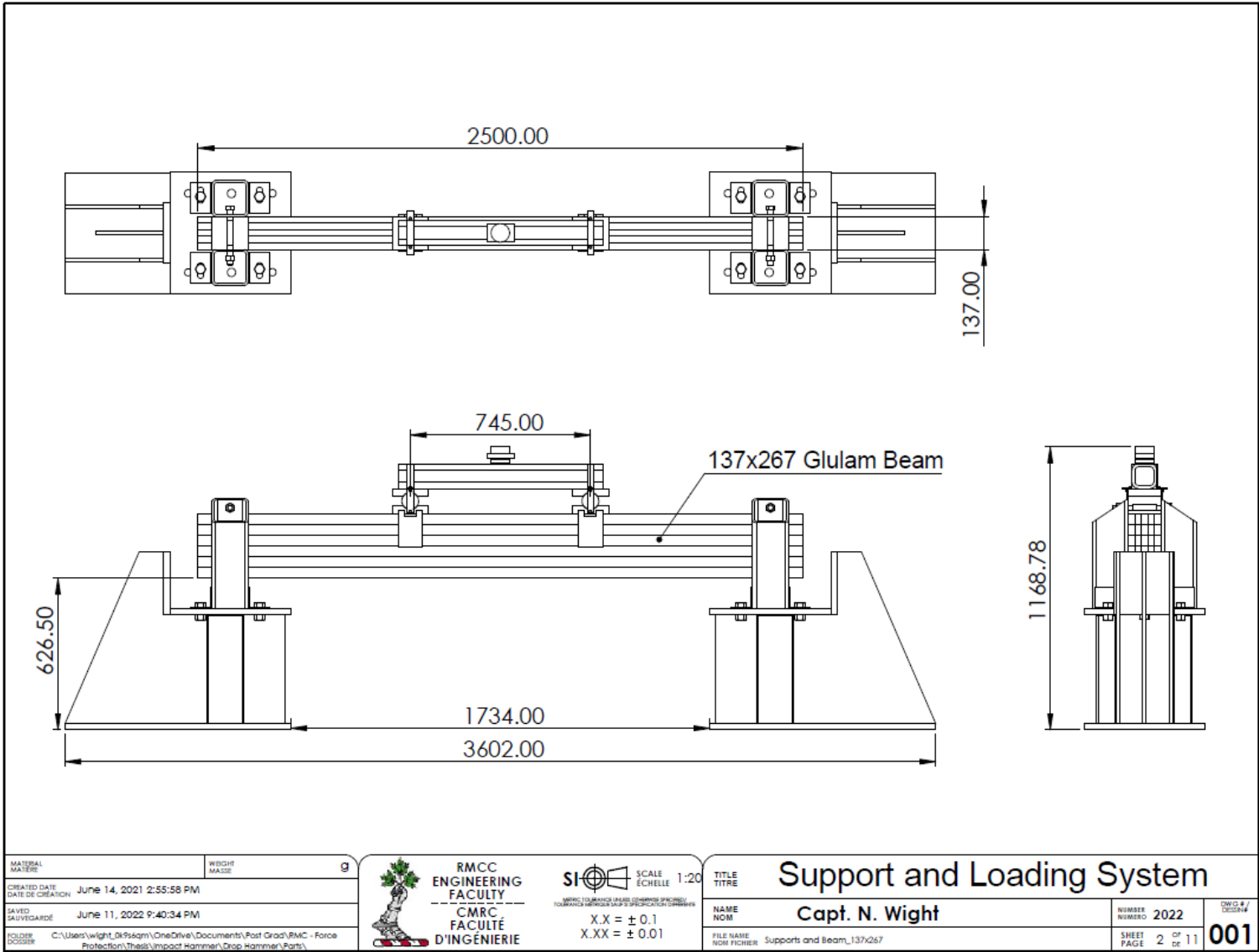
X.X = ± 0.1
 X.XX = ± 0.01

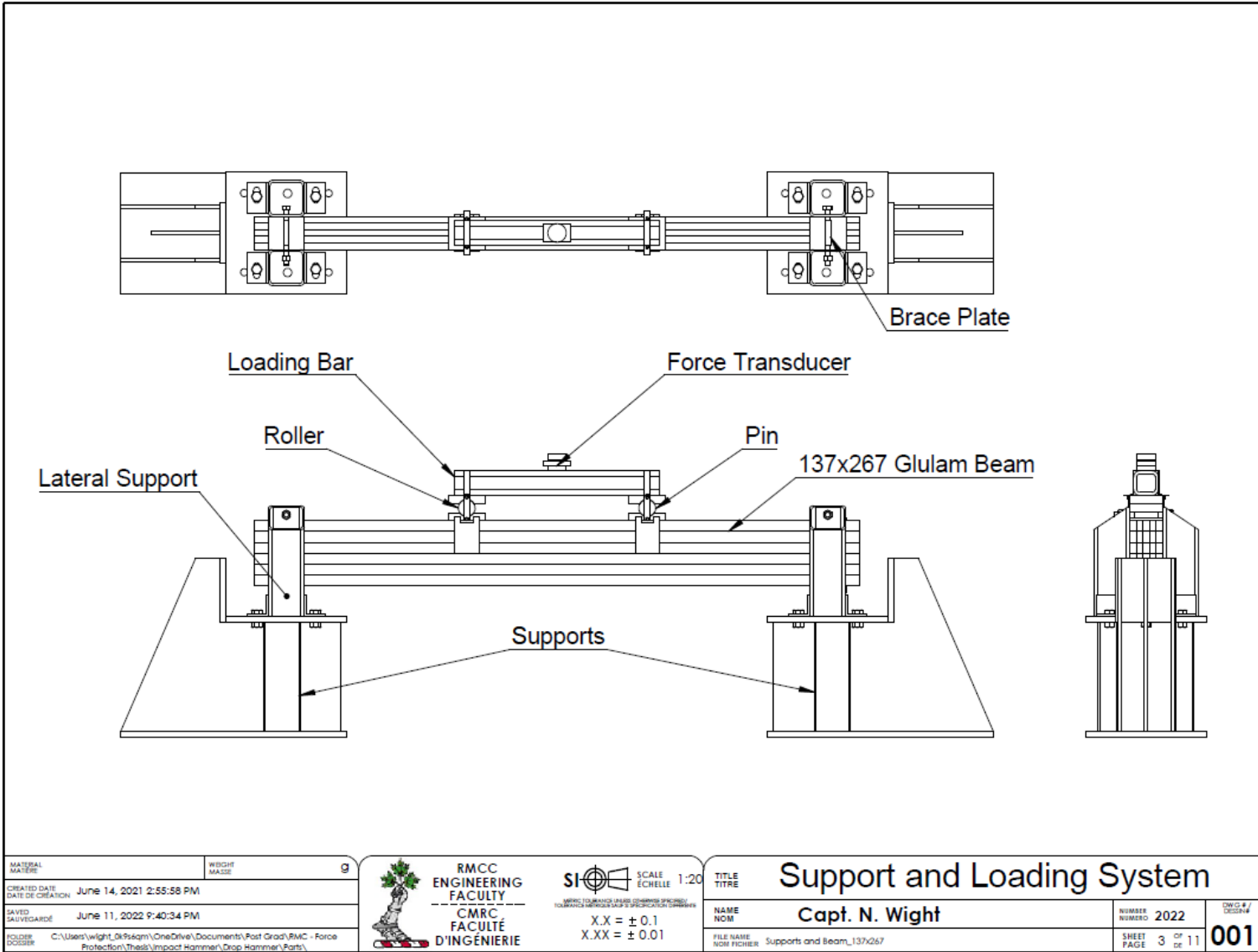
Drop Hammer Experimental Set-up		
TITLE TITRE	NAME NOM Capt. N. Wight	NUMBER NUMÉRO 2022
FILE NAME NOM FICHIER	SHEET PAGE 2 OF 2	001

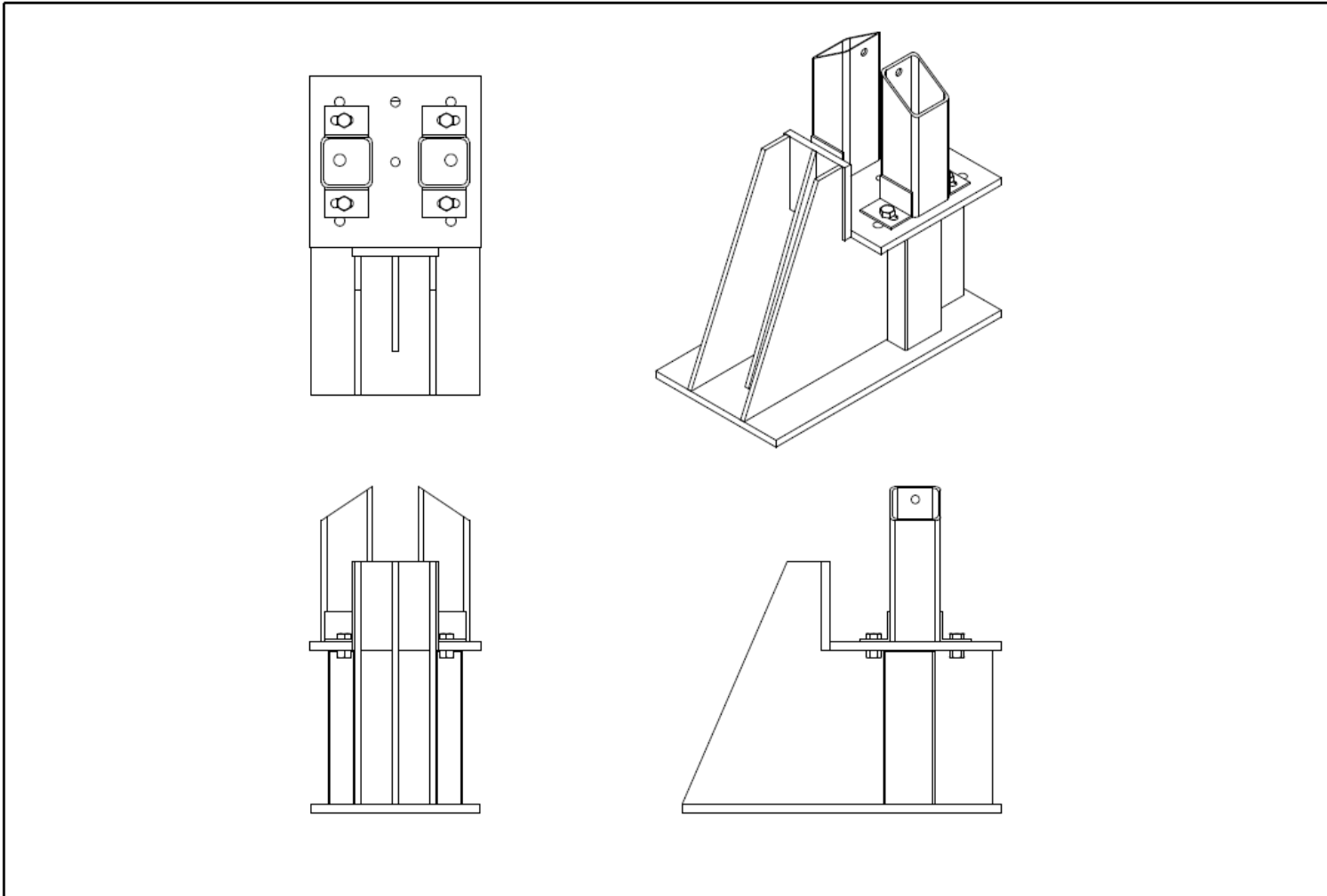
Support and Loading System





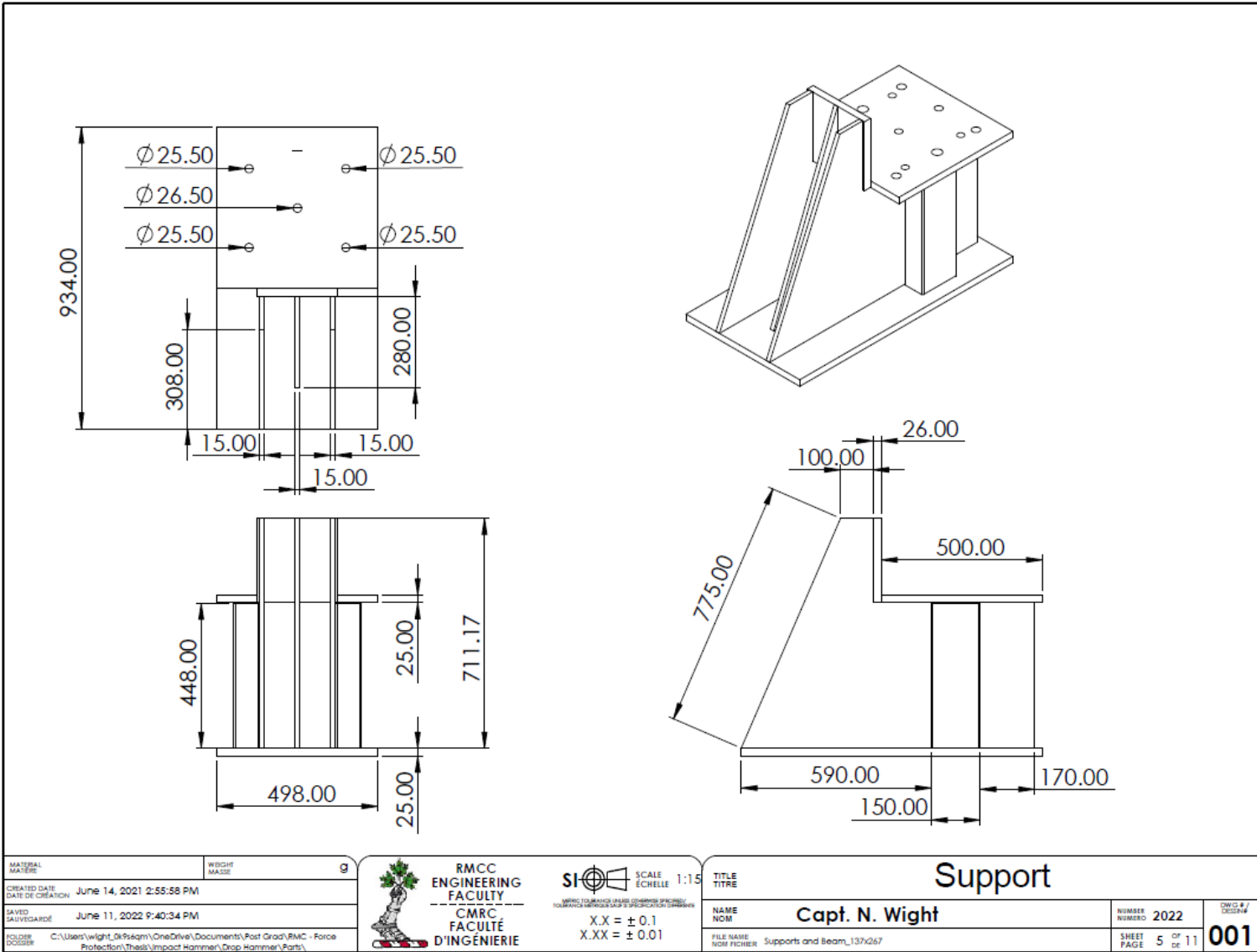
MATERIAL MATIÈRE	WEIGHT MASSE	 RMCC ENGINEERING FACULTY CMRC FACULTÉ D'INGÉNIÉRIE	 SCALE ÉCHELLE 1:1 <small>UNITS TO BE USED (UNITS À UTILISER)</small> X.X = ± 0.1 X.XX = ± 0.01	Support and Loading System		NUMBER NUMÉRO	2022	DWG # / Dessin # 001
CREATED DATE DATE DE CRÉATION	June 14, 2021 2:55:58 PM			NAME NOM	Capt. N. Wight		SHEET PAGE	
SAVED SAUVÉGARDE	June 11, 2022 9:40:34 PM	FILE NAME NOM FICHIER	Supports and Beam_1379267					
HOLDER DOSSIER	C:\Users\wight_n\OneDrive\Documents\Fost Grad\RMCC - Force Protection\Thesis\Impact Hammer\Drop Hammer\Parts\							

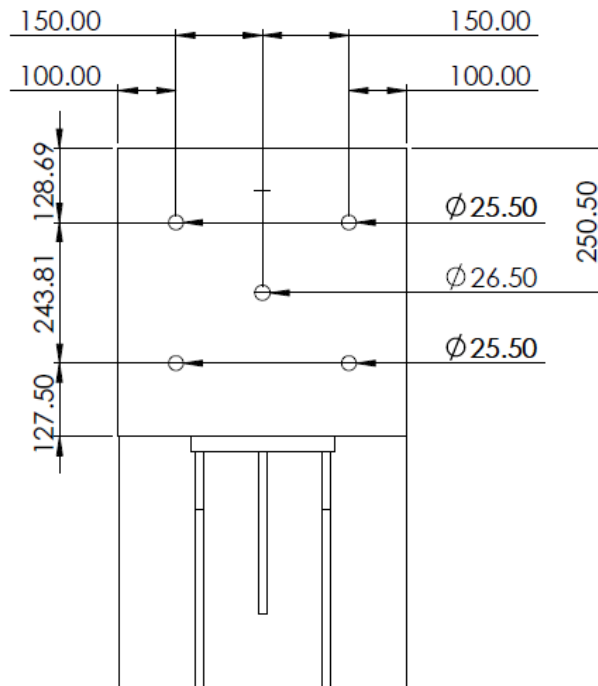




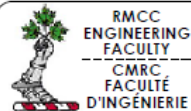


MATERIAL MATIÈRE	WEIGHT MASSE	g	 RMCC ENGINEERING FACULTY CMRC FACULTÉ D'INGÉNIÉRIE	 SCALE ÉCHELLE 1:15 <small>RMCC IS MANUFACTURED TO THE DIMENSIONS SPECIFIED FOR MANUFACTURING PURPOSES AND IS NOT TO BE USED FOR OTHER PURPOSES</small> X.X = ± 0.1 X.XX = ± 0.01	Support TITLE TITRE		NUMBER NUMÉRO 2022	DWG.# DESIGN#
CREATED DATE DATE DE CRÉATION June 14, 2021 2:55:58 PM SAVED SAUVÉGARDE June 11, 2022 9:40:34 PM FOLDER DOSSIER C:\Users\wight_0k\fsqm\OneDrive\Documents\Post Grad\RMCC - Force Protection\Thesis\Impact Hammer\Drop Hammer\Parts\	NAME NOM Capt. N. Wight				SHEET PAGE 4 of 11	001		



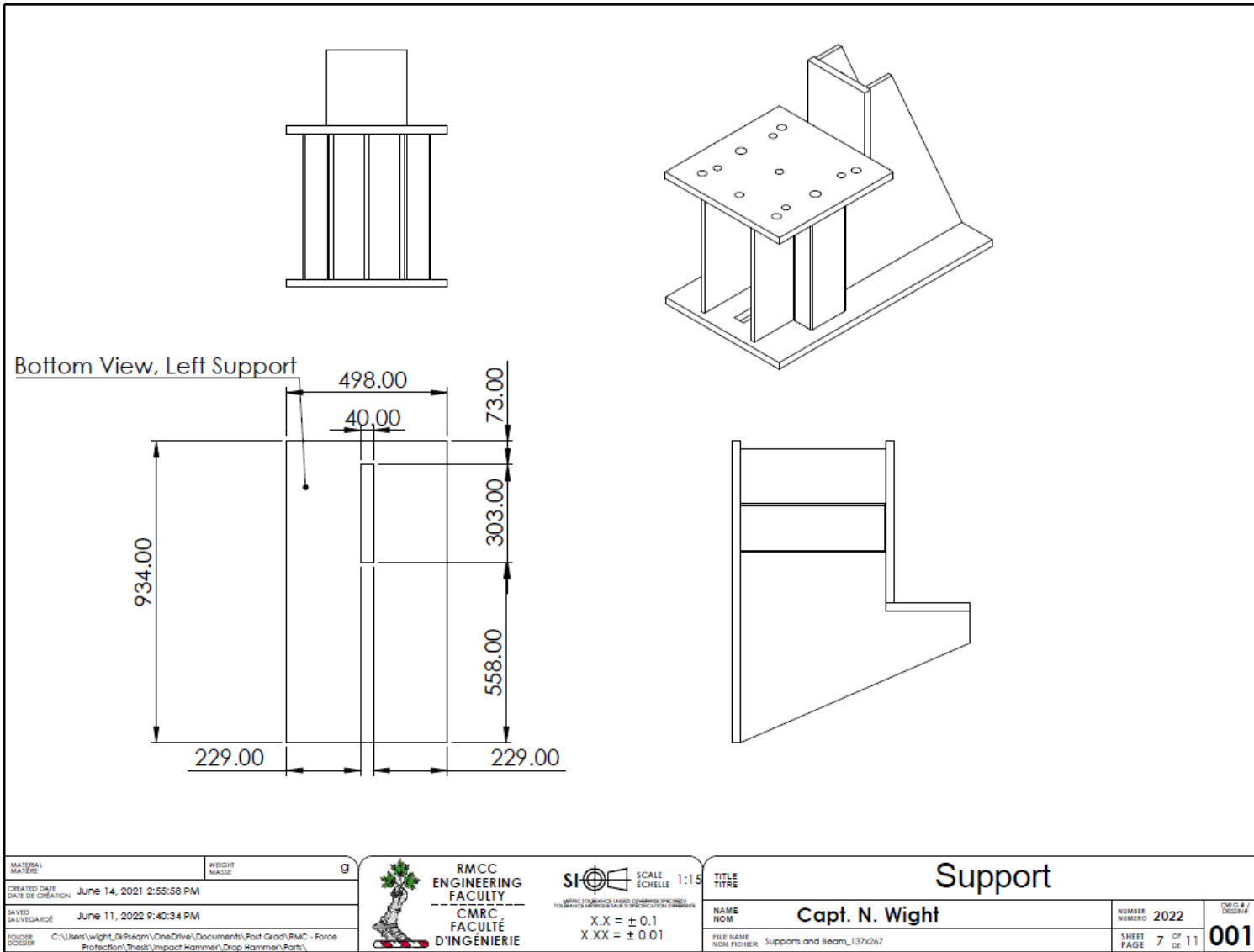


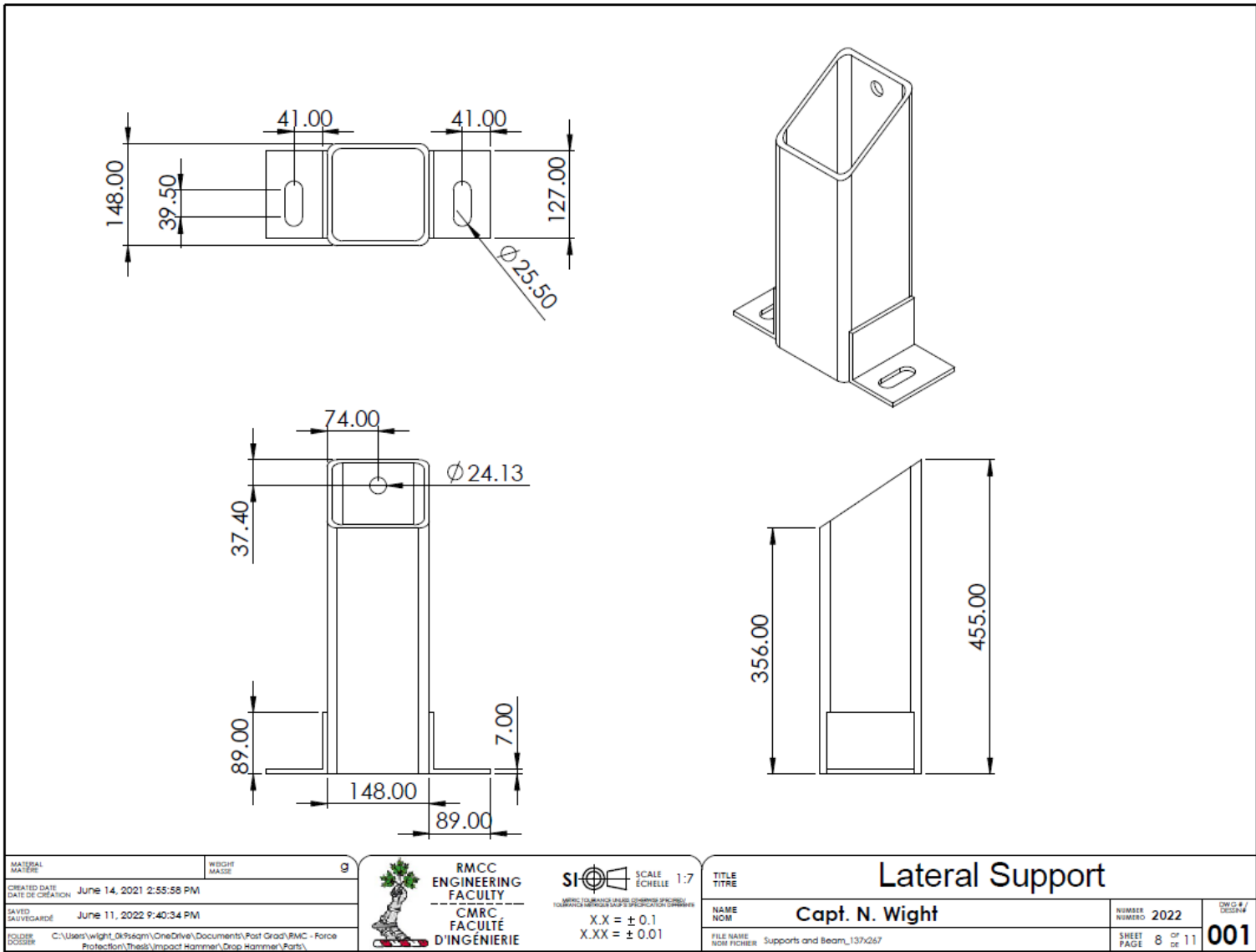
MATERIAL MATÉRIE	WEIGHT MASSE	9
CREATED DATE DATE DE CRÉATION	June 14, 2021 2:55:58 PM	
SAVED SAUVÉGARDE	June 11, 2022 9:40:34 PM	
FOUNDER FONDEUR	C:\Users\wight_dp9sqm\OneDrive\Documents\Fost Grad\BMC - Force Protection\Thesis\Impact Hammer\Crap Hammer\Parts\	

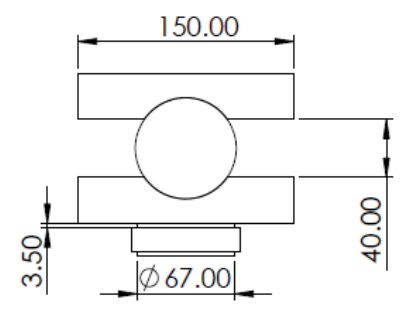
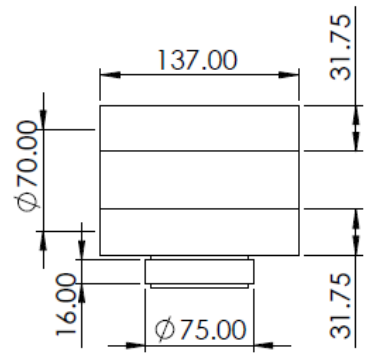
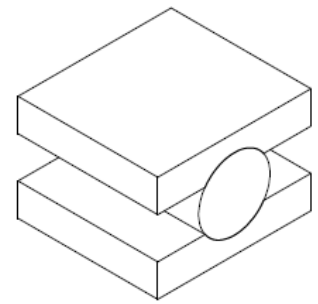
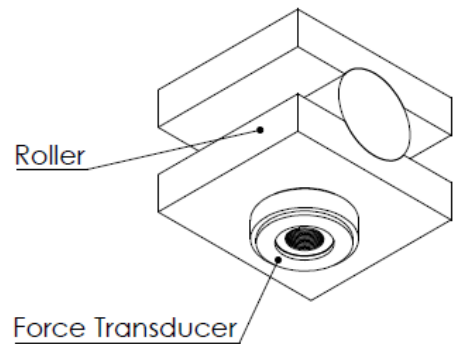


SI SCALE
ÉCHELLE 1:10
MÉTRES (SI) MILLIMÈTRES (SI) POUCES (SI) INCHES (SI)
MILLIMÈTRES (SI) POUCES (SI) MILLIMÈTRES (SI) POUCES (SI)
X.X = ± 0.1
X.XX = ± 0.01

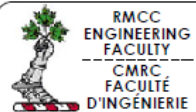
TITLE TITRE	Support		
NAME NOM	Capt. N. Wight	NUMBER NUMÉRO	2022
FILE NAME NOM FICHIER	Supports and Beam_137x267	SHEET PAGE	6 of 11
			001







MATERIAL MATIÈRE	WEIGHT MASSE	g
CREATED DATE DATE DE CRÉATION	June 14, 2021 2:55:58 PM	
SAVED SAUVÉGARDE	June 11, 2022 9:40:34 PM	
CAD FILE DOSSIER	C:\Users\wight_nk\OneDrive\Documents\Fost Grad\RMCC - Force Protection Thesis\Impact Hammer\Drop Hammer\Parts	

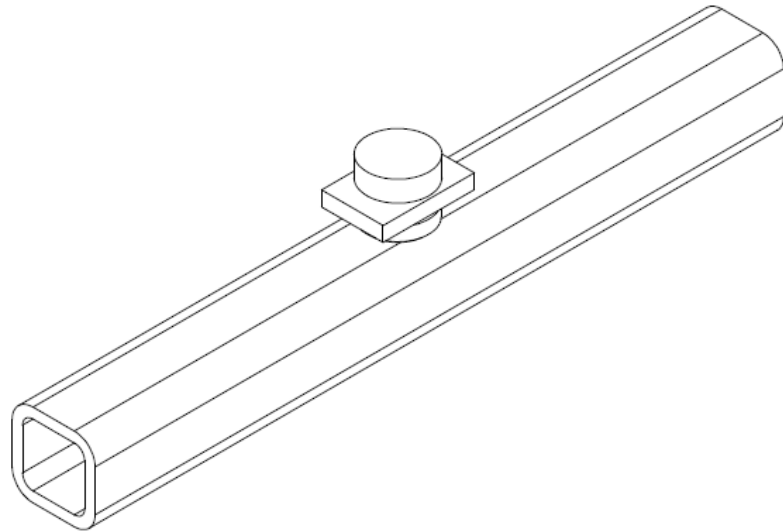


SI SCALE
ÉCHELLE 1:4

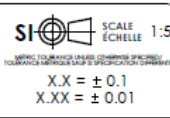
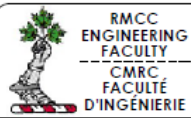
UNITS TO BE USED IN THIS DRAWING (SI UNITS)
LES UNITÉS À UTILISER DANS CE DOCUMENT (UNITS SI)

X.X = ± 0.1
X.XX = ± 0.01

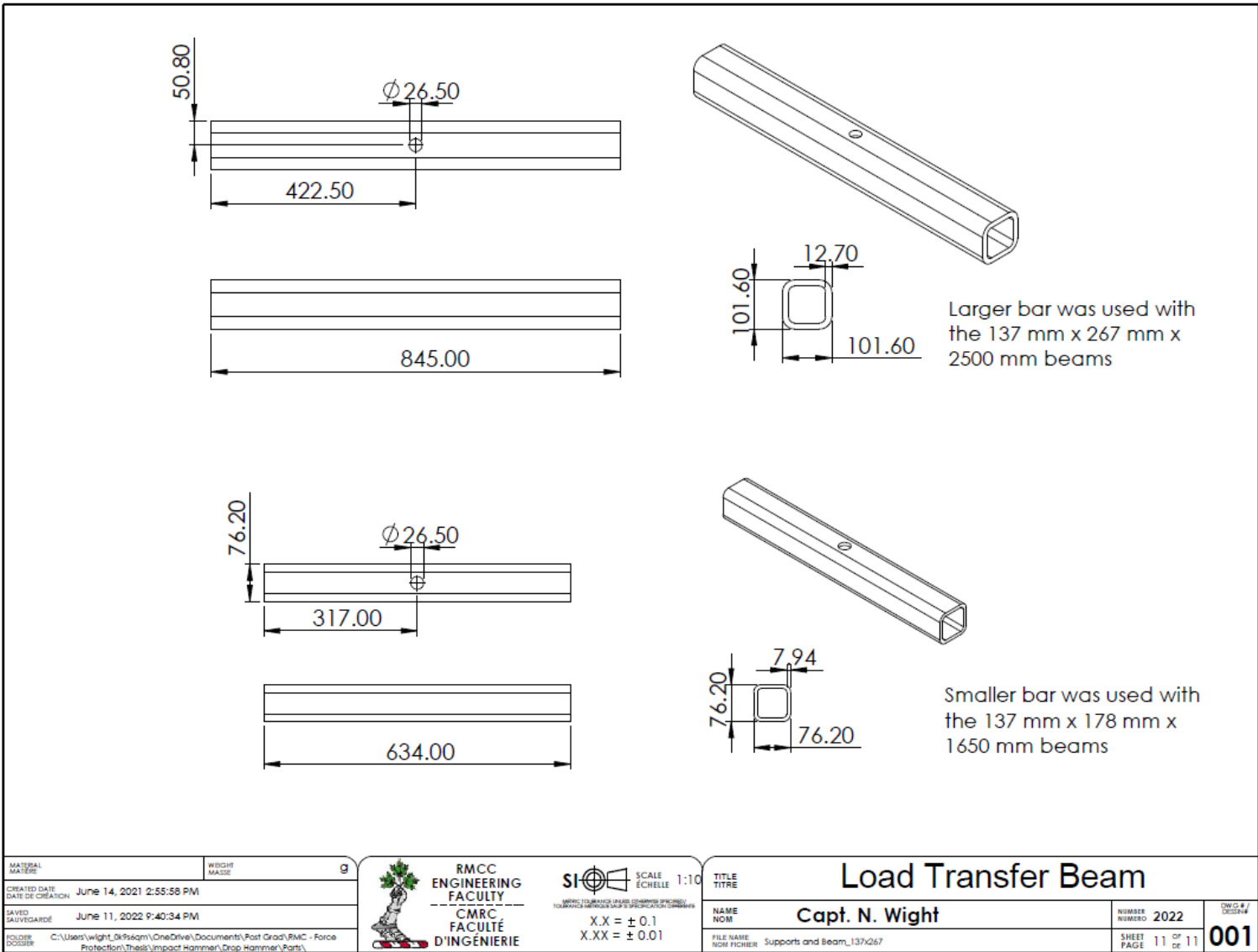
TITLE TITRE	Roller and Force Transducer	
NAME NOM	Capt. N. Wight	NUMBER NUMÉRO 2022
FILE NAME NOM FICHIER	Supports and Beam_137Q267	SHEET PAGE 9 of 11
		001



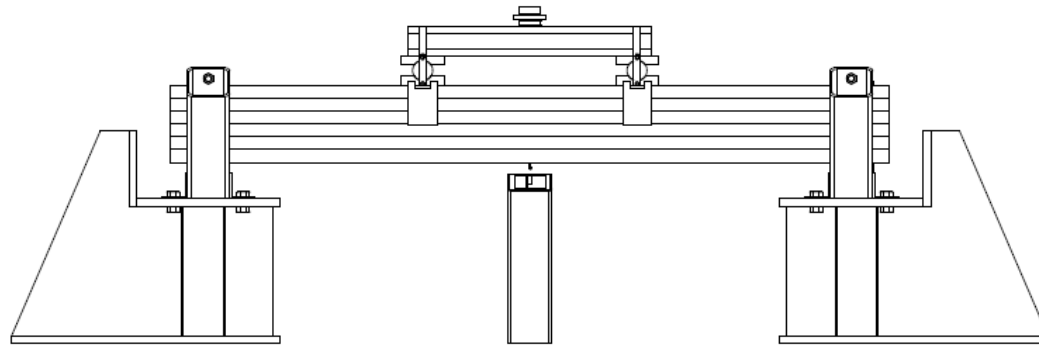
MATERIAL MATIÈRE	WEIGHT MASSE	9
CREATED DATE DATE DE CRÉATION	June 14, 2021 2:55:58 PM	
SAVED SAUVÉGARDE	June 11, 2022 9:40:34 PM	
FOLDER DOSSIER	C:\Users\wight_0k7\Documents\OneDrive\Documents\Post Grad\RMCC - Force Protection\Thesis\Impact Hammer\Drop Hammer\Parts\	



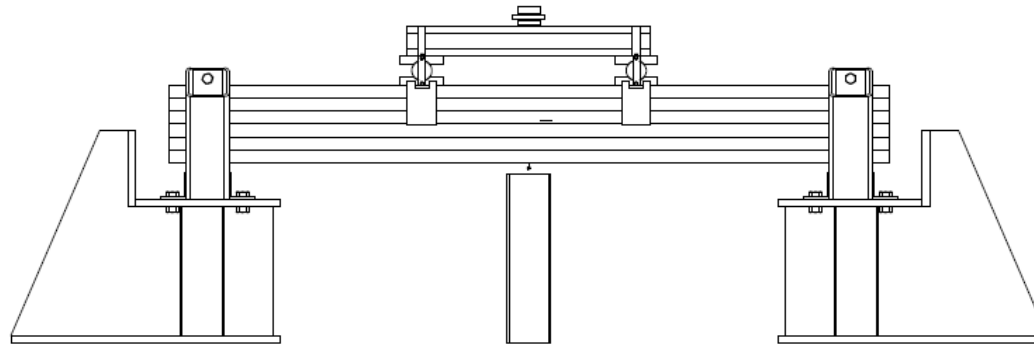
TITLE TITRE	Loading Beam & Force Transducer		
NAME NOM	Capt. N. Wight		DWG.# DESIGN#
FILE NAME NOM FICHIER	Supports and Beam_137x267	NUMBER NUMÉRO	2022
		SHEET PAGE	10 of 11
			001





Instrumentation

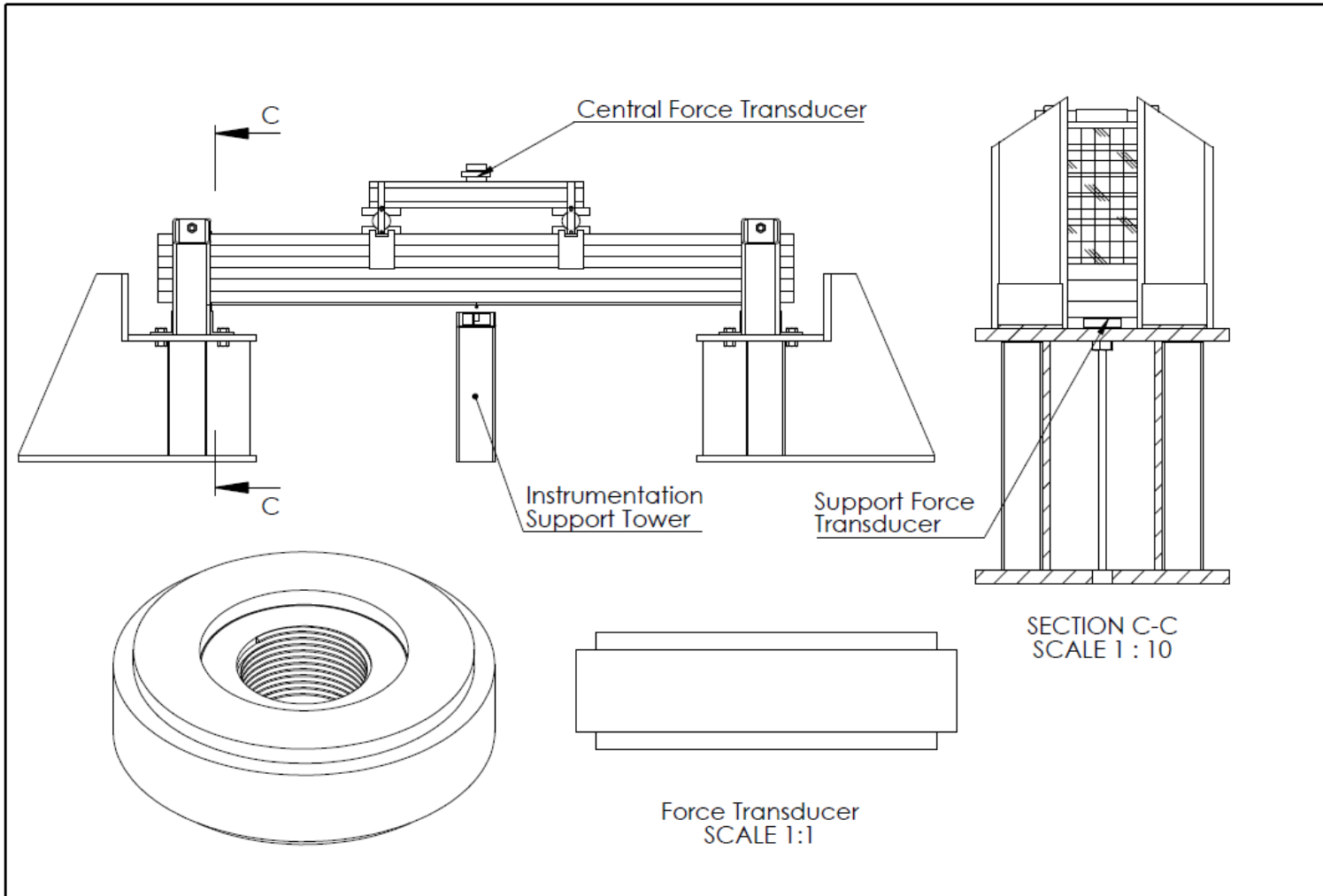


North Facing Side of Beam

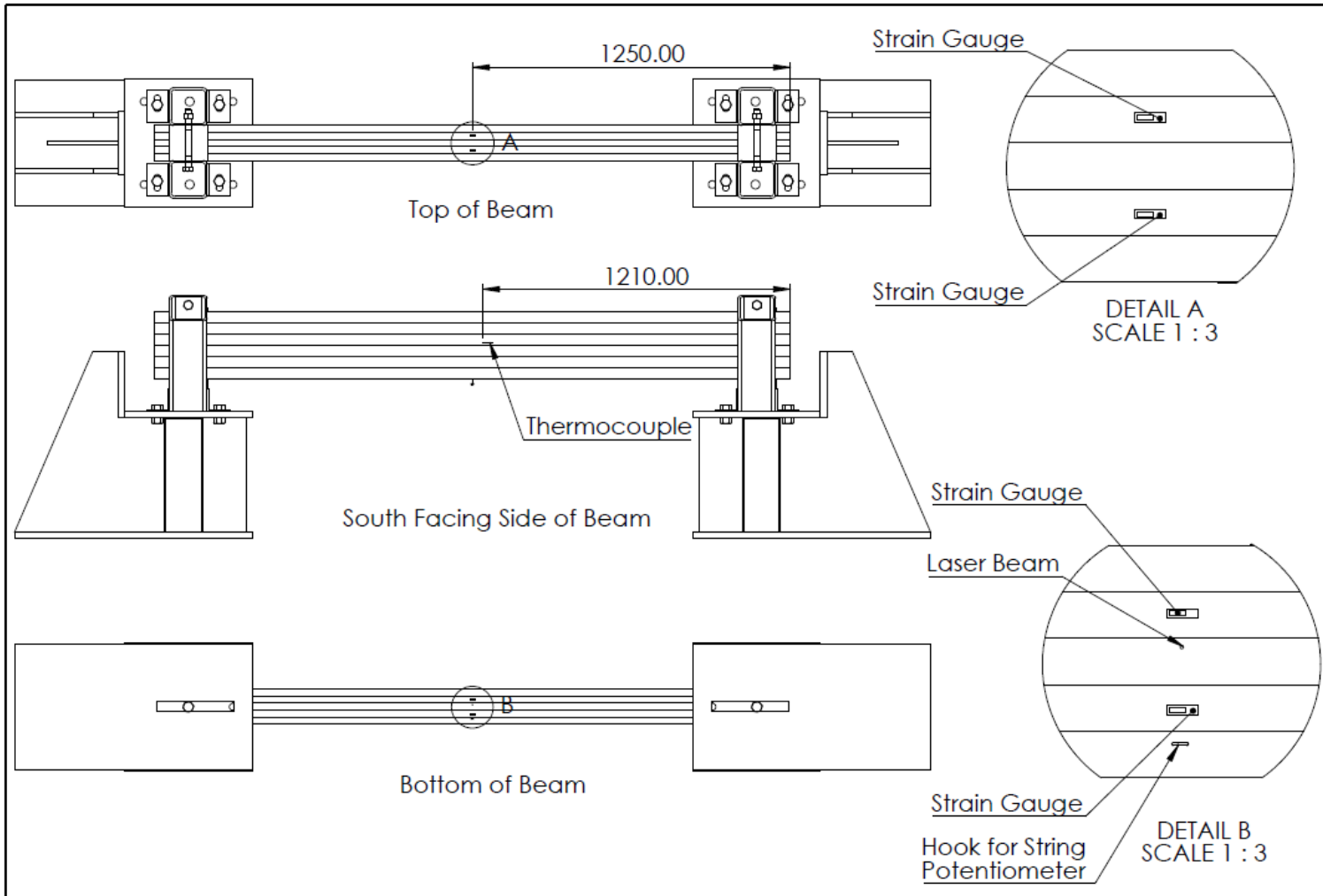




South Facing Side of Beam

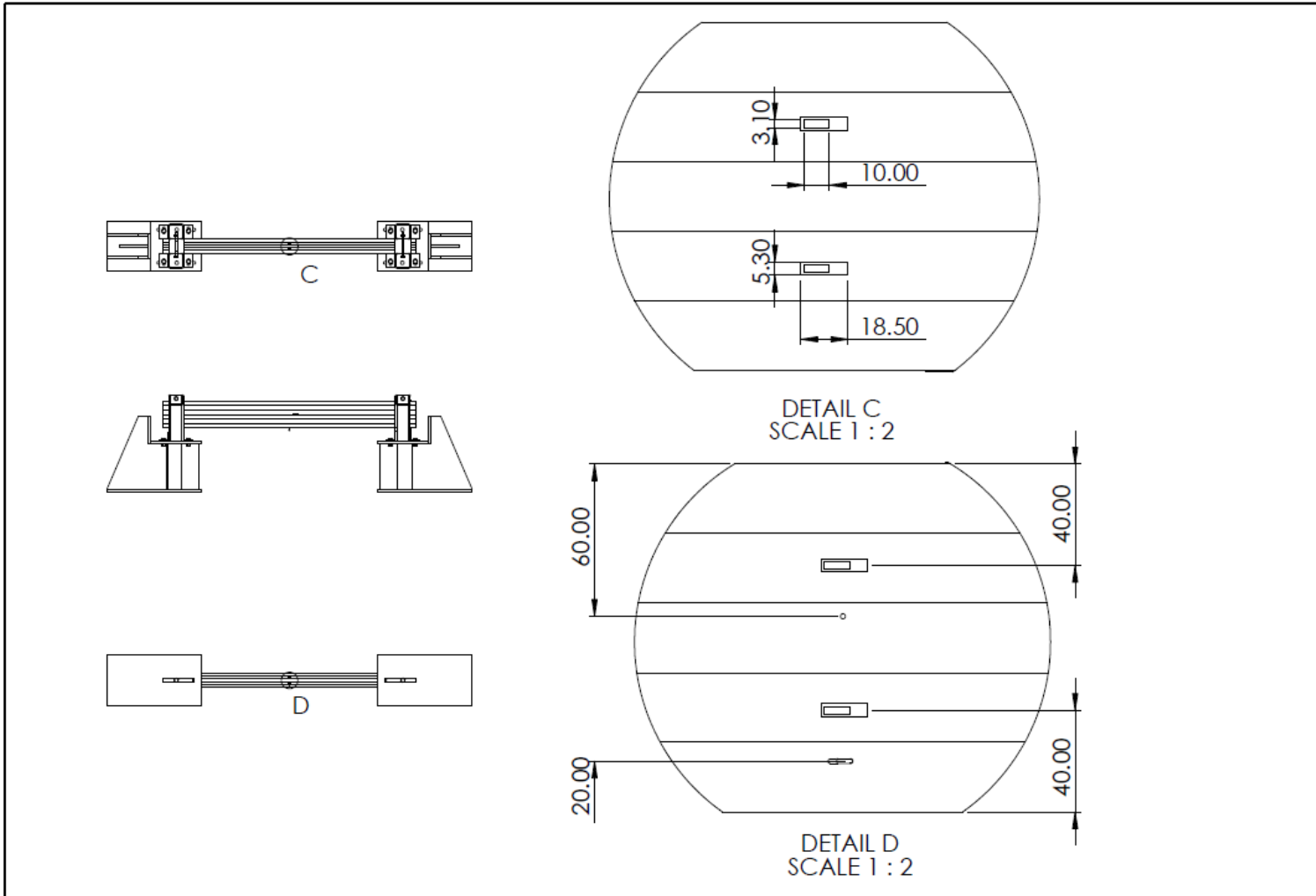
MATERIAL MATIÈRE	WEIGHT MASSE	 RMCC ENGINEERING FACULTY CMRC FACULTÉ D'INGÉNÉRIE	 SCALE ÉCHELLE 1:20 <small>NOTE TO MANUFACTURER: DIMENSIONS SPECIFIED TO UNLESS OTHERWISE NOTED IN APPLICATION SPECIFICATIONS</small> X.X = ± 0.1 X.XX = ± 0.01	Instrumentation		NUMBER NUMÉRO 2022	DWG # / DESIGN#
CREATED DATE DATE DE CRÉATION June 14, 2021 2:55:58 PM				NAME NOM Capt. N. Wight	SHEET PAGE 1 of 4	001	
SAVED SAUVÉGARDE June 11, 2022 9:36:24 PM			FILE NAME NOM FICHIER Instrumentation_137x267				
HOLDER POSEUR C:\Users\wight_n\OneDrive\Documents\Post Grad\RMCC - Force Protection\Thesis\Impact Hammer\Drop Hammer\Parts							





MATERIAL MATIÈRE	WEIGHT MASSE	9	<p>RMCC ENGINEERING FACULTY CMRC FACULTÉ D'INGÉNIÉRIE</p>	<p>SCALE ÉCHELLE 1:20</p> <p>XXXX ± 0.1 X.XX ± 0.01</p>	<p>TITLE TITRE</p> <h2 style="text-align: center;">Instrumentation</h2>		NUMBER NUMÉRO	2022	DWG.# / DESIGN#
CREATED DATE DATE DE CRÉATION	June 14, 2021 2:55:58 PM				NAME NOM	Capt. N. Wight		SHEET PAGE	2 OF 4
SAVED SAUVÉGARDE	June 11, 2022 9:36:24 PM		FILE NAME NOM FICHIER	Instrumentation_137x267					
FOLDER DOSSIER	C:\Users\wight_0k\OneDrive\Documents\Post Grad\RMCC - Force Protection\The\Impact Hammer\Drop Hammer\Parts\								



MATERIAL MATERIE	WEIGHT MASSE	 RMCC ENGINEERING FACULTY CMRC FACULTÉ D'INGÉNIÉRIE	 SCALE ÉCHELLE 1:20 <small>NUMERIC DIMENSIONS UNLESS OTHERWISE SPECIFIED TO BE IN SI UNITS (MM OR M) UNLESS OTHERWISE SPECIFIED</small> X.X = ± 0.1 X.XX = ± 0.01	Instrumentation		NUMBER NUMERO 2022 SHEET PAGE 3 of 4 001	
CREATED DATE DATE DE CREATION	June 14, 2021 2:55:58 PM			NAME NOM	Capt. N. Wight		
SAVED SAUVÉGARDE	June 11, 2022 9:36:24 PM			FILE NAME NOM FICHIER	Instrumentation_137x267		
FOLDER DOSSIER	C:\Users\wight_0k9aqm\OneDrive\Documents\Post Grad\RMCC - Force Protection\Thesis\Impact Hammer\Drop Hammer\Parts\						



MATERIAL MATIÈRE	WEIGHT MASSE	g	 SCALE ÉCHELLE 1:20 <small>UNITS TO BE INDICATED IN ALL DIMENSIONS UNLESS SPECIFIED OTHERWISE</small> X.X = ± 0.1 X.XX = ± 0.01	Instrumentation		NUMBER NUMÉRO	2022	DWG.# DESIGN#
CREATED DATE DATE DE CRÉATION	June 14, 2021 2:55:58 PM			NAME NOM	Capt. N. Wight		SHEET PAGE	4 of 4
SAVED SAUVÉGARDE	June 11, 2022 9:36:24 PM		FILE NAME NOM FICHIER	Instrumentation_137x267				
COLORS COULEUR	C:\Users\wight_nk\pqsqm\OneDrive\Documents\Fost Grad\RMCC - Force Protection\Thesis\Impact Hammer\Grap Hammer Parts		 RMCC ENGINEERING FACULTY CMRC FACULTÉ D'INGÉNIÉRIE					

Appendix B: Test Results of Glulam Specimens

This appendix contains the experimental dynamic results of all tests conducted on glulam specimens. Typical data presented in the appendix includes a brief synopsis of each test, as well as relevant test results and photographs taken after testing.

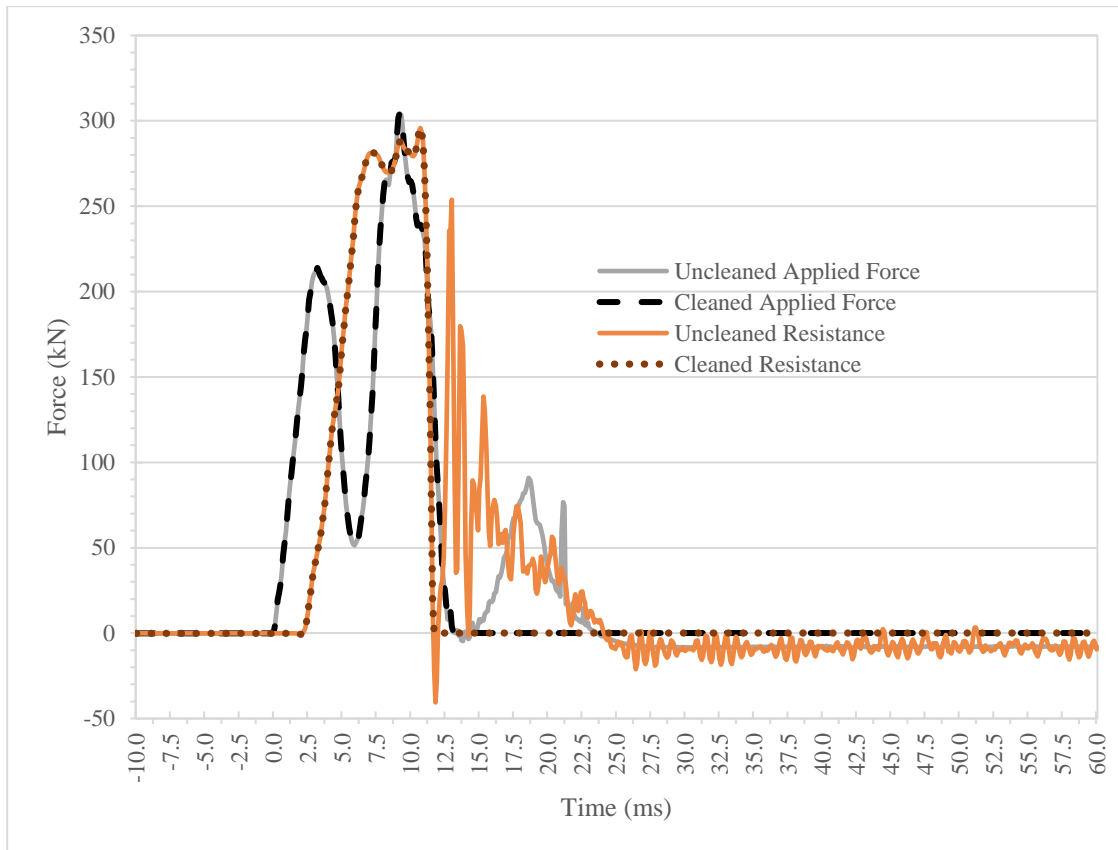
Specimen: DNP1-267

Peak Force: 304.3 kN

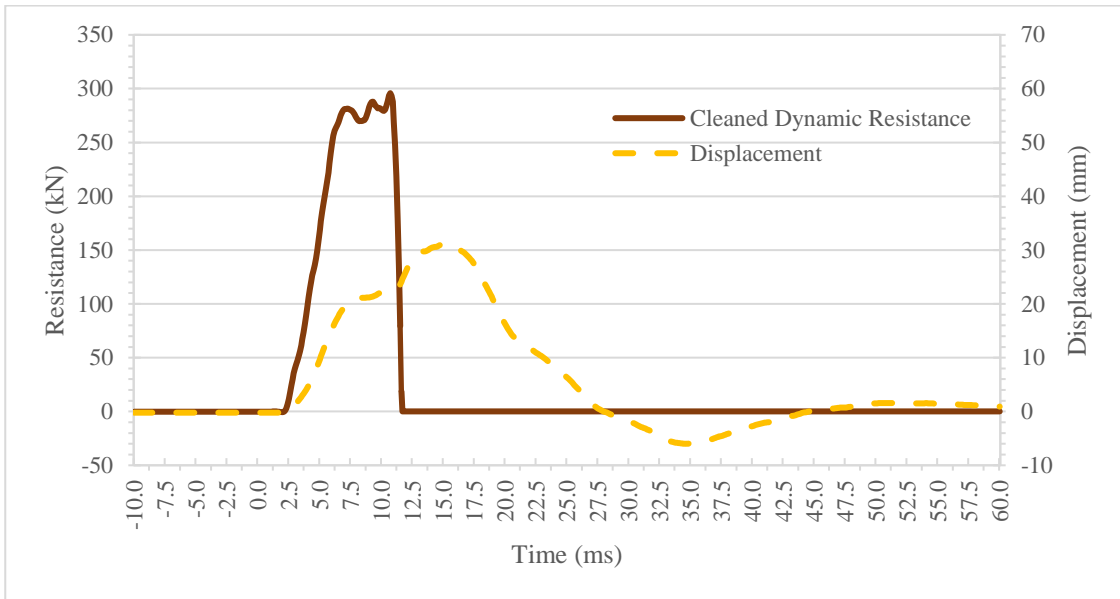
Load Duration: 13.3 ms

Peak Resistance: 295.0 kN

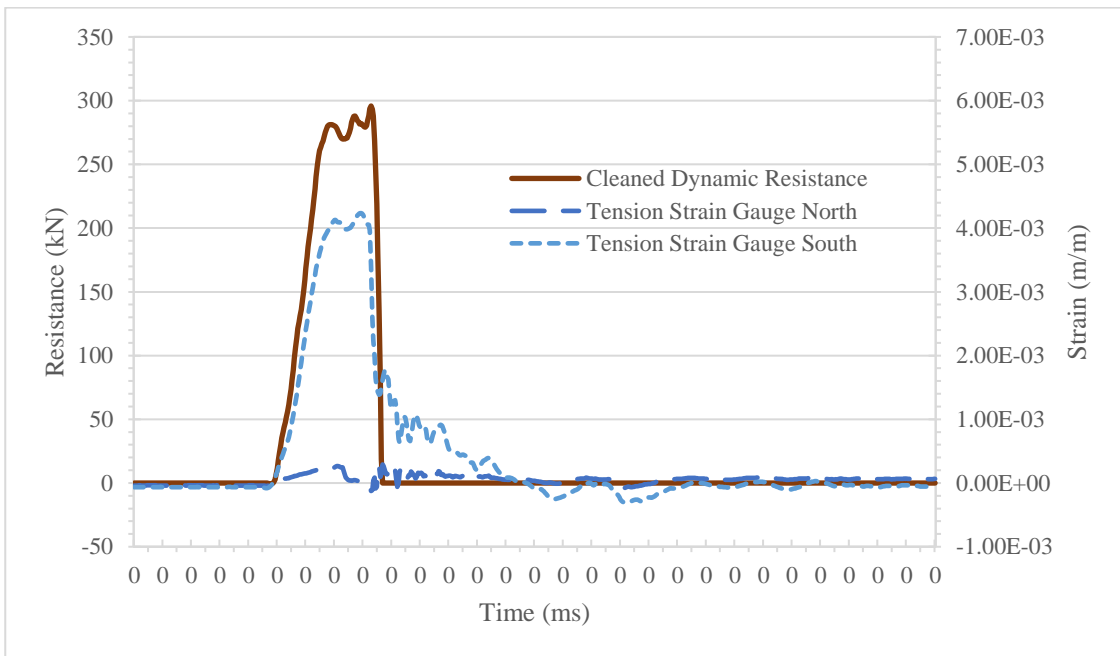
Failure Mode: Flexure



(a) Cleaned and uncleaned applied load and dynamic resistance over time



(b) Dynamic resistance and displacement over time

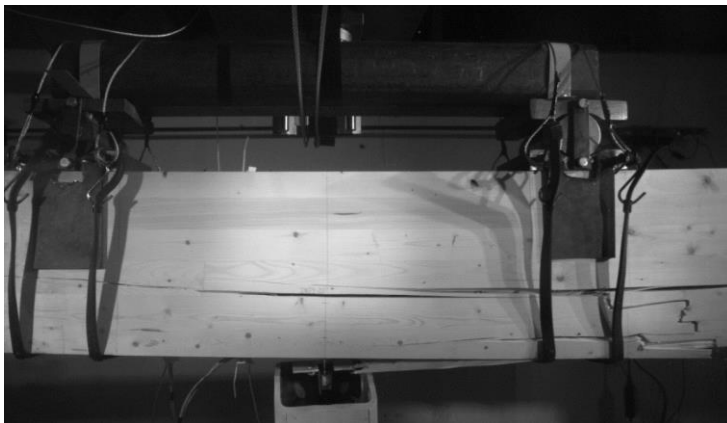


(c) Dynamic resistance and tensile strain over time

Figure B-0-1: Dynamic Test Results for Specimen DN1-267



(a) Specimen after testing



(b) Footage from the high-speed phantom camera of specimen at its maximum deflection



(c) Underside of specimen after failure

Figure B-0-2: Damage for Specimen DNP1-267

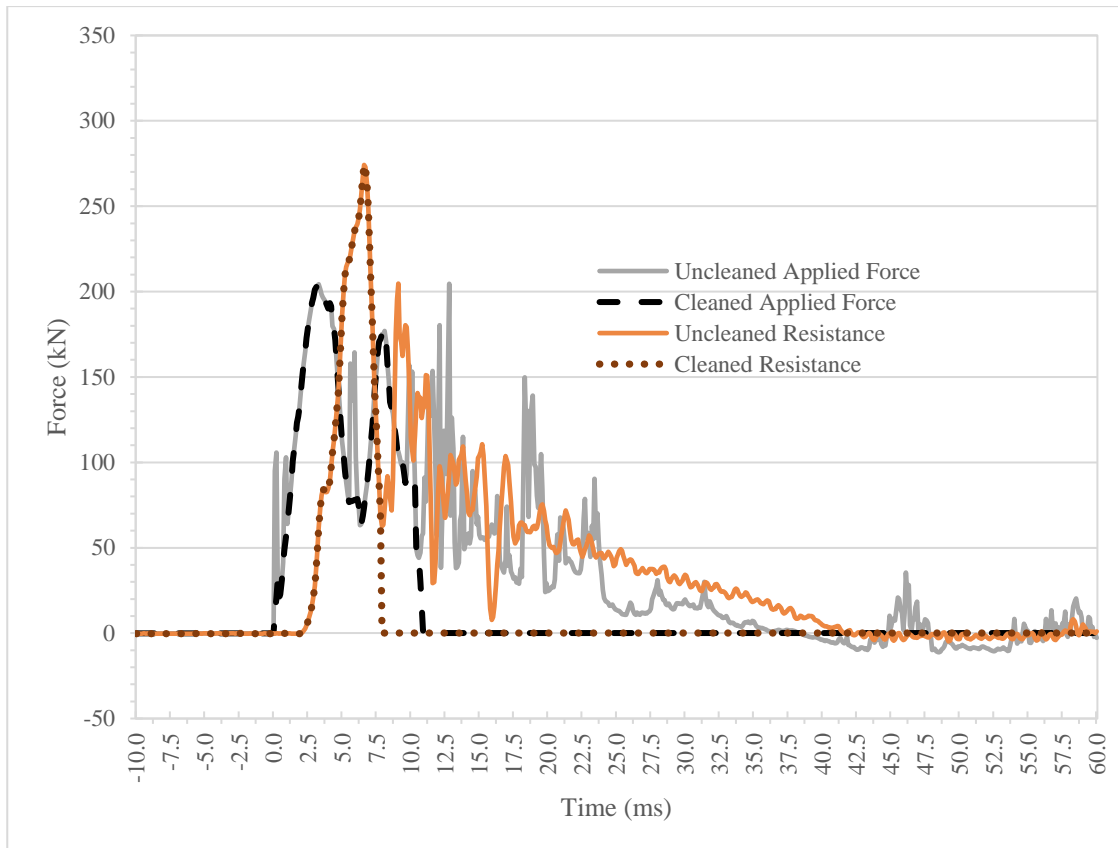
Specimen: DN1-267

Peak Force: 204.3 kN

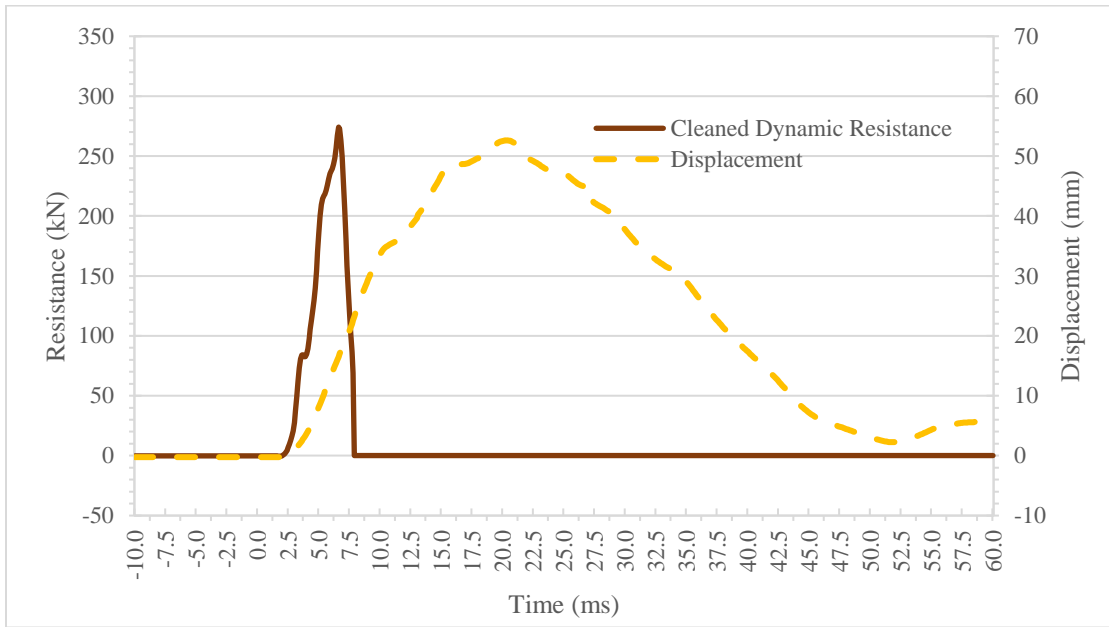
Load Duration: 11.0 ms

Peak Resistance: 271.2 kN

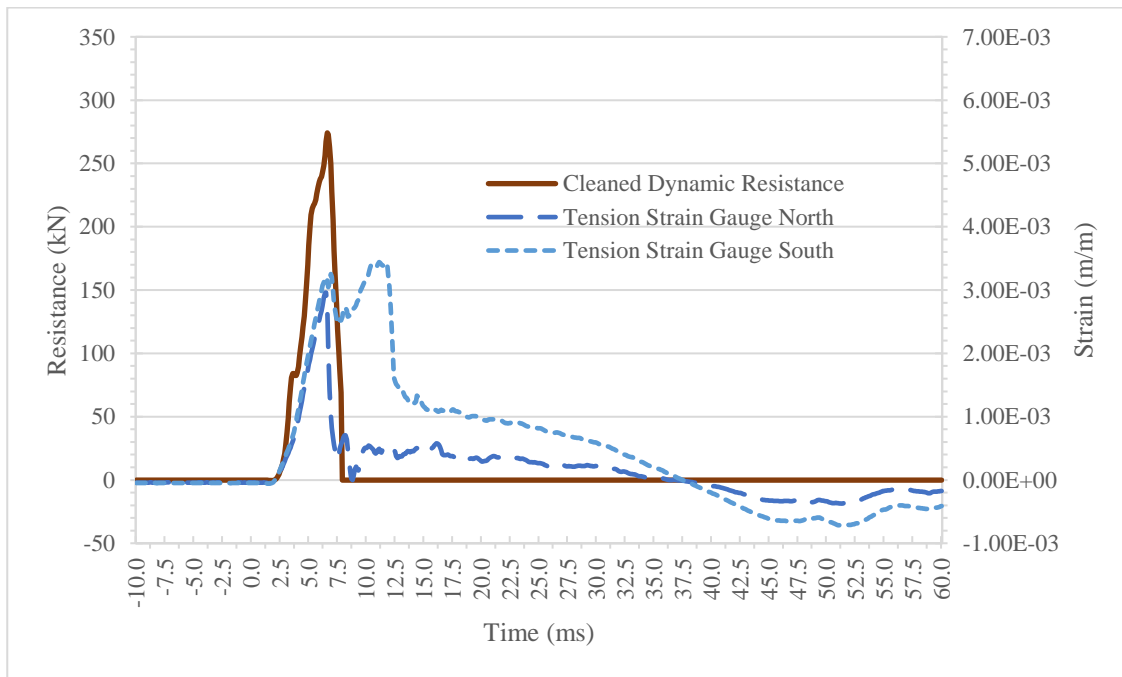
Failure Mode: Flexure



(a) Cleaned and uncleaned applied load and dynamic resistance over time

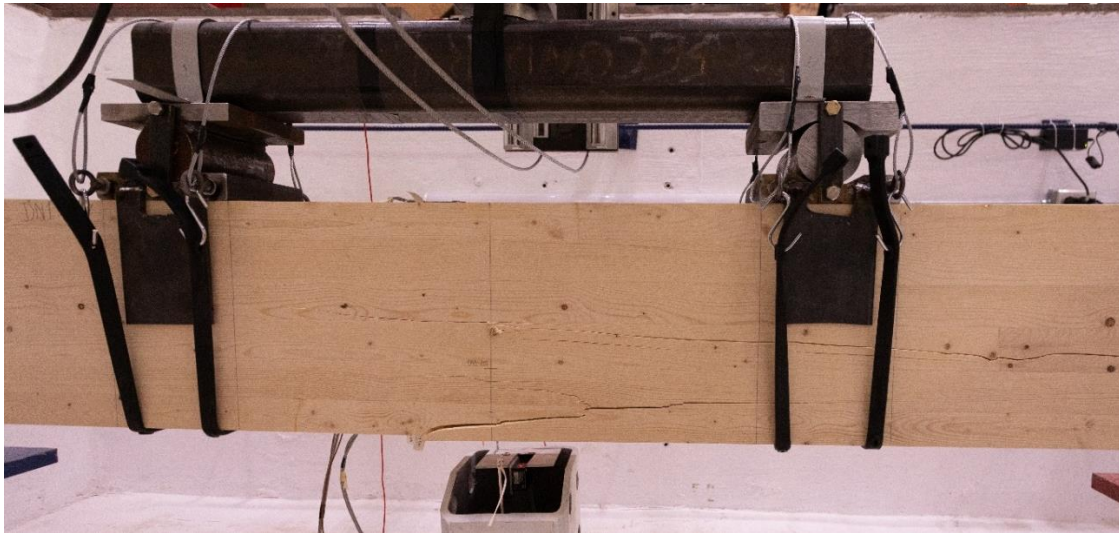


(b) Dynamic resistance and displacement over time

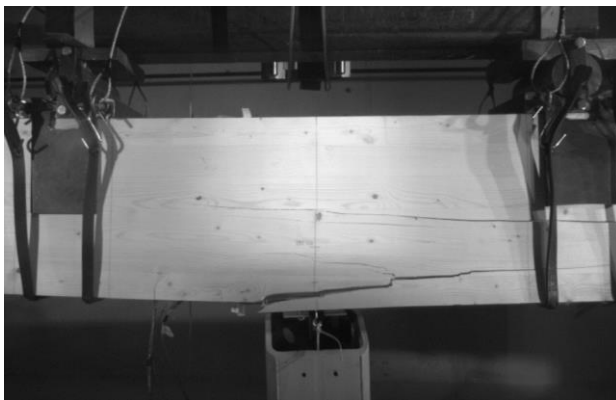


(c) Dynamic resistance and tensile strain over time

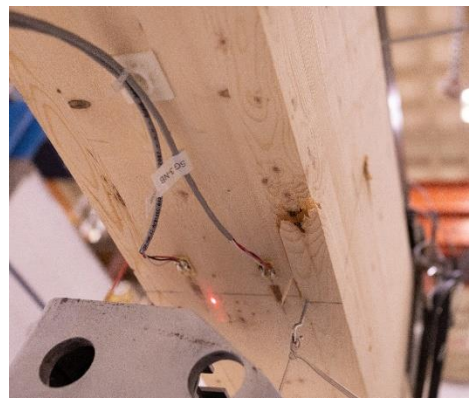
Figure B-0-3: Dynamic Test Results for Specimen DN1-267



(a) Specimen after testing



(b) Footage from the high-speed phantom camera of specimen at its maximum deflection



(c) Underside of specimen after failure

Figure B-0-4: Damage for Specimen DN1-267

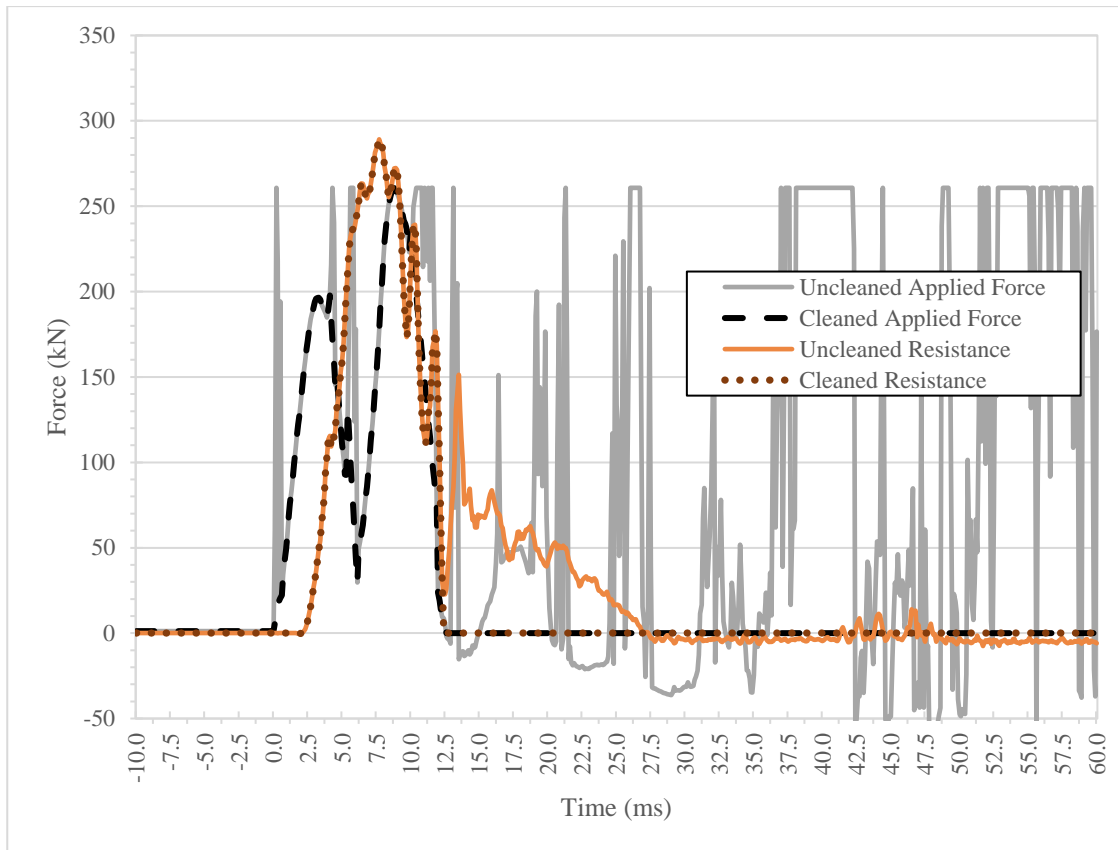
Specimen: DN2-267

Peak Force: 260.6 kN

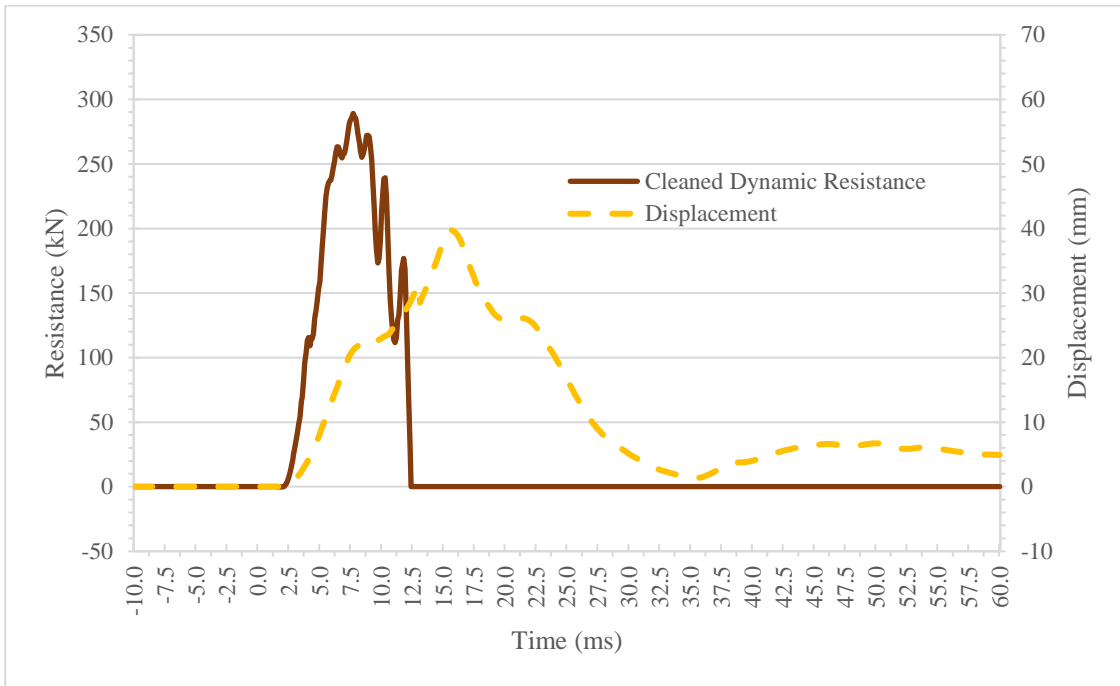
Load Duration: 12.6 ms

Peak Resistance: 287.5 kN

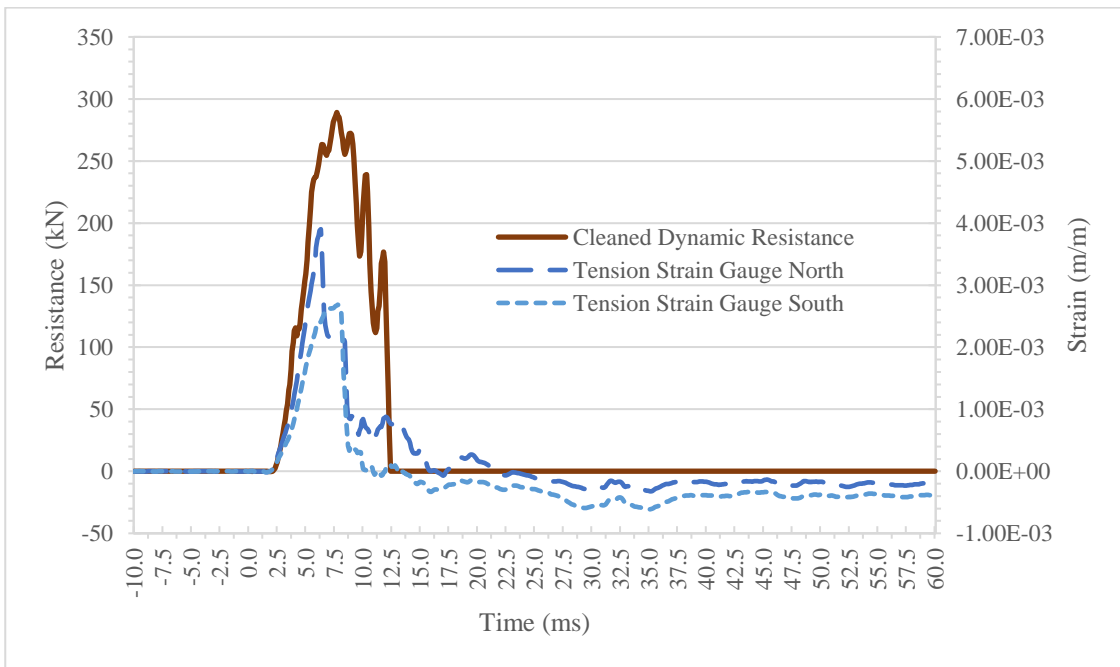
Failure Mode: Flexure



(a) Cleaned and uncleaned applied load and dynamic resistance over time

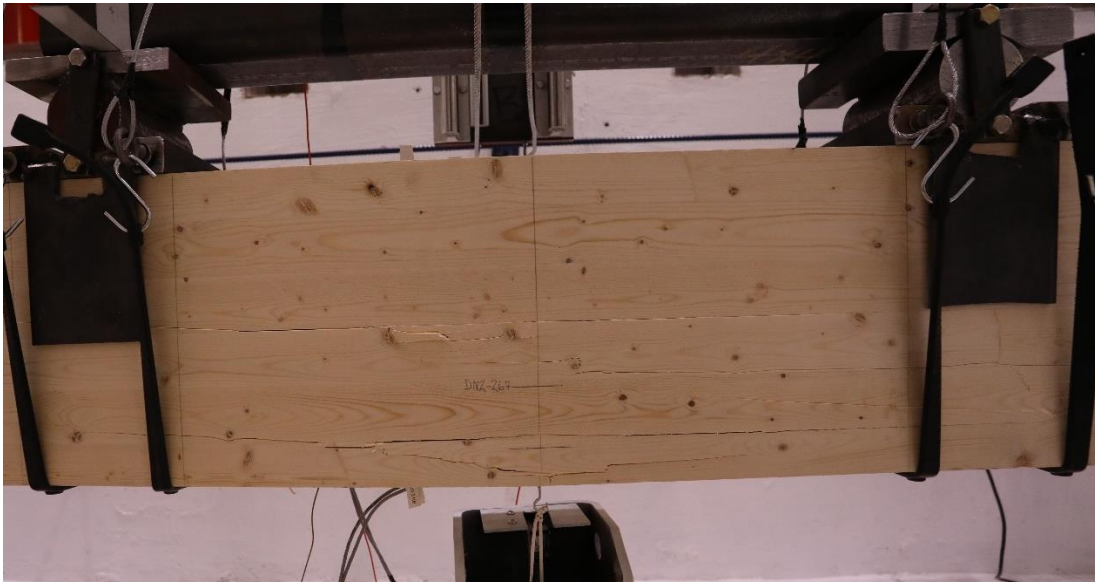


(b) Dynamic resistance and displacement over time

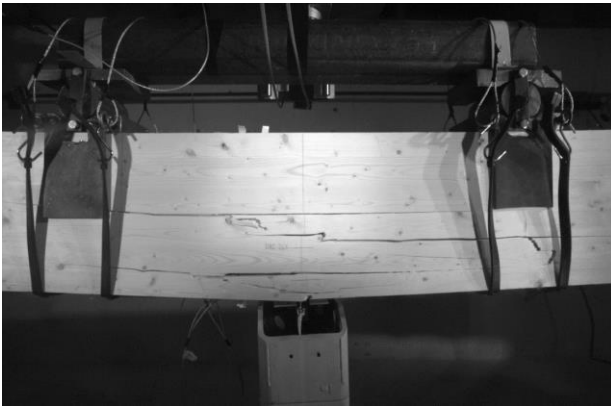


(c) Dynamic resistance and tensile strain over time

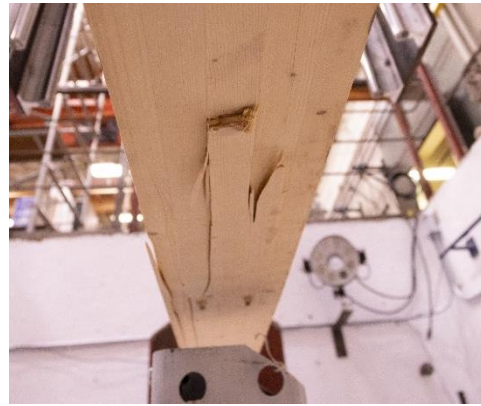
Figure B-0-5: Dynamic Test Results for Specimen DN2-267



(a) Specimen after testing



(b) Footage from the high-speed phantom camera of specimen at its maximum deflection



(c) Underside of specimen after failure

Figure B-0-6: Damage for Specimen DN2-267

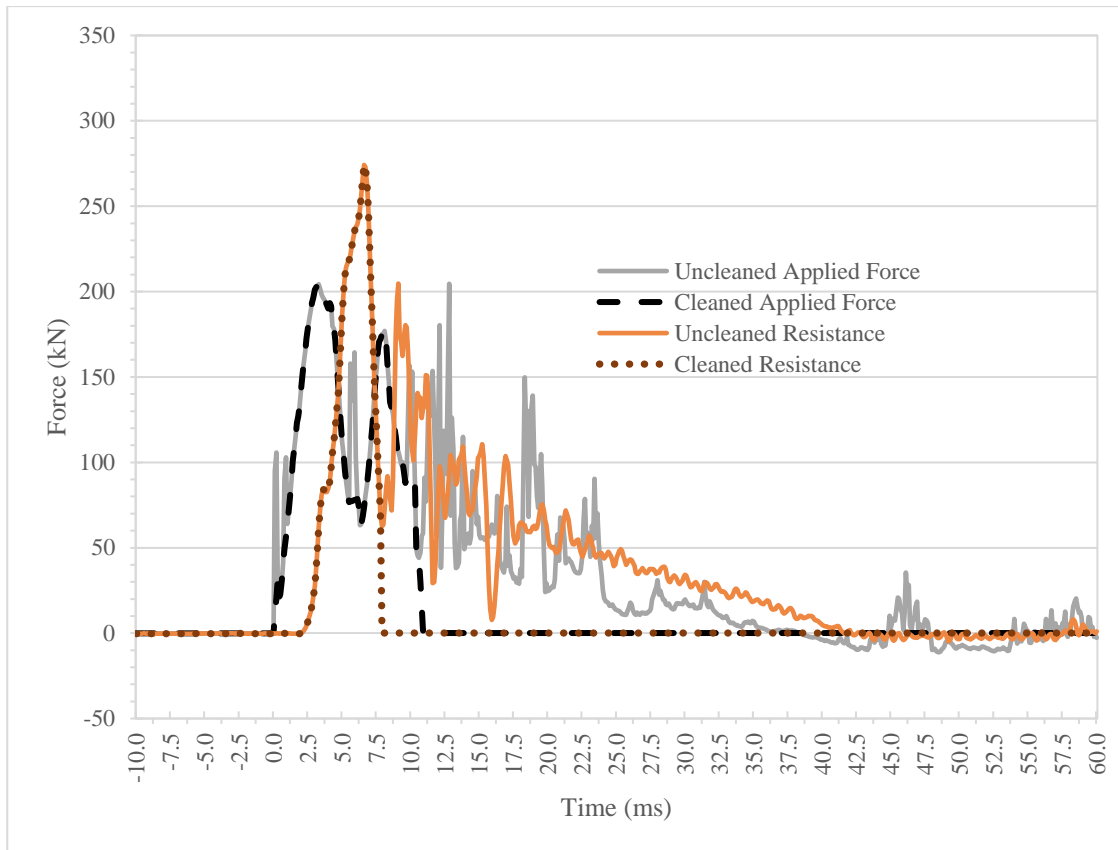
Specimen: DN3-267

Peak Force: 332.0 kN

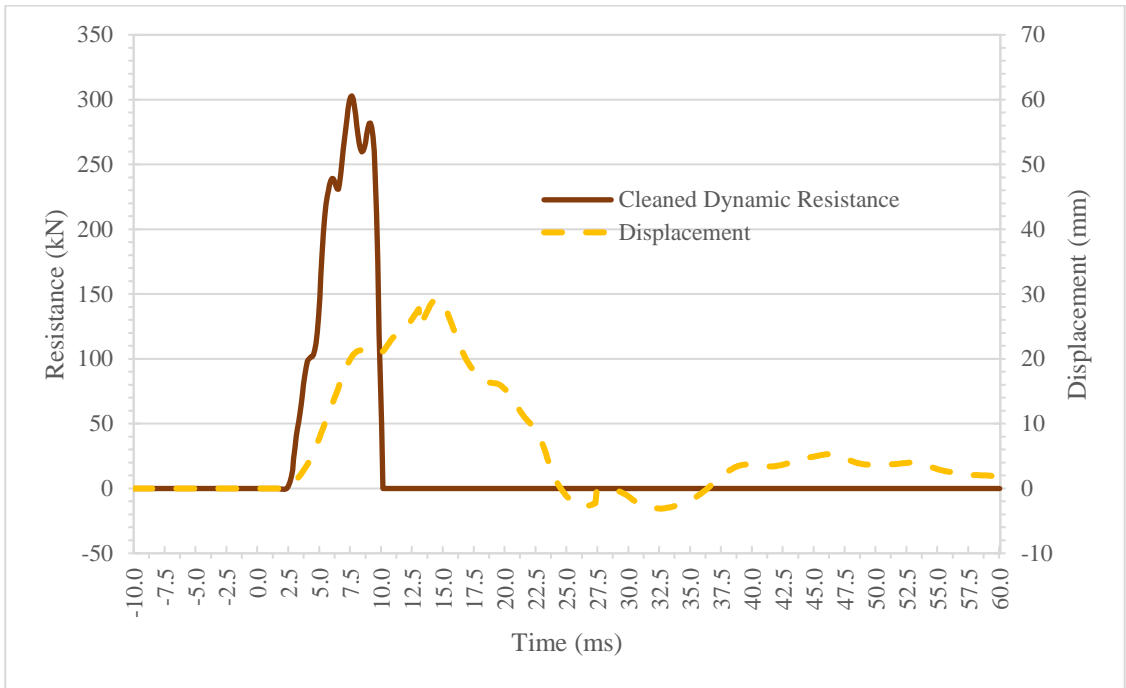
Load Duration: 12.1 ms

Peak Resistance: 301.0 kN

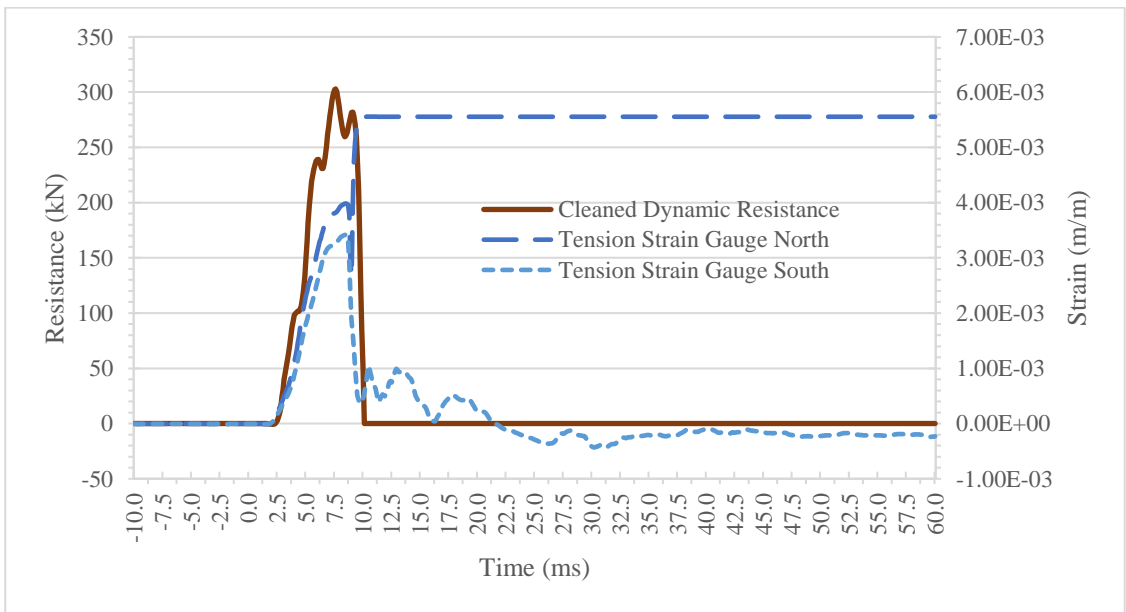
Failure Mode: Flexure



(a) Cleaned and uncleaned applied load and dynamic resistance over time

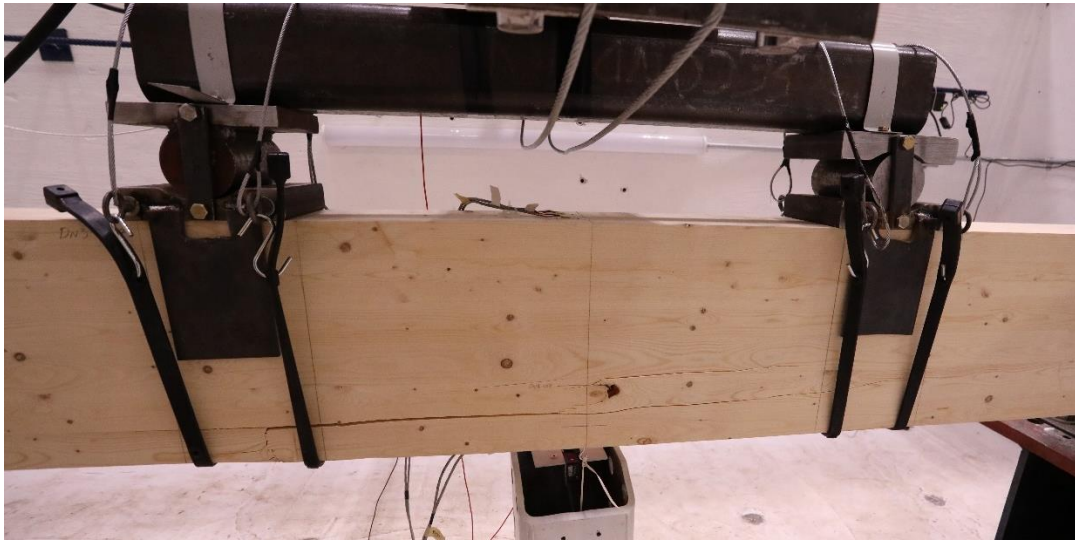


(b) Dynamic resistance and displacement over time

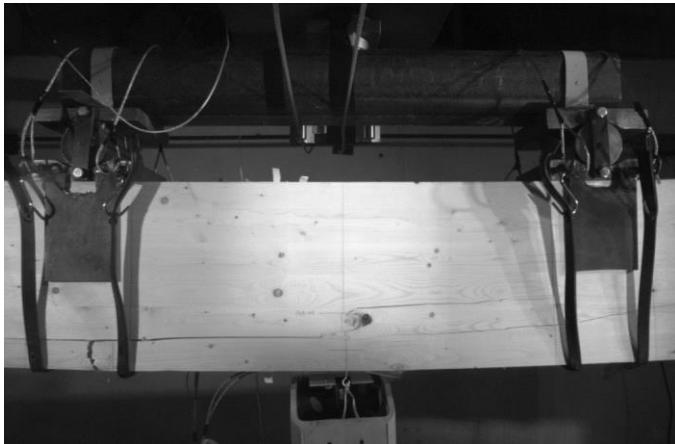


(c) Dynamic resistance and tensile strain over time

Figure B-0-7: Dynamic Test Results for Specimen DN3-267



(a) Specimen after testing



(b) Footage from the high-speed phantom camera of specimen at its maximum deflection



(c) Underside of specimen after failure

Figure B-0-8: Damage for Specimen DN3-267

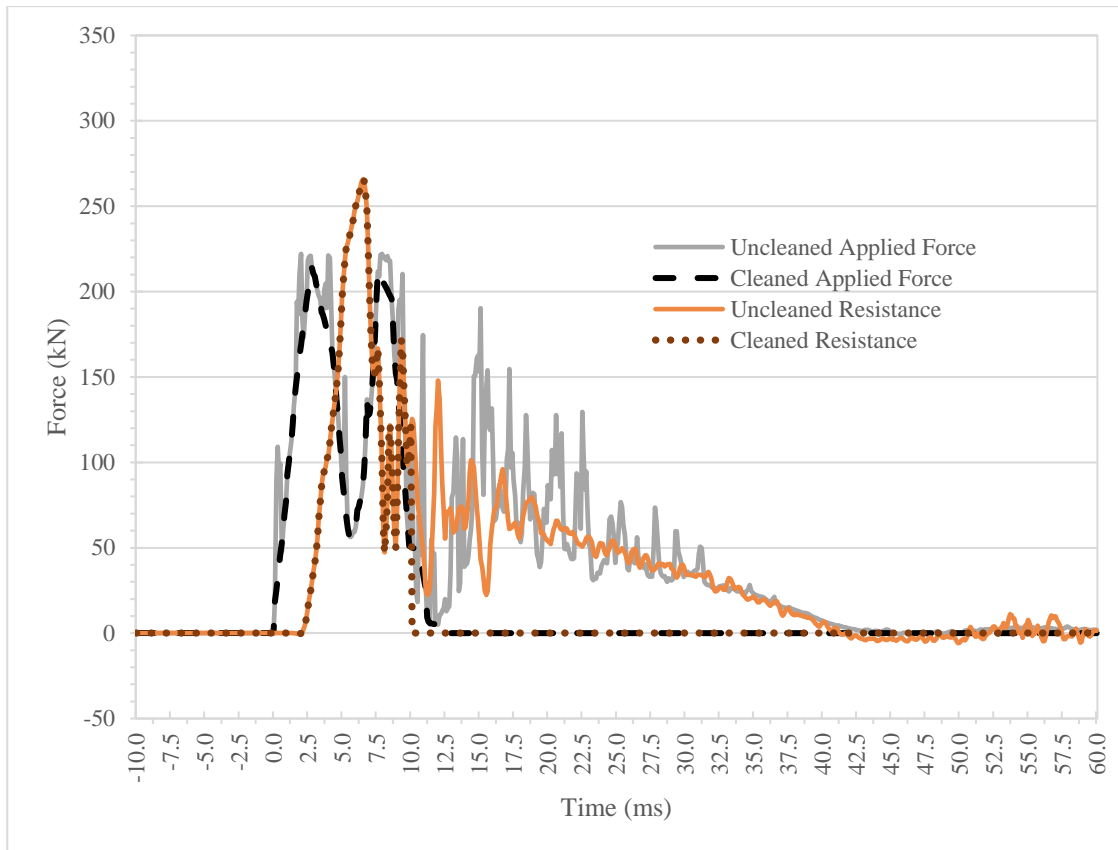
Specimen: DN4-267

Peak Force: 213.8 kN

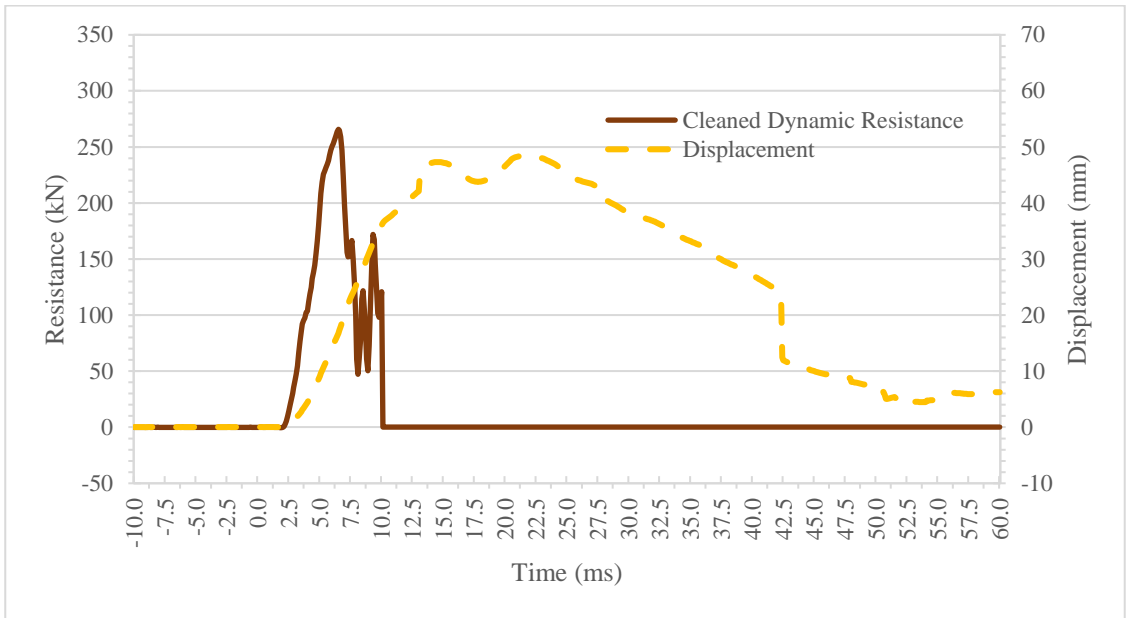
Load Duration: 12.1 ms

Peak Resistance: 263.2 kN

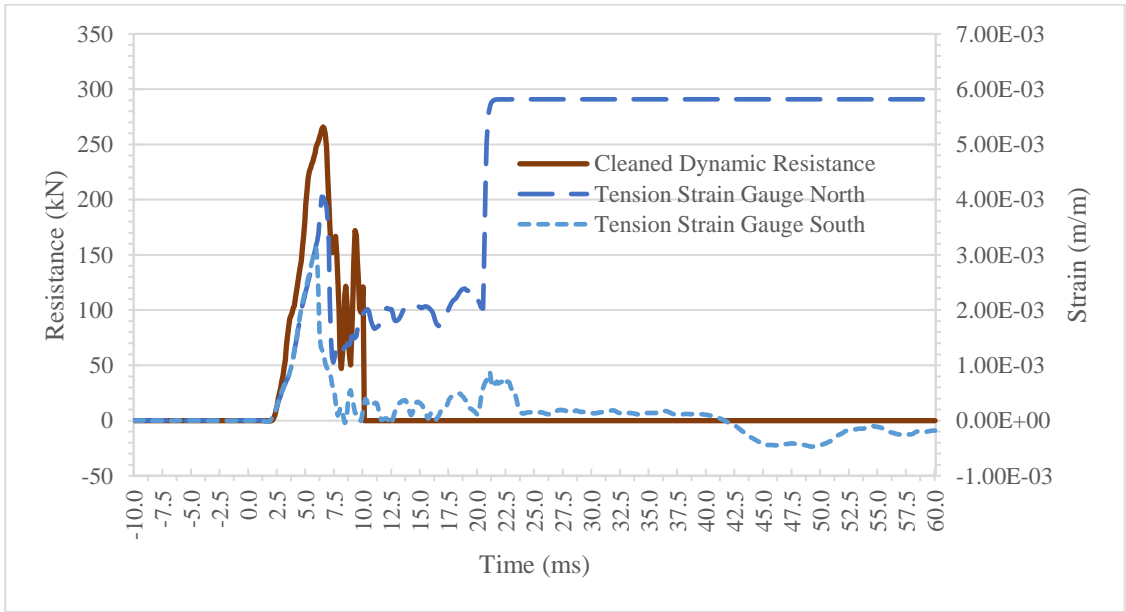
Failure Mode: Flexure



(a) Cleaned and uncleaned applied load and dynamic resistance over time

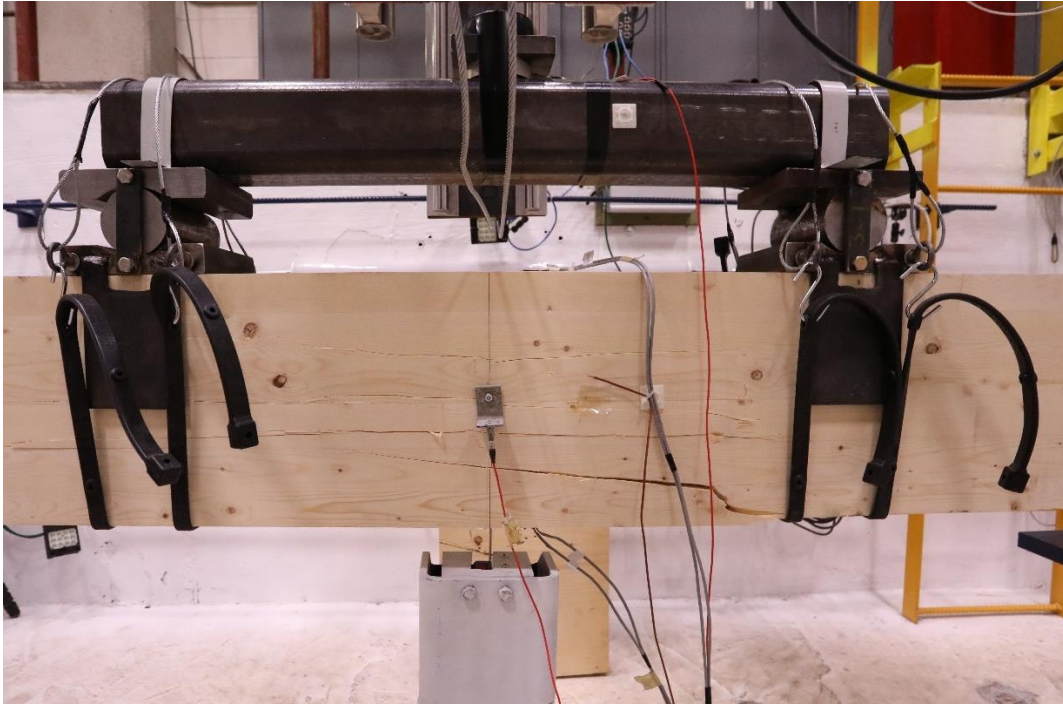


(b) Dynamic resistance and displacement over time

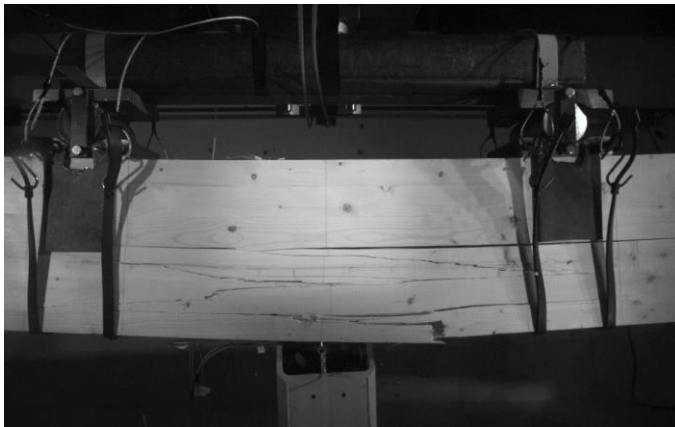


(c) Dynamic resistance and tensile strain over time

Figure B-0-9: Dynamic Test Results for Specimen DN4-267



(a) Specimen after testing



(b) Footage from the high-speed phantom camera of specimen at its maximum deflection



(c) Underside of specimen after failure

Figure B-0-10: Damage for Specimen DN4-267

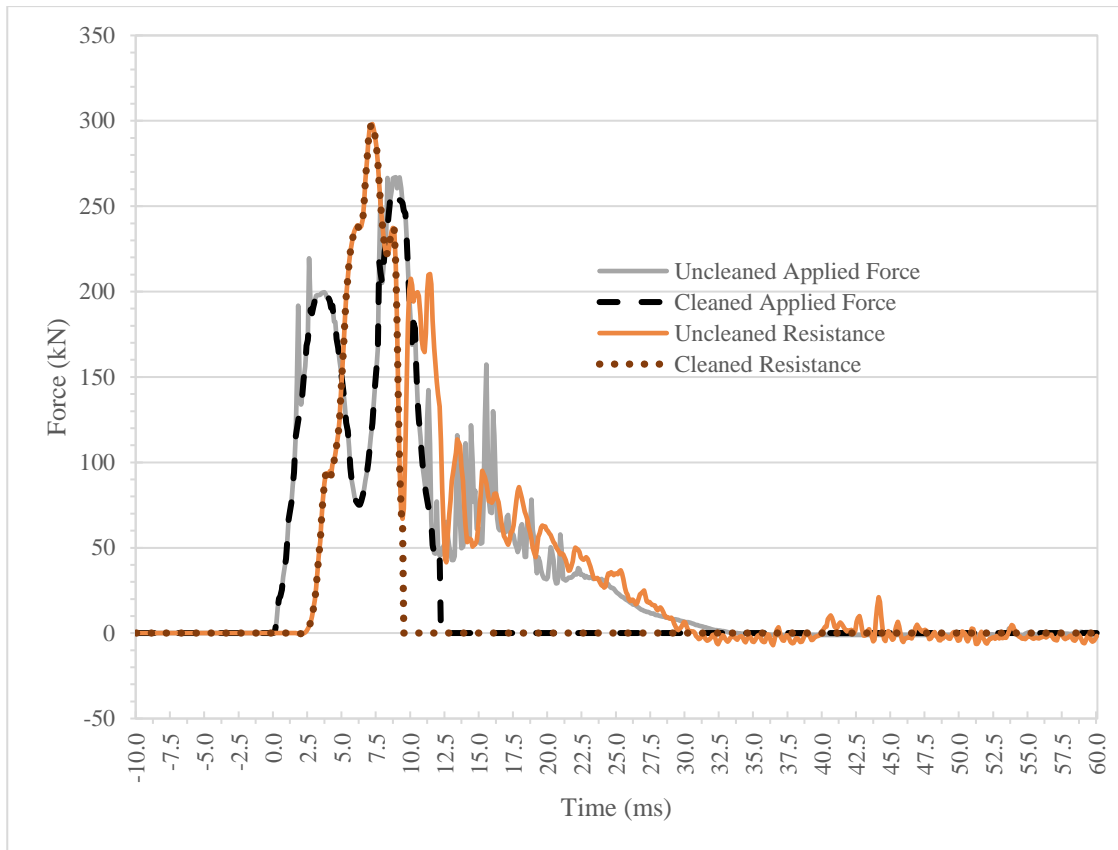
Specimen: DN5-267

Peak Force: 259.0 kN

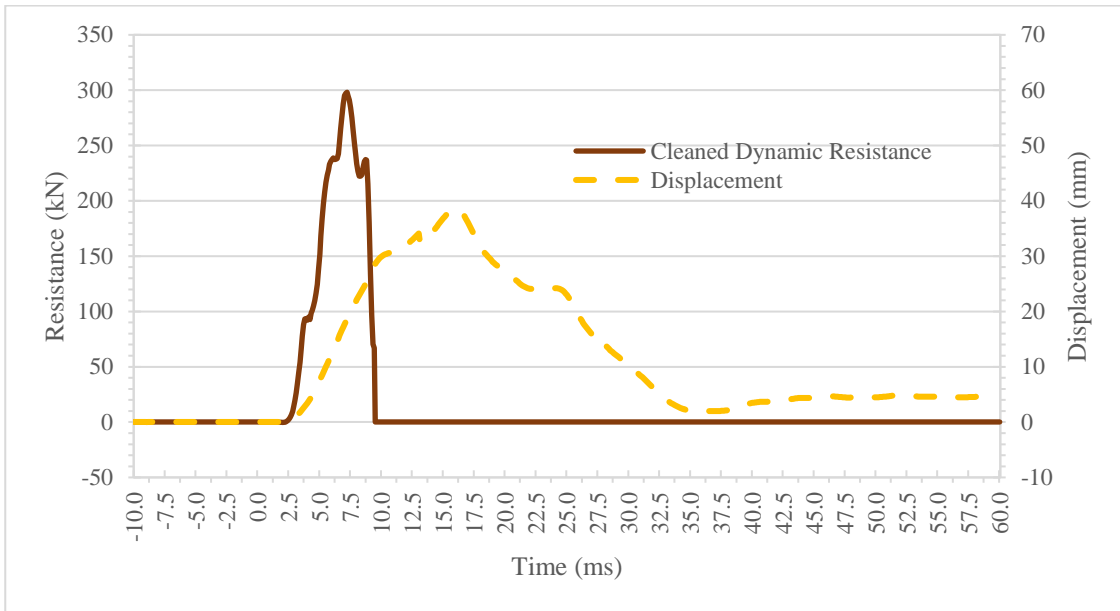
Load Duration: 12.2 ms

Peak Resistance: 295.5 kN

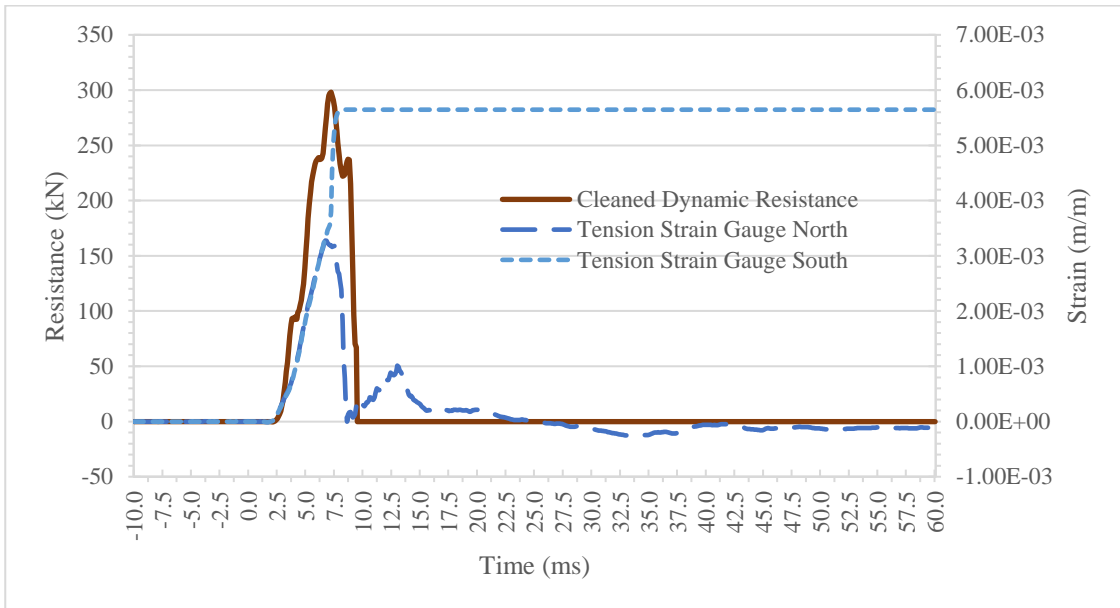
Failure Mode: Flexure



(a) Cleaned and uncleaned applied load and dynamic resistance over time

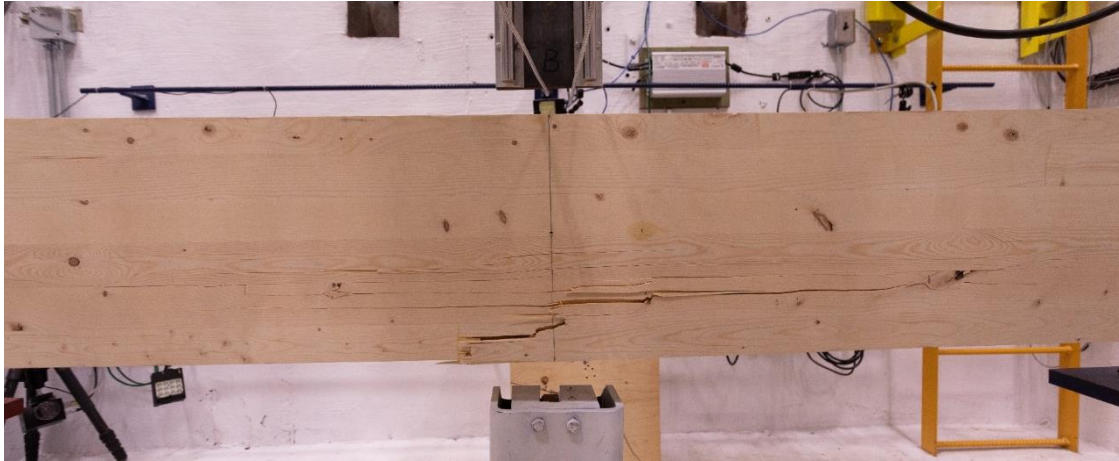


(b) Dynamic resistance and displacement over time

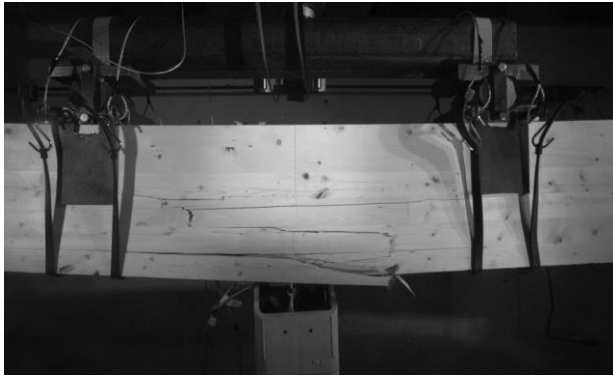


(c) Dynamic resistance and tensile strain over time

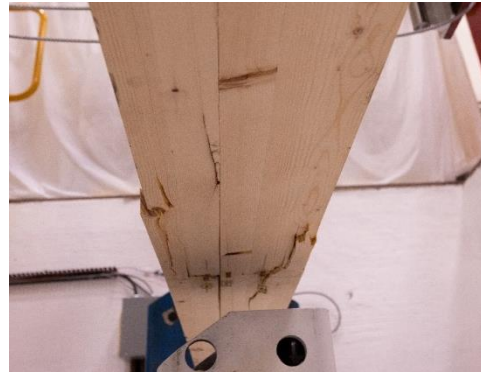
Figure B-0-11: Dynamic Test Results for Specimen DN5-267



(a) Specimen after testing



(b) Footage from the high-speed phantom camera of specimen at its maximum deflection



(c) Underside of specimen after failure

Figure B-0-12: Damage for Specimen DN5-267

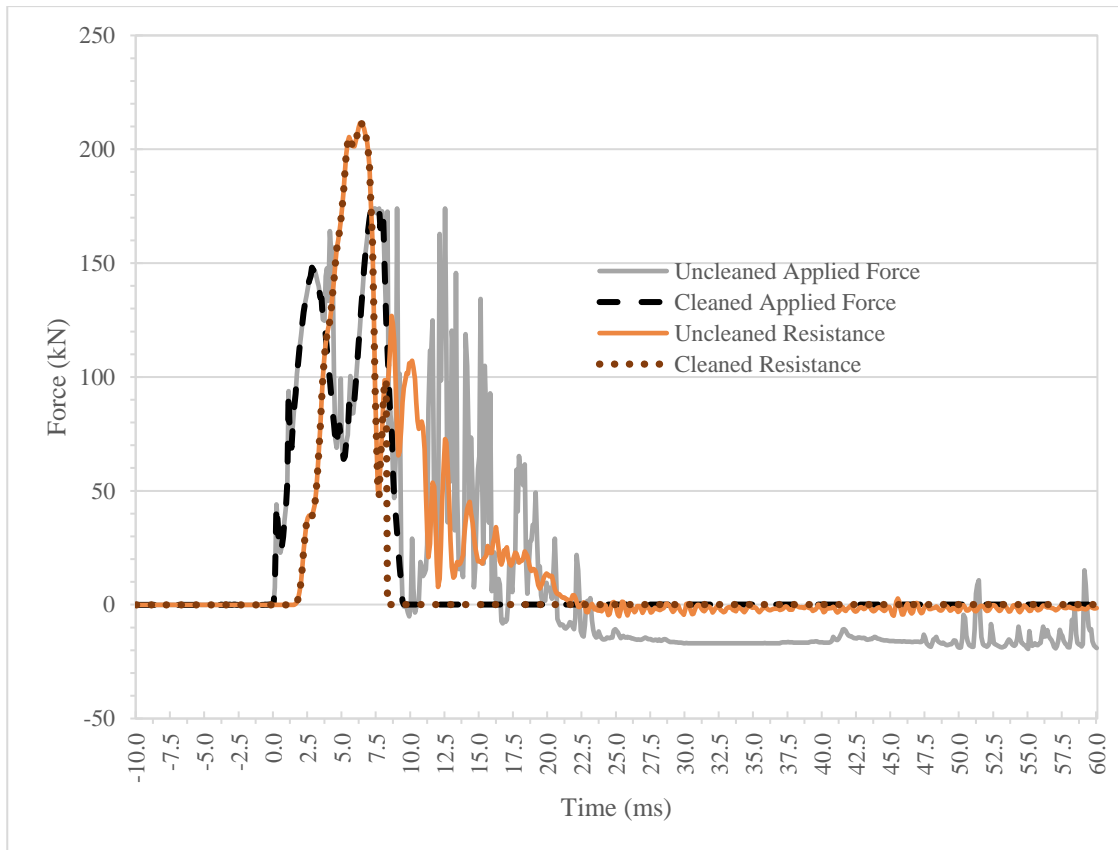
Specimen: DN1-178

Peak Force: 174.0 kN

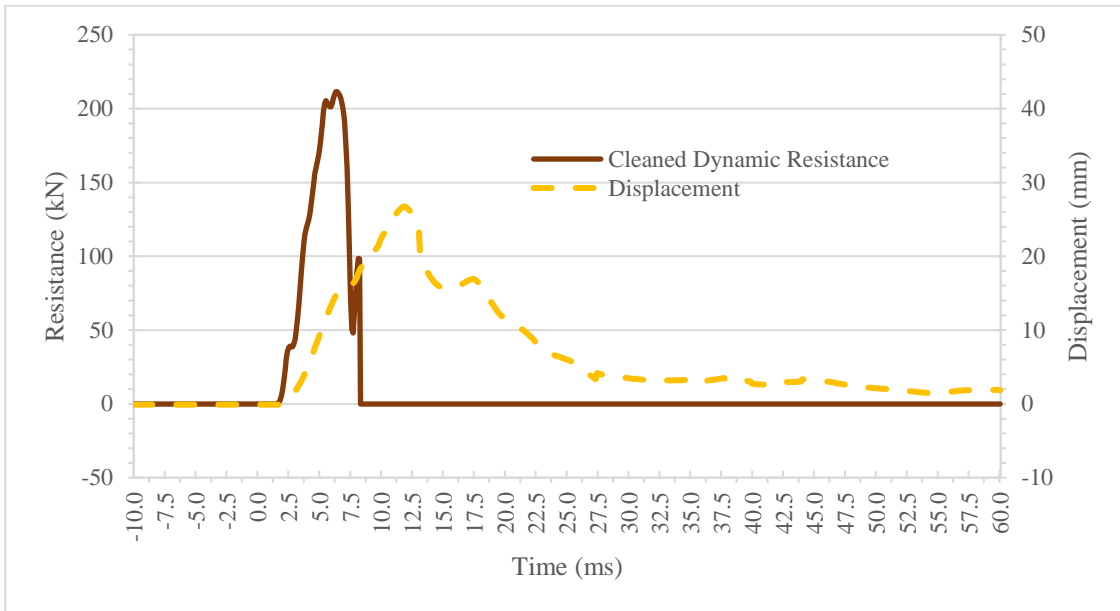
Load Duration: 9.5 ms

Peak Resistance: 210.7 kN

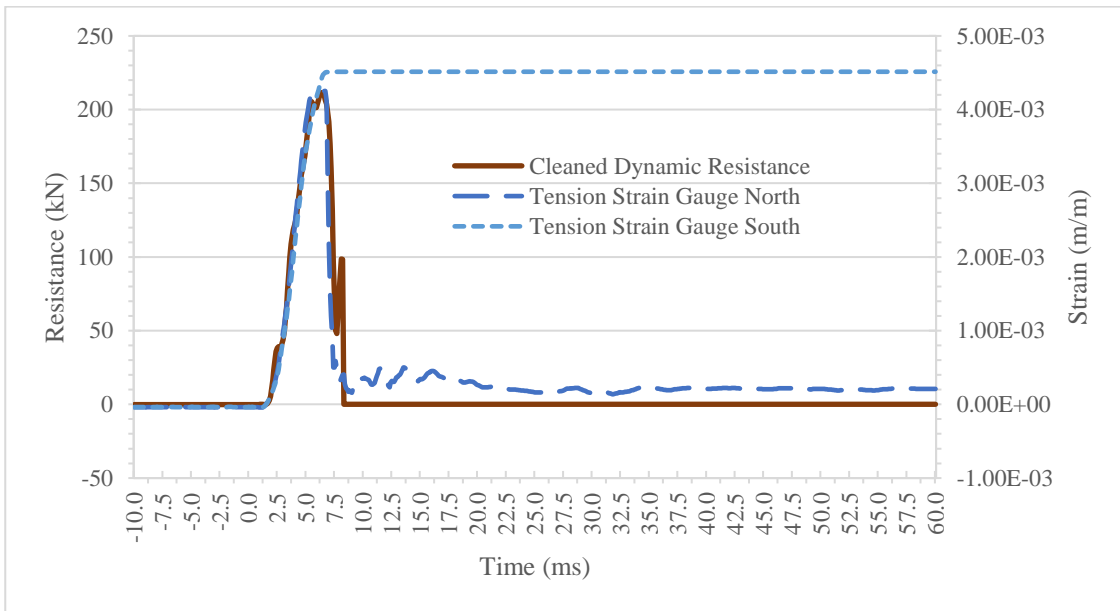
Failure Mode: Flexure



(a) Cleaned and uncleaned applied load and dynamic resistance over time

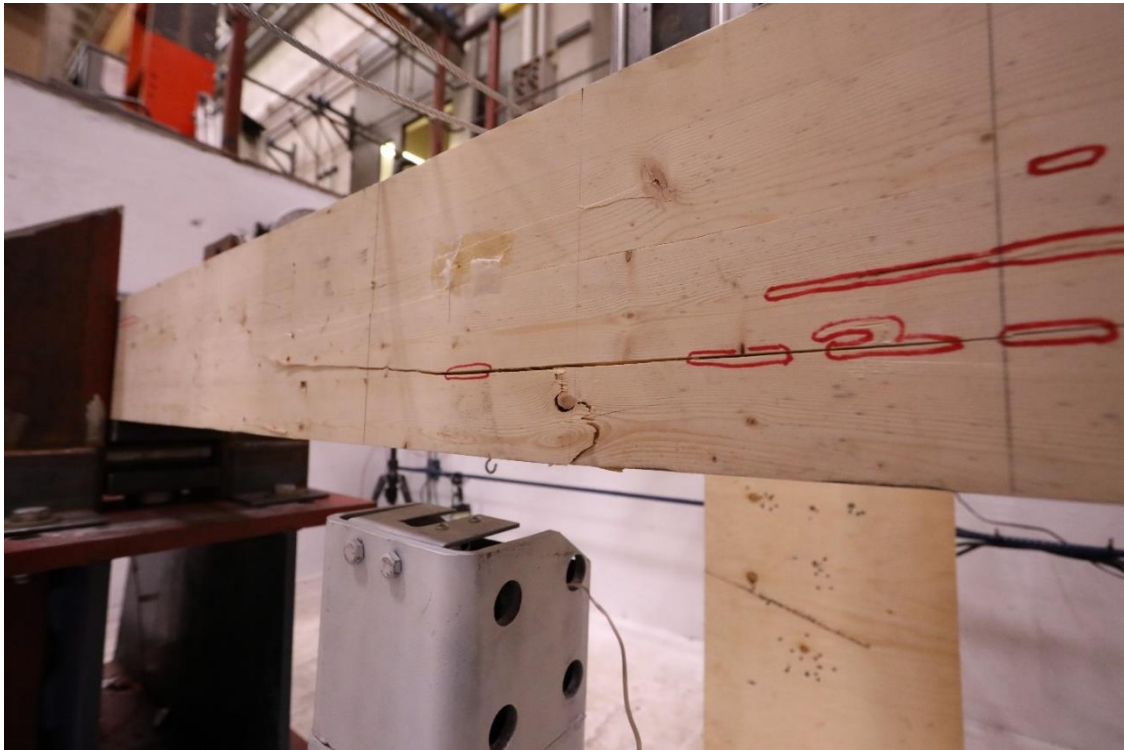


(b) Dynamic resistance and displacement over time

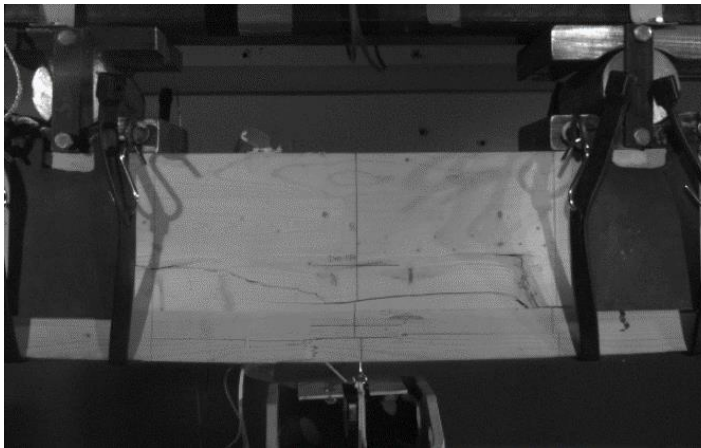


(c) Dynamic resistance and tensile strain over time

Figure B-0-13: Dynamic Test Results for Specimen DN1-178



(a) Specimen after testing



(b) Footage from the high-speed phantom camera of specimen at its maximum deflection



(c) Underside of specimen after failure

Figure B-0-14: Damage for Specimen DN1-178

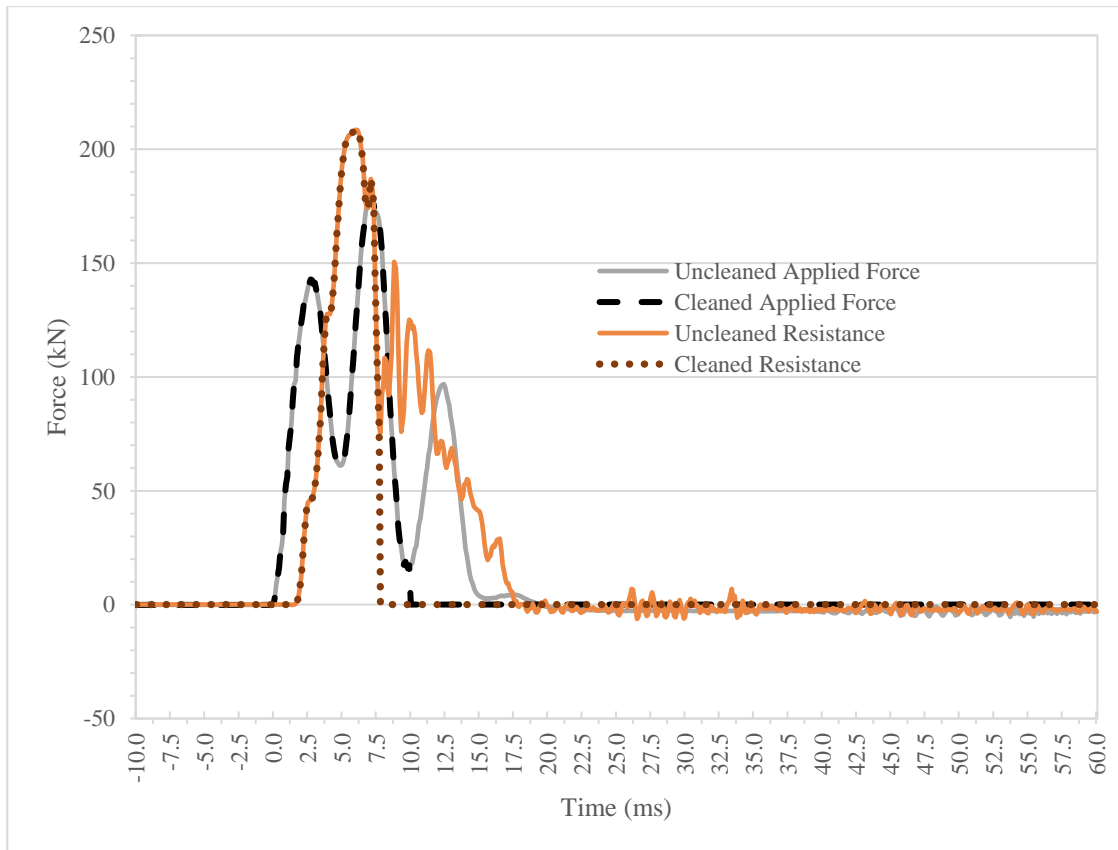
Specimen: DN2-178

Peak Force: 179.2 kN

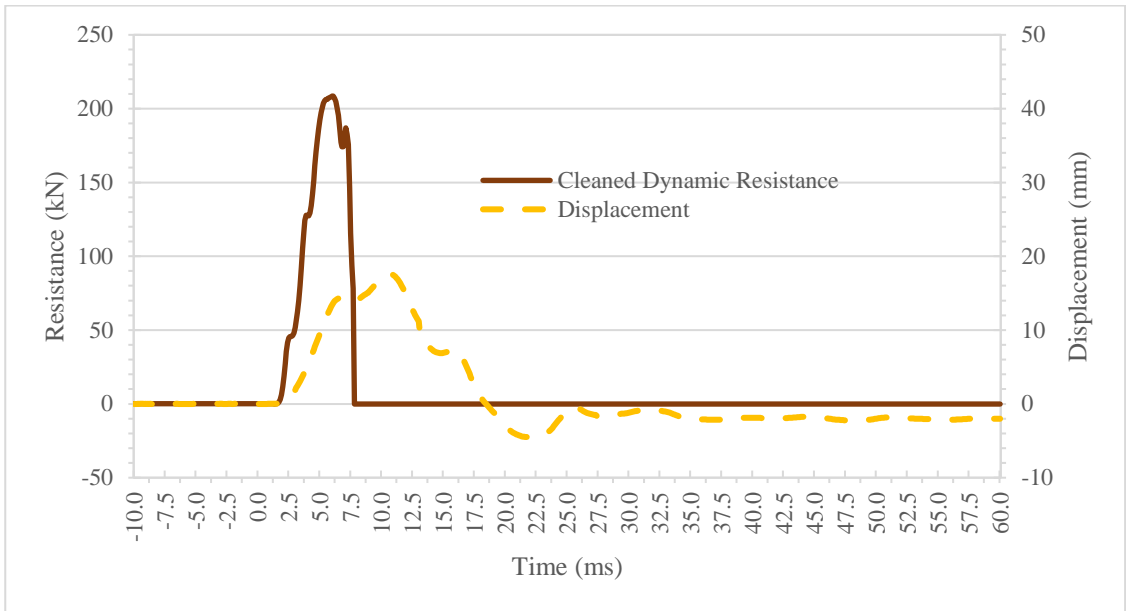
Load Duration: 10.0 ms

Peak Resistance: 207.7 kN

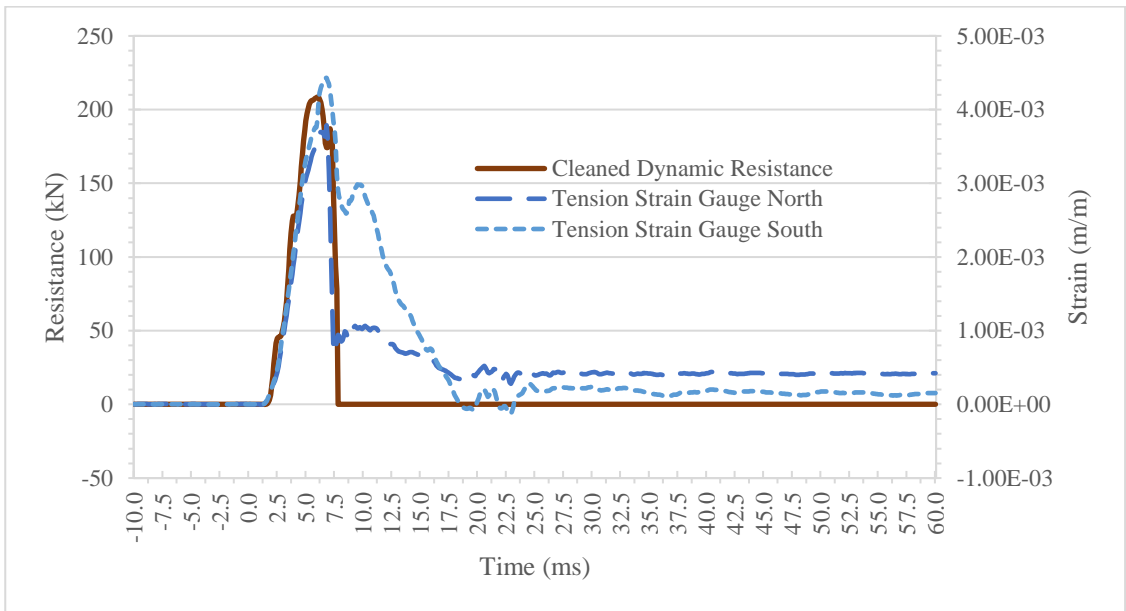
Failure Mode: Flexure



(a) Cleaned and uncleaned applied load and dynamic resistance over time

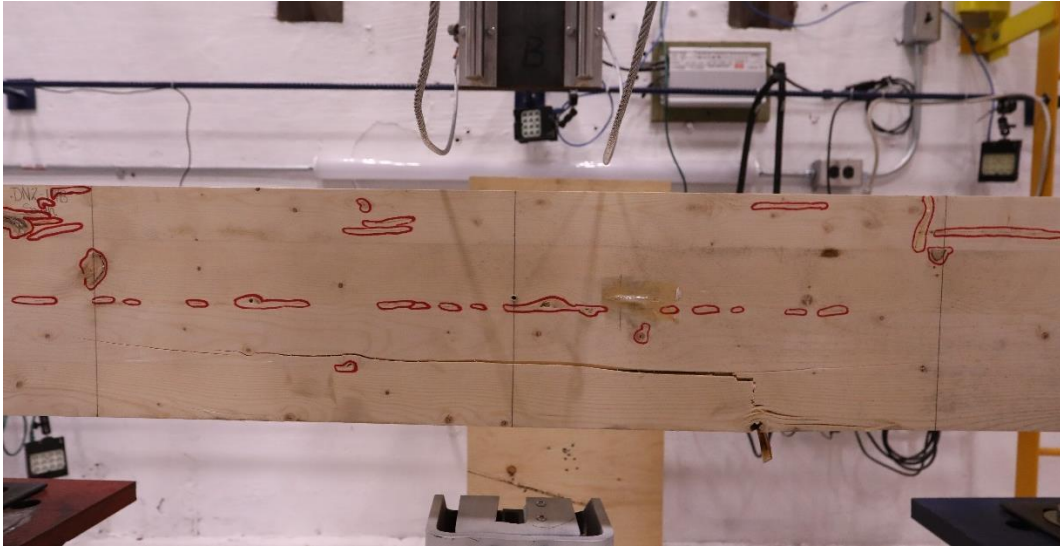


(b) Dynamic resistance and displacement over time

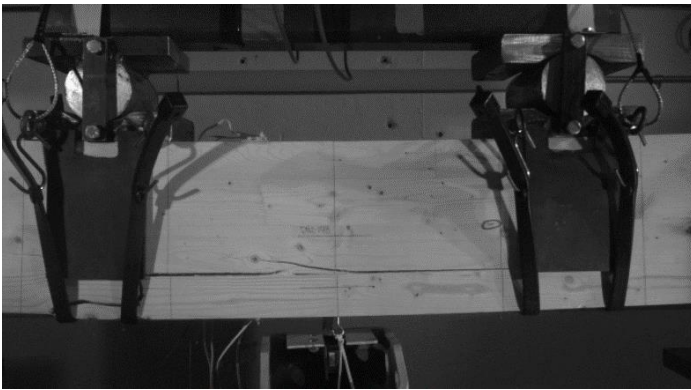


(c) Dynamic resistance and tensile strain over time

Figure B-0-15: Dynamic Test Results for Specimen DN2-178



(a) Specimen after testing



(b) Footage from the high-speed phantom camera of specimen at its maximum deflection



(c) Underside of specimen after failure

Figure B-0-16: Damage for Specimen DN2-178

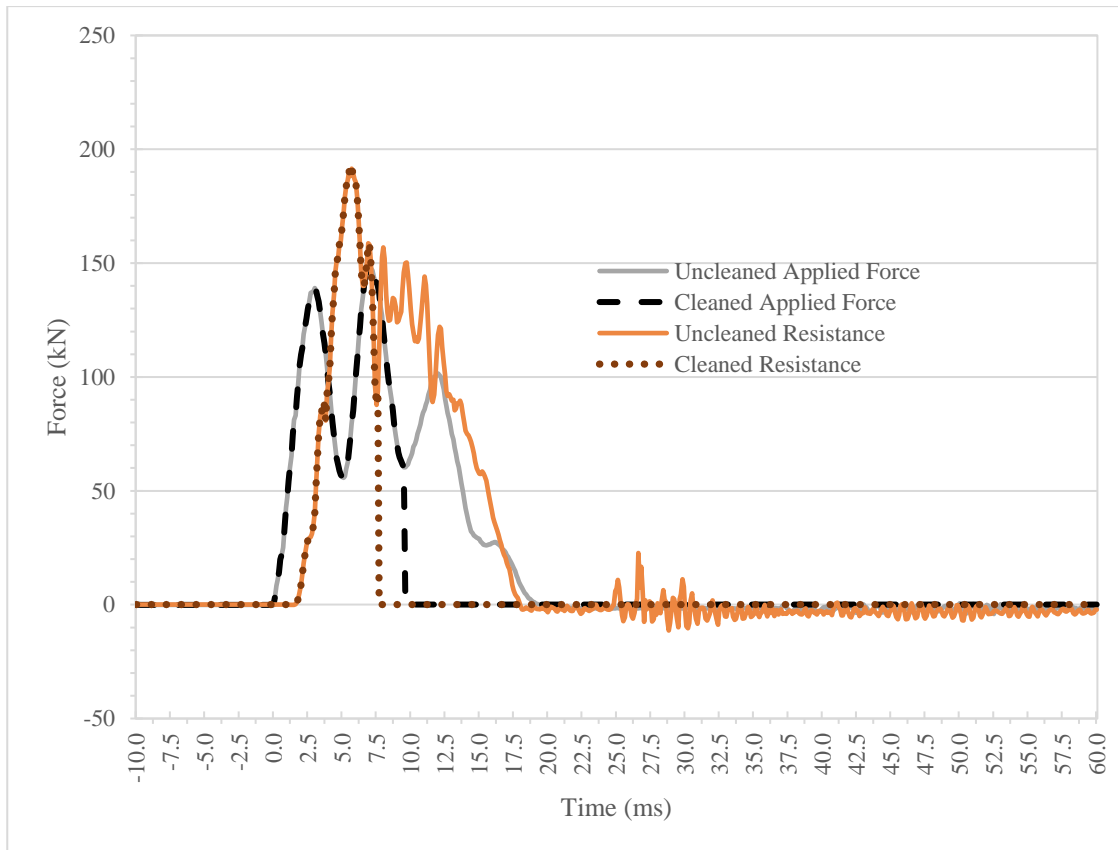
Specimen: DN3-178

Peak Force: 148.3 kN

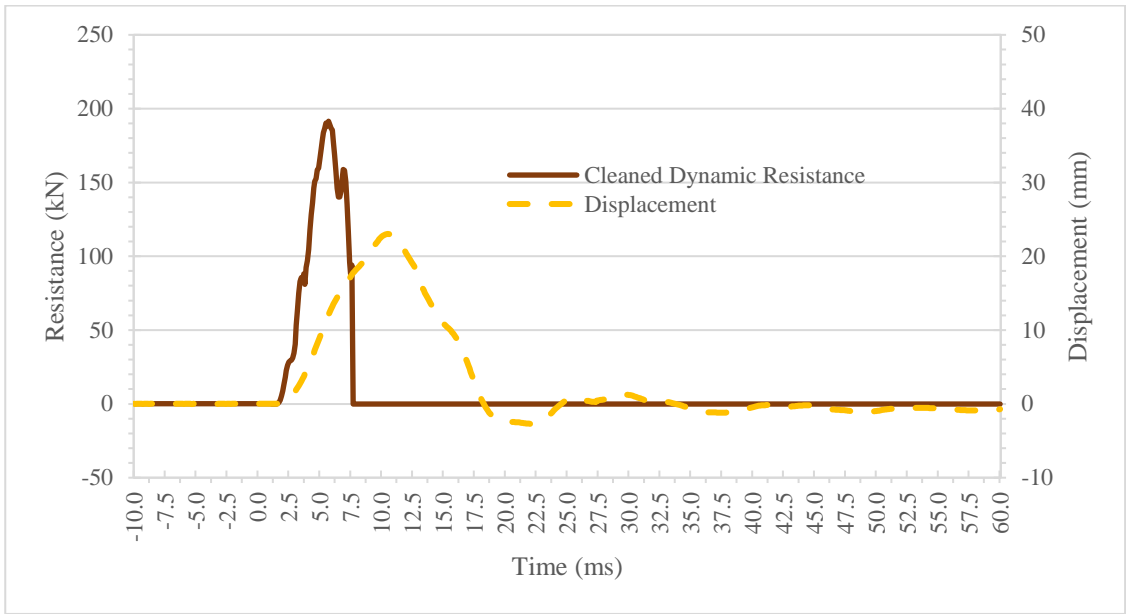
Load Duration: 9.5 ms

Peak Resistance: 174.0 kN

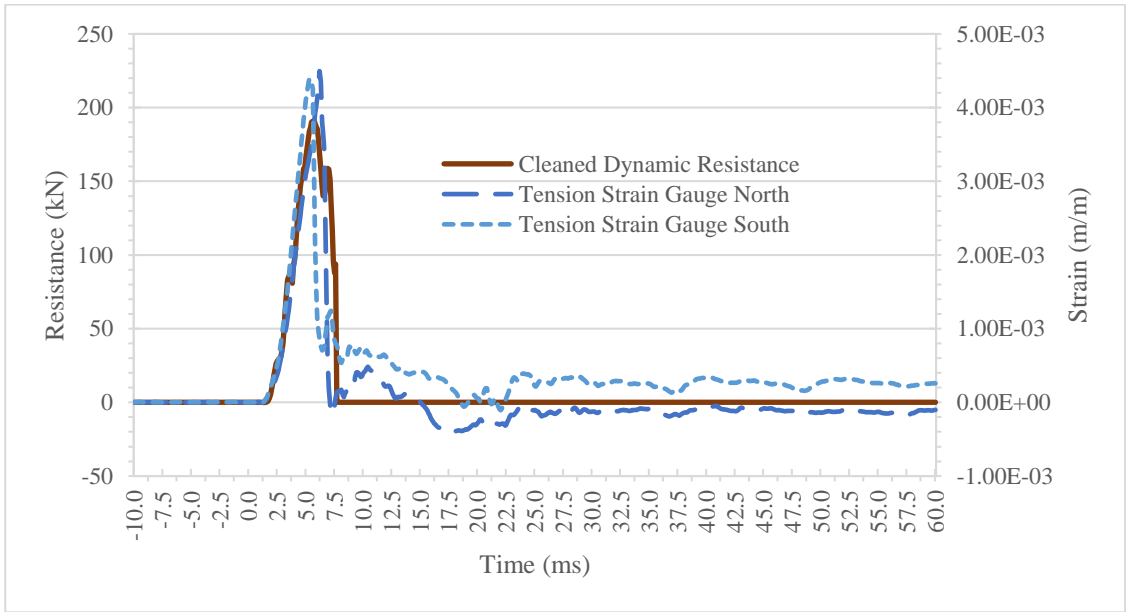
Failure Mode: Flexure



(a) Cleaned and uncleaned applied load and dynamic resistance over time

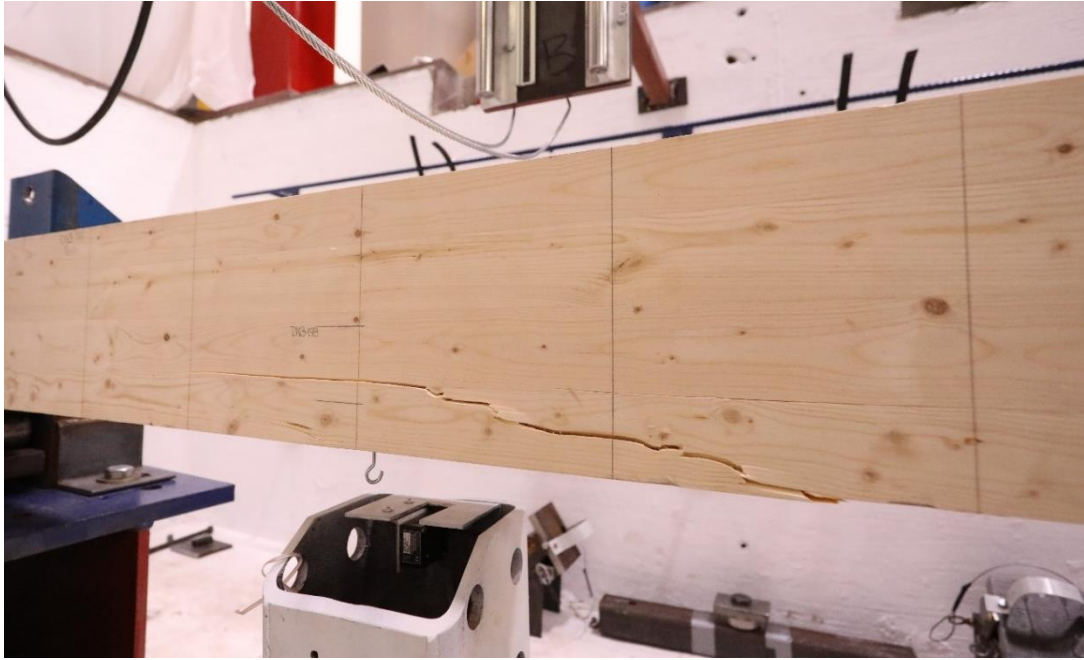


(b) Dynamic resistance and displacement over time

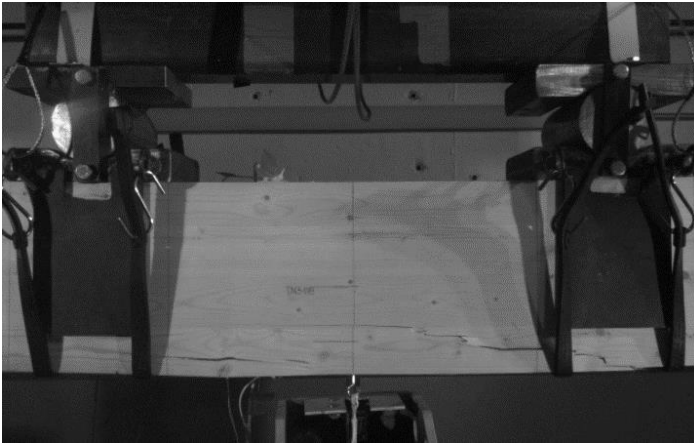


(c) Dynamic resistance and tensile strain over time

Figure B-0-17: Dynamic Test Results for Specimen DN3-178



(a) Specimen after testing



(b) Footage from the high-speed phantom camera of specimen at its maximum deflection



(c) Underside of specimen after failure

Figure B-0-18: Damage for Specimen DN3-178

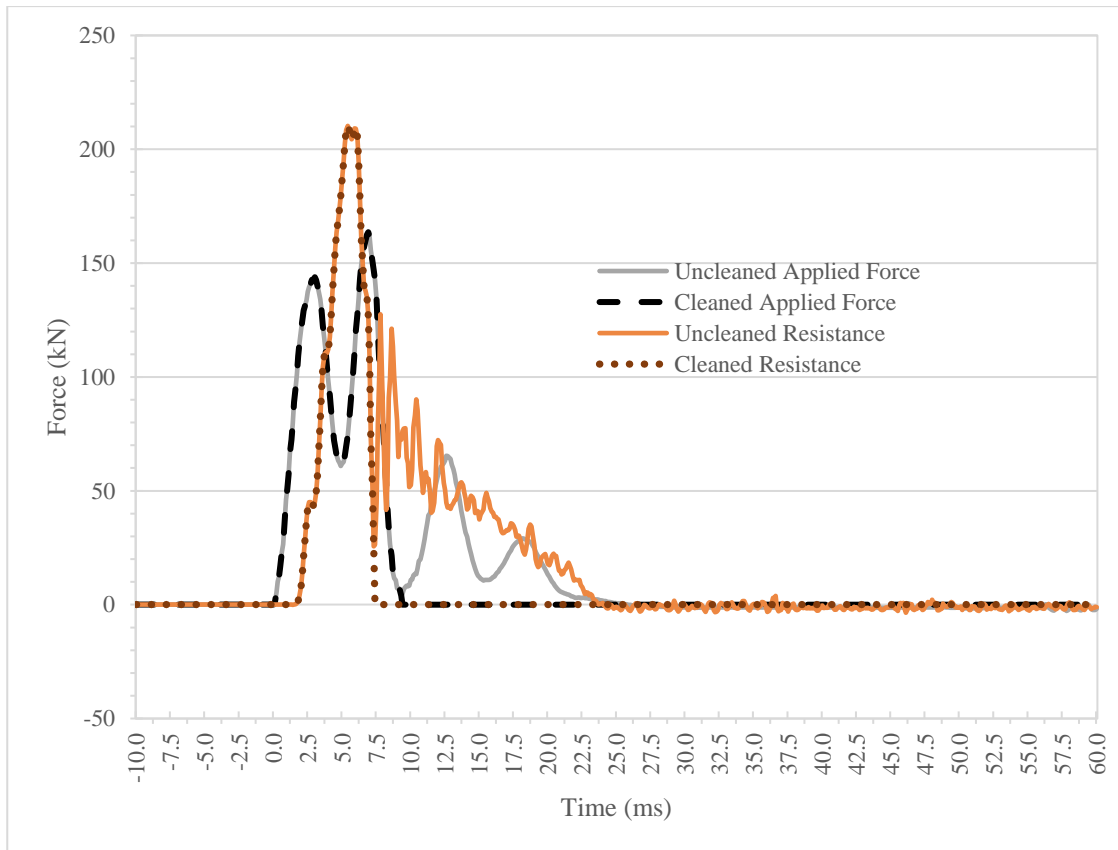
Specimen: DN4-178

Peak Force: 163.6 kN

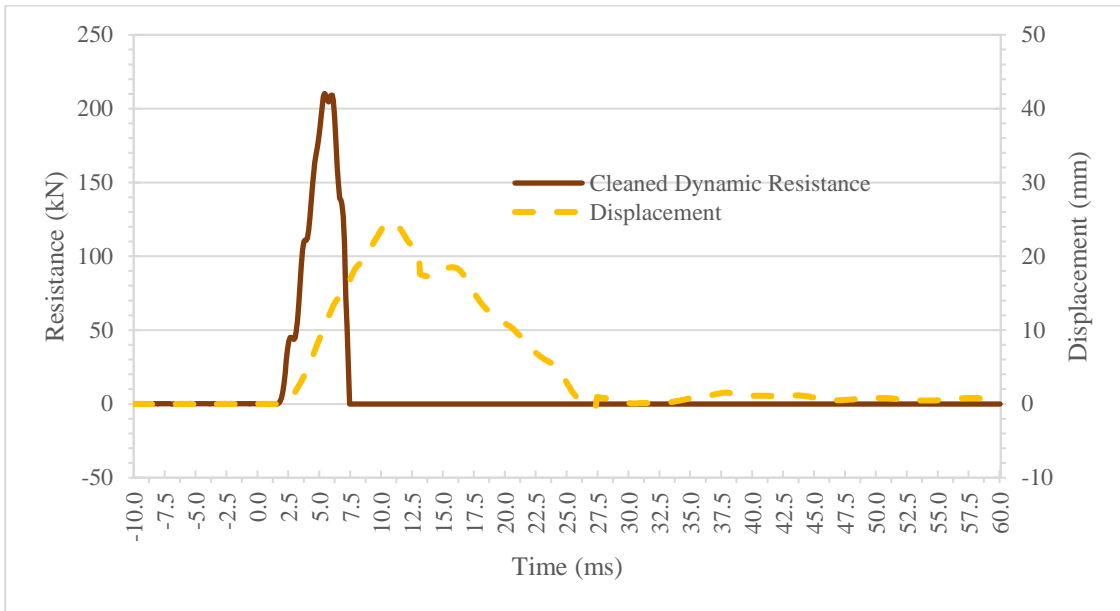
Load Duration: 9.4 ms

Peak Resistance: 208.9 kN

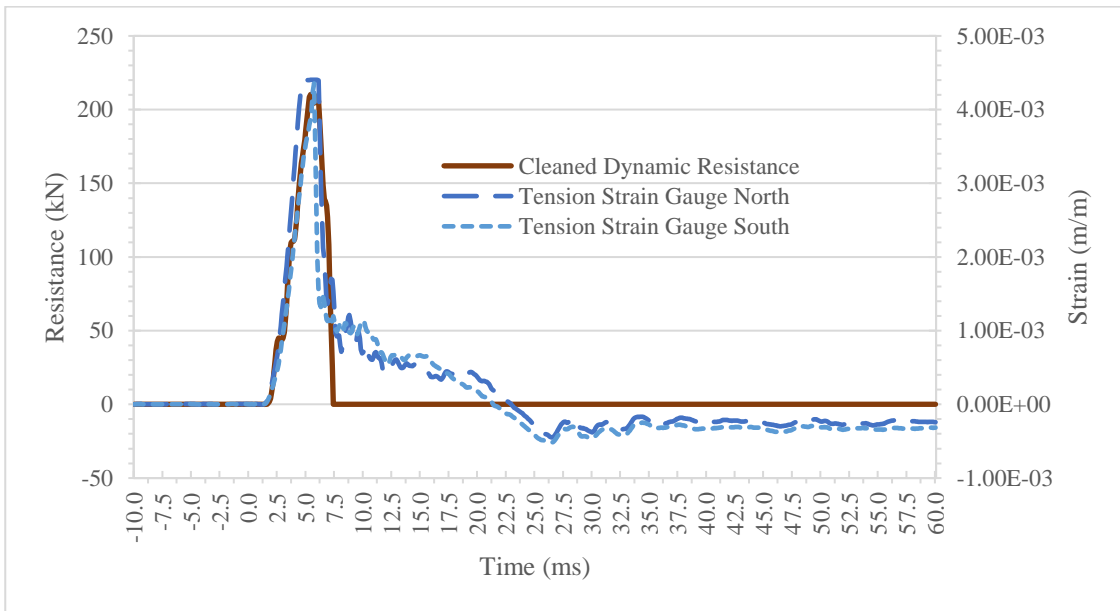
Failure Mode: Flexure



(a) Cleaned and uncleaned applied load and dynamic resistance over time

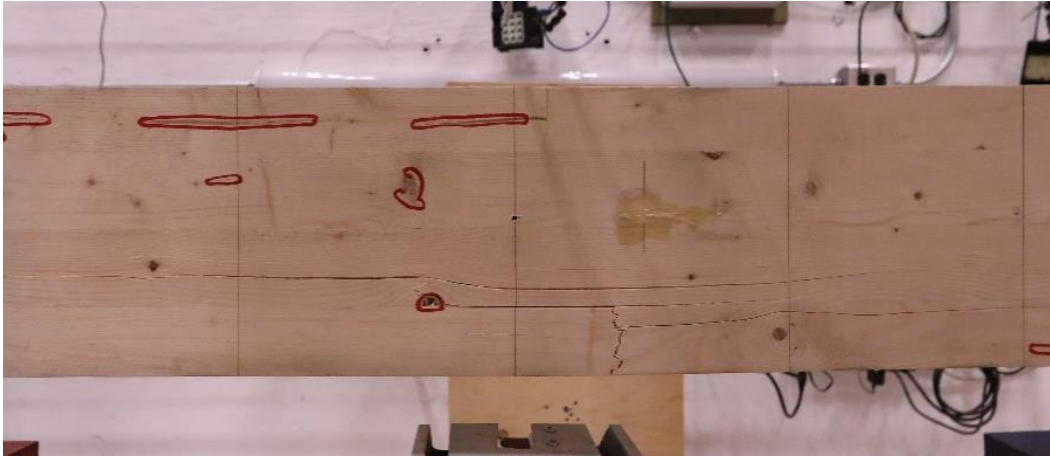


(b) Dynamic resistance and displacement over time

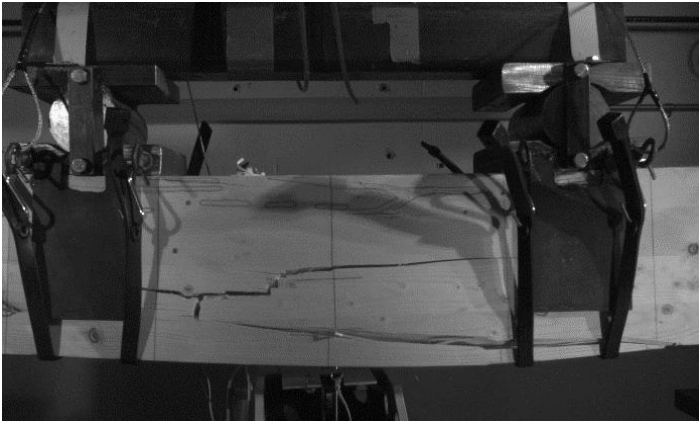


(c) Dynamic resistance and tensile strain over time

Figure B-0-19: Dynamic Test Results for Specimen DN4-178



(a) Specimen after testing



(b) Footage from the high-speed phantom camera of specimen at its maximum deflection



(c) Underside of specimen after failure

Figure B-0-20: Damage for Specimen DN4-178

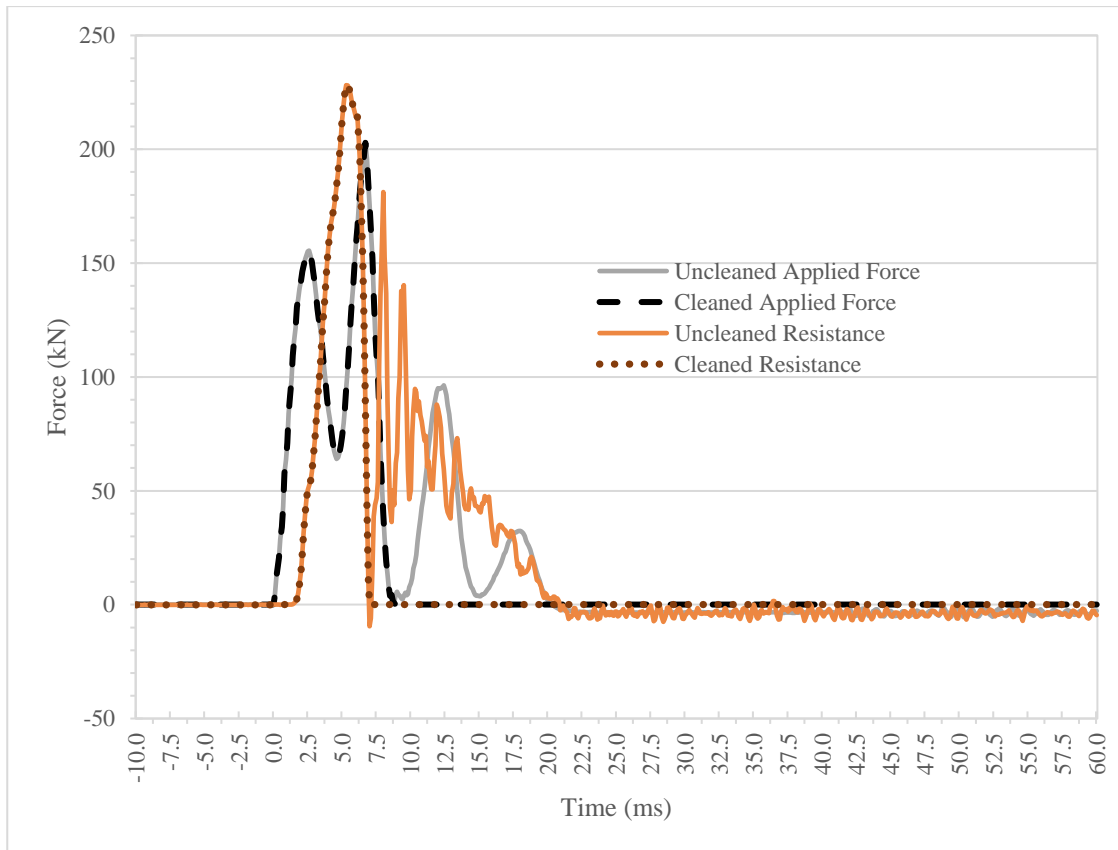
Specimen: DC1-178

Peak Force: 202.9 kN

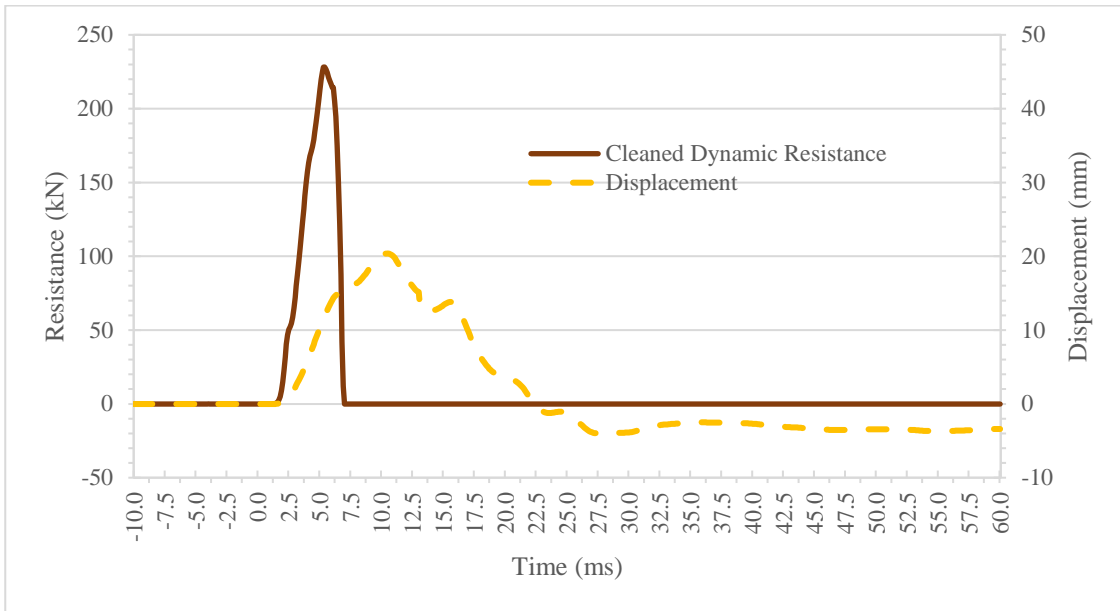
Load Duration: 9.1 ms

Peak Resistance: 226.0 kN

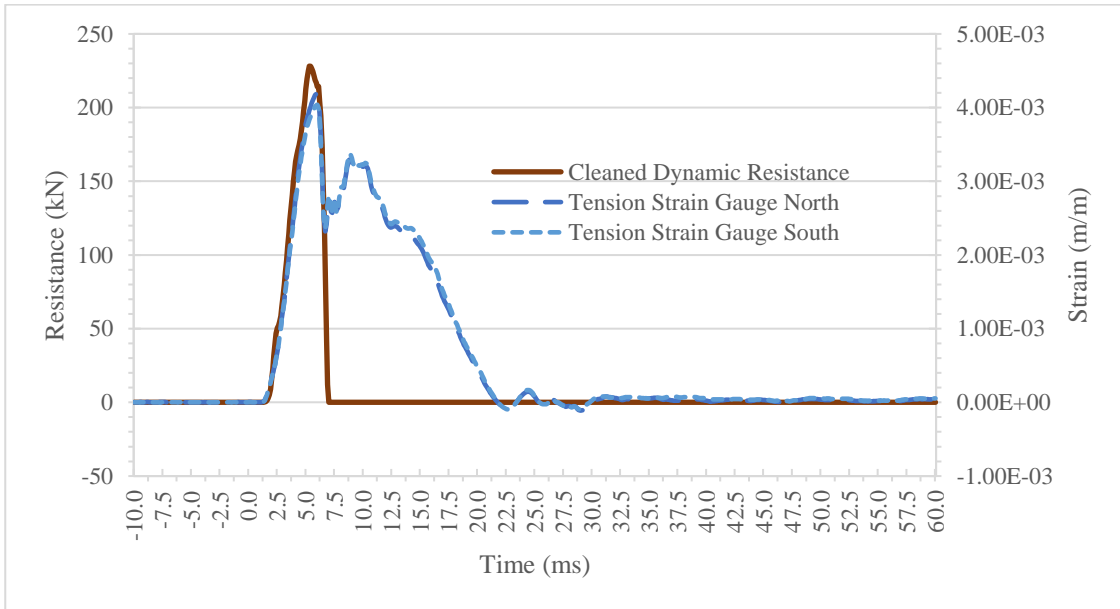
Failure Mode: Shear



(a) Cleaned and uncleaned applied load and dynamic resistance over time

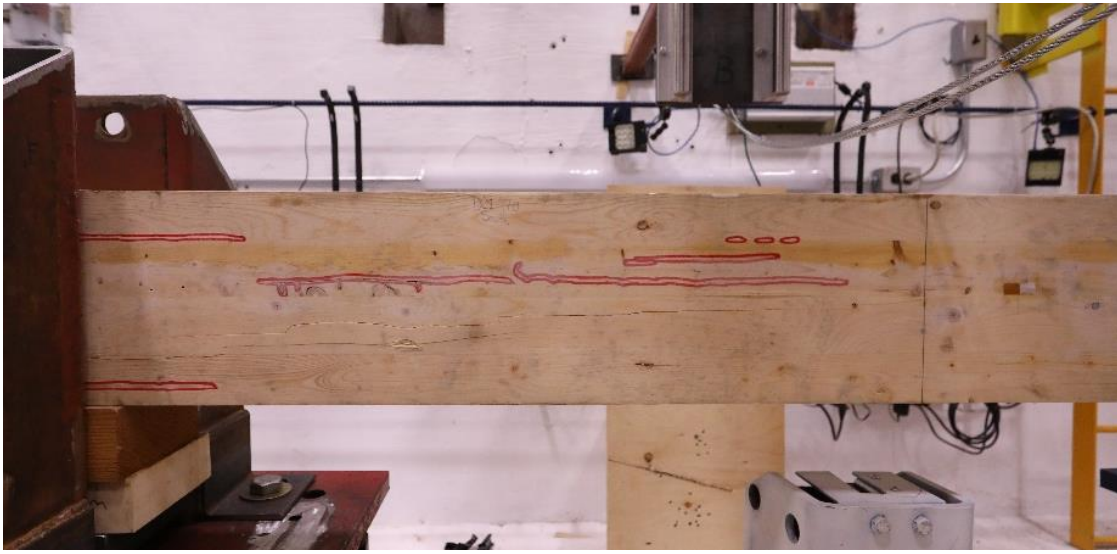


(b) Dynamic resistance and displacement over time

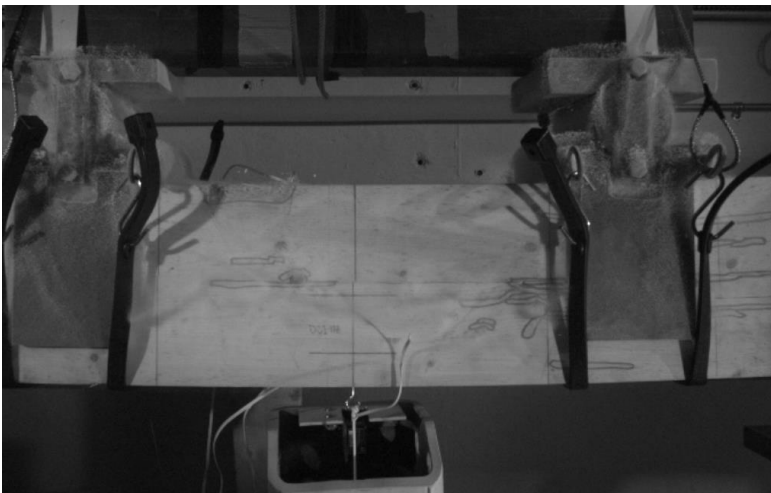


(c) Dynamic resistance and tensile strain over time

Figure B-0-21: Dynamic Test Results for Specimen DC1-178



(a) Specimen after testing



(b) Footage from the high-speed phantom camera of specimen at its maximum deflection



(c) West end of specimen after failure

Figure B-0-22: Damage for Specimen DC1-178

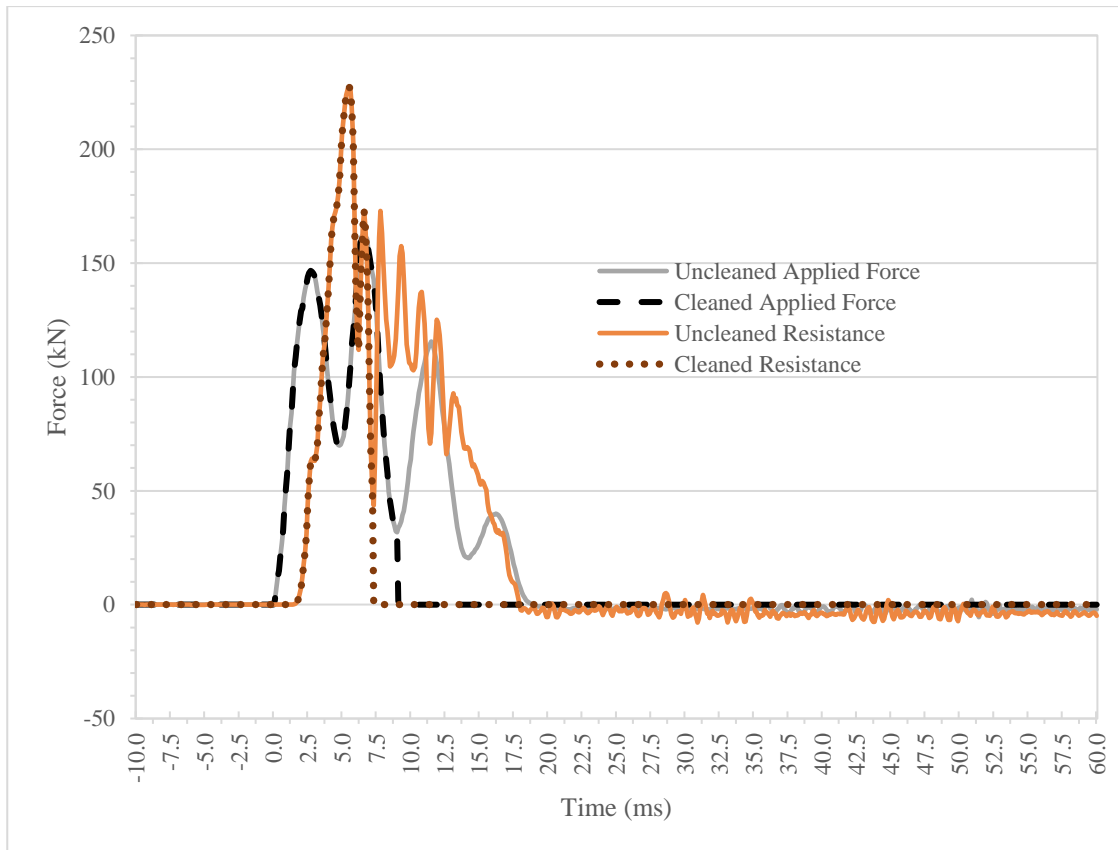
Specimen: DC2-178

Peak Force: 162.1 kN

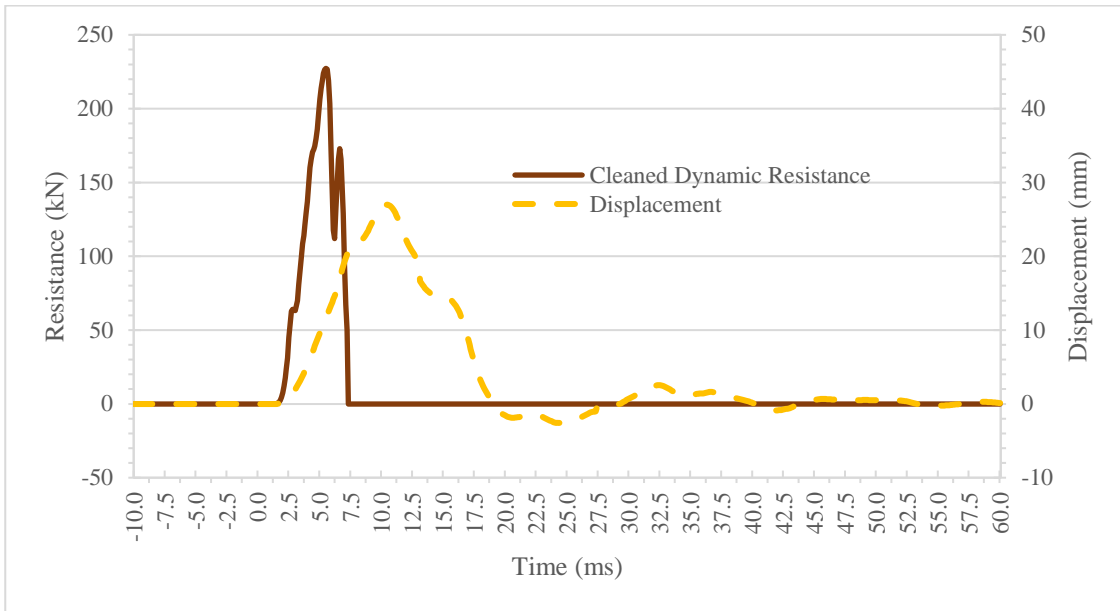
Load Duration: 9.1 ms

Peak Resistance: 226.0 kN

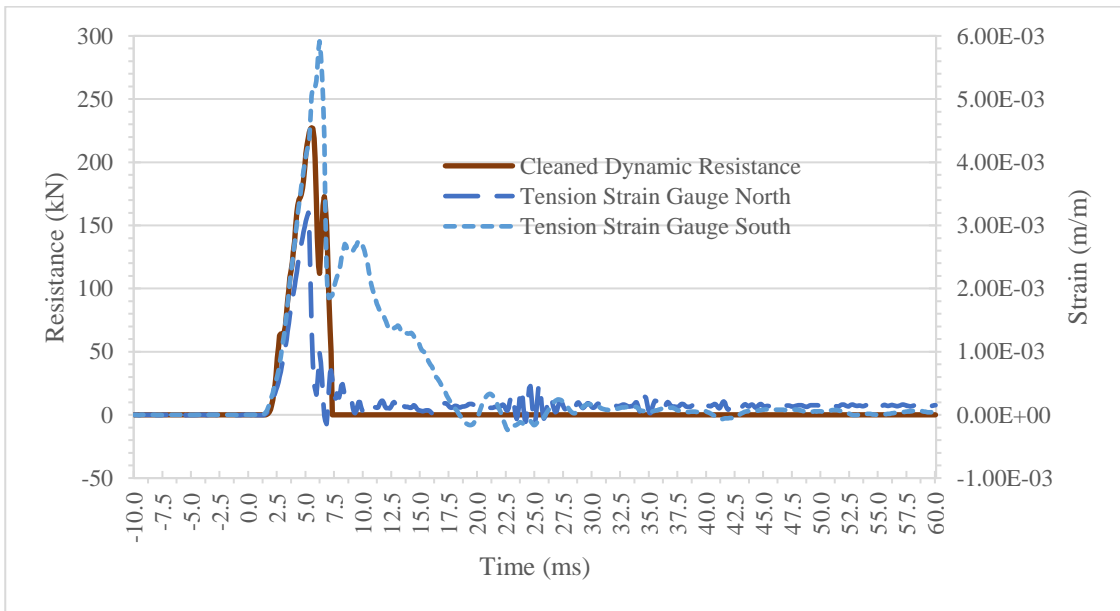
Failure Mode: Flexure



(a) Cleaned and uncleaned applied load and dynamic resistance over time

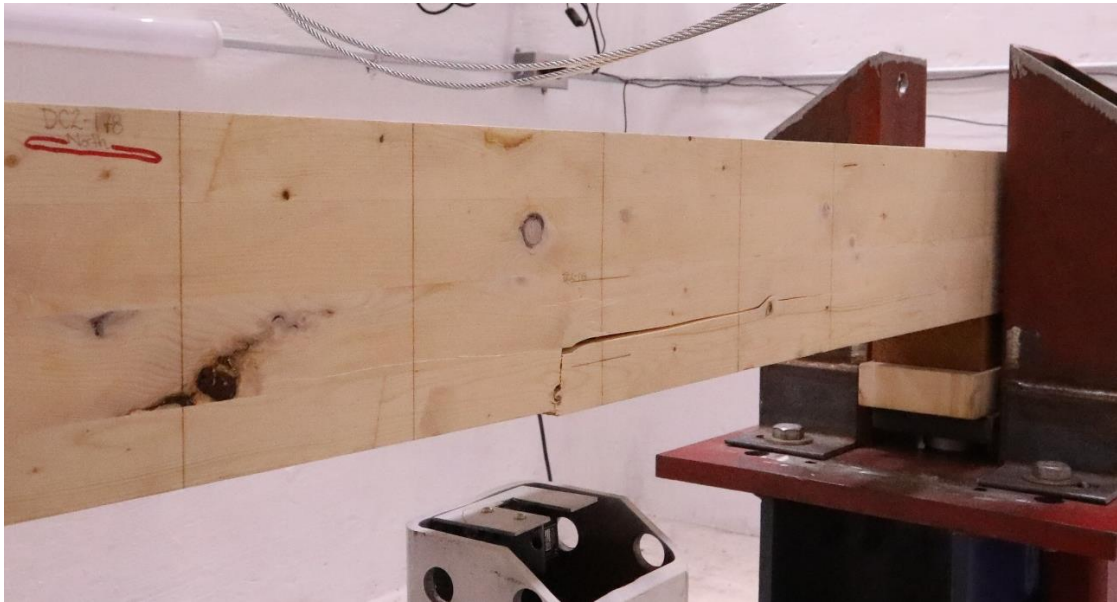


(b) Dynamic resistance and displacement over time

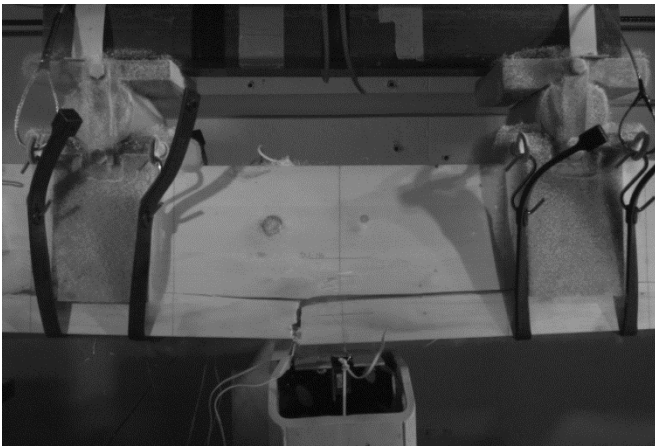


(c) Dynamic resistance and tensile strain over time

Figure B-0-23: Dynamic Test Results for Specimen DC2-178



(a) Specimen after testing



(b) Footage from the high-speed phantom camera of specimen at its maximum deflection



(c) Underside of specimen after failure

Figure B-0-24: Damage for Specimen DC2-178

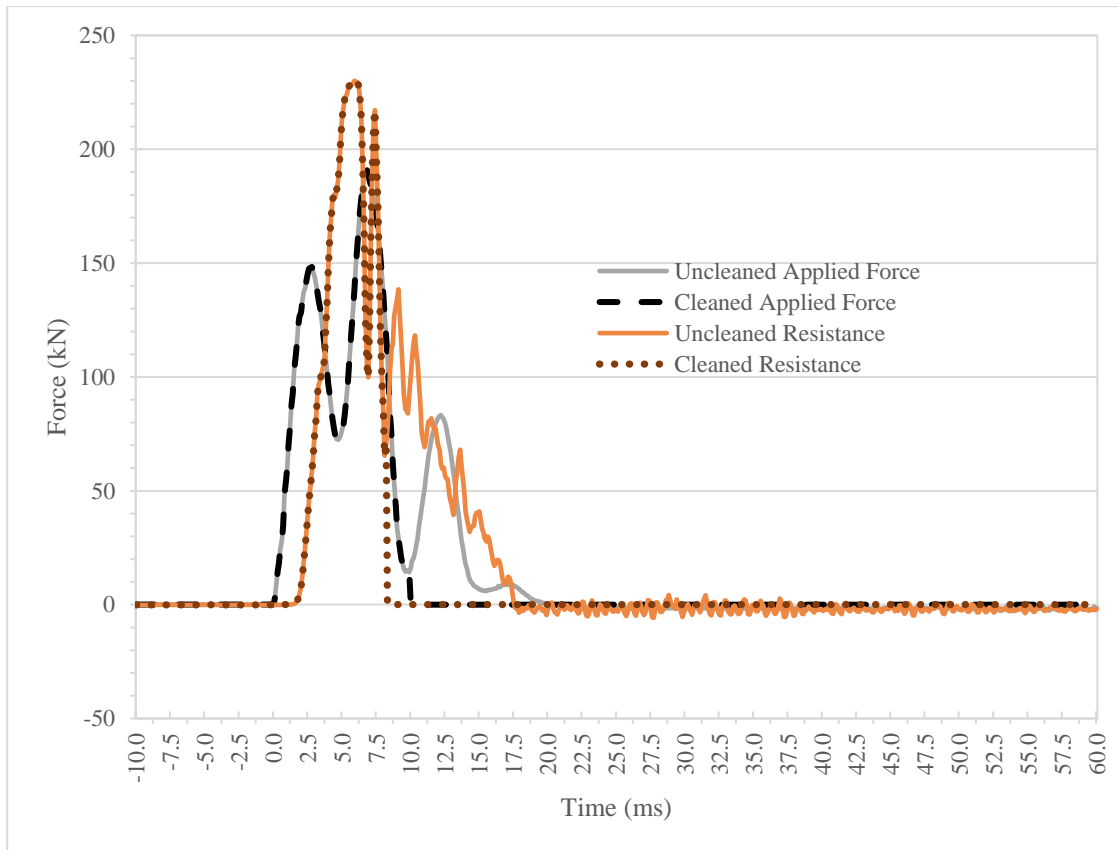
Specimen: DC3-178

Peak Force: 190.8 kN

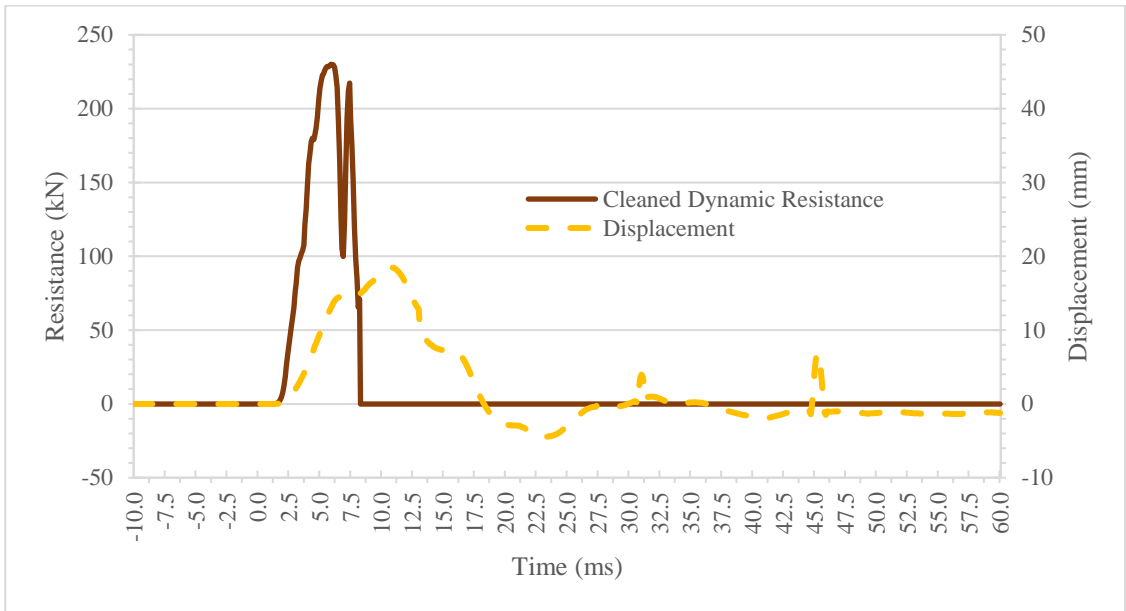
Load Duration: 10.0 ms

Peak Resistance: 229.2 kN

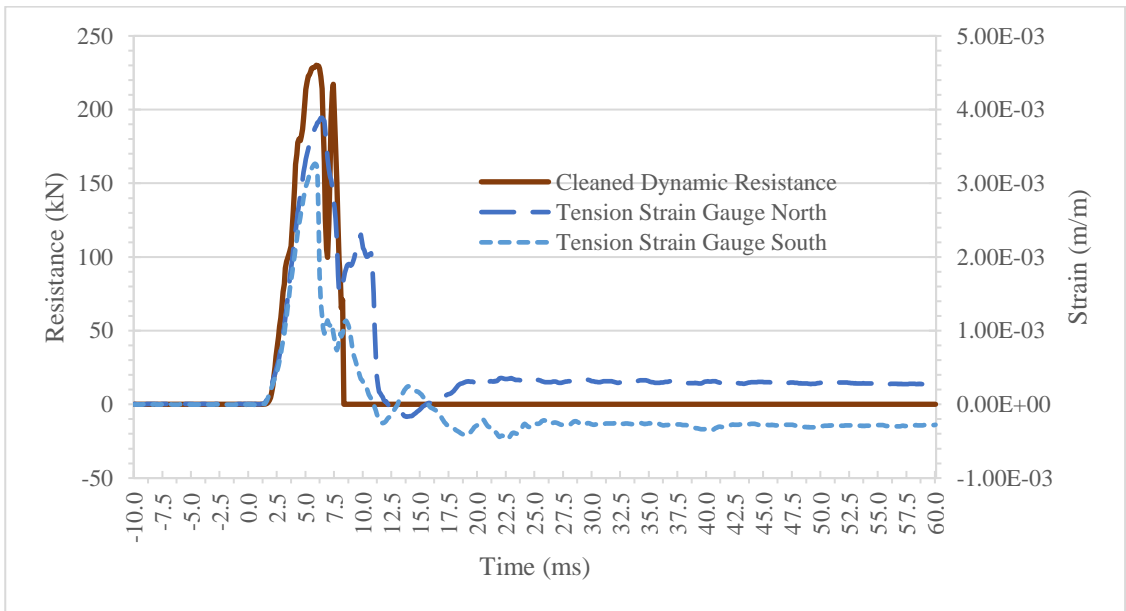
Failure Mode: Flexure



(a) Cleaned and uncleaned applied load and dynamic resistance over time

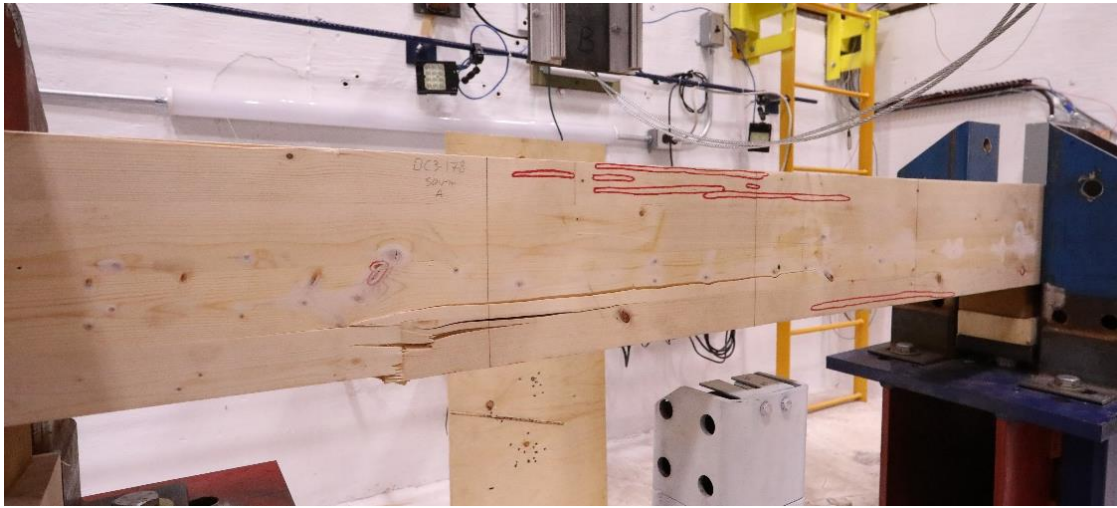


(b) Dynamic resistance and displacement over time

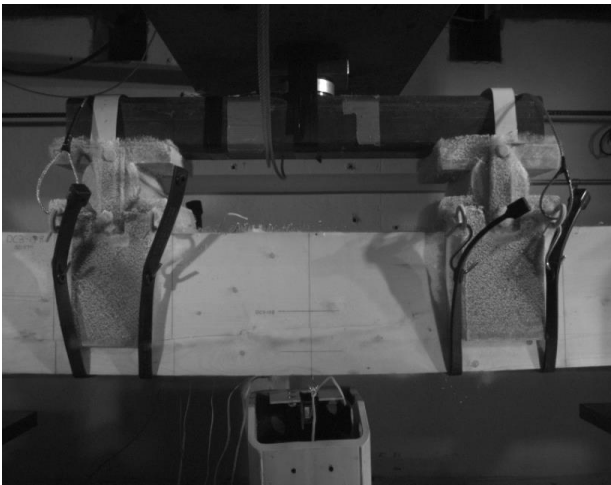


(c) Dynamic resistance and tensile strain over time

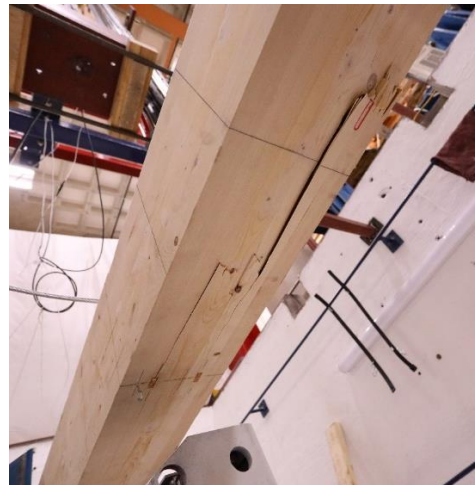
Figure B-0-25: Dynamic Test Results for Specimen DC3-178



(a) Specimen after testing



(b) Footage from the high-speed phantom camera of specimen at its maximum deflection



(c) Underside of specimen after failure

Figure B-0-26: Damage for Specimen DC3-178

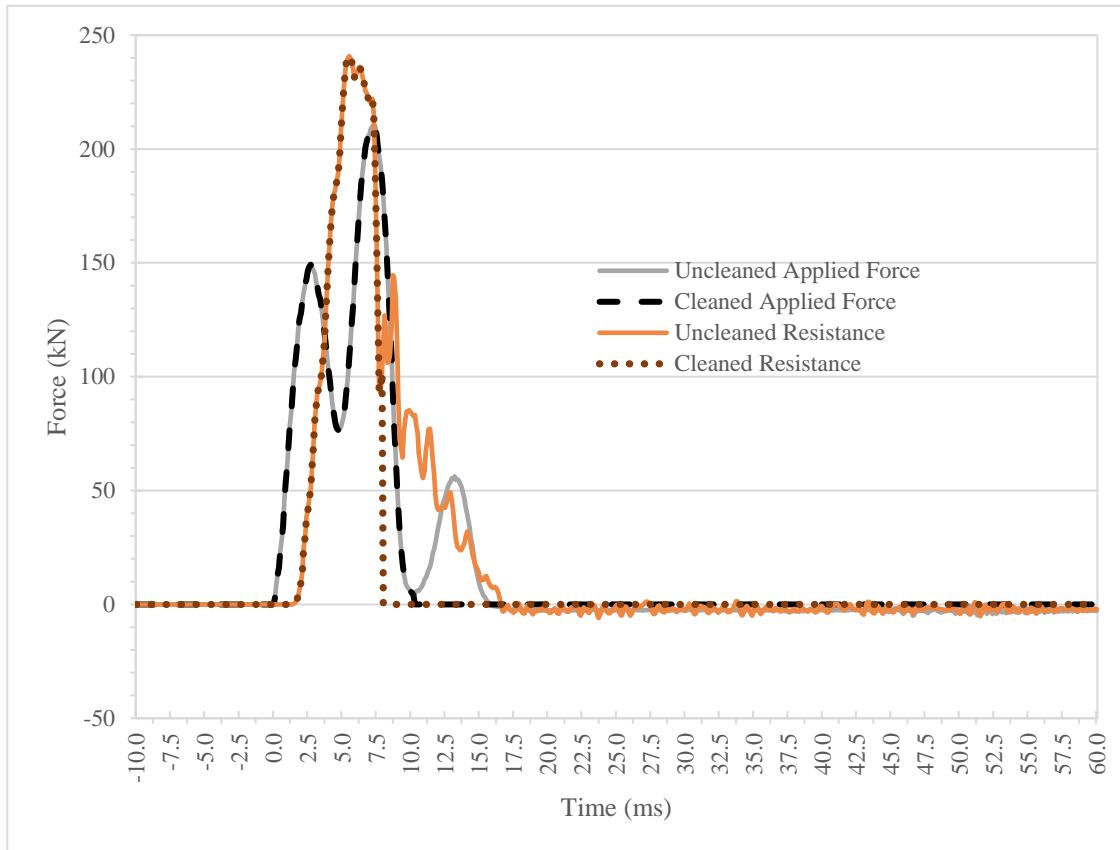
Specimen: DC4-178

Peak Force: 210.4 kN

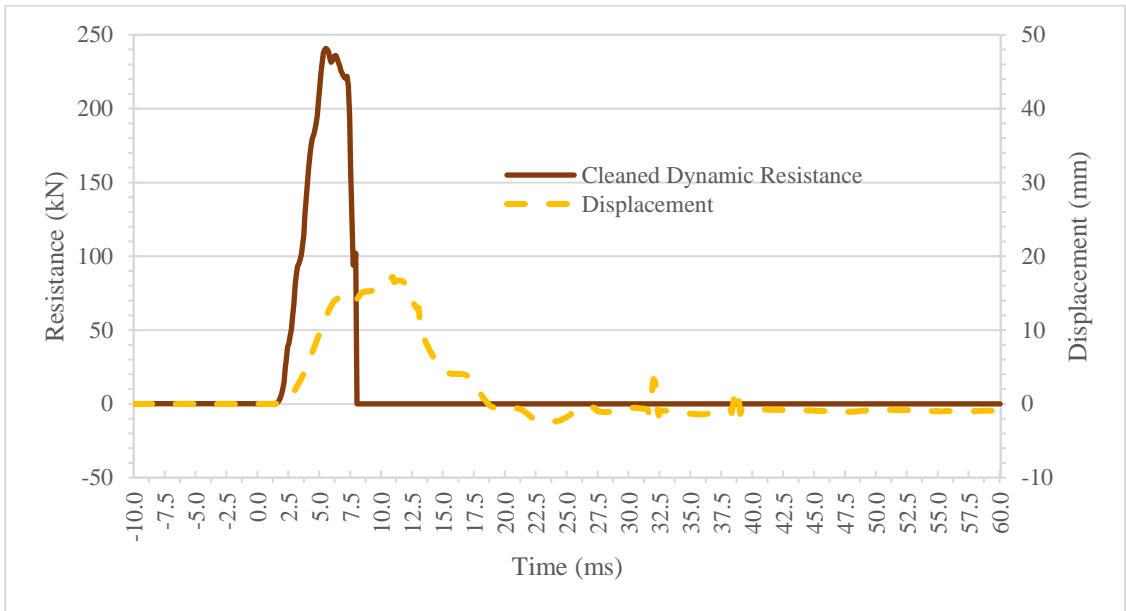
Load Duration: 10.3 ms

Peak Resistance: 239.4 kN

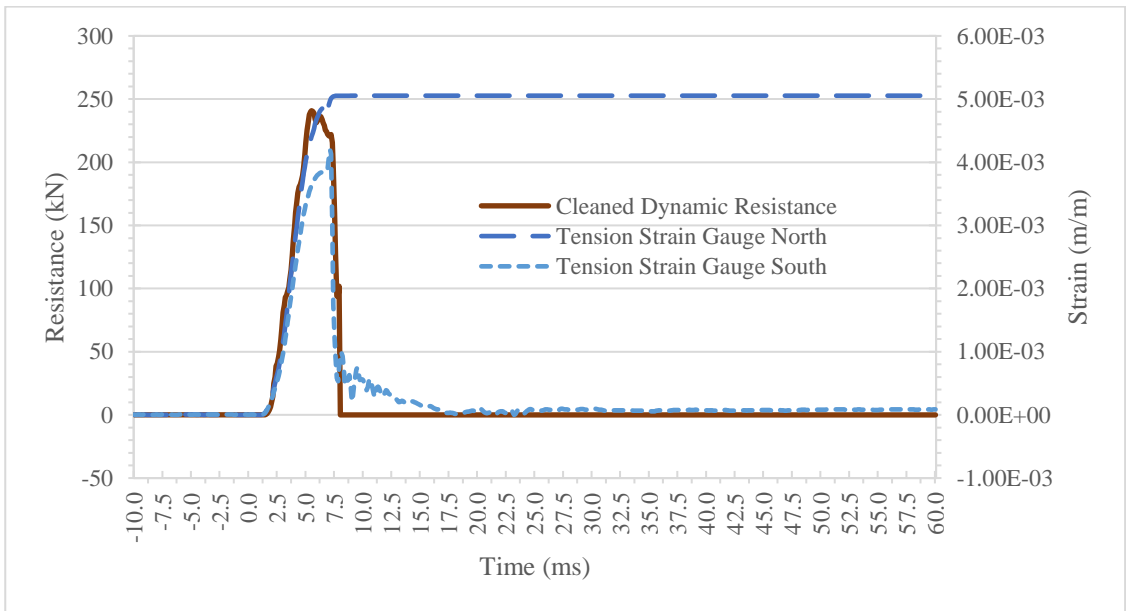
Failure Mode: Flexure



(a) Cleaned and uncleaned applied load and dynamic resistance over time

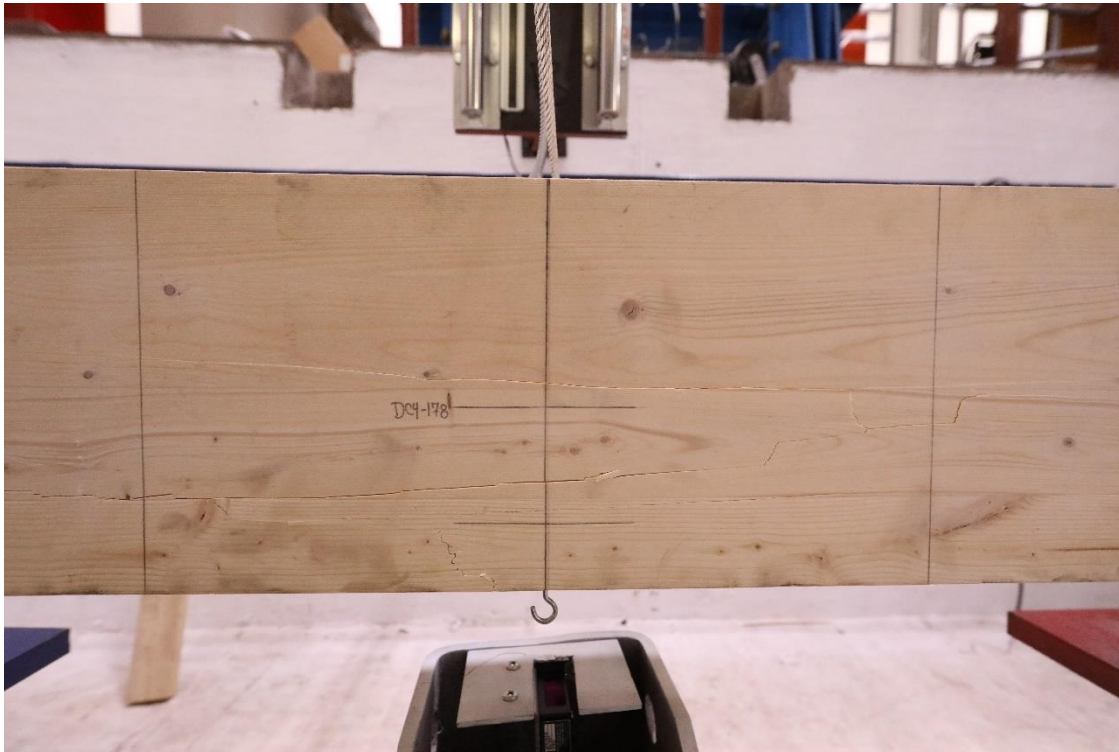


(b) Dynamic resistance and displacement over time

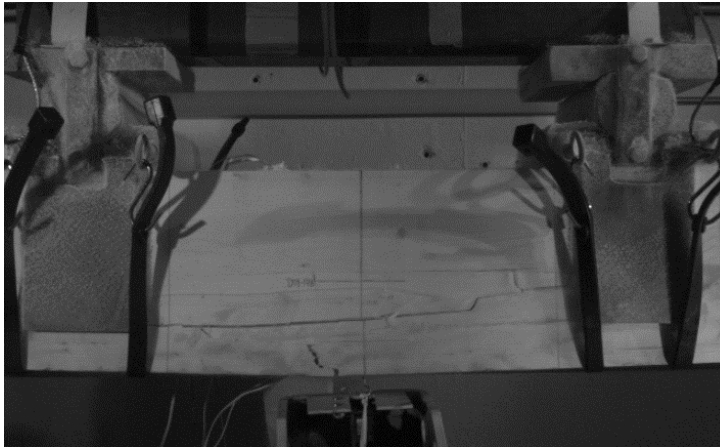


(c) Dynamic resistance and tensile strain over time

Figure B-0-27: Dynamic Test Results for Specimen DC4-178



(a) Specimen after testing



(b) Footage from the high-speed phantom camera of specimen at its maximum deflection



(c) Underside of specimen after failure

Figure B-0-28: Damage for Specimen DC4-178